Imperial College London
Department of Surgery and Cancer

Cable-Driven Parallel Robot for Transoral Laser Phonosurgery

Ming Zhao

April 2021

Supervised by
Dr. George P. Mylonas
Mr. Guri Sandhu
Prof. Daniel S. Elson

Submitted in part fulfilment of the requirements for the degree of Doctor of Philosophy in Clinical Medicine Research (Surgery and Cancer) of Imperial College London and the Diploma of Imperial College London

Declaration

I hereby declare that this thesis presents original work of the author and any work that is not from the author has been accordingly referenced.

Ming Zhao

'The copyright of this thesis rests with the author. Unless otherwise indicated, its contents are licensed under a Creative Commons Attribution-Non Commercial 4.0 International Licence (CC BY-NC).

Under this licence, you may copy and redistribute the material in any medium or format. You may also create and distribute modified versions of the work. This is on the condition that: you credit the author and do not use it, or any derivative works, for a commercial purpose.

When reusing or sharing this work, ensure you make the licence terms clear to others by naming the licence and linking to the licence text. Where a work has been adapted, you should indicate that the work has been changed and describe those changes.

Please seek permission from the copyright holder for uses of this work that are not included in this licence or permitted under UK Copyright Law.'

Abstract

Transoral laser phonosurgery (TLP) is a common surgical procedure in otolaryngology. Currently, two techniques are commonly used: free beam and fibre delivery. For free beam delivery, in combination with laser scanning techniques, accurate laser pattern scanning can be achieved. However, a line-of-sight to the target is required. A suspension laryngoscope is adopted to create a straight working channel for the scanning laser beam, which could introduce lesions to the patient, and the manipulability and ergonomics are poor. For the fibre delivery approach, a flexible fibre is used to transmit the laser beam, and the distal tip of the laser fibre can be manipulated by a flexible robotic tool. The issues related to the limitation of the line-of-sight can be avoided. However, the laser scanning function is currently lost in this approach, and the performance is inferior to that of the laser scanning technique in the free beam approach.

A novel cable-driven parallel robot (CDPR), *LaryngoTORS*, has been developed for TLP. By using a curved laryngeal blade, a straight suspension laryngoscope will not be necessary to use, which is expected to be less traumatic to the patient. Semi-autonomous free path scanning can be executed, and high precision and high repeatability of the free path can be achieved. The performance has been verified in various bench and *ex vivo* tests. The technical feasibility of the *LaryngoTORS* robot for TLP was considered and evaluated in this thesis. The *LaryngoTORS* robot has demonstrated the potential to offer an acceptable and feasible solution to be used in real-world clinical applications of TLP.

Furthermore, the *LaryngoTORS* robot can combine with fibre-based optical biopsy techniques. Experiments of probe-based confocal laser endomicroscopy (pCLE) and hyperspectral fibre-optic sensing were performed. The *LaryngoTORS* robot demonstrates the potential to be utilised to apply the fibre-based optical biopsy of the larynx.

Acknowledgements

First of all, I would like to express my appreciation to Prof. Daniel Elson and Dr. George Mylonas, for providing me with such an excellent opportunity to work in this fantastic field of surgical robotics. I would like to express my sincere gratitude to Prof. Daniel Elson for granting me precious opportunities to collaborate with other outstanding researchers and explore more possibilities of my project during my PhD. I would also like to especially thank Dr. George Mylonas for giving me enormous freedom and trust to indulge in the research topic I am interested in.

Additionally, my thanks go to Dr. Guri Sandhu for sharing clinical knowledge of transoral laser microsurgery in the process of preparing cadaver trial. Despite the inability to continue the cadaver trial due to the COVID-19 pandemic, I still learnt a lot from the process we worked together. Special thanks to Prof. Neil Tolley, Dr. George Garas and Dr. Taranjit Tatla for their clinical advice and help.

Also, I would like to say thank you to my colleagues and friends, Joric, Alexandros, Mark, Jianyu, Ji, Fernando, Alex, James, Khushi, Haojie, Eftychios and Jian for your generous help and robust support in my project, warm talks when I felt down and also the lovely video for my wedding.

As always, the biggest thank you goes to my family for their love and support. Without their understanding, care and company, I could not have been where I am today.

Contents

Declaration ..... **II**

Abstract ..... **III**

Acknowledgements ..... **IV**

Contents ..... **V**

List of Figures ..... **IX**

List of Tables ..... **XXI**

Abbreviations ..... **XXII**

Chapter 1 Introduction **1**

1.1 An Overview of the Development of Medical Lasers 1

1.1.1 A brief introduction of medical lasers 1

1.1.2 Laser delivery techniques 3

1.1.2.1 Computer-assisted laser scanning and autonomous surgery 4

1.1.2.2 Surgical robotics and medical lasers 8

1.2 Cable-Driven Parallel Robot and Potential Surgical Applications 10

1.2.1 CDPR for endoscopic surgery 10

1.2.2 CDPR for laparoscopic surgery 15

1.3 Motivation and Objectives 17

1.4 Thesis Structures and Contributions 18

1.5 Publications 19

1.6 Technical Acknowledgements 20

Chapter 2 Transoral Laser Surgery of the Larynx 22

2.1 Transoral Laser Surgery of the Larynx 22

2.2 Free Beam Delivery Technique in Transoral Laser Surgery 24

2.3 Fibre Delivery Technique in Transoral Laser Surgery 29

2.4 Related Works of Fibre-Based Laser Scanning 35

2.5 Summary 43

Chapter 3 Simulation, Design and Prototypes 44

3.1 Modelling and analysis of CDPM for TLP 44

3.1.1 CDPM 44

3.1.2 Versatility of configuration of CDPM 46

3.1.3 Kinematic analysis 51

3.1.4 Dynamic analysis 52

3.1.5 Tension forces distribution 53

3.1.6 Controllable workspace 54

3.2 Configuration Simulation of the CDPM for TLP 56

3.2.1 Required specifications of TLP CDPM 57

3.2.2 Configuration simulation and controllable workspace 58

3.2.3 Collision-free operation simulation 63

3.3 Designs and prototypes of TLP CDPR 64

3.3.1 Design and prototype of *EndoTORS* robot 65

3.3.2 Design and prototype of *LaryBladeTORS* robot 67

3.3.3 Design and prototype of *LaryngoTORS* robot 70

3.4 Conclusion 76

Chapter 4 Validations and Feasibility Considerations 78

4.1 Motion Control 78

4.2 Validations of *LaryngoTORS* Robot 80

4.2.1 Bench Test 81

4.2.1.1 Semi-autonomous path scan 81
4.2.1.2 Force exertion of *LaryngoTORS* end-effector 90
4.2.2 *Ex vivo* Test 93
4.2.2.1 *Ex vivo* tissue test of laser ablation 94
4.2.2.2 *Ex vivo* tissue test of the semi-autonomous free path scan 96
4.3 Second version of *LaryngoTORS* robot 98
4.4 Discussion 103
4.4.1 Technical feasibility analysis 103
4.4.1.1 Workspace and customised laryngeal blade 103
4.4.1.2 Ventilation and smoke management 104
4.4.1.3 Biocompatibility and sterilisation 105
4.4.1.4 Electrical safety 105
4.4.1.5 Fibre compatibility 105
4.4.1.6 Device ergonomics 106
4.4.2 Technical comparison with other fibre-based laser scanning robotics systems 106
4.5 Conclusion 110
Chapter 5 Robotic-assisted Fibre-based Optical Biopsy of the Larynx 111
5.1 Fibre-based Optical Biopsy of the Larynx 112
5.2 Robotics-assisted Probe-based Confocal Laser Imaging of the Larynx 114
5.2.1 Materials and Methods 114
5.2.2 Experimental Results 117
5.2.3 Discussion 120
5.3 Robotics-assisted Hyperspectral Fibre-optic Sensing of the Larynx 120
5.3.1 Materials and Method 121
5.3.2 Experimental Results 123
5.3.3 Discussion 124
5.4 Conclusion 125
Chapter 6 Conclusion and Future Work 127

6.1 Achievements of this Thesis 127

6.2 Future Research Directions 129

6.3 Conclusion 132

References 134

Appendix A: A Qualitative Study of Photometric Stereo in Robotics Surgery via Fibre-delivered Illumination 151

A.1 Learning-Based Photometric Stereo 151

A.2 Materials and Method 152

A.3 Experimental Results 154

A.4 Discussion 156

Appendix B: Copyright Permissions for usage of Figures 157

List of Figures

Figure 1.1: Absorption curves over wavelength of four typical components of tissue: oxyhaemoglobin, deoxyhaemoglobin, melanin and water [1].....3

Figure 1.2: a) A slit lamp-coupled argon laser used for retinal photocoagulation [2]. b) An example of flexible optic-fibre (CO2 laser fibre, Omni Guide Inc, USA). c) An optic-fibre working with a flexible endoscope [53].....4

Figure 1.3: Left column: An example of fractional ablative laser resurfacing of facial skin. (A) immediately after treatment, (B) The photo was taken 3 days after the laser treatment [56]. *Right column: Two representative results of different areas of the retina after PRP* [60].....5

Figure 1.4: a) Schematic of the optical path of the femtosecond laser beam and OCT beam. The optical axes of these two beams are aligned from the scanner to the eye [66]. *b) An example of the surgical plan interface of a cataract laser system (LenSx, Alcon, Inc. USA). The capsulotomy pattern and lens segmentation pattern are defined on the microscopic and OCT image. The laser cutting depth range is adjusted and decided on the OCT image* [67].....6

Figure 1.5: a) The microscope view of a perfectly circular shaped laser anterior capsulotomy. b) The microscope view of the cataract lens after laser fragmentation and segmentation [61]. 7

Figure 1.6: The combination of the laser fibre and robotic instrument. a) A CO2 laser fibre was fixed on the robotic instrument with rubber rings [85]. *b) A fibre guiding tube (FlexGuide, OmniGuide Inc., USA) is held by a robotic needle driver* [86]. *c) A robotic laser introducer (Intuitive Surgical Inc., USA) is used to manipulate the distal tip of a laser fibre* [84].....9

Figure 1.7: a) A robotic system with two concentric tube manipulators designed for transurethral laser prostate surgery [87]. *b) Micron, a hand-held robotic tool for intraocular laser photocoagulation* [88]

©2014 IEEE. 9

Figure 1.8: The first CYCLOPS working prototype at its early stage of development [97] *© 2014 IEEE.*. 11

Figure 1.9: a) Close-up view of the ESD CYCLOPS with fully deployed scaffold [98]. *b) The undeployed scaffold, the size is 30 × 18 × 72.9 mm3 (W × H × L)* [99]..... 12

Figure 1.10: Overview of the ESD CYCLOPS system. (A) The deployable scaffold with a soft silicone sleeve. (B) Bowden cables used to guide the cables from the motor units to the end-effectors and the flexible instruments along the endoscope. (C) The flexible GI endoscope for visualisation. (D) A flexible injector needle is inserted into the endoscope working channel and used to lift the mucosa by injecting a liquid. (E) The diathermy surgical tool. (F) A cable splitter for cables separation between the motor units and CDPM. (G) Motor units for controlling two instruments, each motor unit containing 6 motors. (H) Instrument control device for opening and closing of the forceps [95] *©2018 IEEE.* ... 13

Figure 1.11: In vivo test - pre-clinical validation in the porcine intestine tract [95] *©2018 IEEE.*..... 14

Figure 1.12: The early prototype of the inflatable scaffold [95] *©2018 IEEE.*..... 14

Figure 1.13: The conceptual setup of the CDPM laparoscopic instrument mounted as a robotic surgical instrument on the da Vinci® robot [99]. 15

Figure 1.14: The conceptual scheme of SIMPLE [99]. 16

Figure 1.15: The prototype of SIMPLE. a) Side view from the outside of the exterior scaffold and b) Inner view [99]. 16

Figure 2.1: The setup of transoral laser laryngeal microsurgery [116]..... 24

Figure 2.2: The laser manipulator with a focus adjustment unit coupled with a surgical microscope [115]. 25

Figure 2.3: a) Selection of various laryngoscopes used in TLM for larynx exposure. b) Insertion of suspension laryngoscope [115]..... 25

Figure 2.4: Specially designed microlaryngeal instruments, such as forceps and scissors, for use in TLM

[115]. 25

Figure 2.5: a) Schematic of a combination of a surgical microscope and a laser manipulator with the scanner; b) Example scanning patterns: straight line, arc line and circle, the position and the rotation of patterns can be adjusted by a joystick [117]. 26

Figure 2.6: The setup of the suspension the laryngoscope introduced into the larynx [121]. 27

Figure 2.7: The IIT robot-assisted laser phonomicrosurgery system: a) the motorised laser scanner; b) the surgical microscope with a built-in CCD camera and c) the virtual scalpel control system [120]. .. 28

Figure 2.8: A "steady-hand" microsurgery platform and the setup for transoral microlaryngeal surgery [122]. 28

Figure 2.9: a) side view [124] *and b) front view* [82] *of settings of the multi-arm da Vinci® surgical robotic system in TORS: ① FK retractor, ② stereo endoscope, ③ teleoperated robotic instruments.* ... 29

Figure 2.10: Comparison of the triangular shape between instruments for oropharyngeal and hypopharyngeal lesion [126]. 30

Figure 2.11: *a) Flex Robotic system* [129] *and b) compatible flexible instruments* [104]. 31

Figure 2.12: a) the end tip of the flexible robot with a camera, light source, and two flexible instruments [101]. *b) demonstration of the operational position of the Flex Robotic System in the larynx* [130]. 31

Figure 2.13: Endo views of the right side cordectomy successfully performed by Flex Robotic System with two flexible instruments: a Maryland dissector (*) and a laser fibre holder (#) with a CO2 laser [128]. 32

Figure 2.14: Instrument operation of Flex Robotic System [131]. 32

Figure 2.15: a) the da Vinci® SP robotic system with b) three instrument arms and one endoscopic arm. All robotic arms have two joggle joints [79]. 33

Figure 2.16: a) the settings of da Vinci® SP in TORS and b) the end view in transoral phonosurgery [79]. 34

Figure 2.17: Comparison of the endo view between a) da Vinci® Xi and b) da Vinci® SP in TORS. The endoscope of da Vinci® SP can be driven close to the surgical field and offers better visualisation of the lesion in the larynx [126]. 34

Figure 2.18: (a) μRALP robotic surgery system, picture taken during the last cadaver trial; (b) multifunctional tip, include a stereo camera, light source, fluorescence imaging, laser deflecting micro-mechanism unit [143] *©2017 IEEE.* 36

Figure 2.19: (a) SOI-based micromirror and (b) the components of the micromirror [143] *©2017 IEEE.* 36

Figure 2.20: (a) the micro piezoelectric linear actuator (2.8 x 2.8 x 6 mm) and (b) the assembly of the SOI-based micromirror and the piezoelectric linear actuators [143] *©2017 IEEE.*..... 37

Figure 2.21: The CAD design (a) and the assembled prototype of the SOI mirror-based miniature laser scanner [143] *©2017 IEEE.* 37

Figure 2.22: The functioning principle of the laser beam steering mechanism [143] *©2017 IEEE.* 37

Figure 2.23: a) Conceptual design of the magnetic laser scanner as a flexible endoscopic tip [140] *and b) Schematic illustration of one DoF magnetic control and the focusing laser light on the target with collimating and focusing lenses* [139] *©2017 IEEE.*..... 39

Figure 2.24: Components (a) and assembled prototype (b) of the magnetic laser scanner [140]. 40

Figure 2.25: (a) Experimental setup of the magnetic laser scanner, including optical fibre, lenses, laser source, and camera. (b) Schematic presentation of the 2 DoF control and the laser beam focusing on the target [141] *©2019 IEEE.*..... 40

Figure 2.26: a) experimental result of circular path following [139] *©2017 IEEE, and repeatability tests of the scan trajectories for 10 passes of a '8' shape b)* [140]. 41

Figure 2.27: a) Conceptual set-up of the image-guided focal positioning teleoperated robotic endoscope for non-contact tissue laser ablation. b) The extendable monolithic continuum structure. c) The endoscope tip, sampled surface phantom and master controller. d) Example of the colour map (CM) with associated laser caustics (LC) of distance [144] *©2019 IEEE*..... 42

Figure 3.1: An example demonstrates the core concept of CDPM [151]. 45

Figure 3.2: a) The cable-driven Skycam used for sports events broadcasting [148]. *b) Prototype of the CoGiRo, a CDPM for goods handling* [149]. 46

Figure 3.3: Conceptual design of a cable-driven storage and retrieval system [152] *©2018 IEEE.* 46

Figure 3.4: Possible DoF and motion types of CDPM (T stands for translation and R for rotation) [155]. 47

Figure 3.5: Two types CDPM: a) Fully restrained and b) under-restrained CDPM [151]. 48

Figure 3.6: Some examples of different controllable workspaces (regions in grey) generated by different cable configuration within the same available space (circle) provided by the supporting scaffold. . 50

Figure 3.7: A single over-tube parallel robot mechanisms driven by six cables. a) The base frame {B} and the moving frame {P}. b) Six entry points (Bi) on the scaffold and six attachment points (Pi) on the over-tube. 51

Figure 3.8: Structure analysis of the parallel robot mechanism. a) Loop closure (Po, Pi, Bi, B0) and b) Forces and torques on the over-tube. 52

Figure 3.9: The flowchart of the framework of the TLP CDPM simulation. 56

Figure 3.10: Configuration simulation and controllable workspace. a) Configuration simulation with the dimensions. b) Controllable workspace without rotation. c) Controllable workspace with rotation [168] *©2020 IEEE.* 59

Figure 3.11: Scheme of the position of the tumour region and the operative area [102]. 60

Figure 3.12: Different configurations (rotated the current configuration 45, 90, 135, 225, 270 and 315 degrees respectively). 61

Figure 3.13: Corresponding workspace of the laser arm for the 6 configurations shown in figure 3.12. .. 61

Figure 3.14: The total controllable workspace of the laser fibre arm for the 6 configurations in figure 3.12 (28 mm diameter cylinder with 11 mm depth). 62

Figure 3.15: Relationship between a maximum range of translation and rotation and the distance between entry points in one plane. a) Longest distance between entry points: larger range of translation but smaller range of rotation. b) Short distance between entry points: smaller range of translation but larger range of rotation. 62

Figure 3.16: Result of the simulation operation of laser pattern scanning with collision detection. 64

Figure 3.17: Render and core components of the EndoTORS robot, showing the CDPMs at the end of an endoscope. 65

Figure 3.18: Surgical instruments, ENDOEYE FLEX endoscope and the close view of the deflectable tip (left) and the setup of TOUSS (right). A support arm held an ENDOEYE FLEX 3D endoscope. The surgeon and assistant stuff wore 3D glasses to watch the 3D imaging offered by the 3D endoscope [169]. 66

Figure 3.19: Early prototype of the EndoTORS robot. a) Front view of the robot showing the scaffold, cables and two over-tubes. b) and c) The robot mechanism assembled on a tip-articulating endoscope...... 66

Figure 3.20: a) The EndoTORS robot connected with the motor units via cable splitters. b) The head and neck phantom with a mouth gag which is used to keep the mouth open. 67

Figure 3.21: a) Setup of the EndoTORS robot on a head and neck phantom. b) Endoscopic view of the robot scaffold. A 20 mm diameter plastic cylinder with a 2D vocal cord lesion image was inserted in the phantom to simulate a target for laser incision. 67

Figure3.22: a) Flex Retractor with curved laryngeal blades. b) The Curved laryngeal blade demonstrated with the Flex robotics system (Medrobotics Inc., USA) [172]. 68

Figure 3.23: 2 DoF rotations of the curved laryngeal blade of the Flex Retractor [103]..... 69

Figure 3.24: The render of LaryBladeTORS robot. a) overview, b) sideview and c) front view. 69

Figure 3.25: The prototype of LaryBladeTORS robot. a) side view, b) front view and c) view from camera, a red laser spot aiming beam projected on a paper screen placed at in front of the robot. 69

Figure 3.26: a) Side view of the curved laryngeal blade based CDPM. b) View of the inbuilt rail of the

curved laryngeal blade. 70

Figure 3.27: Conventional and video laryngoscope: Airtraq®NT video laryngoscopes (left), Macintosh laryngoscope (middle) and the new McGrath®MAC video laryngoscope (right) [175]. 70

Figure 3.28: Demonstration of the curvature of the laryngeal blade and the view axis of different direct laryngoscopes (top row) and indirect video laryngoscopes (middle and bottom rows) [174]. 71

Figure 3.29: Design of the LaryngoTORS robotic system. a) Side view showing the main parts: motor unit, handle, Bowden cables for cable transmission and the curved laryngeal blade with the scaffold. b) Inner view showing the cable transmission. A force sensor is used to achieve tension control. c) Top view of the robot body [168] *©2020 IEEE.* 72

Figure 3.30: Early prototype of the LaryngoTORS robot. 73

Figure 3.31: a) The motor mount unit, includes a base of the motor mount, an Oldham coupling and a cable spool. b) The force sensing unit, when the cable is transmitted through the pulley, the tension force can pass to the force sensor. c) Top view of the early prototype of the LaryngoTORS robot, six force sensing units are presented. 74

Figure 3.32: The side view and front view of the laryngeal blade of the early prototype LaryngoTORS robot [168] *©2020 IEEE.* 74

Figure 3.33: The detachable part (c) of the LaryngoTORS robot can be connected/disconnected from the robot (b) via cable connectors (a) [168] *©2020 IEEE.* 75

Figure 3.34: Schematic diagram of the positioning of LaryngoTORS robot in TLP (left) and demonstration of the operational position of the robot, based on a head and neck phantom (middle and right) [168] *©2020 IEEE.* 75

Figure 4.1: The workflow of the semi-autonomous free path scan. 82

Figure 4.2: The test setup: a) A laser was inserted in the over-tube, a red aiming beam is transmitted through the fibre. A USB camera with 6 LEDs provides the visualisation of the operation field. b) A paper screen mounted in front of the scaffold [168] *©2020 IEEE.* 84

Figure 4.3: The control panel interface of the semi-autonomous free path scan (left) and the operation platform (right). The control panel interface includes 8 function buttons. ① push button: record the pose data of the control point; ② slider button: select the scan speed; ③ push button: generate the scan path; ④ push button: execute the path scan; ⑤ push button: save the current scan path; ⑥ push button: delete current control points and scan path; ⑦ push button: delete current generated path; ⑧ push button: display the imaging from the USB camera on the screen. 84

Figure 4.4: The bench test of a user-defined 6 × 2 mm arc line semi-autonomous scan on the paper screen. a) The camera view of 5 selected control points, b) control points (blue) and generated path (green), c) The actual executed scan path [168] *©2020 IEEE.* 85

Figure 4.5: The experimental results of the arc line scan. a) Path scan precision and b) scanning repeatability over 6 scans [168] *©2020 IEEE.* 85

Figure 4.6: The measured tension forces (top) and respective measured motor positions (bottom) for three consecutive arc scans [168] *©2020 IEEE.* 86

Figure 4.7: The experimental results of the horizental line path scan. a) 4 control points (blue) described horizontal line path (green). b) The actual executed scan path detected by the camera. c-d) Precision and repeatability over 6 scans [168] *©2020 IEEE.* 87

Figure 4.8: The experimental results of the vertical line path scan. a-b) The camera view of a 4 control points (blue) that described a vertical line path (green) (a) and the executed scan path (b). c-d) Scan precision and repeatability over 6 scans [168] *©2020 IEEE.* 87

Figure 4.9: The bench test of semi-autonomous path scan at increasing velocities of 1.0, 1.5, 2.0, 2.5 and 3.0 mm/s. a) A positive optical tracking marker was attached at the end of over-tube. b) Two calibrated Optitrack Prime 13 cameras. c) The measured results of path scan with different speed via optical tracking [168] *©2020 IEEE.* 88

Figure 4.10: The setup of the force exertion test of the end-effector of LaryngoTORS robot. a) The overview of the experimental setup. b) The front view of the CDPM which the end-effector at the homing position. c) The top view of the experimental setup. The end-effector was aligned with the centre of

the force sensor and was mounted on it. The axes directions of the force test are axes are shown in b) and c). 91

Figure 4.11: Measured results of exerted forces and cable tensions along +X, -X, +Y, -Y, +Z and -Z axes directions. 92

Figure 4.12: The medical laser equipment: a) 272 µm laser fibre (FlexiFib-SU fiber, LISA Laser Products GmbH, Germany). b) Setup of the thulium YAG laser device (RevoLix jr, LISA Laser Products GmbH, Germany). The laser fibre was connected to the laser aperture. A footswitch pedal was used to control the laser output. c) An example of laser setting screen. The laser output power was set to 3 W at CW mode. 94

Figure 4.13: a) Rear view of the tissue holder, a piece of chicken tissue was screwed on the tissue holder. b) Front view of the tissue holder, the chicken tissue was used to simulate the right-side vocal cord. c) Attached the tissue holder at the front of the robot. 95

Figure 4.14: a-f) Time sequence of the procedure of the laser ablation on a piece of chicken tissue [168] *©2020 IEEE.* 95

Figure 4.15: The result of the ex vivo tissue laser ablation. A 7×4 mm sized piece of chicken tissue was successfully removed. The incision path was an approximately 10 × 5 mm arc line[168] *©2020 IEEE.* 96

Figure 4.16: The ex vivo semi-autonomous laser path scan along with the straight (top row) and arc (bottom row) margins of the attached target [168] *©2020 IEEE.* 97

Figure 4.17: Ex vivo laser arbitrary path scans, The scan paths shaped as a number "3" (top row) and a letter "D" (bottom row) [168] *©2020 IEEE.* 97

Figure 4.18: Results of laser cutting with different laser power and scanning speeds. a) 1 W, 2 mm/s. b) 5 W, 2 mm/s. c) 3 W at 0.5, 1.5 and 3 mm/s. 98

Figure 4.19: a) Conceptual schematic of the second version of LaryngoTORS robot. b) The manufactured LaryngoTORS robot based on the new design. c) The new laryngeal blade is semi-closed which can

keep the mouth open and a mouth gag is not required. 100

Figure 4.20: a-b) Side and front view of the rod on the handle. c) The rod can be fitted in a suspension supporter (image source: Charing Cross Hospital, London, UK). 100

Figure 4.21: a) A pair of bent miniature grasping forceps (8593HM, KARL STORZ, GmbH., Germany). b-c) The front and side view of the LaryngTORS robot with the miniature grasping forceps. 101

Figure 4.22: a) The AirSim Advance X head and neck phantom (TruCorp Ltd., Ireland). b) The exposure of the larynx of the phantom. c) A piece of the right-side vocal cord was grasped and held by the miniature grasping forceps. (image source: Charing Cross Hospital, London, UK). 101

Figure 4.23: a) The laryngeal blade can be connected/disconnected via cable connectors. b) The detached right-hand side and left-hand side laryngeal blade. 102

Figure 4.24: a-b) The front view of the right-hand side and left-hand side CDPM. c-d) The performance of two side CDPMs was checked with the laser fibre and aiming beam. 102

Figure 4.25: Two tubes are attached next to the camera—one for air jet ventilation and another one for smoke aspiration. 104

Figure 5.1: A typical confocal image of healthy mucosa (left) and a typical example of the confocal image of SCC (right) [185]. 113

Figure 5.2: The Cellvizio confocal laser imaging system. a) The GastroFlex UHD probe. b) The Cellvizio system. c) The captured imaging displayed on the monitor. 115

Figure 5.3: The experimental setup: a) Overview of the LaryngoTORS robot. b) Side view of the CDPM with a GastroFlex UHD probe. The probe is attached at the end of the over-tube. c) Front view of the robot with the probe. A USB camera was utilised to offer the vision of the operation field. d) A test target sample was attached to the front of the robot. e) The end view from the camera. 116

Figure 5.4: Two porcine tissue samples stained with 0.02% acriflavine solution (a) and with 0.1% fluorescein solution (b). 116

Figure 5.5: Two representative results of the pCLE test on lens paper (top row) and porcine tissue (bottom

row). The endo view from the camera (left) and the acquired confocal imaging (right) are demonstrated. 118

Figure 5.6: The camera view (top row) and confocal imaging (bottom row) captured at 4 control points. 119

Figure 5.7: a-b) Demonstration of the generated scan path of confocal scanning in 3D and 2D respectively. c) The result of video mosaicking of the confocal laser scanning executed on the porcine fat tissue [210]. 119

Figure 5.8: The schematic diagram of the setup of the hyperspectral optical-fibre sensing system. A two fibre cores probe is used to work with LaryngoTORS robot. One fibre is connected to a spectrometer and another fibre is connected to a white light source. 121

Figure 5.9: a) The dimensions of the cross-section of the probe, the unit of all parameters is in mm. b) The end face of the probe was polished by SpecPro Connector Polisher. c) The manufactured two cores fibre probe. The bright one was connected with the light source. The dark one was used to receive the reflection signals and transmitted to the spectrometer. 121

Figure 5.10: a) The experimental setup of the hyperspectral optical-fibre sensing system. Two fibre terminators with SMA 905 connectors were used to fix and connect two proximal ends to the spectrometer and the light source. b) A piece of clean porcine tissue, without any stained, was fixed on the target holder and mounted at the front of the robot. 122

Figure 5.11: The acquired reflectance spectra of the porcine fat tissue. The reflectance is relatively high at the 500 nm to 650 nm region. 124

Figure 5.12: The captured reflectance spectra of the porcine muscle tissue. The reflectance curve is nearly flat, and reflectance is low in all range. 124

Figure 6.1: The top view of the design (a) and manufactured (b) LaryngoTORS robot. 130

Figure 6.2: a) A test target made by silicone rubber was fixed on a target holder, which was attached to the front of the robot. b) The estimated normal map of the target surface via an uncalibrated photometric

stereo fully convolutional network (UPS-FCN). 131

Figure 6.3: The laryngoTORS robot with a mono (a) and stereo (a) camera. 132

Figure A.1: The experimental setup: a) A test target made by silicone rubber. b) The test target was fixed on a target holder c) Front view of the robot with the fibre. A white light beam was delivered by the fibre. A USB camera was utilised to offer the vision of the target field. d) The test target was attached to the front of the robot. e) A fibre terminator with SMA 905 connectors was used to fix and connect the proximal end of the fibre to the light source. 153

Figure A..2: Sample images captured under different light beam directions with high light intensity. 154

Figure A.3: Sample images captured under different light beam directions with medium light intensity. 154

Figure A.4: Sample images captured under different light beam directions with low light intensity. 155

Figure A.5: The generated normal map of the target surface under high, medium and low light intensity level are demonstrated at the bottom row in column a), b) and c) respectively. The images at the top row are used to indicate the light intensity level. The images shown in the middle row are captured only under the light source of the camera. 155

List of Tables

Table 3.1: Type of DoF and the minimum number of cables for over-tube steering 49

Table 3.2: Required specifications of TLP CDPMs 58

Table 3.3: Coordination of cable location 59

Table 4.1:Experimental results of precision and repeatability with different scan paths at a speed of 0.5 mm/s 88

Table 4.2: Experimental results of precision with various speeds 89

Table 4.3: Maximum forces measured in both directions along the three axes. 91

Table 4.4: Technical comparison with other fibre-based laser scanning robotics system 107

Abbreviations

BPH	Benign prostatic hyperplasia
CAD	Computer-assisted design
CDPM	Cable-driven parallel mechanism
CDPR	Cable-driven parallel robot
CLE	Confocal laser endomicroscopy
CO2	Carbon dioxide
CT	Computed tomography
CW	Continuous wave
DoF	Degrees-of-freedom
Er: YAG	Erbium: yttrium aluminium garnet
ESD	Endoscopic submucosal dissection
FOV	Field of view
FPS	Frames per second
Ho: YAG	Holmium: Yttrium-aluminium-garnet
HoLEP	Holmium laser enucleation of the prostate
HSI	Hyperspectral imaging
LASIK	Laser assisted in situ keratomileusis
MAE	Maximum absolute error
MIS	Minimally invasive surgery
MRI	Magnetic resonance imaging
Nd: YAG	Neodymium: yttrium-aluminium-garnet
NOES	Natural orifice endoluminal surgery

NOTES	Natural orifice transluminal endoscopic surgery
OCT	Optical coherence tomography
pCLE	Probe-based confocal laser endomicroscopy
PD	Proportional-derivative
PDL	Pulsed dye laser
PDR	Proliferative diabetic retinopathy
PDT	Photodynamic therapy
PLA	Polylactide
RMS	Root-mean-square
RMSE	Root-mean-square error
SCC	Squamous cell carcinomas
SILS	Single incision laparoscopic surgery
TLM	Transoral laser microsurgery
TLP	Transoral laser phonosurgery
TORS	Transoral robotic surgery

Chapter 1

Introduction

1.1 An Overview of the Development of Medical Lasers

1.1.1 A brief introduction of medical lasers

The first working solid-state laser, Ruby laser, developed by Theodore Maiman in 1960, was based on the principle of stimulated emission theorised by Albert Einstein [1], [2]. After that, various types of laser were developed and applied in clinical use. The neodymium-doped yttrium-aluminium-garnet (Nd: YAG) laser was introduced in 1961 and first used in the treatment of vascular lesions in 1964; the carbon dioxide (CO_2) laser was developed in 1964 and first applied in otolaryngology and gynaecology in 1972 and 1973 respectively; the Argon laser was introduced in 1962 and used in retinal photocoagulation in the late 1970s [3]–[5].

Currently, medical lasers are widely used in ophthalmology [2], [6]–[10], dermatology [11]–[15], urology [16]–[22], gynaecology [23]–[25], gastroenterology [26]–[29], otolaryngology [30]–[35], neurosurgery [36]–[38] and general surgery etc. [1], [39], [40]. In general, for a desired clinical application, a suitable laser system can be decided based on three parameters: laser wavelength, energy/power and pulse duration. Usually, different components of tissue will have different absorption peaks over different wavelengths. Figure

1.1 shows absorption curves of four typical components of tissue: oxyhaemoglobin, deoxyhaemoglobin, melanin and water. Erbium: yttrium aluminium garnet (Er: YAG) lasers and CO_2 lasers can be used to vaporise the water within tissue to perform tissue cutting or ablation because water absorbs the light these lasers emit. Oxyhaemoglobin and deoxyhaemoglobin absorb a high proportion of light from Argon laser, Nd: YAG potassium titanyl phosphate (KTP) laser and pulsed dye laser (PDL). Therefore, these lasers can be utilised in photocoagulation. The 755 nm Alexandrite laser is commonly used in the treatment of pigmented lesions since the energy is mainly absorbed by melanin. Based on the absorption characteristics of different tissues components, the laser wavelength will determine the penetration depth. Generally, a longer wavelength has a better penetration effect. However, only the laser energy which has not been absorbed by the tissues of previous layers can reach the target tissue. Laser energy/power, or energy/power density, will affect the level of tissue interaction and the size of the affected area. The energy/power setting depends on the tissue reaction: too low and the laser will not have sufficient effect, too high and the laser will generate thermal damage to surrounding non-target tissue. The pulse duration will determine the type of tissue interaction. A short pulse duration is used for photodisruption and a long duration or continuous wave (CW) is utilised for ablation, vaporisation or photocoagulation. For instance, in Q-switched Nd: YAG lasers, the pulse duration is commonly few nanoseconds and can be utilised for the photodisruption effect to be used in tattoo removal [11], [41] or in the treatment of vitreous floaters [42]. A long-duration pulse (dozens or hundreds of milliseconds) Nd: YAG laser can be used for superficial cutaneous vascular lesions due to the photocoagulation effect [43]. The effects of wavelength, energy/power and pulse duration with tissue have been summarised as the theory of selective photothermolysis proposed by Anderson and Parrish [44], [45].

With the advances of the past few decades, the three parameters of medical lasers have almost reached the boundary of the applicable range. In current medical laser applications, to the author's knowledge, the shortest wavelength is 193 nm. This wavelength is used by excimer lasers in laser assisted in situ keratomileusis (LASIK) surgery [46], [47]. The longest wavelength used is 10.6 μm in CO_2 lasers, which is mainly used in dermatology,

otolaryngology, gynaecology and general surgery. The minimum laser power is 50 mW, produced by diode lasers that are used in photodynamic therapy (PDT) [48]. In the treatment of benign prostatic hyperplasia (BPH), the maximum laser power can reach 300 W (980 nm diode laser) for vaporisation of the prostate [49]. The shortest pulse duration is only hundreds of femtoseconds for laser cataract surgery [8]. The infinite pulse duration, CW mode, can be provided by many laser types and is used in various clinical applications [40].

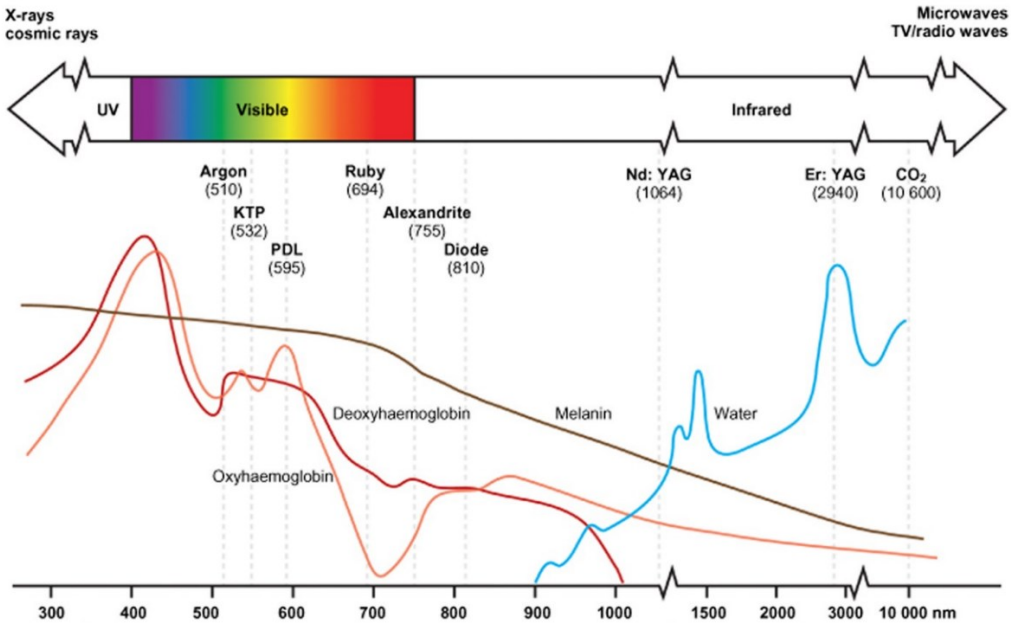


Figure 1.1: Absorption curves over wavelength of four typical components of tissue: oxyhaemoglobin, deoxyhaemoglobin, melanin and water [1].

The laser techniques have been well developed and widely used in clinical work. For known medical laser applications, proper laser interaction with the target tissue can be achieved with a relevant laser, and the outcomes of laser treatments are satisfactory [40], [45].

1.1.2 Laser delivery techniques

The development of laser delivery techniques also plays a vital role in medical laser applications. Highly steerable, accurate and reliable laser beam transmission are essential to ensure the outcomes of laser treatments. There are two main laser delivery approaches: free beam delivery and fibre delivery. In general, in the free beam delivery approach, the laser beam is transmitted by optical mirrors and lens and is limited by the constraint of the line-of-

sight. An articulated arm controlling reflection mirrors is a typical device used in free beam delivery [50]. A handpiece or a laser beam manipulator can be attached at the end of the arm. Figure 1.2 a) shows an example: the articulated arm was connected to a slit lamp in the treatment of retinal photocoagulation. In contrast, in the approach of fibre delivery, the laser beam is transmitted via a flexible optic-fibre (Fig 1.2 b) and the laser output aperture is usually inside the patient's body closed to the target tissue. The optical fibre can be inserted into the working channel of an endoscope and used in endoscopic surgery, such as lithotripsy of bile duct stones [51], [52] or urinary calculi [17], [19]. Initially, the controllability of the two approaches was quite limited. However, advanced computer-assisted laser scanning and robotic techniques significantly improved the outcomes of both the free beam delivery and fibre delivery approaches, respectively.

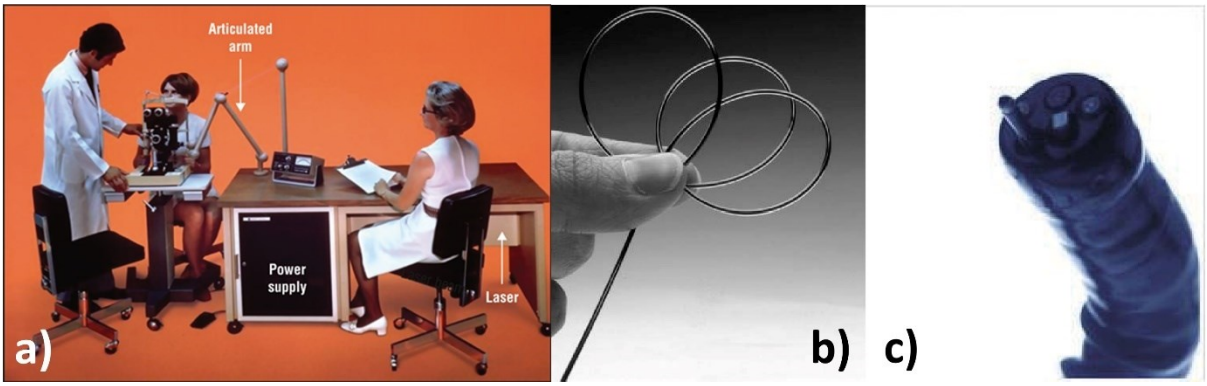


Figure 1.2: a) A slit lamp-coupled argon laser used for retinal photocoagulation [2]. *b) An example of flexible optic-fibre (CO2 laser fibre, Omni Guide Inc, USA). c) An optic-fibre working with a flexible endoscope* [53].

1.1.2.1 Computer-assisted laser scanning and autonomous surgery

The technique of computer-assisted laser scanning has been widely used in the free beam delivery approach in various medical laser applications, such as laser treatments in otolaryngology [54], [55], dermatology [56]–[58] and ophthalmology [46], [59]–[61]. In the computer-assisted laser scanning technique, a laser scanning unit is attached at the laser output aperture or combined with a handpiece or a laser manipulator. Usually, the laser scanning unit includes two mirror-based laser beam scanners that are used to manipulate the laser spot in the X and Y-axes, as well as a steerable focusing unit acting along the Z-axis (depth) to control the laser spot (Fig 1.4 a). With a laser scanning unit, patterns such as straight lines, arc lines,

circles or matrixes can be generated for performing vaporisation, incision, excision, ablation, or photocoagulation of soft tissue. Pattern scanning improves the surgical outcomes by accurate laser targeting and removing diseased tissue while preserving non-targeted areas. Due to the speed of pattern scanning, the operation time can be reduced, and the thermal damage is also limited, especially for non-sequential laser scanning. Thus, the depth and width of thermal damage can be adequately controlled and the surrounding tissue can be optimally protected from the thermal damage [58].

Figure 1.3 shows two typical applications of matrix pattern laser treatment in dermatology and ophthalmology: fractional ablative laser resurfacing of facial skin [56] and pan-retinal photocoagulation (PRP) for proliferative diabetic retinopathy (PDR) [60]. As demonstrated in Figure 1.3, in these two applications, numerous laser spots were generated on the facial skin and retina. It is rarely possible to finish the treatment manually in one time without the matrix scanning function.

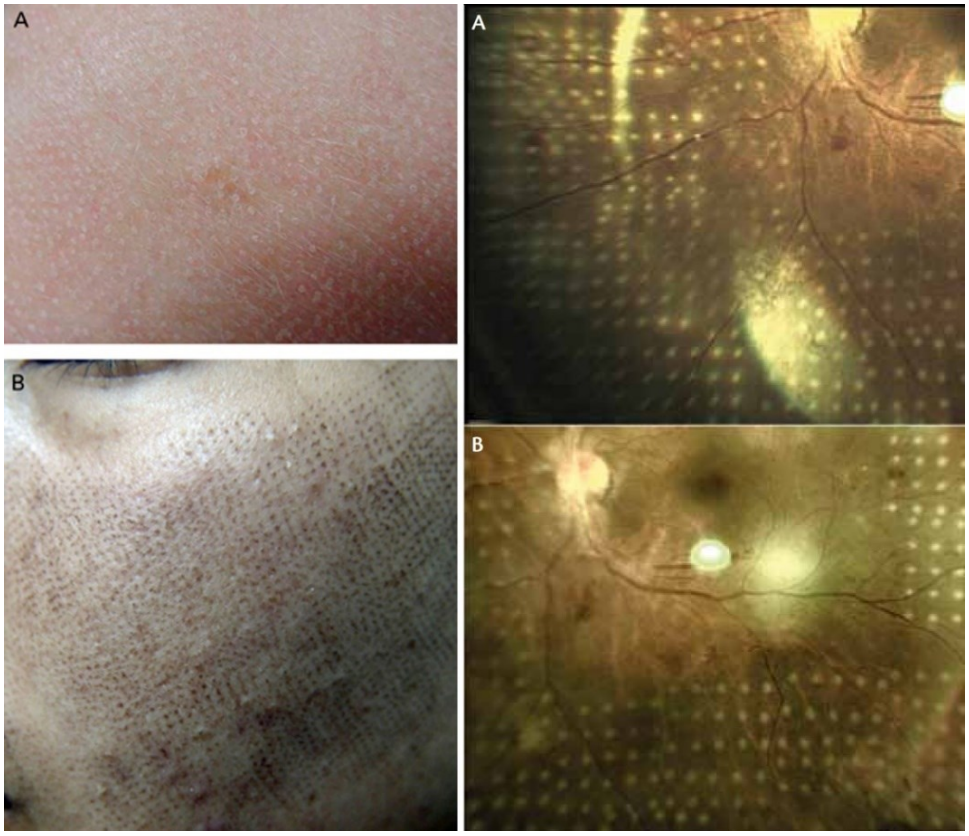


Figure 1.3: Left column: An example of fractional ablative laser resurfacing of facial skin. (A) immediately after treatment, (B) The photo was taken 3 days after the laser treatment [56]. *Right column: Two representative results of different areas of the retina after PRP* [60].

Furthermore, by combining the computer-assisted laser scanning technique with advanced computer vision and image navigation techniques, high-level autonomous laser surgery can be achieved. A well-known case is laser-assisted in situ keratomileusis (LASIK) surgery. In the wavefront-guided or topographic-guided LASIK surgery, once the planning stage is completed, the laser system will perform the surgery automatically [62]–[65]. Besides LASIK surgery, laser cataract surgery and retinal laser photocoagulation surgery also achieve high autonomy level. As shown in Figure 1.4, a surgical plan can be decided with the guidance of optical coherence tomography (OCT). The optical path of the femtosecond laser beam and OCT beam from the scanner to the eye are the same. The anterior capsulotomy pattern and lens segmentation and fragmentation pattern can be planned and registered on the OCT image. The anterior capsulotomy and fragmentation of the cataract lens can be executed by the laser scanning system precisely and safely [66]–[69]. Figure 1.5 demonstrates the representative results of anterior capsulotomy and cataract lens fragmentation performed by the OCT-guided laser system.

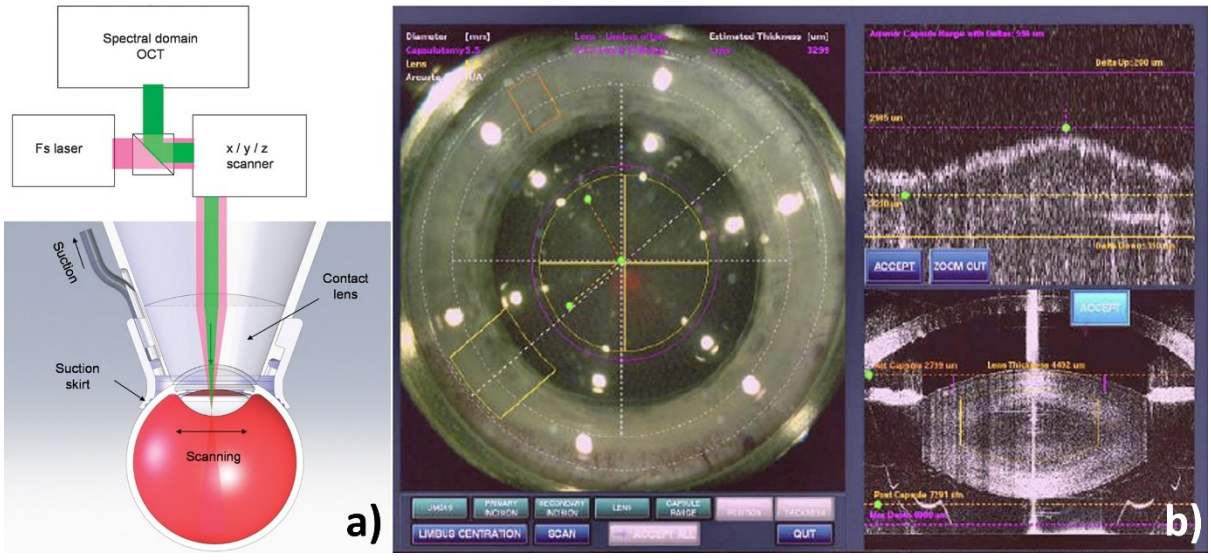


Figure 1.4: a) Schematic of the optical path of the femtosecond laser beam and OCT beam. The optical axes of these two beams are aligned from the scanner to the eye [66]. *b) An example of the surgical plan interface of a cataract laser system (LenSx, Alcon, Inc. USA). The capsulotomy pattern and lens segmentation pattern are defined on the microscopic and OCT image. The laser cutting depth range is adjusted and decided on the OCT image* [67].

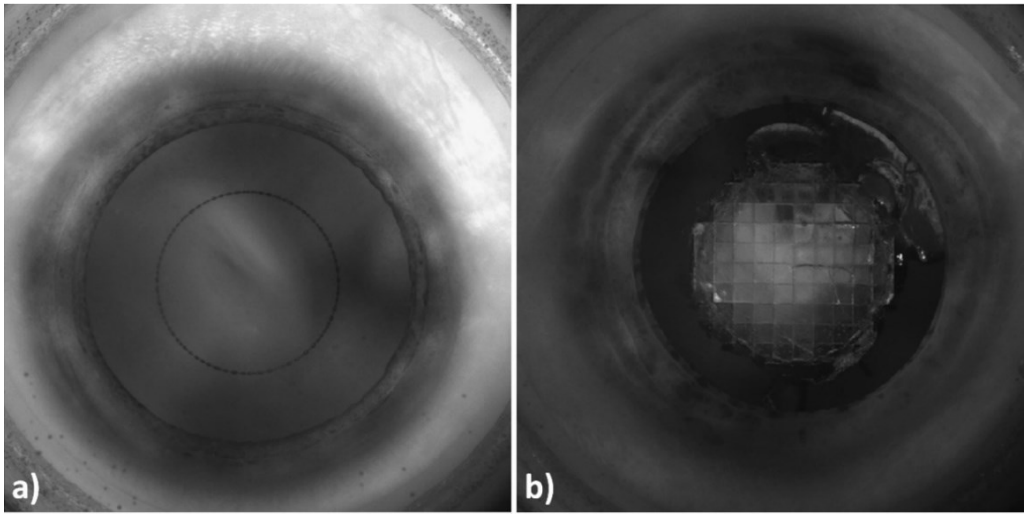


Figure 1.5: a) The microscope view of a perfectly circular shaped laser anterior capsulotomy. b) The microscope view of the cataract lens after laser fragmentation and segmentation [61].

The above examples have demonstrated the superior performance of the laser scanning technique in various clinical applications. The treatment outcomes of these applications have been significantly improved by the laser scanning technique [58], [63], [66], [67], [70], [71]. One common feature of these applications mentioned above is that the line-of-sight requirement can be fulfilled effortlessly. A scanning laser beam can be easily projected onto the target tissue such as the skin surface, cornea or retina under the line-of-sight constraint. However, in some clinical applications such as the Holmium: YAG (Ho: YAG) laser enucleation of the prostate (HoLEP) [19], [20] or laser lithotripsy of urinary calculi [17], [72], the line-of-sight constraint cannot be met so easily and a fibre delivery technique is required. Furthermore, in transoral laser microsurgery (TLM), advanced laser scanning technology can be utilised to generate accurate and highly repeatable path scans on the target soft tissue such as vocal folds [54]. However, a suspension laryngoscope needs to be used to create a straight working channel for the scanning laser beam. Complications caused by using a suspension laryngoscope are also introduced, such as lesions of the cervical vertebra and dental arch postoperative pain for the patient [73]. Besides the surgical trauma, the current laser scanning technique in TLM also has other limitations, such as poor manipulability and ergonomics (more details are presented in Chapter 2). An advanced method that can achieve safety and better performance than the current laser scanning technique is required for TLM.

1.1.2.2 Surgical robotics and medical lasers

With the advent of robotics technology, more and more surgical robots are used clinically [74], [75]. The most renowned is the da Vinci® surgical robot (Intuitive Surgical Inc., USA), which is widely used in clinical practice, with applications ranging from orthopaedic, urologic, cardiac, gastroenterological and gynaecologic surgery, to general surgery and neurosurgery [75], [76]. There are 5,669 da Vinci® systems installed globally and more than 7 million procedures performed to date (based on Intuitive Surgical company's data on 31st March 2020) [77].

The four robotic arm da Vinci® surgical systems, for example the da Vinci® Si/Xi, have been successfully used in laparoscopic surgery. However, there are still a number of limitations, such as invasive lesions and the setup time for robotic surgery being more prolonged than conventional minimally invasive surgery (MIS) and open surgery [78]. To reduce the invasive lesions and the setup time, robotics for single-access surgery, including single incision laparoscopic surgery (SILS), natural orifice endoluminal surgery (NOES) and natural orifice transluminal endoscopic surgery (NOTES) robotics are possible future directions of surgical robotics. The da Vinci® SP is an advanced system for single access robotic surgery. One endoscopic arm and three robotic instrument arms can be inserted through a single port cannula [79]. The da Vinci® SP system has been reported in transanal and transoral surgery [80]–[82]. Both the da Vinci® Si/Xi and da Vinci® SP surgical system can be used in medical laser surgery, such as laparoscopic endometriosis laser surgery [83] and transoral laser surgery [32], [35], [84]. Figure 1.6 shows the combination of the laser fibre and robotic instruments. When use of laser fibres was beginning, the laser fibre was simply fixed to the robotic tool with rubber rings (Fig 1.6a). Currently, a laser fibre guiding tube has been developed by medical laser corporations, where the distal tip of the tube can be held by the robotic instrument such as a needle driver (Fig 1.6b). Also, a specific robotic laser tool, a laser introducer, is available to use with da Vinci® surgical robotic systems (Fig 1.6c). The robotic instrument arm can steer the distal tip of the laser fibre. The controllability of the laser fibre operation can be significantly improved via robotic control [53].

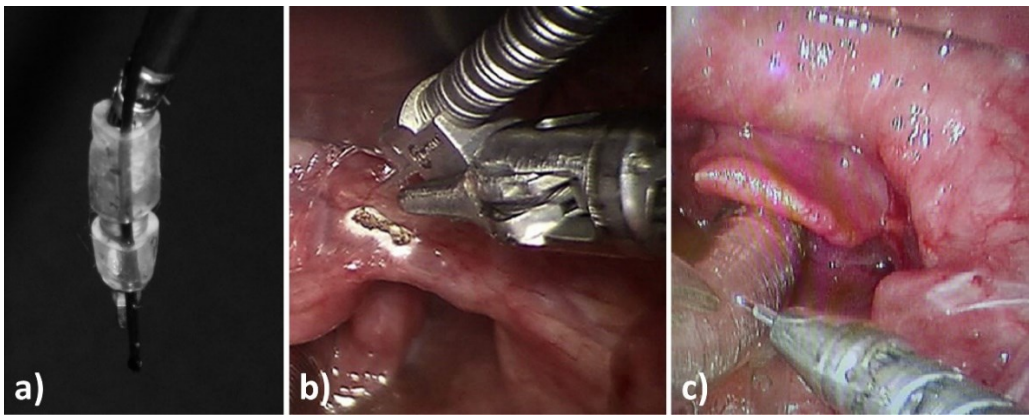


Figure 1.6: The combination of the laser fibre and robotic instrument. a) A CO2 laser fibre was fixed on the robotic instrument with rubber rings [85]*. b) A fibre guiding tube (FlexGuide, OmniGuide Inc., USA) is held by a robotic needle driver* [86]*. c) A robotic laser introducer (Intuitive Surgical Inc., USA) is used to manipulate the distal tip of a laser fibre* [84]*.*

Besides the combination of the laser fibre and the robotic instrument, as shown in Figure 1.6, the laser fibre can also be steered by other mechanisms developed for laser surgery. Figure 1.7a demonstrates a hand-held transendoscopic robotic system with two concentric tube manipulators designed for the laser treatment of BPH. The laser fibre can be inserted and accommodated in the concentric tube manipulator. The concentric tube mechanism is utilised to manipulate the distal tip of the fibre [87]. The Micron robotic system, as shown in Figure 1.7b, is a hand-held robotic tool for intraocular retina photocoagulation. The distal tip of the fibre probe is driven by a miniature Gough-Stewart platform which is a parallel mechanism actuated by six linear actuators. Highly accurate laser beam control was achieved via visual servoing control and precise miniature parallel mechanism [88].

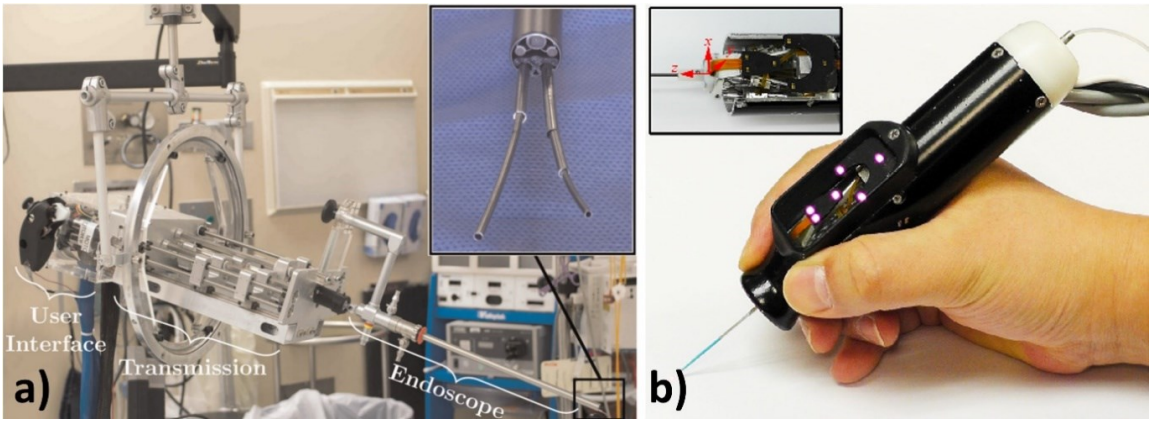


Figure 1.7: a) A robotic system with two concentric tube manipulators designed for transurethral laser prostate surgery [87]*. b) Micron, a hand-held robotic tool for intraocular laser photocoagulation* [88] *©2014 IEEE.*

High-level autonomous robotic surgery is also desired and pursued by scientists and engineers. Patients, surgeons and hospitals will benefit from the improved surgical precision and accuracy, enhanced efficiency and execution offered by robotic automation in surgery [89]–[91]. Several surgical robots have achieved a high autonomy level in their clinical applications, such as the TSolution One Surgical System (formerly called ROBODOC, THINK Surgical Inc., USA), which offered image-guided automatic knee arthroplasty and CyberKnife stereotactic radiosurgery system (Accuray Inc., USA) for autonomous radiation therapy with image-guided robotic positioning [92], [93]. Currently, to the author's knowledge, there is no fibre-delivered laser surgery robotic system that can achieve the autonomous performance realised in the wavefront-guided/topographic-guided LASIK surgery or OCT-guided laser cataract surgery mentioned in the previous section. However, with advanced mechanisms design and robotic automation technology, high autonomy level fibre-delivered robotic-assisted laser surgery is a promising direction to continue to pursue.

1.2 Cable-Driven Parallel Robot and Potential Surgical Applications

Cable-driven parallel robot (CDPR) is a type of parallel robot that uses cables as the actuation link [94]. CDPR have some intrinsic advantages such as a relatively large workspace, high payload and force transmission, high speed and accurate motions. Additionally, the entry and attachment points of cables are highly configurable, resulting in versatility in the workspace, and when the scaffold of CDPR is made foldable or inflatable, the mechanism can be rapidly deployed. Earlier research has shown that the CDPR can be designed for minimally invasive robotic surgery, such as neurosurgery, gastrointestinal (GI) surgery and laparoscopic surgery [95]–[99]. Although these prototypes are still in the pre-clinical stage, the studies have shown the technical advantages of the CDPR compared to other conventional medical devices. In this section, the CDPRs developed for endoscopic and laparoscopic surgery are presented.

1.2.1 CDPR for endoscopic surgery

In order to reduce the invasiveness of procedures, endoscopic techniques have been developed that gain access to the surgical field through natural orifices, such as NOES and NOTES. As

a result, the invasiveness is reduced when compared to open surgery and multiple keyholes laparoscopic surgery. Typically, the control of endoscopic instruments such as graspers is limited to the insertion and withdrawing through the endoscope's working channel. The positioning of the instruments is achieved predominantly by the motion of the steerable distal tip of the endoscope, and therefore this can not be performed independently from the field of view of the camera and, in case of multiple instruments, from each other. The independent control of multiple instruments is essential for performing triangulation and traction required to dissect tissue. Many surgery robotics research projects are focused on solving this problem [100].

CDPRs can be used to offer adequate triangulation and enhanced manipulability of the instruments in endoscopic surgery and therefore improve the performance and safety of surgical tasks. Additionally, the scaffold can be used to fixate the peripheral tissue and provide a stable operative space. The CYCLOPS robotic system is a CDPR for single-access, NOES and NOTES [97]. Figure 1.8 shows the early prototype of the CYCLOPS robot with core components. It is composed of a cable-driven parallel mechanism (CDPM) and a cable driving motor unit. The manipulator includes a rigid scaffold, one hollow shaft, six cables and one over-tube. The shape of scaffold is an open-ended bulb. The conventional endoscopic surgical instruments can be placed in the over-tube. The CDPM manipulator can manipulate the end tip of the surgical instrument, which are close to the operative field. High force delivery and good manipulability of surgical instruments can be achieved. The maximum execution force of the end-effector can reach up to 65 N [97].

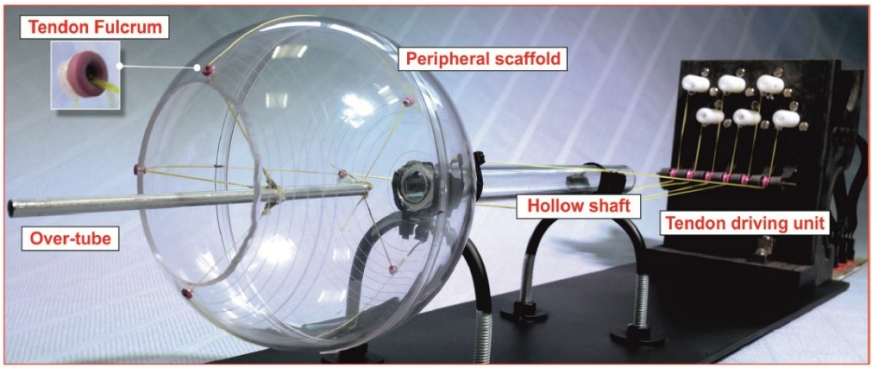


Figure 1.8: The first CYCLOPS working prototype at its early stage of development [97] *© 2014 IEEE.*

The ESD CYCLOPS robot is designed for GI surgery, especially for endoscopic submucosal dissection (ESD) in the GI tract. The ESD CYCLOPS is a bimanual CDPR system. Two six-cable CDPMs are used to manipulate surgical instruments which are placed in the over-tubes. Two over-tubes are accommodated in a deployable scaffold (Fig 1.9) [95]. The overview and main components of the ESD CYCLOPS system are shown in Figure 1.10.

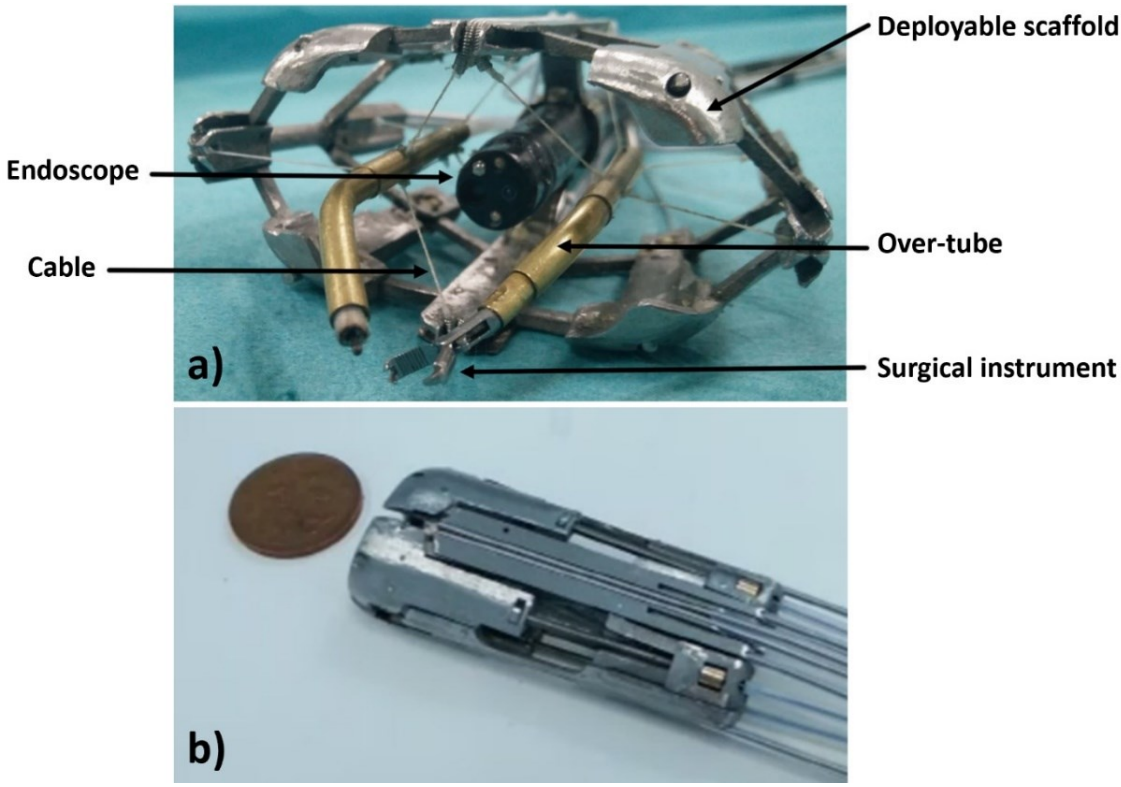


Figure 1.9: a) Close-up view of the ESD CYCLOPS with fully deployed scaffold [98]. *b) The undeployed scaffold, the size is 30 × 18 × 72.9 mm3 (W × H × L)* [99].

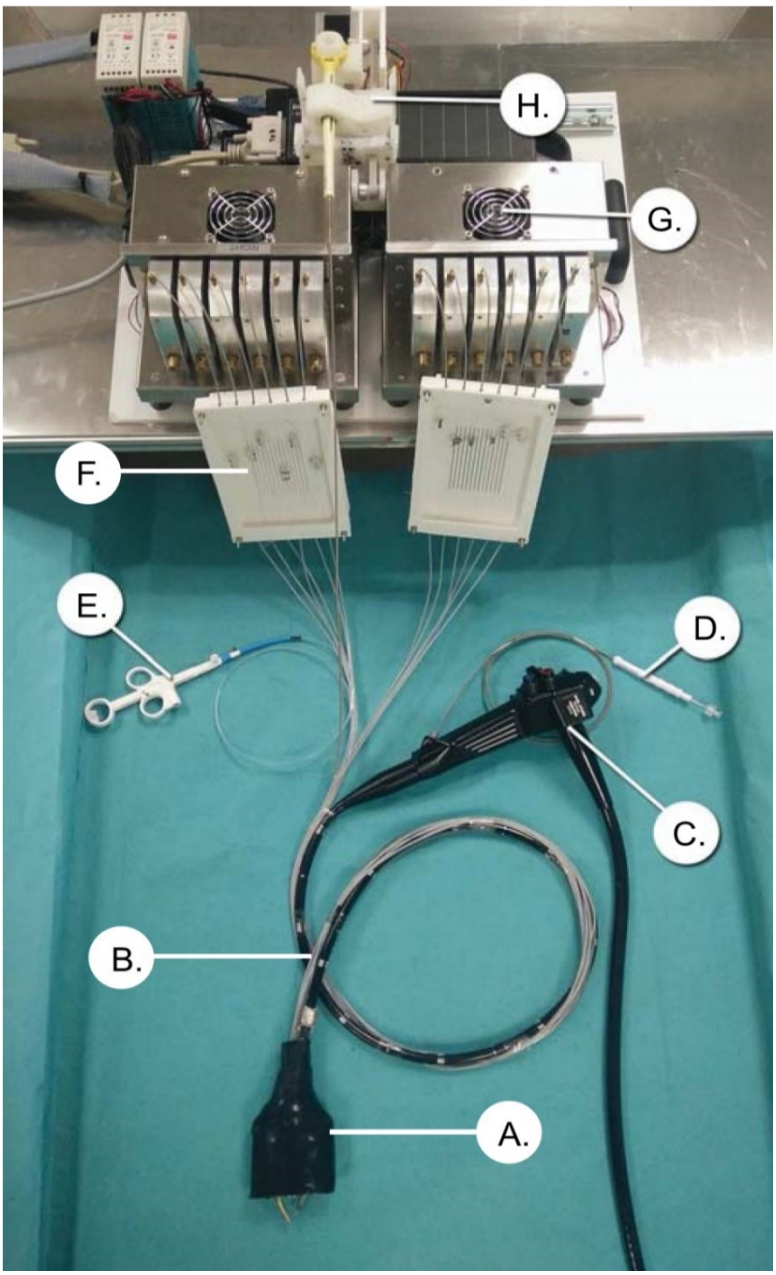


Figure 1.10: Overview of the ESD CYCLOPS system. (A) The deployable scaffold with a soft silicone sleeve. (B) Bowden cables used to guide the cables from the motor units to the end-effectors and the flexible instruments along the endoscope. (C) The flexible GI endoscope for visualisation. (D) A flexible injector needle is inserted into the endoscope working channel and used to lift the mucosa by injecting a liquid. (E) The diathermy surgical tool. (F) A cable splitter for cables separation between the motor units and CDPM. (G) Motor units for controlling two instruments, each motor unit containing 6 motors. (H) Instrument control device for opening and closing of the forceps [95] *©2018 IEEE.*



Figure 1.11: In vivo test - pre-clinical validation in the porcine intestine tract [95] *©2018 IEEE.*

Compared to the conventional method, the ESD CYCLOPS system significantly decreased the execution time in an *ex vivo* ESD test on a piece of chicken tissue. The system has undergone pre-clinical validation (Fig 1.11) [95]. To navigate in the GI tract and generate enough workspace to perform ESD surgery, the scaffold of the CDPM has been made deployable. Figure 1.9 shows a deployable rigid link mechanism. The deployed shape and size of the scaffold can be precisely adjusted, and a strong and stable supporting frame can be offered during the ESD task operation. However, with the metal linkage-based deployable scaffold, the difficulty of endoscopic navigation in the GI tract may increase. The inflatable scaffold can overcome this limitation and perform better GI tract navigation (Fig 1.12) [95], [96].

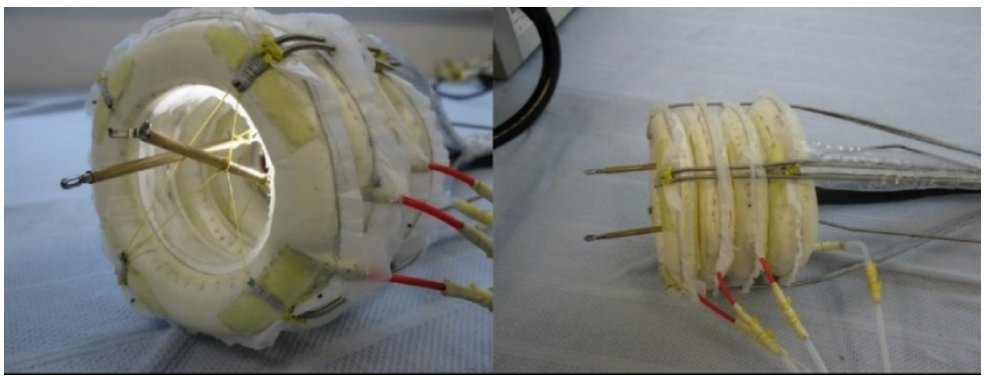


Figure 1.12: The early prototype of the inflatable scaffold [95] *©2018 IEEE.*

1.2.2 CDPR for laparoscopic surgery

The CDPR also could be utilised in laparoscopic surgery. Similar to the CDPR for endoscopic surgery, a folded CDPM can be inserted through a trocar deployed at the target location. As well as holding the laser fibre distal tip (Fig 1.6), the CDPM can be held by a conventional or robotic laparoscopic instrument such as a grasper, and then be positioned and held in place by exploiting the motion of the holding instrument. Also, the CDPM can also be designed as a laparoscopic tool. Figure 1.13 shows the conceptual design of a robotic CDPM instrument which can be mounted on a da Vinci® robotic platform. A standard laparoscope can be used to provide the visualisation of the operative field. Such application of the CDPM offers advantages in terms of increasing the dexterous workspace and precision operation. By introducing one or more surgical instruments steered by CDPMs, the fine control for a specific task can be realised, thus potentially reducing the number of access ports while improving the manipulability and safety. Furthermore, the operational time of the laparoscopic procedure may be reduced.

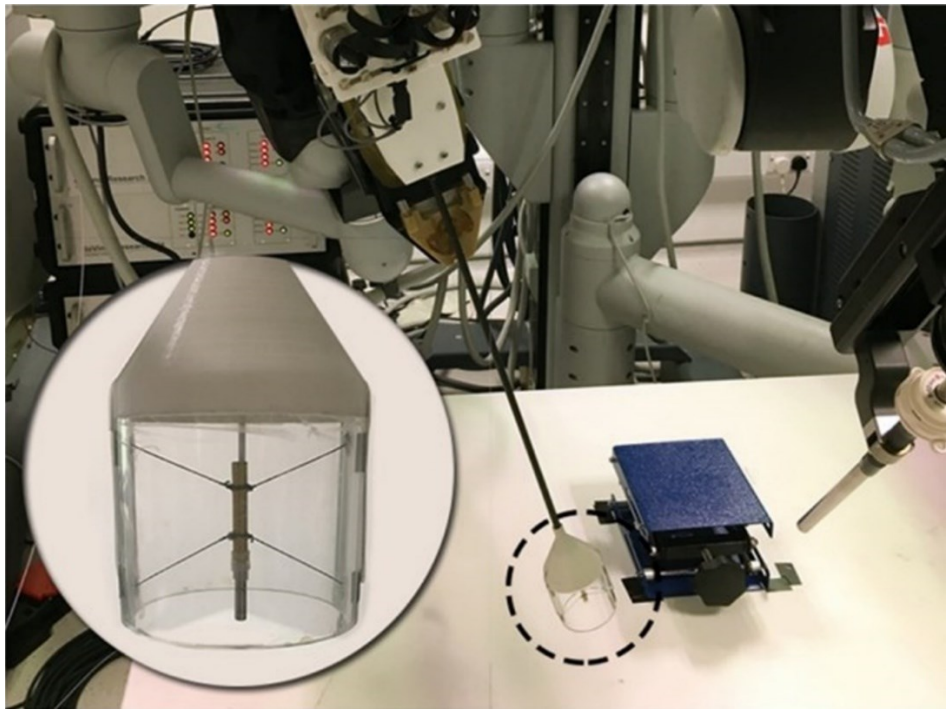


Figure 1.13: The conceptual setup of the CDPM laparoscopic instrument mounted as a robotic surgical instrument on the da Vinci® robot [99].

Another CDPR designed for laparoscopic surgery is called the SIMPLE, Single-Incision

Micro-Port Laparo-Endoscopic system. Instead of inserting a CDPM into the patient, the scaffold of the CDPM in the SIMPLE system remains outside (Fig 1.14 and 1.15). Without being limited by anatomy size, the SIMPLE surgical robotic system offers a sizeable dexterous workspace to perform laparoscopic operations. The cable access micro ports can be sited based on the specific surgical task and more details are presented in [99].

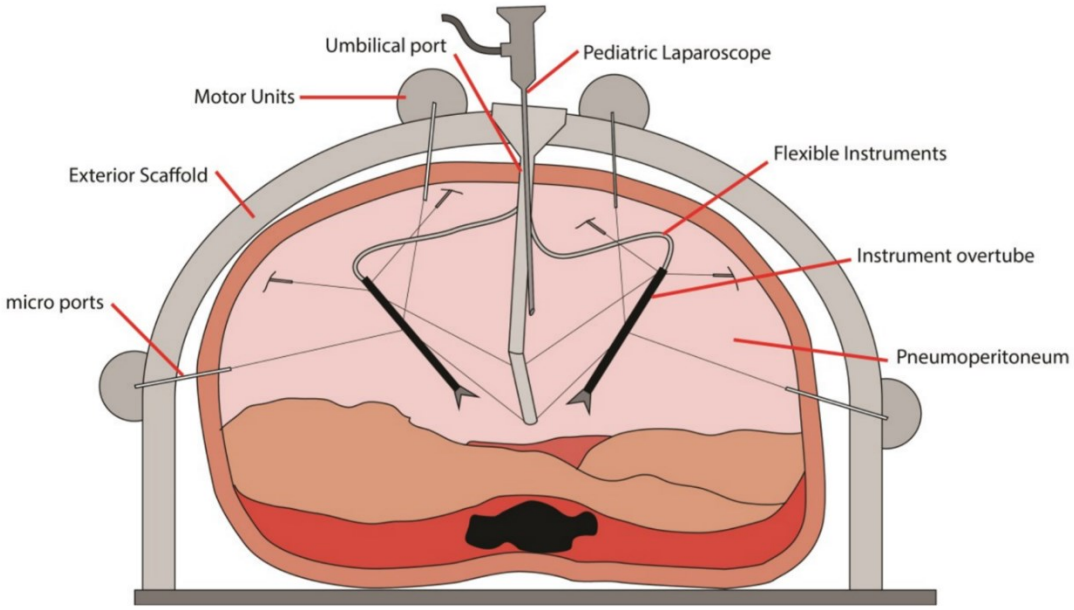


Figure 1.14: The conceptual scheme of SIMPLE [99].

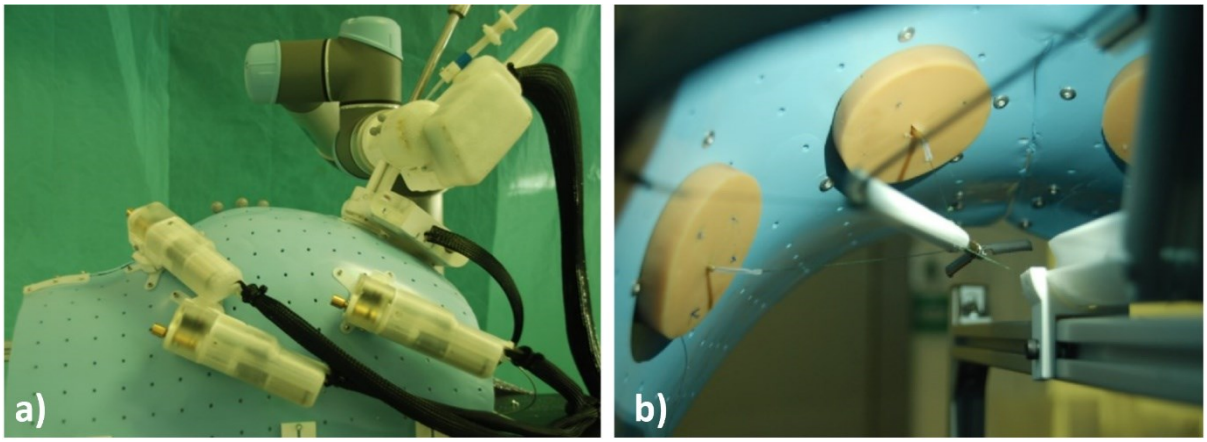


Figure 1.15: The prototype of SIMPLE. a) Side view from the outside of the exterior scaffold and b) Inner view [99].

1.3 Motivation and Objectives

Transoral laser phonosurgery (TLP), uses a laser beam to perform vaporisation, incision, ablation, or photocoagulation on the soft tissues of the larynx, such as the vocal cord [4]. TLP has been developed both in free beam delivery and fibre delivery approaches. The techniques of laser scanning and robotics control are also applied in the two approaches [54], [101], [102]. In the free beam delivery approach, surgical lesions could be introduced by using the straight suspension laryngoscope. For fibre delivery approach, with the development of transoral robotic surgery (TORS) systems such as da Vinci® SP and Flex Robotic System (Medrobotics Inc., USA) have been successfully used in TLP [102]–[104]. A curved laryngeal blade could be used, with the distal tip of the laser fibre manipulated by a flexible or semi-flexible robotic tool. The issues related to the limitation of the line-of-sight can be avoided. However, due to the loss of the laser path scanning function, the performance is inferior to that of the laser scanning technique in the free beam approach.

A CDPR can be utilised to steer surgical instruments [97]. As mentioned in the previous section, various types of CDPR have been developed and have demonstrated the potential to be used in clinical applications, such as ESD CYCLOPS robotic system currently undergoing pre-clinical validation in GI surgery [95], [96]. Precise and repeatable control of an end-effector can be offered by CDPR due to its intrinsic advantages. Thus, a CDPR can be utilised to control the distal tip of the fibre to perform laser scanning. Additionally, the CDPR does not require a direct pathway for actuation. Therefore, CDPR is a suitable candidate for fibre-based laser surgery. This thesis focuses on the development of a CDPR for TLP. Furthermore, as described in the previous section, the use of both the laser technology and robotic systems for surgery can optimise outcomes and improve surgical precision via image guidance. Fibre-based optical biopsy techniques have proven their ability to detect disorders of the larynx, such as probe-based confocal laser endomicroscopy (pCLE) [105]. By steering the fibre probe, the CDPR also can be expected to perform the fibre-based optical biopsy of the larynx.

The main hypothesis of this thesis is:

A CDPR is a technically feasible solution for precise fibre-based laser scanning and

optical biopsies in TLP.

To research this hypothesis, the study aims to design and develop a fibre-delivered laser surgery robot for TLP and evaluate its technical feasibility. Additionally, this study also aims to combine the fibre-based optical biopsy techniques with the developed robotic system to evaluate its technical feasibility for intraoperative optical biopsy in the larynx.

The objectives of this thesis are:

- To identify the technical gaps of current techniques in TLP and clarify the requirements of robotic surgery system for TLP.
- To design and develop a CDPR for TLP and evaluate through a technical feasibility study if it fulfils the proposed requirements of TLP.
- To evaluate through a technical feasibility study if the approach of the developed robot is suitable for fibre-based optical biopsy of the larynx.

1.4 Thesis Structures and Contributions

The outline of the thesis follows:

Chapter 2 introduces the background of TLP and describes the advantages and disadvantages of free beam delivery and fibre delivery techniques in TLP. The related work on robotics-assisted fibre delivered laser scanning for TLP is described and discussed. The current gaps and demands of transoral laser phonosurgery are identified, and the potential solutions are discussed.

Chapter 3 starts with an introduction to the modelling and analysis of CDPM for TLP, including kinematics, dynamics, tension forces distribution and the controllable workspace. Then follows the simulation, various designs and early prototypes of CDPMs for TLP are presented and discussed.

Chapter 4 focuses on the validation tests and technical feasibility analysis of the manufactured CDPR, *LaryngoTORS* robot for TLP. The core technique of motion control of the robot is introduced. An approach to semi-autonomous free path scanning is addressed.

Both the bench tests and *ex vivo* tests are described, and the experimental results are discussed. The design and prototype development of a second version of *LaryngoTORS* robot for further preclinical study are presented. The technical feasibility considerations of the *LaryngoTORS* robot are addressed.

Chapter 5 demonstrates the possibility of the fibre-based optical biopsy of the larynx by using *LaryngoTORS* robot. Experiments of pCLE and hyperspectral fibre-optic sensing were performed by *LaryngoTORS* robot. Experimental results will be presented and discussed. The assessment of CDPM for optical biopsy of the larynx is presented.

Chapter 6 summarises the key achievements of this thesis and addresses the future directions of this study.

The key contributions of this thesis are summarised as follows:

1. Identification of the current gaps in TLP. The requirements of the robotic-assisted TLP have been clarified.
2. Design and development of the first CDPR, *LaryngoTORS* robot for TLP.
3. Development and validation of a novel approach of semi-autonomous free path laser scanning with high precision and high repeatability.
4. Development of a CDPR for TLP and evaluation of the technical feasibility.
5. The first description and demonstration of the use of CDPM in fibre-based optical biopsy of the larynx.

1.5 Publications

The work presented in this thesis has resulted in below peer reviewed conference proceedings and journal publications:

- **M. Zhao**, H. Zhang, G. Mylonas, and D. Elson, "Cable-Driven Parallel Robot Assisted Confocal Imaging of the Larynx", OSA Biophotonics Congress: Biomedical Optics, Florida, 21st April 2020.
  Partial content of Chapter 5 is based on this paper.

- **M. Zhao**, T. J. C. Oude Vrielink, A. Kogkas, M. Runciman, D. Elson, and G. Mylonas, "LaryngoTORS: A Novel Cable-Driven Parallel Robotic System for Transoral Laser Phonosurgery", IEEE Robotics and Automation Letters (RAL) and International Conference on Robotics and Automation (ICRA), VOL. 5, NO. 2, APRIL 2020, pp. 1516-1523.

  Partial content of Chapter 3 and 4 are based on this paper.
- M. Runciman, J. Avery, **M. Zhao**, A. Darzi, and G. Mylonas, "Deployable, Disposable, Self-Propelling and Variable Stiffness Devices for Minimally Invasive Surgery," Frontiers in Robotics and AI. 2020 10th January; p141.

  Partial content of Chapter 1 is based on this paper.
- **M. Zhao**, T. J. C. Oude Vrielink, A. Kogkas, D. Elson, and G. Mylonas, "Prototype Designs of a Cable-driven Parallel Robot for Transoral Laser Surgery," in 12th Hamlyn Symposium on Medical Robotics (HSMR), London, UK, 2019, pp. 103-104.

  Partial content of Chapter 3 is based on this paper.
- M. Runciman, J. Avery, **M. Zhao**, A. Darzi, and G. Mylonas, "Soft, Deployable, Cable Driven Robot for Minimally Invasive Surgery," in 12th Hamlyn Symposium on Medical Robotics (HSMR), London, UK, 2019, pp. 51-52.

  Partial content of Chapter 1 is based on this paper.
- T. J. C. O. Vrielink, **M. Zhao**, A. Darzi, and G. P. Mylonas, “ESD CYCLOPS: A New Robotic Surgical System for GI Surgery,” in 2018 IEEE International Conference on Robotics and Automation (ICRA), May 2018, pp. 150–157.

  Partial content of Chapter 1 is based on this paper.
- Patent application GB 1901147.7 Trans-Oral Surgery Device.

  Partial content of Chapter 3 is based on this patent.

1.6 Technical Acknowledgements

Chapter 4: Dr Alexandros Kogkas provided support for the EtherCAT communications between the PC and motor controllers. Dr Joric Oude Vrielink designed and manufactured the box of the motor controller. The codes of motor control were written on the original codes

developed by Joric.

Chapter 5: Dr Haojie Zhang assisted in the mosaicking generation, as well as the design and manufacturing of the hyperspectral probe.

Chapter 2

Transoral Laser Surgery of the Larynx

This chapter introduces TLP briefly and describes the advantages and disadvantages of two main techniques in the surgery: free beam delivery and fibre delivery. The related works of robotics-assisted fibre delivered laser scanning for TLP are described and discussed. Finally, the current gaps and demands of TLP are identified, and the potential solution is discussed at the end of this chapter.

2.1 Transoral Laser Surgery of the Larynx

Transoral laser surgery is a common procedure in otolaryngology and transoral laser surgery of the larynx has a long history. With the development of laser equipment, the study of transoral laser surgery in the larynx started at the beginning of the 1970s [106]. Carbon dioxide lasers (CO_2) have been used in laryngeal surgeries since 1972 and the first surgical laser treatment of benign laryngeal lesions in human patients was reported by Strong and Jako [4]. TLP uses a laser beam to perform vaporisation, incision, excision, ablation, or photocoagulation on the larynx soft tissues, such as epiglottis, glottis and vocal cords. The

indications include polyps, cysts, nodules, stenosis, leukoplakia, papilloma and early carcinoma (Tis–T2) [4], [107]. Compared to radiation therapy or diathermy treatment, use of surgical lasers may have a better outcome, such as larynx preservation rate, preserving organ function, lower overall morbidity and minimal complications [33], [107].

CO_2 lasers have been widely used and have been well proven in phonosurgery in the past few decades, becoming the gold standard of transoral laser surgery. The wavelength of a CO_2 laser is 10600 nm, matched to the peak of absorption of water. Due to water's strong absorption of light at this wavelength, the CO_2 laser can rapidly vaporise water in the tissue and the high pressure generated by the vaporisation can efficiently perform soft tissue removal. Therefore, the interaction between the CO_2 laser and soft tissue takes place rapidly and the penetration depth is superficial to the tissue surface. Precise tissue cutting can be achieved by CO_2 laser [108]. Besides CO_2 lasers, others laser types are also utilised in phonosurgery, such as Thulium YAG lasers, KTP lasers, diode lasers (805-980 nm) and blue lasers [34], [109], [110]. KTP and diode lasers have excellent haemostasis outcomes and are better in comparison with the CO_2 laser in haemostasis but inferior in tissue cutting. Thulium lasers offer an compromise of cutting and haemostasis, which is utilised in laryngeal surgery since 2006 [32]. Surgeons can select the laser wavelength matched to different outcomes of laser-tissue interactions.

There are two main techniques to perform TLP: free beam delivery and fibre delivery [4], [111], [112]. The free beam delivery technique combines microscopic visualisation and direct laryngoscopy which was developed in 1972. The fibre delivery technique came later than the free beam delivery technique, as it required fibre technology, especially the CO_2 laser. The first commercial hollow-core optical fibre-delivered medical CO_2 laser system was made by OmniGuide (OmniGuide Inc., USA) [38], [111]. Currently, medical laser manufacturers, such as Lumenis (Lumenis Ltd., Israel) and OmniGuide (OmniGuide Inc., USA), can provide integrated CO_2 laser medical devices that combine the modalities of free beam and fibre delivery [113], [114]. Surgeons can shift between the two modalities based on the requirement of the surgery. However, they cannot use the two modalities at the same and the limitations of the two techniques have not been solved. The advantages and disadvantages of free beam

delivery and fibre delivery will be discussed in section 2.2 and 2.3 respectively.

2.2 Free Beam Delivery Technique in Transoral Laser Surgery

In the free beam delivery approach– also known as TLM – an articulated arm with reflective mirrors is used to transmit the laser beam to a laser micromanipulator. The micromanipulator consists of optical lenses and mirrors, which are each used to adjust focus distance and deflect the laser beam to the target tissue, respectively. A joystick is connected to a deflection mirror to control the position of the laser spot (Fig. 2.2) [115]. The micromanipulator is attached to a surgical microscope, which offers the surgeon a magnified view of the surgical field. A rigid suspension laryngoscope (Fig. 2.3) is utilised to create a straight working channel for the laser beam and instruments (Fig. 2.4). Figure 2.1 shows the typical setup of transoral laser laryngeal microsurgery.

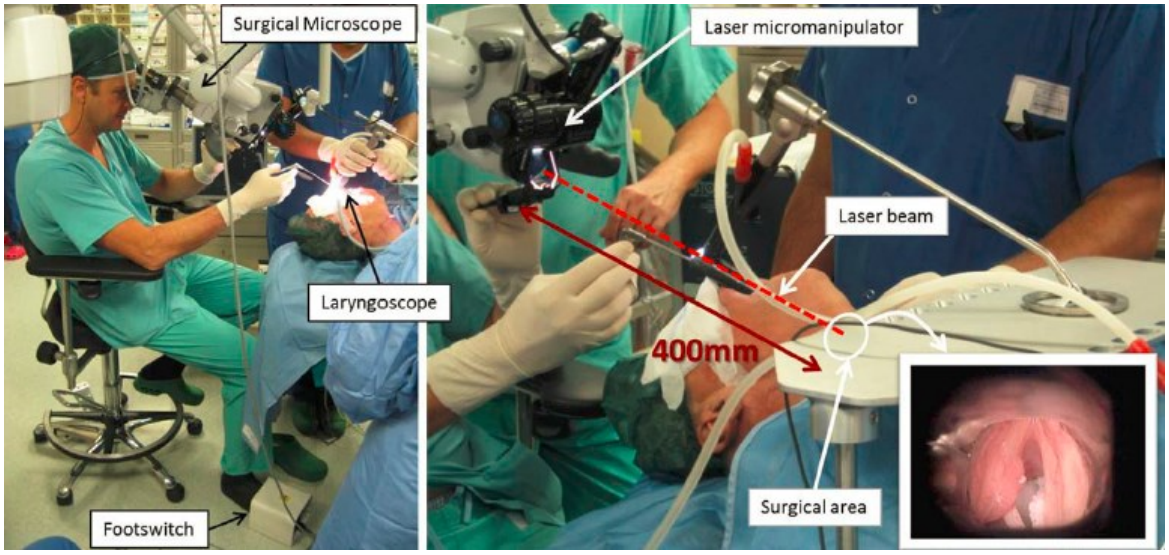


Figure 2.1: The setup of transoral laser laryngeal microsurgery [116].

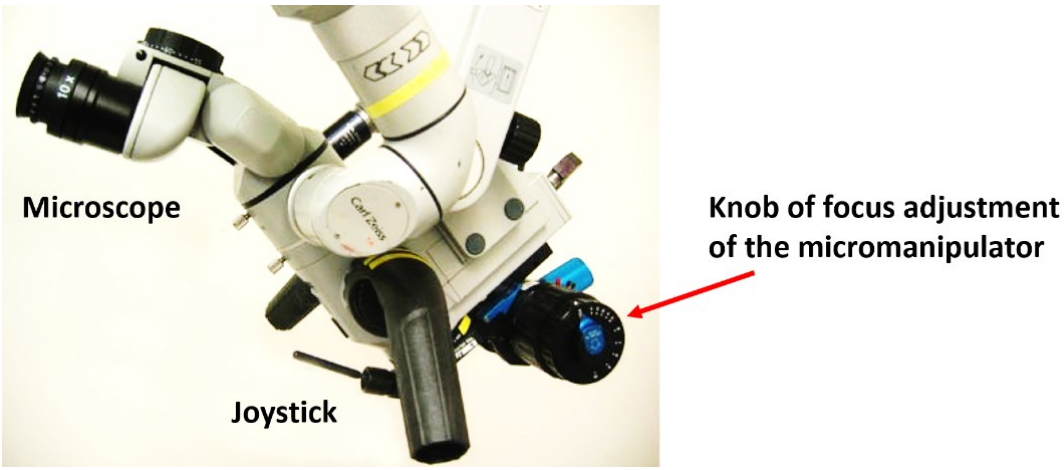


Figure 2.2: The laser manipulator with a focus adjustment unit coupled with a surgical microscope [115].

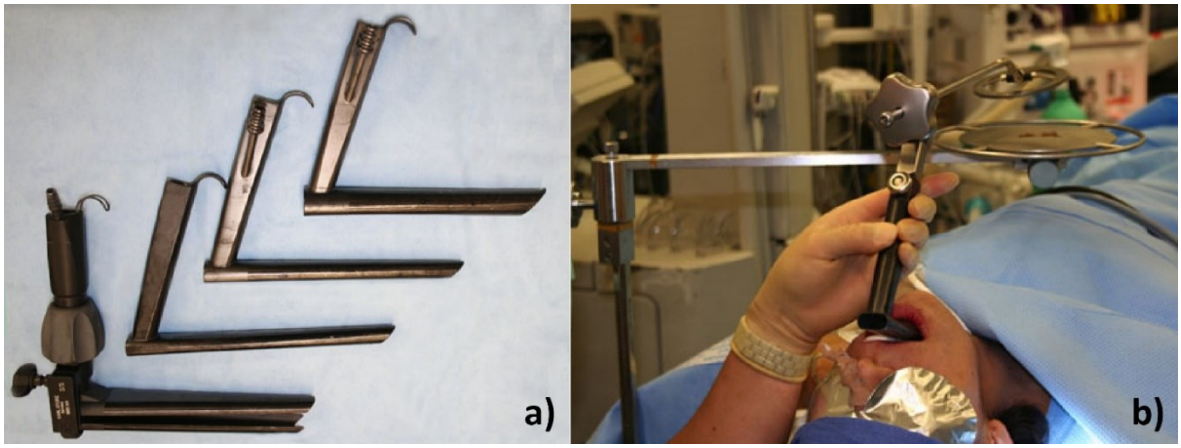


Figure 2.3: a) Selection of various laryngoscopes used in TLM for larynx exposure. b) Insertion of suspension laryngoscope [115].

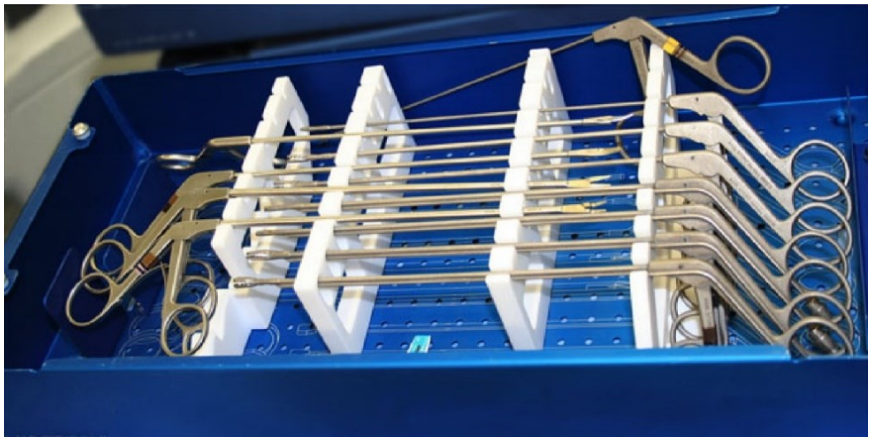


Figure 2.4: Specially designed microlaryngeal instruments, such as forceps and scissors, for use in TLM [115].

With the development of laser scanning technology, a pattern scanner is used in TLM. Two galvanic mirror-based laser beam scanners can be integrated with the laser micromanipulator (Fig. 2.5), allowing pre-defined patterns such as straight lines, arc lines and circles, to be generated for laser cutting on the target soft tissue. The size and shape of the pattern can be changed via the user interface, and accurate, fast and highly repeatable pre-programmed laser scan can be achieved. Furthermore, the operation time and thermal damage can be minimised [54] and the surgical outcome is improved by precisely removing diseased tissue while preserving non-targeted healthy areas. As such, TLM with scanning functionality has become the 'gold standard' of the surgery.

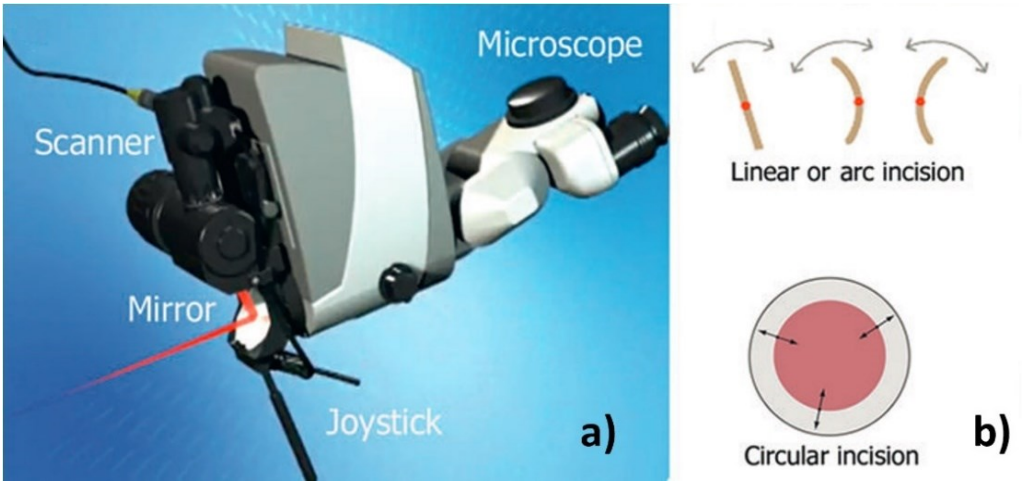


Figure 2.5: a) Schematic of a combination of a surgical microscope and a laser manipulator with the scanner; b) Example scanning patterns: straight line, arc line and circle, the position and the rotation of patterns can be adjusted by a joystick [117].

With regards to autonomy, laser scanning incision and ablation have been achieved in TLM with semi-autonomous control. The location and parameters of laser scanning, such as shape and size, are selected by the surgeon. The joystick on the micromanipulator is used to set the centre of the scanning pattern and to change its direction. Then, a pattern is scanned automatically, using the pre-programmed path. It may be difficult to match irregular pathological margins perfectly while relying on pre-programmed paths. An arbitrary free scan path can overcome this problem and improve the performance of laser scanning.

As shown in Figure 2.1, the working distance between the laser aperture and the target tissue is approximately 400 mm, the joystick has to be carefully controlled, and the length of

the microlaryngeal instruments (Fig. 2.4) is approximately 200 mm [118]. Therefore, hand tremors and fatigue can affect the precision of the operation and extensive training is required [119]. A suspension laryngoscope must be used in TLM to provide a straight working channel for the laser beam, as shown in Figure 2.6, leading to the complications such as of lesions of cervical vertebra and dental arch and postoperative pains [73]. In addition, the manipulability and ergonomics of the current TLM method also need to be improved [119], [120].

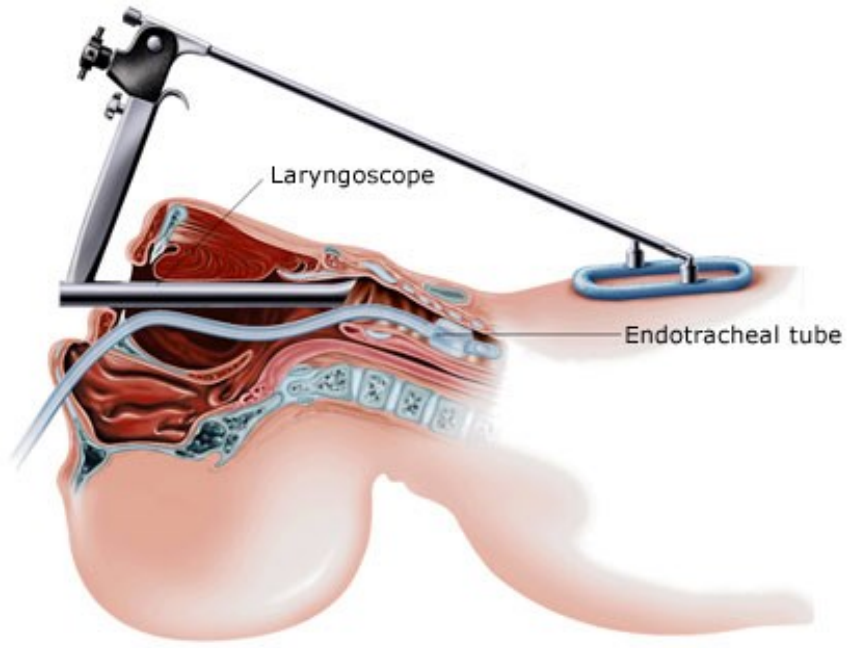


Figure 2.6: The setup of the suspension the laryngoscope introduced into the larynx [121].

Some researchers are focusing on the improvement of TLM. A vision-based laser microsurgical control system was developed by Istituto Italiano di Tecnologia (IIT). As shown in Figure 2.7, the direct line-of-sight can be avoided via a CCD camera. With a virtual scalpel control system and a vision-based laser scanning controller, free trajectory laser scanning could be achieved, with a root-mean-square error (RMSE) of 0.03 mm [120]. Furthermore, some robotic systems are under development aiming to solve the challenge of microlaryngeal instrument control [118], [122]. Figure 2.8 shows an example, a “steady-hand” microsurgery platform that was developed by Johns Hopkins University to mitigate the hand tremor [122].

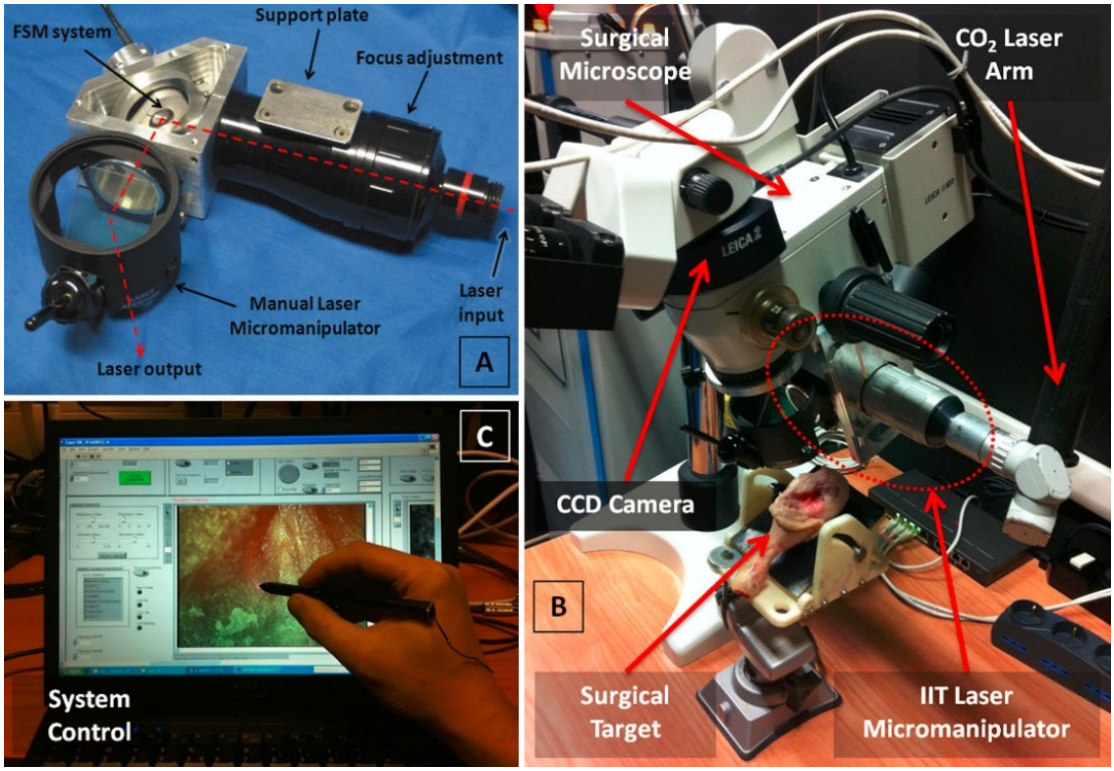


Figure 2.7: The IIT robot-assisted laser phonomicrosurgery system: a) the motorised laser scanner; b) the surgical microscope with a built-in CCD camera and c) the virtual scalpel control system [120].

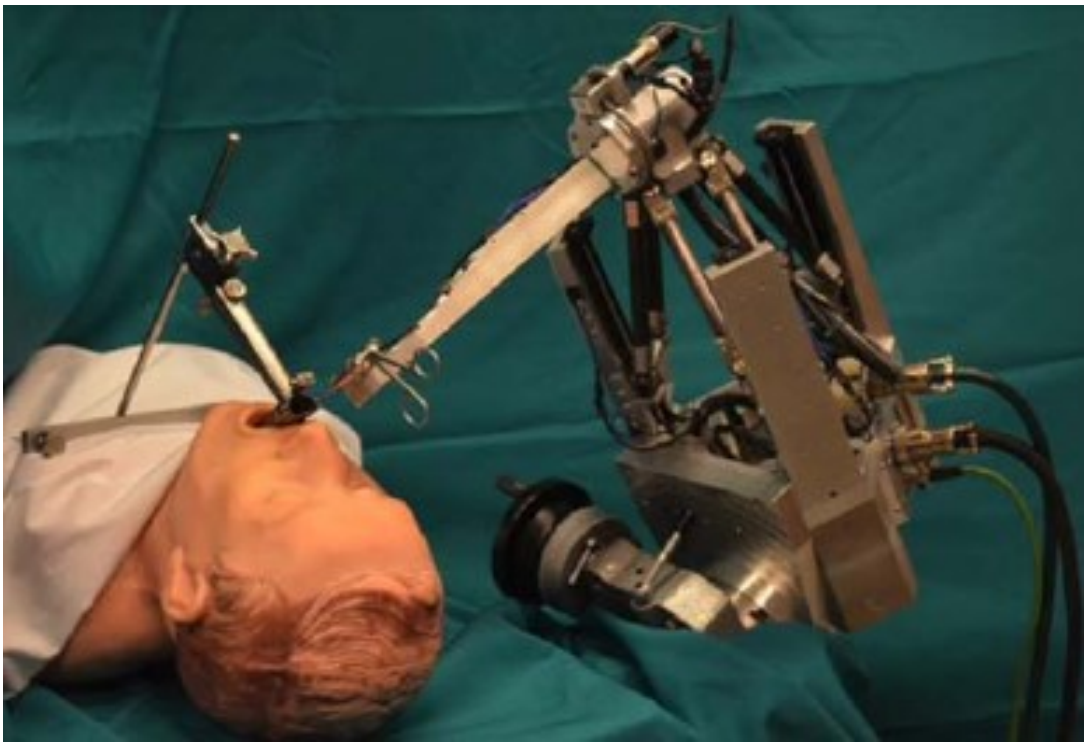


Figure 2.8: A "steady-hand" microsurgery platform and the setup for transoral microlaryngeal surgery [122].

However, these advanced systems - vision-based laser microsurgical control system and the robot-assisted microlaryngeal instrument control system - are currently at the pre-clinical stage and are not being translated routinely into TLM. The combination of these complex systems in TLM remains a challenge. In addition, a less traumatic approach is required that can obviate the need for a straight suspension laryngoscope.

2.3 Fibre Delivery Technique in Transoral Laser Surgery

In fibre delivered transoral laser surgery, a flexible optical fibre is used to transmit the laser beam. In contrast to conventional TLM, a line-of-sight is not required for laser beam transmission. The working distance between the fibre tip and the tissue is commonly 1 mm. The laser fibre tip can be controlled by a hand-held surgical instrument or a teleoperated surgical robot arm.

With the advent of robotics and computer technology, transoral robotic-assisted surgery (TORS) pioneered by Dr Gregory Weinstein and Dr Bert O'Malley is more and more widely used [123]. Dr Weinstein and Dr O'Malley performed the first TORS with a multi-arm da Vinci® surgical robotic system (Intuitive Surgical Inc., USA), including tonsillectomy and tongue base resection [123].

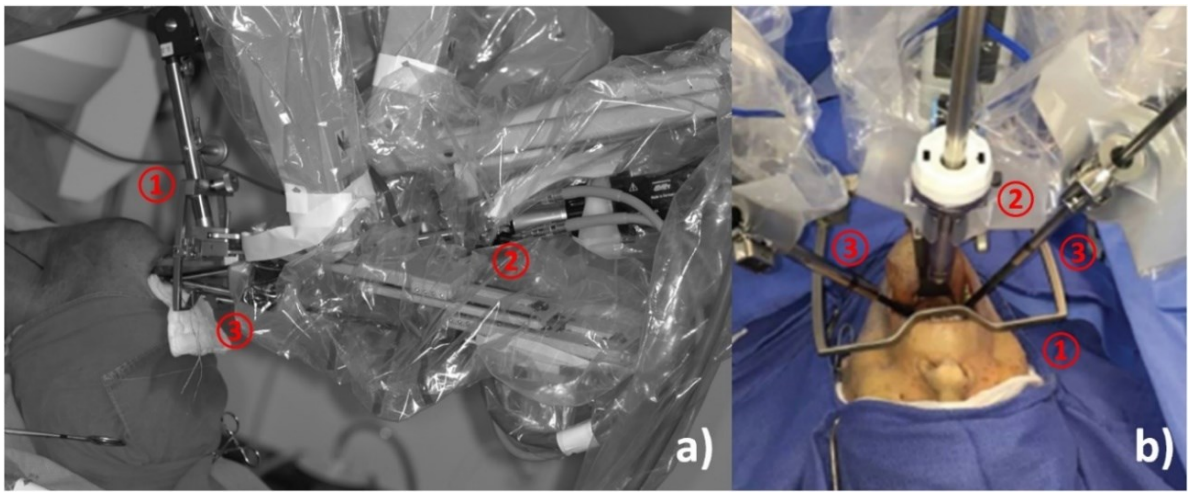


Figure 2.9: a) side view [124] *and b) front view* [82] *of settings of the multi-arm da Vinci® surgical robotic system in TORS: ① FK retractor, ② stereo endoscope, ③ teleoperated robotic instruments.*

Although some research projects have reported the applications of the da Vinci® Si/Xi surgical robotic system in transoral laryngeal surgery [124], [125], the camera and instruments are too large to perform phonosurgery. The workplace in phonosurgery is narrow and deep, and it is difficult to manipulate long, rigid robotic arms. Figure 2.10 shows a comparison of the triangular shape between da Vinci® instruments set up for both oropharyngeal and hypopharyngeal lesions. Due to the deeper lesion location, the instrument triangulation is inadequate in hypopharyngeal surgery. The distance between instruments is closer and collisions will occur more frequently [126]. As shown in Figure 2.9, the settings of the da Vinci® surgical robotic system in TORS are quite complicated. The robotic arms take a large working space around the patient's head, and as a result, the assistant, nurse, anaesthesiologist cannot approach to the patient's head easily. Furthermore, the endoscope is straight and rigid. Even though the endoscope can be offered with different view angle, such as 30°, there is limited exposure of deeper tissues of the larynx. A semi-flexible/flexible laryngoscope or a flexible robotic system with a camera can be expected to offer the visualisation of the surgical area through a curved airway [127].

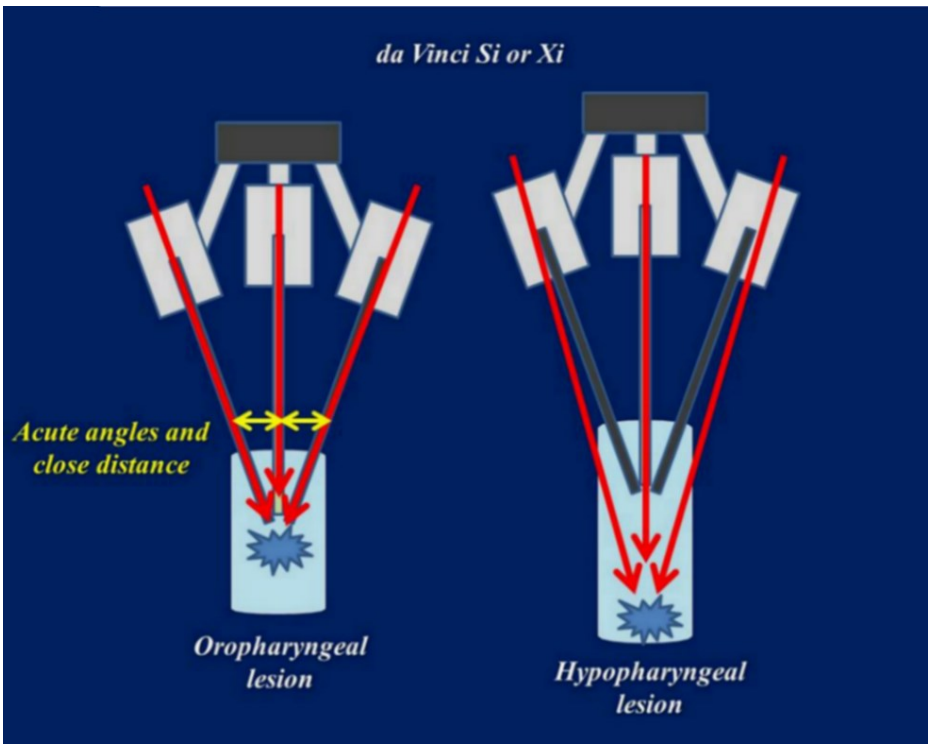


Figure 2.10: Comparison of the triangular shape between instruments for oropharyngeal and hypopharyngeal lesion [126].

Medrobotics Flex® Robotic System (Medrobotics Inc., USA) is a surgical platform consisting of a steerable articulated multi-linked robotic endoscope which is intended for robot-assisted visualisation, with an instrument working channel at each side of the robotic endoscope (Fig. 2.12). The size of the endoscope is 15 x 17 mm (2D camera) [128] or 28 mm (3D camera) [104]. Specific 3.5 mm flexible surgical instruments with different functions are offered by Medrobotics to perform various surgical tasks [129]. Each flexible instrument allows a 4 degrees-of-freedom (DoF) controllable motion. Figure 2.11 shows the Flex Robotic system and the compatible flexible instruments.

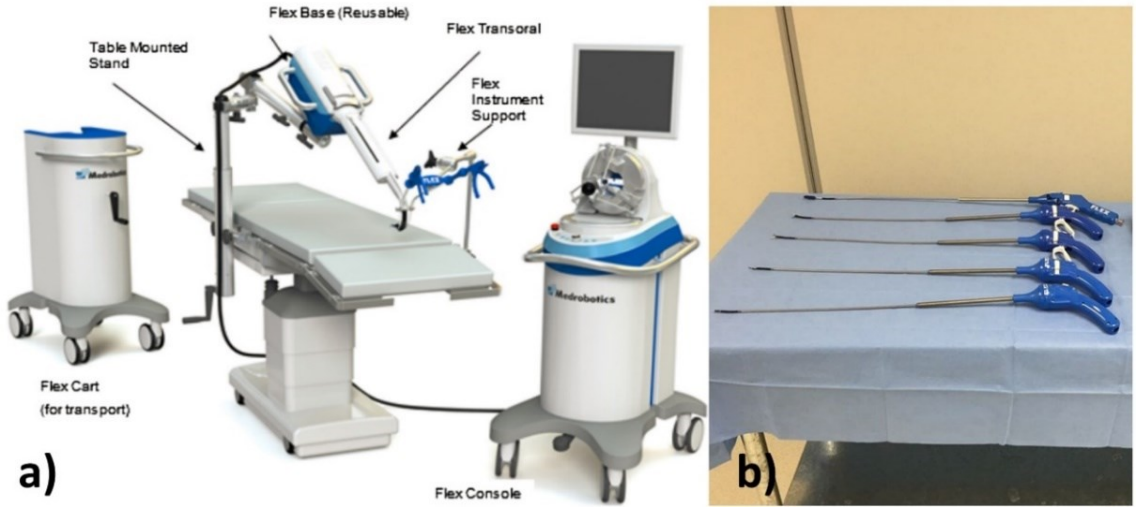


Figure 2.11: *a) Flex Robotic system* [129] *and b) compatible flexible instruments* [104].

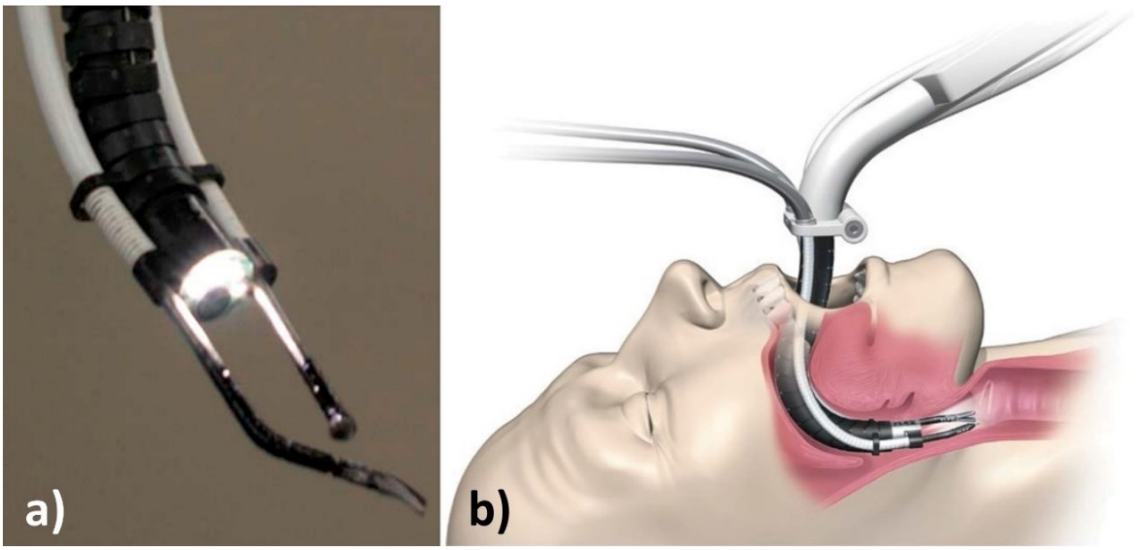


Figure 2.12: a) the end tip of the flexible robot with a camera, light source, and two flexible instruments [101]. *b) demonstration of the operational position of the Flex Robotic System in the larynx* [130].

The Flex Robotic System received FDA approval in 2015 can be used in TORS for oropharynx, hypopharynx and larynx lesions [101], [103], [104]. As demonstrated in Figure 2.12b), both the endoscope and two instruments can fit within the curved airway. One of the flexible instruments is a laser fibre holder with a build-in fibre sheath. The Flex Robotic System can be utilised in transoral laser phonosurgery, such as cordectomy (Fig. 2.13) [128].



Figure 2.13: Endo views of the right side cordectomy successfully performed by Flex Robotic System with two flexible instruments: a Maryland dissector (*) and a laser fibre holder (#) with a CO2 laser [128].



Figure 2.14: Instrument operation of Flex Robotic System [131].

However, the Flex Robotic System may lack the manipulability of the tip of the instrument. As shown in figure 2.14, the tool operation is manual as in conventional laparoscopic surgery, and the levels of precision and manipulability of instruments are inadequate.

The da Vinci® SP is a robotic system for single access surgery. All the robotic and endoscopic arms are inserted through a single 2.5 cm diameter port. The two semi-flexible robotic arms enable more freedom of movement and enough triangulation for surgical operation within a limited working space (Fig. 2.15). The da Vinci® SP robotic system is also intended for use in TORS and received FDA approval for radical tonsillectomy and tongue base resection on 15th March 2019. Although approval has not yet been given for transoral phonosurgery, many case studies of the da Vinci® SP being used in the hypopharynx and larynx have been reported [79], [126]. Figure 2.16a) shows the da Vinci® SP in TORS and the end view of two robotic arms in transoral phonosurgery. With the two joggle joints of the endoscopic arm, the endoscope is semi-flexible and steerable. In comparison to the da Vinci® Si/Xi, the endoscope of da Vinci® SP is slimmer and can reach into the larynx and expose the larynx tissue closely (Fig. 2.16b).

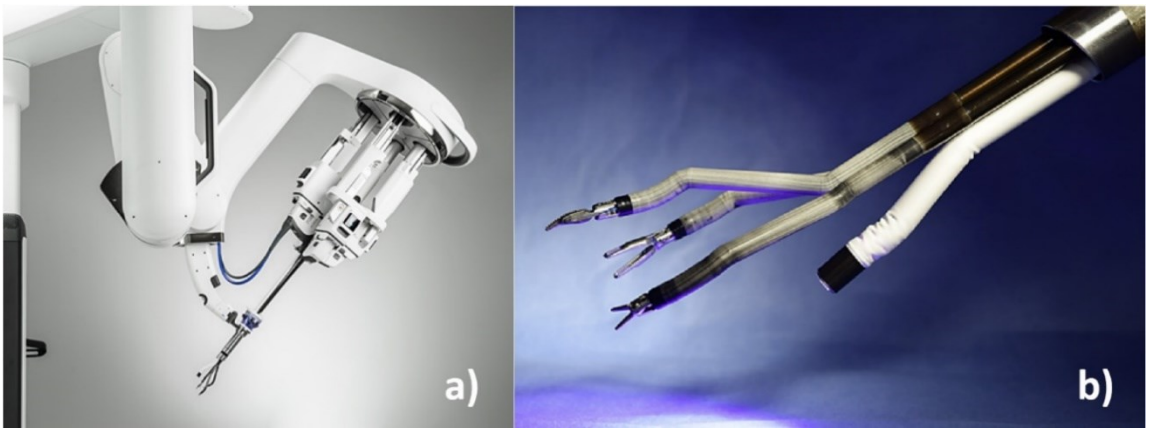


Figure 2.15: a) the da Vinci® SP robotic system with b) three instrument arms and one endoscopic arm. All robotic arms have two joggle joints [79].

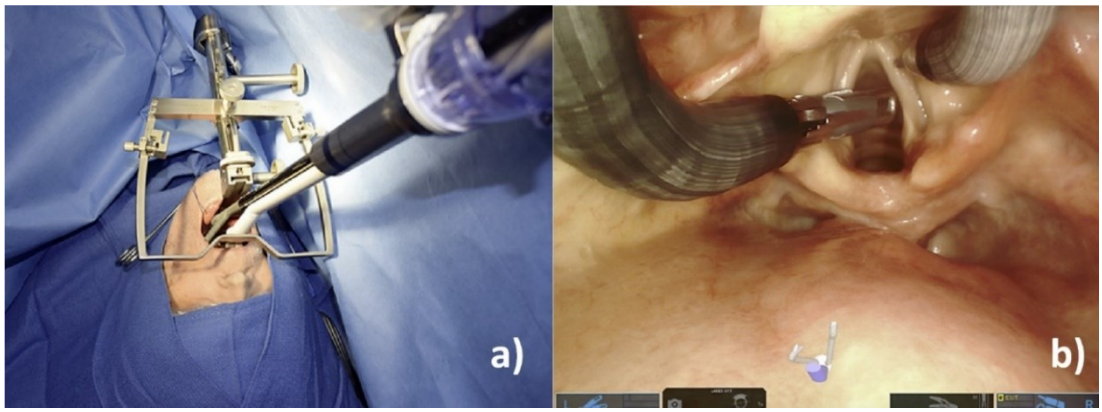


Figure 2.16: a) the settings of da Vinci® SP in TORS and b) the end view in transoral phonosurgery [79].

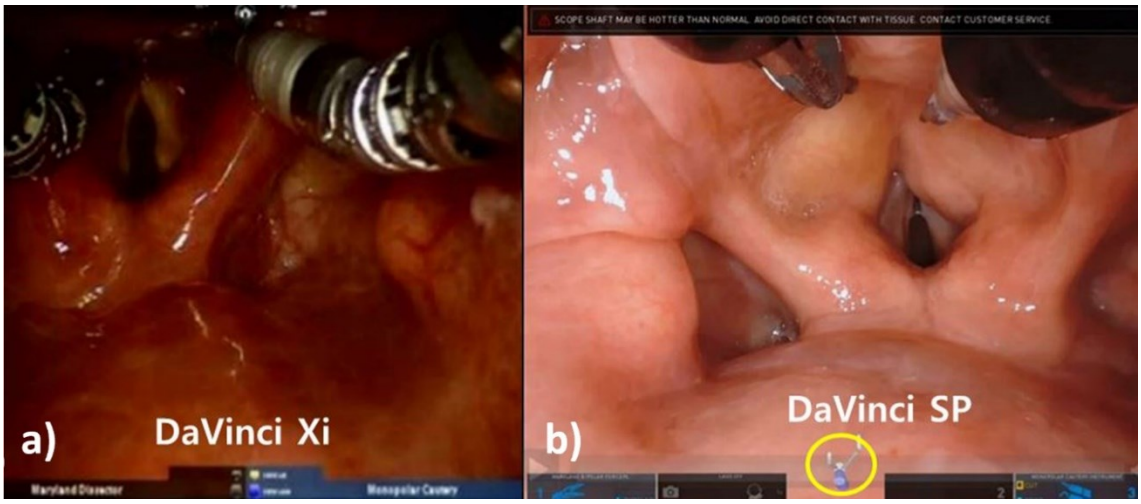


Figure 2.17: Comparison of the endo view between a) da Vinci® Xi and b) da Vinci® SP in TORS. The endoscope of da Vinci® SP can be driven close to the surgical field and offers better visualisation of the lesion in the larynx [126].

The da Vinci® SP can achieve similar visualisation of the surgical field in the larynx compared to the Medrobotics Flex® Robotic System (Fig. 2.13 and Fig. 2.17b), although compared to direct manual control of the surgical instrument, remote control suffers the loss of haptic feedback and tactile sensation. With two teleoperated joggle joints, the robotic arms of da Vinci® SP are more steerable than the Flex Robotic System. The da Vinci® SP appears to be the most successful commercial robotic system in transoral laser phonosurgery. However, the da Vinci® SP is a universal robotic surgery platform with a design aimed at abdominal surgery and transanal surgery [80]. In comparison with the size of microlaryngeal instruments in TLM (Fig. 2.4), the 6 mm robotic arm still makes the operation in the deep narrow larynx difficult. Specific instruments for transoral phonosurgery, such as miniature vocal cord holders and micro forceps are required. Furthermore, the master and slave control type could

only achieve limited precision, repeatability, and velocity, while scanning functionality is missing. The performance cannot compare to TLM with the laser scanning function.

2.4 Related Works of Fibre-Based Laser Scanning

Using a flexible optical fibre to transmit the laser beam can avoid the use of a suspension laryngoscope and the traumas and lesions associated with it. However, even with the assistance of commercial surgical robotic systems as discussed in the previous section, without the laser scanning function, satisfactory laser operation is not achieved. Recently, two types of fibre-based laser scanning robotic system, a micro-electromechanical system (MEMS) controlled mirror steering system [132]–[138] and a magnetically controlled fibre steering laser scanning system [139]–[142], have been developed with the aim of improving fibre-based laser scanning.

To achieve the laser scanning function in fibre delivered transoral laser phonosurgery, it is intuitive to add a miniature laser scanner with steered mirrors or optical lenses at the end of the fibre tip like the conventional laser scanner mounted at the end of the articulated arm in TLM. Since the laser scanner needs to access the deep larynx, it is required to be compact, and miniature actuators need to be used to steer the laser beam to the desired location on the tissue. In addition, the laser scanner needs to carefully connect with the laser fibre tip and integrate with an endoscope to offer the visualisation of the surgical field in the larynx. In recent years, some MEMS controlled mirror steering laser scanning systems have successfully solved these challenges [137], such as the μRALP robotic system developed by Mattos *et al.* [138], a compact laser-steering end-effector manufactured by Bothner *et al.* [136] and a microrobotic laser steering system developed by York *et al.* [137]. These systems have similar working principles and characteristics, as well as similar advantages and limitations. Since the μRALP robotic system has been well developed and validated by cadaver trials [143] (Fig. 2.18), as a typical MEMS controlled mirror steering laser scanning system, μRALP robotic system will be further discussed in this section.

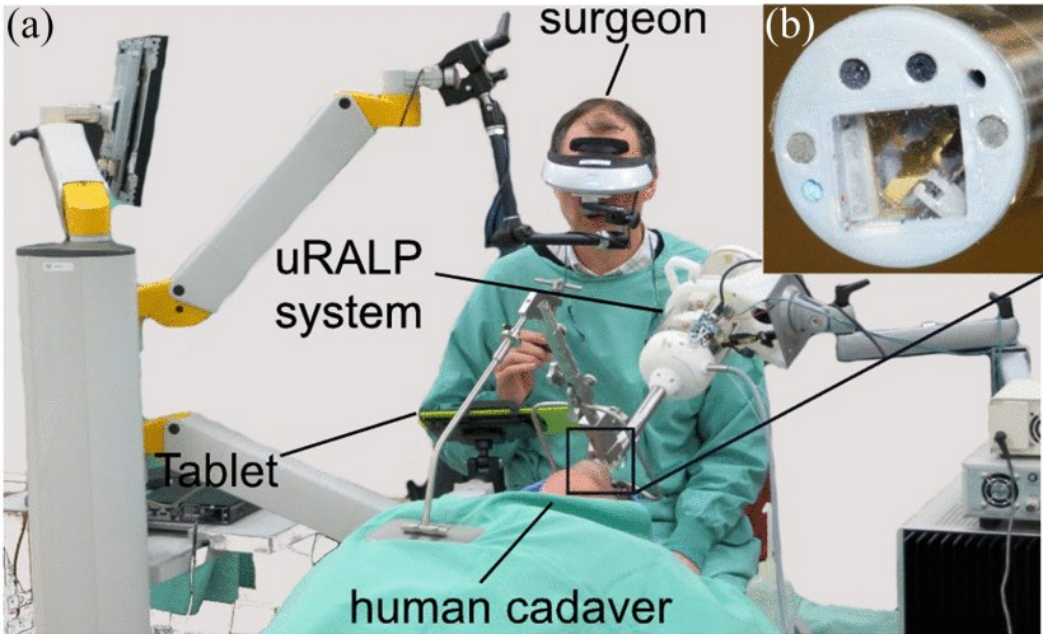


Figure 2.18: (a) µRALP robotic surgery system, picture taken during the last cadaver trial; (b) multifunctional tip, include a stereo camera, light source, fluorescence imaging, laser deflecting micro-mechanism unit [143] *©2017 IEEE*.

In the µRALP robotic system, an elegant micro-fabricated laser deflecting MEMS [143] is built in the distal tip of a semi-flexible robotic endoscope. Figures 2.19 and 2.20 show the delicate parts of the MEMS, a silicon on insulator (SOI)-based micromirror and a micro-piezoelectric linear motor, respectively. The computer-assisted design (CAD) view of the laser micro scanner and the assembled prototype are shown in Figure 2.21. The size of the compact micro scanner is only 11 x 9 x 42 mm.

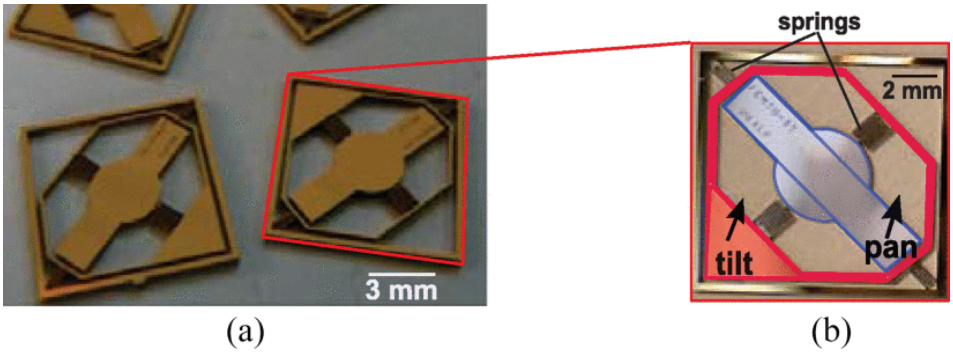


Figure 2.19: (a) SOI-based micromirror and (b) the components of the micromirror [143] *©2017 IEEE.*

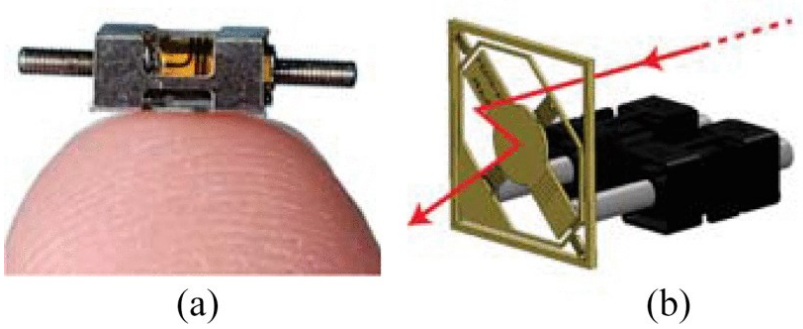


Figure 2.20: (a) the micro piezoelectric linear actuator (2.8 x 2.8 x 6 mm) and (b) the assembly of the SOI-based micromirror and the piezoelectric linear actuators [143] *©2017 IEEE.*

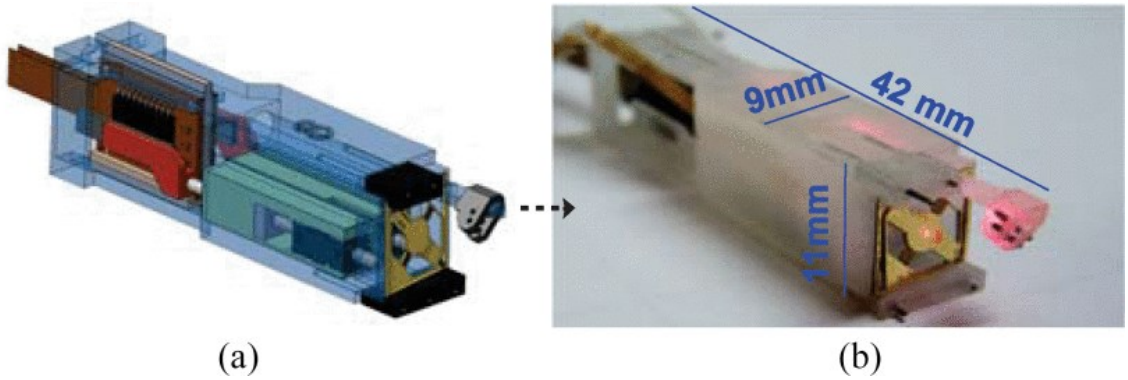


Figure 2.21: The CAD design (a) and the assembled prototype of the SOI mirror-based miniature laser scanner [143] *©2017 IEEE.*

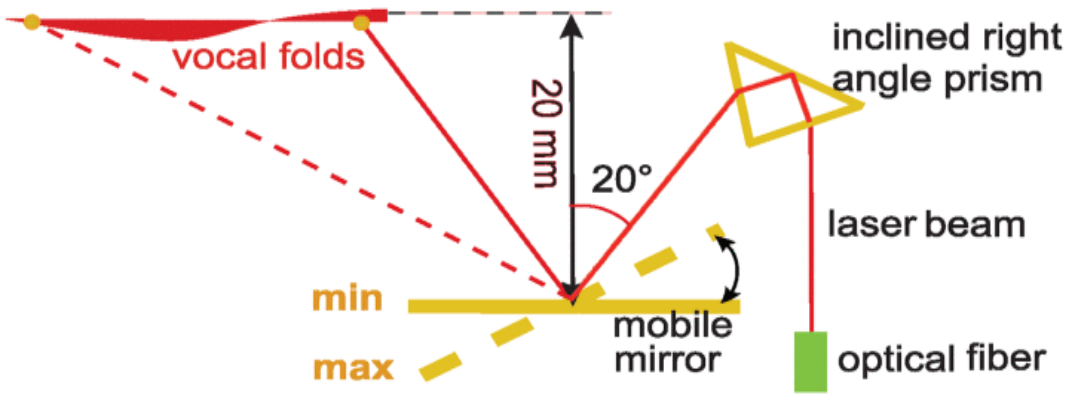


Figure 2.22: The functioning principle of the laser beam steering mechanism [143] *©2017 IEEE.*

The working principle of the laser beam steering and the laser beam pathway is shown in Figure 2.22. An inclined right-angle prism is used to transmit the laser beam from the end of the optical fibre to the steering mirror. The piezoelectric linear motors are used to tilt the mirror to reflect the laser beam to the target tissue. The root-mean-square (RMS) error of the path follow scanning test is 0.08 mm [143]. The miniature laser scanner is assembled into the semi-flexible directional and steerable robotic endoscopic tip with diameter 18 mm. During a

cadaver test, the robotic endoscope with the miniature laser scanner was successfully inserted into the larynx. The working distance between the distal tip and the target tissue such as the vocal cords was 20-25 mm. The laser scanning area depends on the tilt angle of the mirror and the anatomic constraints. The available static scanning area is 20 x 20 mm^2 and can be enlarged by moving the robotic endoscopic tip. The μRALP robotic system has been tested and validated in a cadaver test [143]. With the fibre delivery and the semi-flexible endoscope, the μRALP robotic system can overcome the line-of-sight limitation and achieve laser patterns or path scanning functionality.

However, the μRALP robotic system can only generate 2 degrees-of-freedom (DoF) laser beam steering control. The steerable tilt angle of the mirror is 15º [134], [143] and the angle of incidence to the target tissue is 20º to 35º (Fig. 2.22). In this approach, the laser scanner must be close to the tissue. To achieve a large enough scanning area, the angle of incidence of the laser beam is significant. With the laser beam divergence, the significant incidence angle will enlarge the size of the laser spot and the spot shape will become an ellipse. Non-targeted healthy tissue will be removed due to the resulting tilted cutting. This issue can be minimised by making the laser shoot straight at the target tissue. The MEMS is mounted on a directional robotic endoscope, it can be moved around to increase its workspace and minimise the angle of incidence. A laser focusing unit is required for precision laser cutting. However, good laser focusing remains an issue to be addressed. In contrast, in TLM, two scanning mirrors are used as laser beam scanners and the working distance is approximately 400 mm. For the same scanning area, the laser beam is almost perpendicular to the target tissue compared to the μRALP. The shape of the laser spot is a circle and the focusing distance of the laser beam is adjustable (Fig. 2.2). Therefore, the laser cutting in TLM is precise and will not suffer the problems of μRALP. The approach of MEMS controlled mirror steering laser scanning still needs to be further validated for clinical application.

An alternative is direct control of the distal tip of the optic fibre to generate the laser scanning motion. The second type of fibre-based laser scanning robotic device, a magnetically controlled fibre steering laser scanner, uses magnetic fields to manipulate the motion of the distal tip of the optic fibre. A permanent magnetic ring fixed near the distal tip of the laser

optic fibre and 4 electromagnetic coils were used to generate a magnetic field and produce torque to change the direction of the fibre tip (Fig. 2.23). The main components and a prototype of the magnetic laser scanner are shown in Figure 2.24. The magnetic laser scanner was developed at IIT, which also participated in the development of the μRALP robotic system. To prevent the beam quality issue caused by the beam divergence, two lenses are used to focus the beam (Fig. 24).

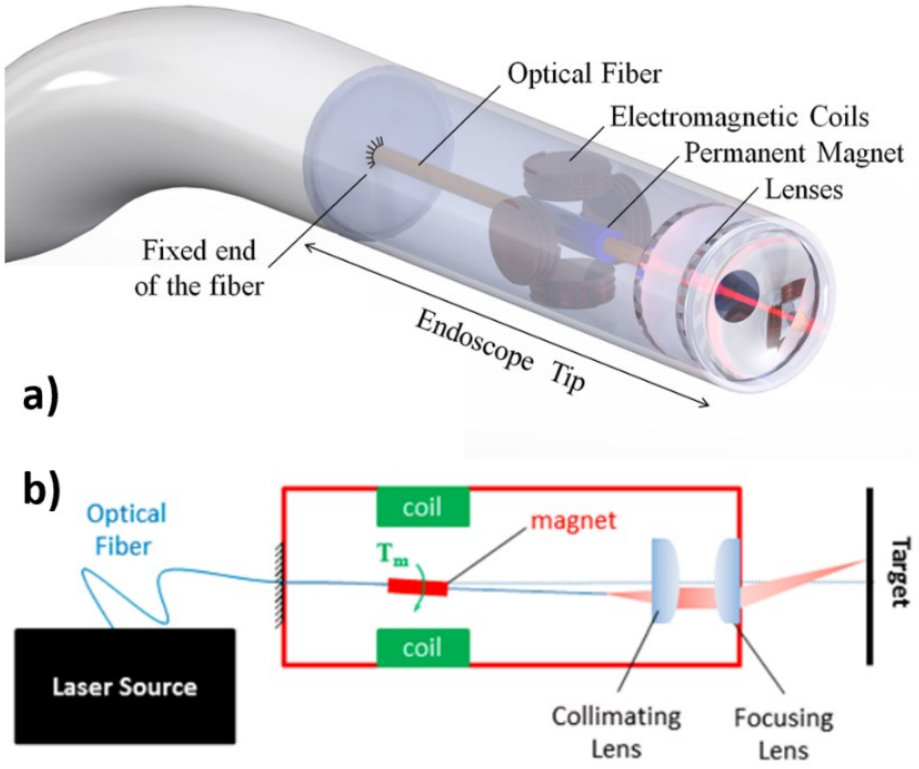


Figure 2.23: a) Conceptual design of the magnetic laser scanner as a flexible endoscopic tip [140] *and b) Schematic illustration of one DoF magnetic control and the focusing laser light on the target with collimating and focusing lenses* [139] *©2017 IEEE.*

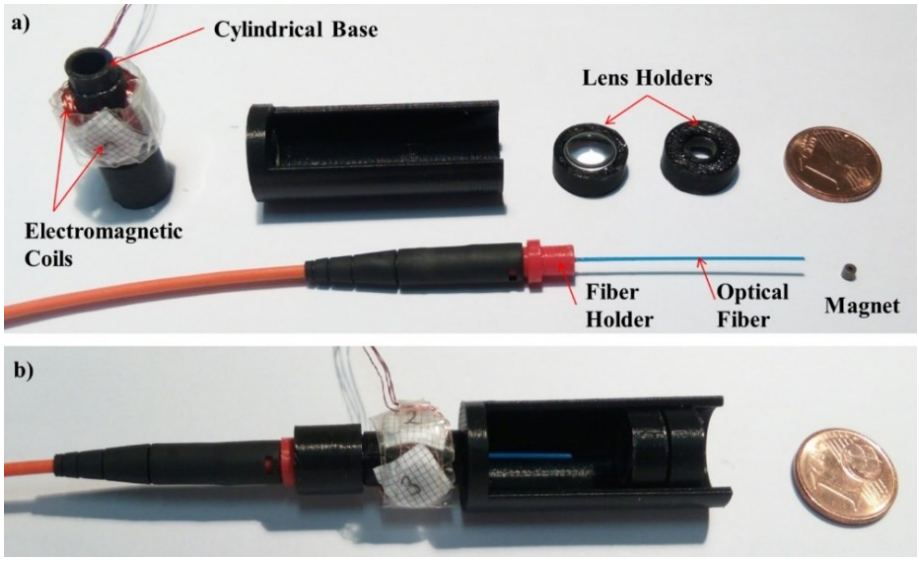


Figure 2.24: Components (a) and assembled prototype (b) of the magnetic laser scanner [140].

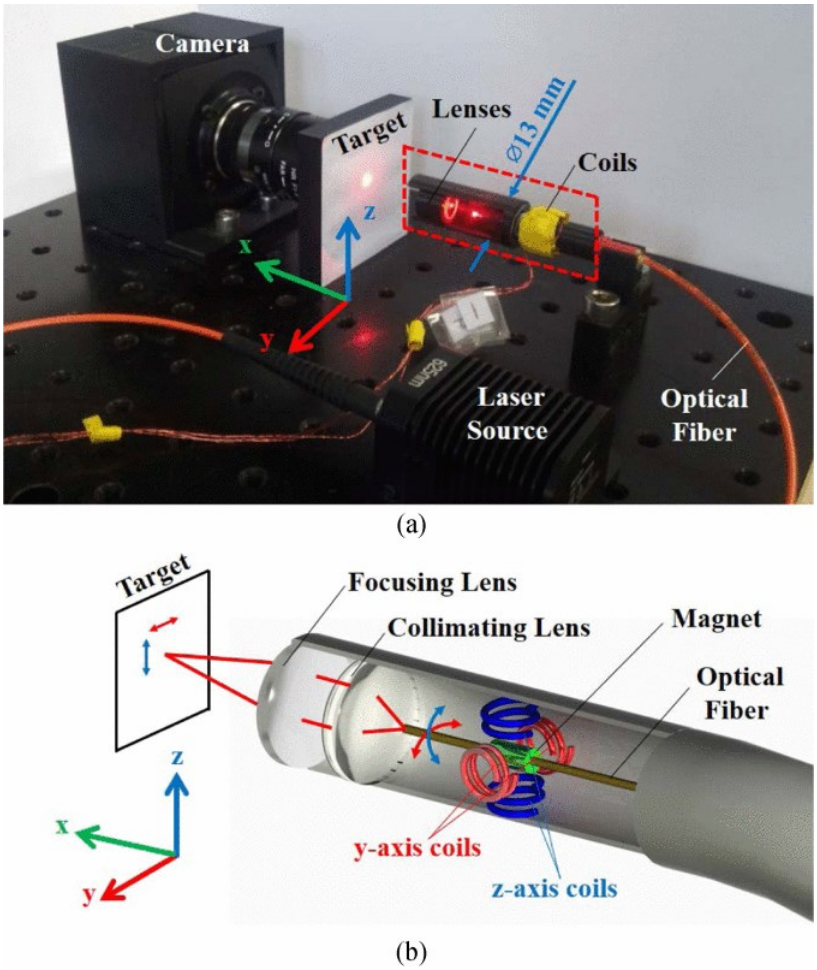


Figure 2.25: (a) Experimental setup of the magnetic laser scanner, including optical fibre, lenses, laser source, and camera. (b) Schematic presentation of the 2 DoF control and the laser beam focusing on the target [141] *©2019 IEEE.*

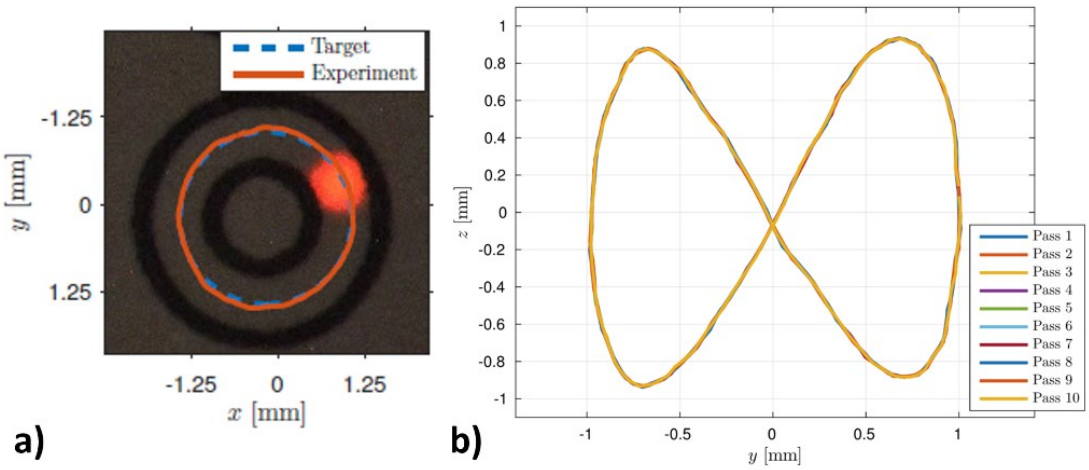


Figure 2.26: a) experimental result of circular path following [139] *©2017 IEEE, and repeatability tests of the scan trajectories for 10 passes of a '8' shape b)* [140].

The laser steering workspace of the magnetic laser scanner depends on the distance between the paired electromagnetic coils in each axis (Fig. 2.25b). The workspace of the 13 mm diameter magnetic laser scanner (Fig. 2.25a) is a 4 × 4 mm square [142]. Similar to the µRALP robotic system, the magnetic laser scanner has 2 DoF laser beam steering (Fig. 2.25b). Path following of an approximately 2.5 mm diameter circular path was performed via teleoperated control and a RMSE of 0.035 ± 0.018 mm was reported (Fig. 2.26a) [139]. The repeatability study performing 10 repeated automated patterns of a figure of 8 shape in a 2 × 2 mm square exhibited a RMSE of 0.021 ± 0.010 mm [140] and an 'M' shape in a 3 × 3 mm square resulted in a RMSE of 0.048 ± 0.016 mm in the y-axis and 0.075 ± 0.035 mm in the z-axis [139]. The experimental results demonstrated high repeatability. The experimental setup of the magnetic laser scanner is shown in Figure 2.25a). The validation of variant automated paths scans also performed. The RMSE will increase with the increasing of the size of the path [141]. However, while the accuracy and repeatability were high, the static workspace of the magnetic laser scanner is quite small. As the magnetic laser scanner was conceived to be used with a driven mechanism such as the end-effector of a robotic arm, the entire workspace can be enlarged by the driven mechanism.

A limitation of non-contact laser scanning is the 2 DoF fibre steering, which in combination with the fixed focal length makes it difficult to maintain the focal point on the target tissue, as identified by a research group at Leibniz University Hannover. A steerable and extendable

robotic endoscopic tip for teleoperated robotic non-contact laser surgery was developed by this group. A vision-based colour map with associated laser caustics of distance can be offered as user guidance to teleoperate the position of the robotic endoscopic tip (Fig. 2.27) [144]. However, the complexity is increased, and if the visual camera is moved with the endoscopic tip, the unstable imaging of the surgical field will cause discomfort to the user.

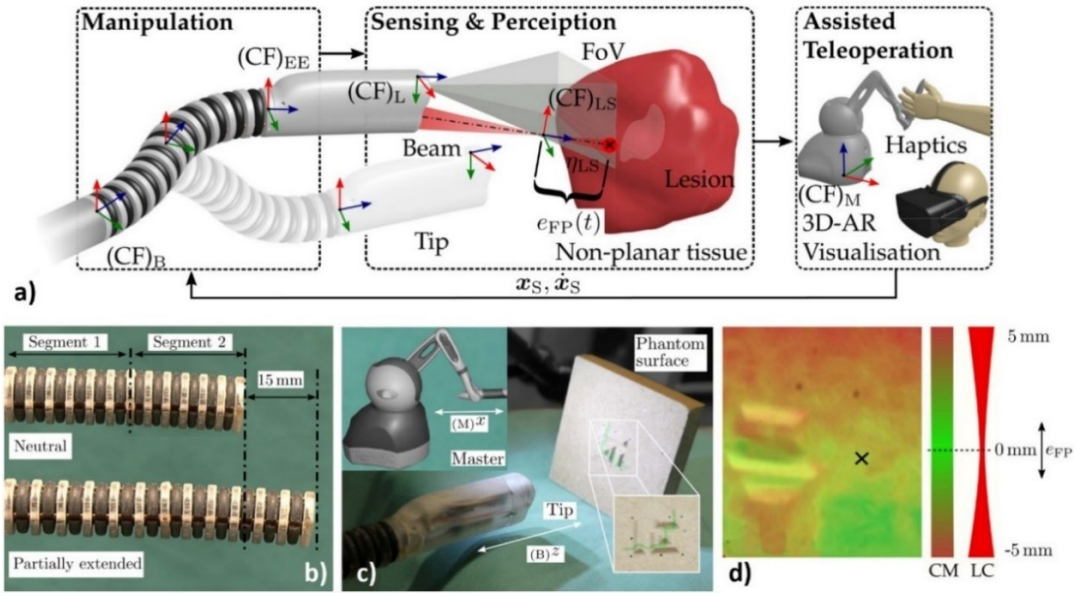


Figure 2.27: a) Conceptual set-up of the image-guided focal positioning teleoperated robotic endoscope for non-contact tissue laser ablation. b) The extendable monolithic continuum structure. c) The endoscope tip, sampled surface phantom and master controller. d) Example of the colour map (CM) with associated laser caustics (LC) of distance [144] *©2019 IEEE*.

The two types of fibre-based laser scanning robotic system, a MEMS controlled mirror steering and a magnetically controlled fibre steering laser scanning system, can achieve non-contact laser ablation with laser scanning. This avoids damaging the fibre tip through contact and prevents the tip sticking to the tissue [140], [145]. However, unlike in TLM, where the laser scanner is located outside of the patient, the aperture of the laser scanner needs to be inserted into the larynx. The laser aperture can be contaminated easily, causing damage and eventually breakage of the laser aperture, such as a focusing lens. Currently, almost all laser fibres are single-use or reusable up to a limited number of times. As presented, there does not seem to be a practical way of replacing the fibre. Finally, the two types of fibre-based laser scanning robotic systems must also consider sterilisation issues and performance degradation due to repeated sterilisation and reuse.

2.5 Summary

As discussed above, both the free beam delivery and fibre delivery techniques, as currently practised, have significant drawbacks. A system for TLP should fulfil the following fundamental requirements:

- Avoid the use of a suspension laryngoscope by obviating the need for a line-of-sight. Provide a solution to access and exposure the larynx through a curved pathway.
- Provide precision, repeatable, healthy-tissue sparing, through user-driven and semi-autonomous control of the laser.
- Provide a technically feasible and practicable proposition.

The MEMS controlled mirror steering and a magnetically controlled fibre steering laser scanning systems have demonstrated the potential to overcome the limitations of current methods and use in TLP. However, as discussed above, some issues such as good laser beam focusing, and laser aperture quality control are needed to be addressed. These two types of fibre-based laser scanning robotic systems still have to face critical challenges to become practical for clinical use. As discussed in the previous chapter, CDPRs have proven their ability to control surgical instruments through the use of multiple cables working in a parallel and antagonistic fashion [146], [147]. High force transmission, relatively large workspace and low cost are some of the intrinsic advantages of such mechanisms. Unlike serial mechanisms, parallel approaches do not suffer from errors accumulating through the kinematic chain and thus could provide precise and repeatable control of an end-effector accommodating a laser fibre. A laser fibre can be inserted in the end-effector through a fibre sheath. The laser fibre is replaceable through the fibre sheath during the surgery. If the fibre tip is damaged, it can be renewed easily, a common routine in clinical practice and costing less than replacing the aperture of the above laser scanners. For TLP, the CDPM can be attached at the end of a flexible or curved instrument, obviating the need for a suspension laryngoscope. Therefore, this approach has the promise to overcome the limitations related to the line-of-sight and perform accurate laser scanning. The details of simulation, design, prototyping and validation of the CDPR for the TLP will be discussed in following chapters.

Chapter 3

Simulation, Design and Prototypes

In this chapter, the modelling and analysis of CDPM for TLP will be introduced, including kinematics, dynamics, tension forces distribution and the controllable workspace. Then follows the simulation, various designs and early prototypes of CDPM for TLP are presented and discussed.

3.1 Modelling and analysis of CDPM for TLP

3.1.1 CDPM

A CDPR is usually composed by a CDPM and a motor control system. A typical CDPM includes a moving platform or end-effector, an outer frame referred to as scaffold and the actuation cables. Each actuation cable goes through the entry point on the scaffold and connects to the attachment point of the end-effector (Fig 3.1). Hybrid type mechanisms, in which actuation cables are combined with rigid links, can provide partial advantages of serial and parallel mechanisms [148]–[150]. However, the hybrid type mechanisms may increase the complexity of the control and the design, which can compromise the advantages CDPMs have. Therefore, this thesis focuses on purely cable actuated CDPMs.

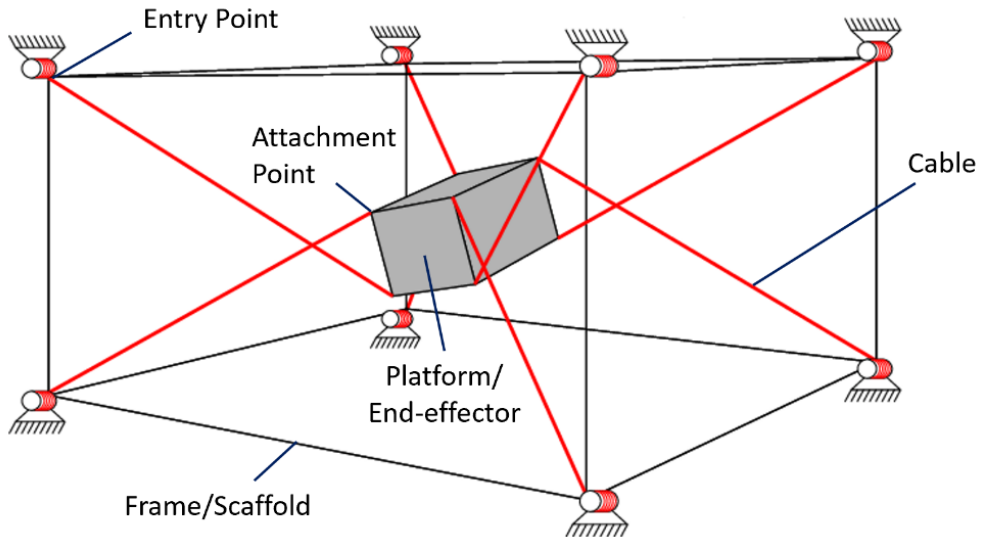


Figure 3.1: An example demonstrates the core concept of CDPM [151].

The shape and size of the scaffold and the end-effector can be specified to fit a wide range of workspace and force requirements. This is achieved by changing the position of the entry and attachment points on the scaffold and the end-effector, respectively. Since the actuation cable is soft, the scaffold can be folded and deployed at the desired location. And due to the parallel mechanism, all the cables act on the end-effector directly and simultaneously. Therefore, high payload and fast motion of the end-effector can be generated. The parallel mechanisms do not accumulate positional errors through the kinematic chain, and therefore a precise and repeatable control of end-effector can be achieved. For a better understanding of the capability of CDPMs, some feature-based applications of CDPM are shown in Figure 3.2 and 3.3. Utilising the feature of large workspace and high speed and accurate motion control, the CDPM can be used for sports events transmission (Fig 3.2a). And combined with the capability of high payload, the CDPM is utilised for handling, storage and retrieval of goods (Fig 3.2b and Fig 3.3) [148], [152]. Furthermore, the CDPM is developed as a motion simulator due to the outstanding dynamics capability[150]. More applications of CDPMs can be found in [148]–[150], [153], [154].

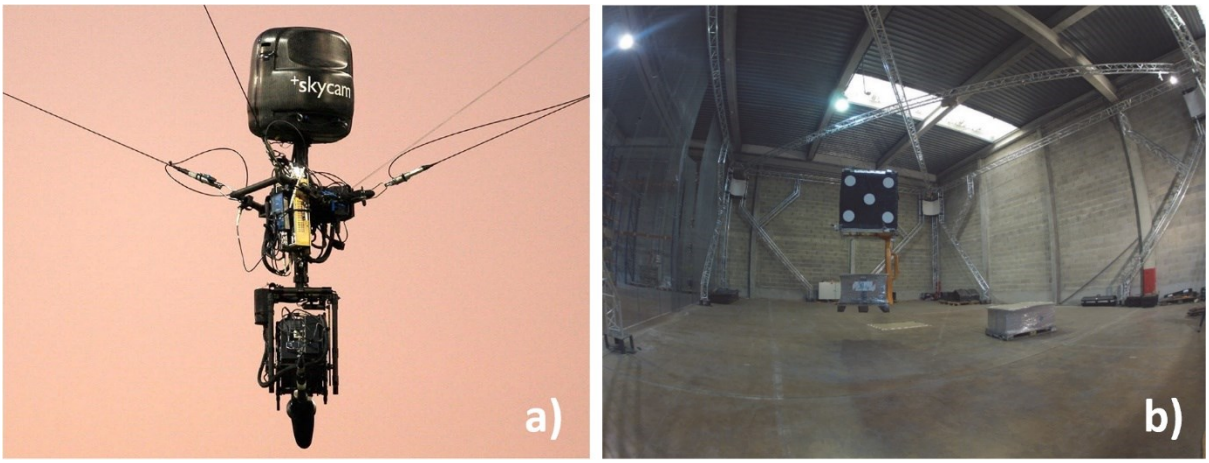


Figure 3.2: a) The cable-driven Skycam used for sports events broadcasting [148]*. b) Prototype of the CoGiRo, a CDPM for goods handling* [149]*.*

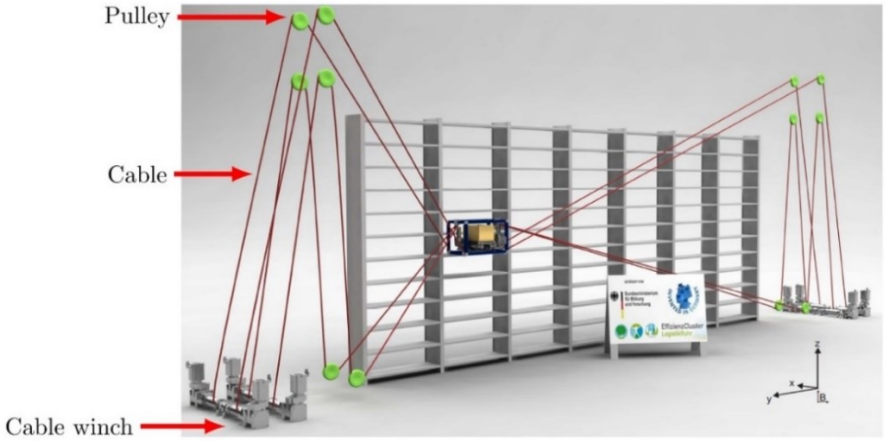
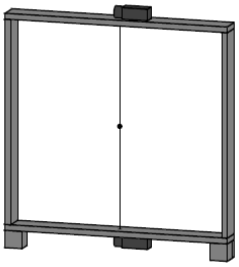


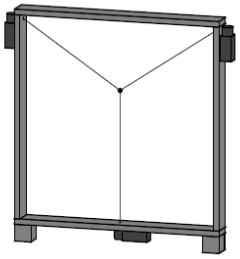
Figure 3.3: Conceptual design of a cable-driven storage and retrieval system [152] *©2018 IEEE.*

3.1.2 Versatility of configuration of CDPM

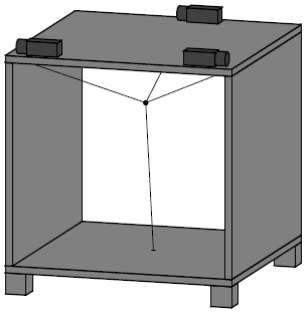
The CDPM can achieve different combinations of degrees-of-freedom (DoF) depending on the distribution of cable connection and the number of cables. Figure 3.4 shows possible DoF of various types of CDPM [155].



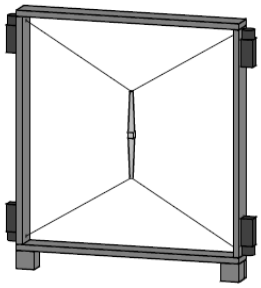
a) 1T, linear motion of a point



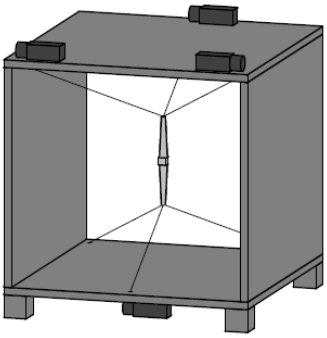
b) 2T, planar motion of a point



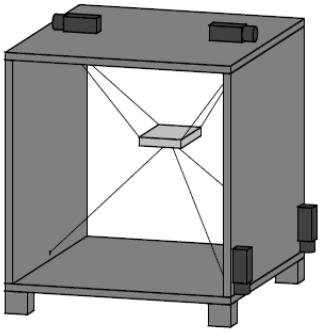
c) 3T, spatial motion of a point



d) 2T1R, planar motion of a beam



e) 3T2R, spatial motion of a beam



f) 3T3R, spatial motion of a body

Figure 3.4: Possible DoF and motion types of CDPM (T stands for translation and R for rotation) [155].

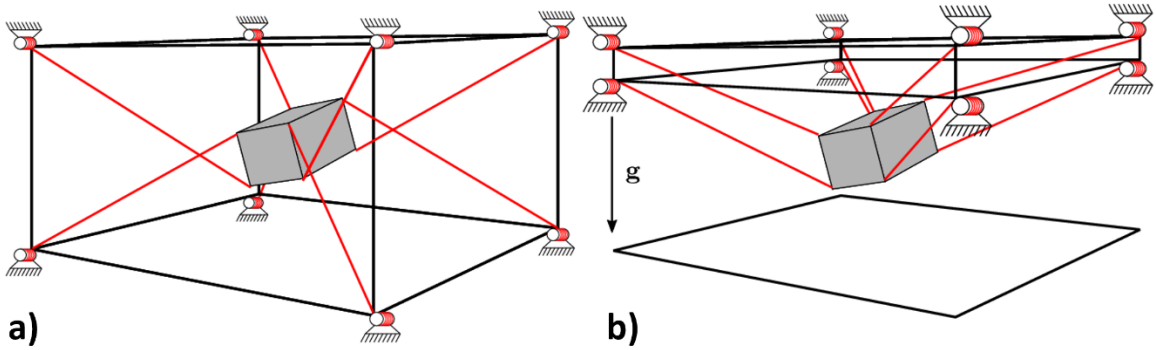


Figure 3.5: Two types CDPM: a) Fully restrained and b) under-restrained CDPM [151].

In general, there are two types of CDPM: fully restrained and under-restrained CDPM. The two types of CDPM are differentiated by the control approach on the end-effector. The under-restrained CDPM utilises an external force, such as gravity, to achieve the desired DoF control of the moving platform (Fig 3.5b). Fully restrained CDPM depend on an additional cable to provide this reactionary force. Therefore, these mechanisms are redundantly actuated: the number of cables is larger than the DoF of the moving platform, so that $m \geq n + 1$, where m denotes the number of cables and n indicates the DoF of the moving platform. And thanks to this redundancy, a singularity free workspace can be achieved [156].

For the surgical application of TLP, a singularity-free workspace is preferred and a fully restrained CDPM should be used. To accommodate the distal tip of a laser fibre, a slim over-tube is used as the moving platform to place and steer the fibre tip. As shown in Figure 3.4 d) and e), the over-tube can have 3 DoF planar motion driven by four cables or 5 DoF spatial motion steered by six cables. To reduce the complexity of control and have a stable structure, in the TLP CDPM, only one entry point on the scaffold and one attachment point on the over-tube can be connected by one cable. To achieve a fully restrained CDPM and to avoid unexpected flipping and rotation of the over-tube, the relationship between the type of DoF and the minimum number of cables of CDPM to manipulate an over-tube are shown in Table 3.1.

Table 3.1: Type of DoF and the minimum number of cables for over-tube steering (T stands for translation and R for rotation)

Type of DoF	Total DoF	Minimum number of cables
1T0R	1	4
2T0R	2	4
0T1R	1	4
1T1R	2	4
2T1R	3	4
3T0R	3	6
0T2R	2	6
1T2R	3	6
2T2R	4	6
3T1R	4	6
3T2R	5	6
0T3R	3	8
1T3R	4	8
2T3R	5	8
3T3R	6	8

The controllable workspace of CDPMs depends on the number of cables, their positioning and configuration within the scaffold. For example, Figure 3.6 shows how a different number of cables within the same available space (circle provided by the supporting scaffold) can generate different controllable workspaces (regions in grey).

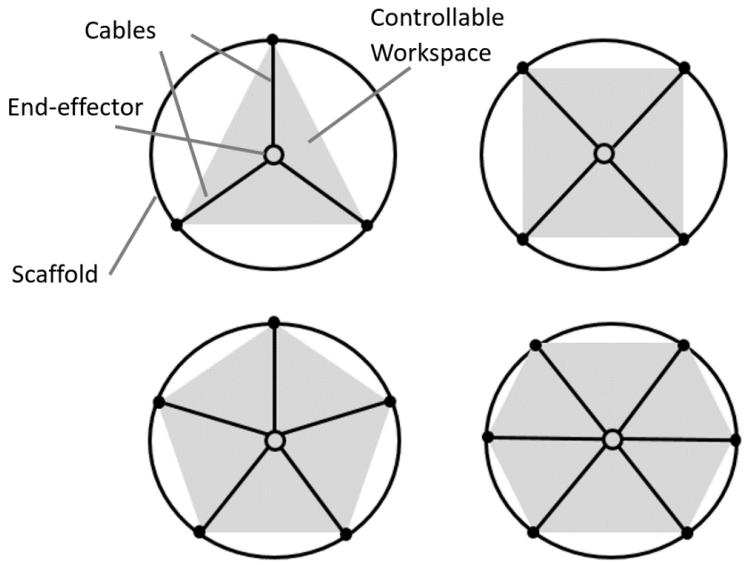


Figure 3.6: Some examples of different controllable workspaces (regions in grey) generated by different cable configuration within the same available space (circle) provided by the supporting scaffold.

The size and shape of the scaffold, as well as the number and positioning of the cables controlling the over-tube, will also affect the resulting controllable workspace. Furthermore, the configuration of cables, over-tube and scaffold will affect the force exertion capabilities. By increasing the number of cables, it is possible to achieve greater dexterity, manipulability and exertion force. However, a large number of actuators and cables will also increase system complexity and costs.

To develop a CDPM for TLP, the main CDPM parameters to be considered include configuration, kinematics, dynamics and controllable workspace analysis, and tension forces distribution calculation. A single over-tube driven by six cables will be discussed as an example. As shown in Figure 3.7, in this configuration, the over-tube can achieve 5 DoF motion, three translations and pitch and yaw rotations. Therefore, it is defined as a redundantly restrained mechanism [157]. The cables are connected between the scaffold and the over-tube, where the fixation entry points on the scaffold are B_i (i=1, 2, …, 6), and the attachment points on the over-tube are P_i (i=1, 2, …, 6). The length of six cables $\left\|\vec{l_i}\right\|$ can therefore be defined as $\left\|\vec{l_i}\right\| = \left\|\overrightarrow{P_iB_i}\right\|, (\mathrm{i} = 1,2, \ldots ,6)$.

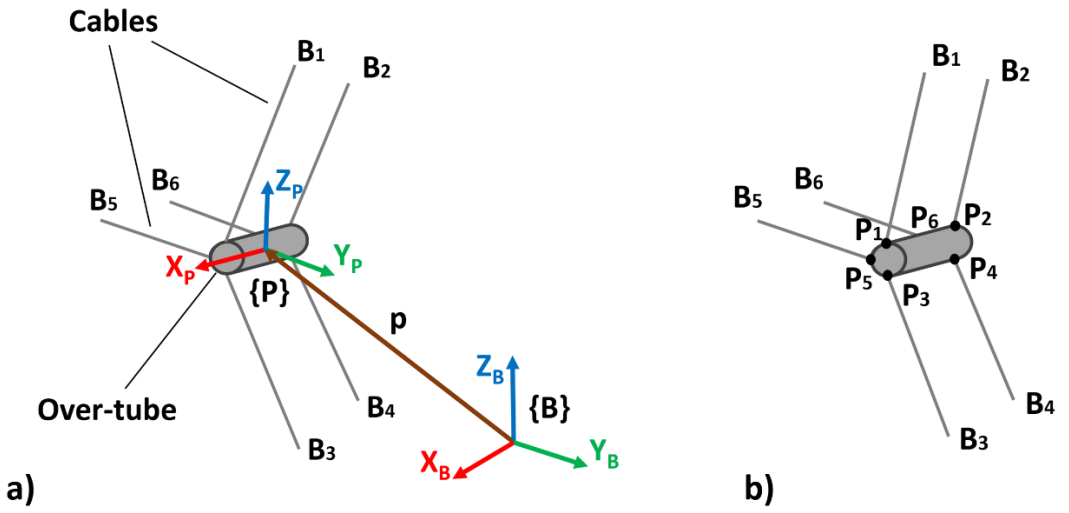


Figure 3.7: A single over-tube parallel robot mechanisms driven by six cables. a) The base frame {B} and the moving frame {P}. b) Six entry points (Bi) on the scaffold and six attachment points (Pi) on the over-tube.

The motion of the over-tube is described by the moving frame $\{P\}$ attached to it with origin P_0 located at its centre of mass. With respect to the base frame $\{B\}$, the moving frame can have a rotation along the Z-axis of angle θ_z and along the Y-axis of angle θ_y, and have a translation $P = [x, y, z]^T$ corresponding to the distance from the origin of the base frame to P_o. The rotation along the X-axis (*i.e.,* the axial rotation of the over-tube) cannot be actuated by this specific cable configuration. The corresponding rotation and transformation matrix describing the motion of the over-tube in the base frame can therefore be derived as equations 3-1 and 3-2 respectively, where s stands for sine and c stands for cosine.

$$R = \begin{bmatrix} c\theta_z & -s\theta_z & 0 \\ s\theta_z & c\theta_z & 0 \\ 0 & 0 & 1 \end{bmatrix} \begin{bmatrix} c\theta_y & 0 & s\theta_y \\ 0 & 1 & 0 \\ -s\theta_y & 0 & c\theta_y \end{bmatrix} = \begin{bmatrix} c\theta_z c\theta_y & -s\theta_z & c\theta_z s\theta_y \\ s\theta_z c\theta_y & c\theta_z & s\theta_z s\theta_y \\ -s\theta_y & 0 & c\theta_y \end{bmatrix}, \quad (3\text{-}1)$$

$$T_B^P = \begin{bmatrix} R & p \\ 0 & 1 \end{bmatrix}. \quad (3\text{-}2)$$

3.1.3 Kinematic analysis

In TLP, once the motion of the over-tube (and the instrument it accommodates) has been defined by the surgeon, the position and orientation of the instrument in the base frame are known. The 3D position of the origin of the moving frame $P_0(x, y, z)$ and the rotations (θ_y, θ_z)

can be computed and the transformation matrix can be derived using equations 3-1 and 3-2. The lengths of the 6 cables ($\|l_1\|, \|l_2\|, \ldots, \|l_6\|$) corresponding to the desired instrument pose are unknowns. Using loop closure analysis as shown in figure 3.8 a), equation 3-3 can be derived, where B_0 denotes the origin of frame $\{B\}$ [94], [157].

$$\vec{l_i} = \overrightarrow{P_iB_i} = \overrightarrow{B_0B_i} - \overrightarrow{P_0P_i} - \vec{P} \quad \text{for } i=1, 2, \ldots, 6, \tag{3-3}$$

By expressing the P_0 and P_i points in the base frame via the transformation matrix in equation 3-2, six equations can be generated and a single solution can be derived. The length of the cables should be limited by the size of the scaffold; otherwise, the desired point in the trajectory may lie out of the workspace.

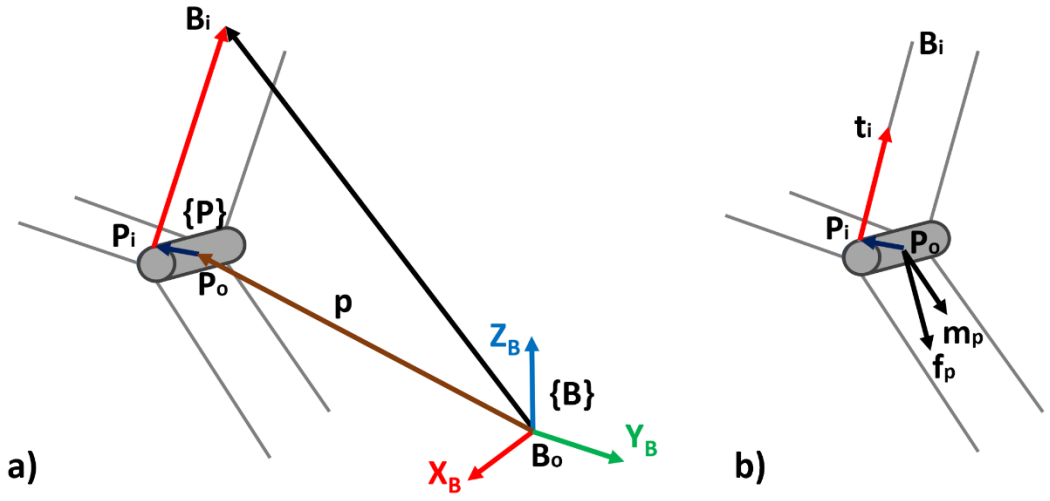


Figure 3.8: Structure analysis of the parallel robot mechanism. a) Loop closure (Po, Pi, Bi, B0) and b) Forces and torques on the over-tube.

3.1.4 Dynamic analysis

As shown in figure 3.8 b), the forces t_i along cables can be expressed as equation 3-4 and the torques m_i generated by the cable tensions applied on the over-tube can be expressed as equation 3-5:

$$\vec{t_i} = \frac{1}{l_i}\vec{l_i}t_i \tag{3-4}$$

$$\vec{m_i} = \vec{t_i} \times \vec{r_i}, where\ \vec{r_i} = \overrightarrow{P_0P_i} \tag{3-5}$$

The total forces f_P and torques m_P acting on the over-tube can then be calculated as:

$$f_P = \sum_{i=1}^{6} \frac{1}{l_i} \vec{l}_i t_i \tag{3-6}$$

$$m_P = \sum_{i=1}^{6} \vec{t}_i \times \vec{r}_i \tag{3-7}$$

Equations 3-6 and 3-7 can be expressed as one equation [157]:

$$At + f = 0 \tag{3-8}$$

Where:

$$A = \begin{bmatrix} \frac{1}{l_1}\vec{l}_1 & \dots & \frac{1}{l_6}\vec{l}_6 \\ \vec{r}_1 \times \frac{1}{l_1}\vec{l}_1 & \dots & \vec{r}_6 \times \frac{1}{l_6}\vec{l}_6 \end{bmatrix}, t = [t_1, t_2, \dots, t_6]^T$$

The structure matrix $A = J^T$ [158], where J is the Jacobian matrix. f denotes the external forces and torques (the wrench) acting on the over-tube.

The actuator dynamics can be represented by equation 3-9 [159]:

$$D\ddot{q} + C\dot{q} + rt = \tau \tag{3-9}$$

Where D is the diagonal matrix of motor inertia, C is the diagonal matrix of motor viscous friction coefficients, $\tau = [\tau_1, \tau_2, \dots, \tau_6]^T$ is the motor toques vector and $t = [t_1, t_2, \dots, t_6]^T$ is the cable tension vector. The vector $q = [q_1, q_2, \dots, q_6]^T$ are the motor angles and $\dot{q}$, $\ddot{q}$ denote the angular velocity and acceleration, and r is the radius of the drum of the motor.

3.1.5 Tension forces distribution

In this section, the tension forces distribution of completely restrained CDPM will be discussed. As shown in Figure 3.7, the number of cables (m) is six and the number of DoF (n) is five. Since the CDPM is redundant ($m = n + 1$), if the end-effector with a specific pose is in the controllable workspace, the rank of structure matrix A should be n. The structure matrix A can be divided into two parts:

$$A = [B \quad h] \tag{3-10}$$

Where B is an *n* x *n* matrix, and vector *h* is an *n* x 1 vector which represents the redundant cable. Then the tension forces could be expressed as below equation 3-11:

$$t = \begin{bmatrix} -B^{-1}h \\ 1 \end{bmatrix} t_i + \begin{bmatrix} -B^{-1}f \\ 0 \end{bmatrix} \tag{3-11}$$

Where t_i is representative of the cable tension force of one of *m* cables which is treated as redundant, and f is the external wrench. The first term of the right side of equation 3-11 denotes the internal tension distribution contributing to internal force equilibrium, and the second term denotes the forces distribution for external equilibrium [160], [161]. The selection of the redundant cable needs to avoid singularities (the rank of matrix B is less than n). By choosing every cable in turn as the redundant cable and calculating the eigenvalues of the corresponding matrix B, cable with the minimum eigenvalue can be selected. The tension force level can be adjusted by changing the value of t_i within the range of the limitations.

3.1.6 Controllable workspace

As mentioned above, once the size and shape of the scaffold and the cable configuration are fixed, the controllable workspace can be computed. The tension forces of all cables satisfy two conditions:

(1) $At + f = 0$

(2) $t_i \in [t_{min}, t_{max}]^i$

For condition (1) to be fulfilled, the cable tensions t_i need to meet the so-called force closure condition given by equation 3-8. The tension of all cables needs to keep the end-effector in equilibrium. For condition (2), each cable tension needs to be constrained above a small pretension (t_{min}) which needs to be maintained in the mechanical system and below a maximum force (t_{max}) which can be generated by the motors or endured by the cable.

The stiffness of the end-effector also depended on the pose of the over-tube and the distribution of cable tensions. The stiffness matrix K_x can describe the relationship between an infinitesimal wrench δf working on the end-effector and the corresponding displacements

of it δx (Equation 3-12). Combining this with equation 3-8, the stiffness matrix K_x can be computed as equation 3-13 [162]:

$$\delta f = K_x \delta X \tag{3-12}$$

$$K_x = -\frac{\partial A}{\partial X} t - A K_l A^T \tag{3-13}$$

As defined above, A is the structure matrix, t is the cable tension vector, and X is the pose of end-effector $[x, y, z, \theta_y, \theta_z]$. The matrix K_l is the stiffness matrix in joint space and denotes the relationship between infinitesimal cable tensions and the resulting changes in cable length. The right side of equation 3-13 indicates that the stiffness of the end-effector relies on the cable tension distribution and the pose of the end-effector [162], [163]. The stiffness will be affected significantly when the end-effector approaching to the boundary of the workspace, where the extreme value of cable tension may occur. Tension factor (*TF*) is defined as the ratio of the maximum tension over the minimum tension of all cables (Equation 3-14). The value of tension factor will decrease when the end-effector is close to the boundary of the workspace. The tension factor can be utilised as a threshold to prevent the end-effector gets too close to the boundary of the workspace [164].

$$TF = \frac{min(t)}{\max(t)} \tag{3-14}$$

In addition, a geometrical constraint is required that does not allow any cable to cross the over-tube for the evaluation of the controllable workspace. Within the reachable workspace, there will be specific end-effector positions for which a small torque will result in the over-tube to rotate around its axis, causing the cables in mathematical simulations to cross the over-tube. In practice, the cable will not cross the over-tube but will roll around the tube. The rolling around the over-tube does not necessarily prevent that specific end-effector positions are not reachable. However, this can affect the positional precision of the end tip of fibre or instrument. When the robot is controlled by a master manipulator, the position could be corrected by the operator. However, the unexpected cable rolling will compromise the controllability.

3.2 Configuration Simulation of the CDPM for TLP

As discussed in section 2.5, the CDPM can be used to manipulate the distal end tip of a laser fibre to perform laser incision, ablation or photocoagulation in TLP. Due to the intrinsic advantages of CDPM, high precise and repeatable laser scanning can be achieved. A simulator has been developed via MATLAB software for the TLP CDPM, including below main procedures as shown in Figure 3.9:

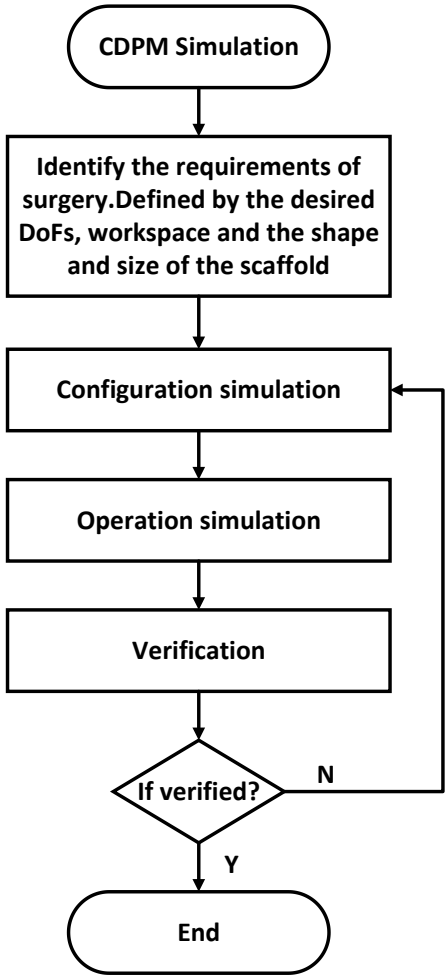


Figure 3.9: The flowchart of the framework of the TLP CDPM simulation.

(1) Identify the requirements of the TLP CDPM, including the desired operation, DoF of motion, workspace, shape and size of scaffold etc.

(2) Perform the configuration simulation, generate cable distributions and calculate the controllable workspace.

(3) Carry out a collision-free operation simulation, implement the desired motions of end-effectors to simulate the task operation, such as pattern scanning.

(4) Perform the verification test to check if the configuration of CDPM can meet the requirements proposed in step (1).

3.2.1 Required specifications of TLP CDPM

For the TLP laser operations, such as cutting, two surgical instruments are engaged, a laser fibre and an auxiliary tool such as a vocal cord holder/forceps/gripper. Therefore, two CDPMs can be used to manipulate the two surgical tools, one over-tube for the laser fibre and one over-tube for another surgical instrument such as forceps. As discussed in section 2.4, the laser fibre over-tube will need 5 DoF motion to manage the laser beam quality, 3 DoF of translation and 2 DoF of pitch and yaw rotation. Since the shape of the laser fibre is a slim cylinder, a roll DoF rotation is not required for the laser fibre. The three translational DoF are required to move the fibre tip to the desired position and control its distance from the tissue. Approximately 1 mm distance is needed for laser incision or dissection, and 2–5 mm for photocoagulation or haemostasis. The two rotational DoF are used to improve manipulability. The 5 DoF motion could make the laser spot projection is circular or close to circular. The other surgical instrument over-tube will also need at least 5 DoF motion, while a stepper motor can be placed external to the surgical system units to rotate torsionally stiff flexible instruments if a roll DoF is required. An external manipulator could be used to control the operation of the auxiliary surgical instrument during the surgery (e.g. open and close the forceps or gripper) [95]. To accommodate the fibre tip, the inner size of over-tube is 1.2 mm diameter, with an outer diameter is 1.5 mm. The size of over-tube for the auxiliary surgical instrument could be larger based on the size of the instrument.

There are two cues to estimate the desired workspace for TLP. One is the size of an adult vocal cord. Another cue is the maximum size of the distal tip of conventional laryngoscopes. The length of an adult vocal cord is between 11–21 mm, and the width approximately half of that [165]. And the thickness of the laryngeal tissue is around 3-5 mm [166]. Currently, the maximum size of the distal tip of conventional laryngoscopes is 27 mm in diameter [167].

Based on these, the desired workspace for one side vocal cord and glottis should be approximately a 27 mm diameter half-cylinder with 10 mm depth. The size and shape of the scaffold depend on the specific data of the patient. The shape of the scaffold is based on the distal tip of conventional laryngoscopes [167], which is a hollow cylinder or elliptical cylinder. To achieve the workspace of the maximum size of the distal tip of conventional laryngoscopes, 27 mm in diameter, the size of the scaffold is defined as a 22 x 20 mm ellipse. In summary, the required specification of CDPMs for TLP is presented in Table 3.2.

Table 3.2: Required specifications of TLP CDPMs

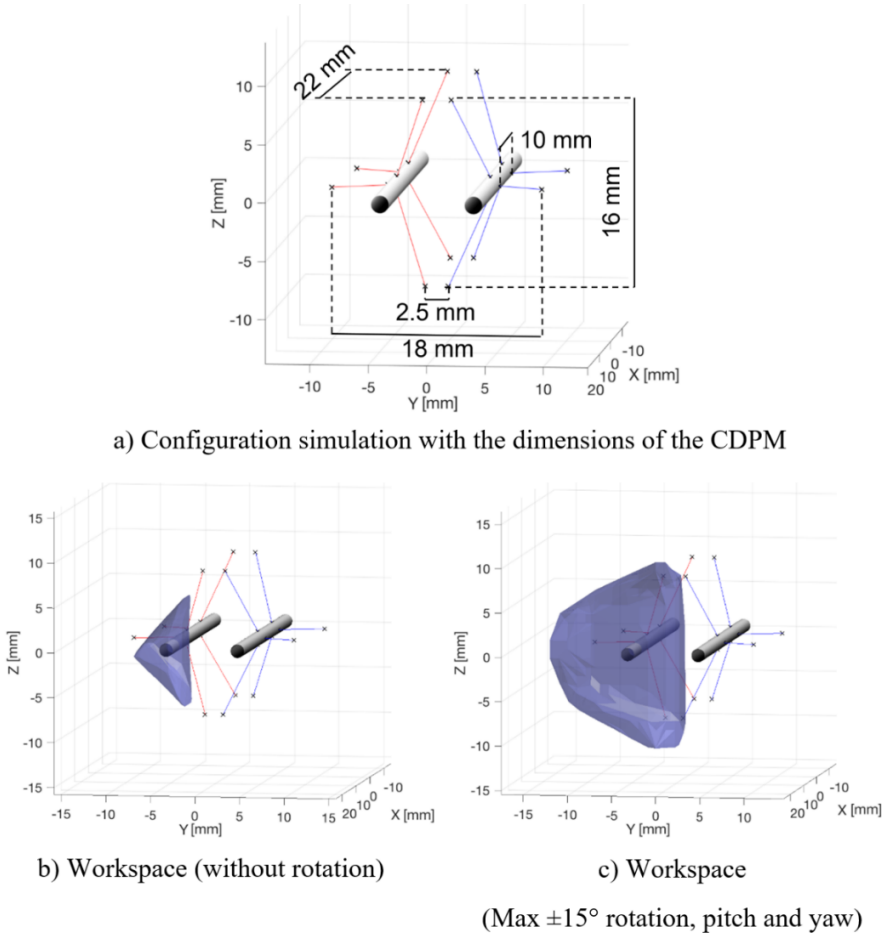
Item	**Required Specification**
Shape of scaffold	Elliptic cylinder
Size of scaffold	22 x 20 mm (W x H)
Size of over-tube for laser fibre	ø1.5 mm diameter, 10-20 mm length
Size of over-tube for auxiliary surgical instruments	ø1.5-3.0 mm diameter, 10-20 mm length
Desired DoF for laser fibre	5 DoF
Desired DoF for other surgical instruments	5 DoF
Desired workspace	27 mm diameter cylinder with 10 mm depth

3.2.2 Configuration simulation and controllable workspace

Based on the required specification, and as shown in Table 3.1, the minimum number of cables for steering of one over-tube is six. Following the procedures of the simulation framework (Fig 3.9), the resulting configuration and parameters of TLP CDPMs are defined, as shown in Figure 3.10a). The diameter of the over-tube is 1.5 mm. The distance between the end tip of the simulated instrument and the front set of cables is 20 mm. The dimensions of the scaffold and the cable positioning of the laser arm are shown in Table 3.3. The origin ([0, 0, 0]) of the robotic coordinate system is located at the centre of twelve cable entry points on the scaffold. The X-axis is the longitudinal axis of the cylindrical scaffold and points to the target end of the scaffold (Fig. 3.10a). The cable configuration of the both end-effectors are symmetrical along the X-Z plane.

Table 3.3: Coordination of cable location

Cable location ([x, y, z])	**Scaffold [mm]**	**Over-tube [mm]**
Laser arm cable 1	[11, -1.25, 8]	[5, 0, 0.75]
Laser arm cable 2	[-11, -1.25, 8]	[-5, 0, 0.75]
Laser arm cable 3	[11, -8.25, 0]	[5, -0.75, 0]
Laser arm cable 4	[-11, -8.25, 0]	[-5, -0.75, 0]
Laser arm cable 5	[11, -1.25, -8]	[5, 0, -0.75]
Laser arm cable 6	[-11, -1.25, -8]	[-5, 0, -0.75]



a) Configuration simulation with the dimensions of the CDPM

b) Workspace (without rotation)

c) Workspace

(Max ±15° rotation, pitch and yaw)

Figure 3.10: Configuration simulation and controllable workspace. a) Configuration simulation with the dimensions. b) Controllable workspace without rotation. c) Controllable workspace with rotation [168] *©2020 IEEE.*

The configuration and the controllable workspace of the laser fibre and the auxiliary tool is symmetrical along the XZ-plane. The workspace is numerically calculated using the force-closure and wrench-feasible workspace on a grid search overall five dimensions. The resulting workspace is fulfilling the geometry and cable tension constraint mentioned in section 3.1.6 are used to determine feasible points, for which a cable tension range of [0.3N, 30N] and a TF of 0.05 is used. The workspace for an unloaded instrument (i.e. zero wrench) is shown in Figure 3.10b) and 3.10c). Without rotation, the controllable workspace can be approximated by a 5.5×12 mm triangle with a 10 mm depth. When rotations with a maximum rotation angle both in pitch and yaw is $\pm 15^{\circ}$, the controllable workspace expands to a 28 mm diameter half cylinder with 11 mm depth. As the laser fibre can be placed into either left or right over-tube, the entire workspace of the laser arm is approximately that of a full cylinder with a 28 mm diameter. The resulting workspace is more than adequate, as the maximum size of the distal tip of conventional laryngoscopes is 27 mm [167]. And the workspace can be enlarged dramatically by moving the scaffold or extending more fibre tip out from the over-tube.

Figure 3.11 shows some examples of possible positions of the supraglottic tumour. The scaffold could be positioned via the attached support device (such as a flexible endoscope or curved laryngeal blade) to align the operative field (blue area) to the cysts or tumour region. If the target is large, then it could be divided into subparts, with surgery performed sequentially.

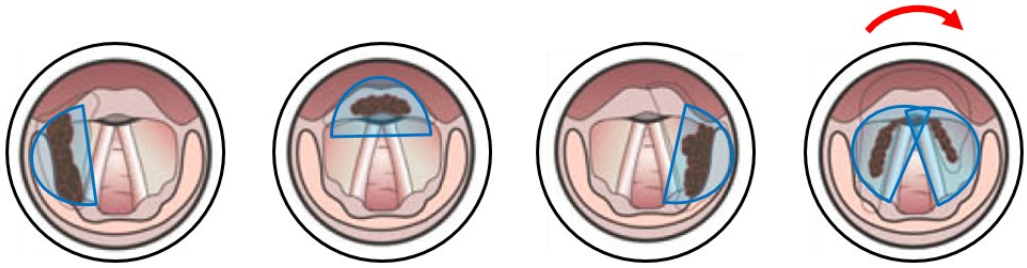


Figure 3.11: Scheme of the position of the tumour region and the operative area [102].

The configuration of cable distributions can be allocated based on the position of the target tissue. Figures 3.12 to 3.14 demonstrate six different configurations (rotated along the axis of scaffold) together with the controllable workspace of the laser fibre arm and the total controllable workspace of the laser fibre arm of the six configurations.

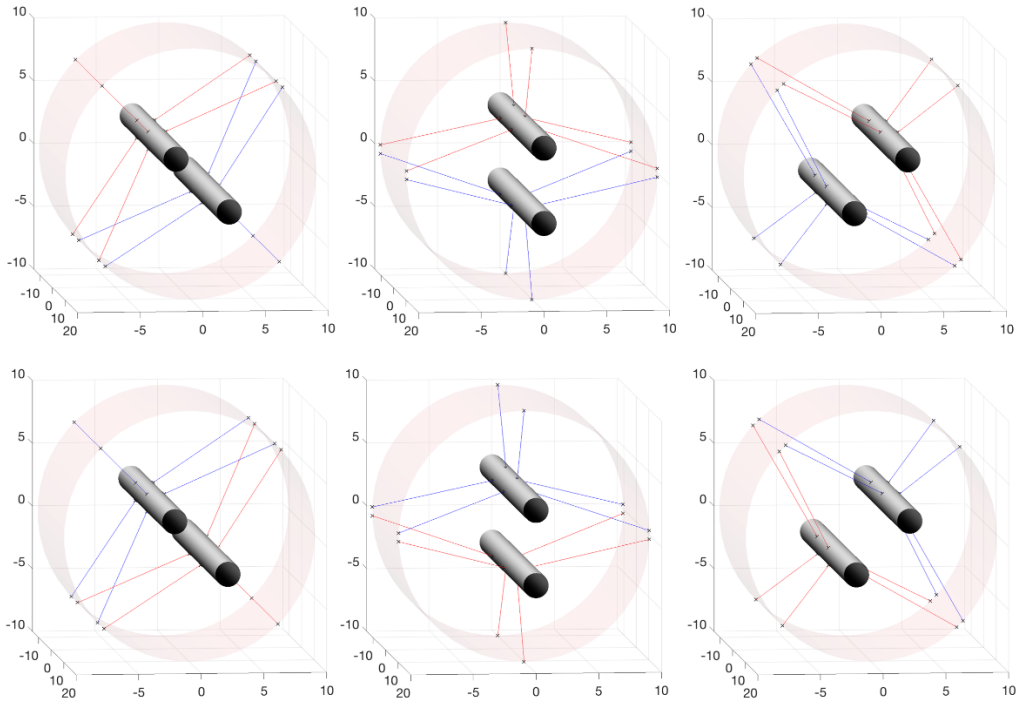


Figure 3.12: Different configurations (rotated the current configuration 45, 90, 135, 225, 270 and 315 degrees respectively).

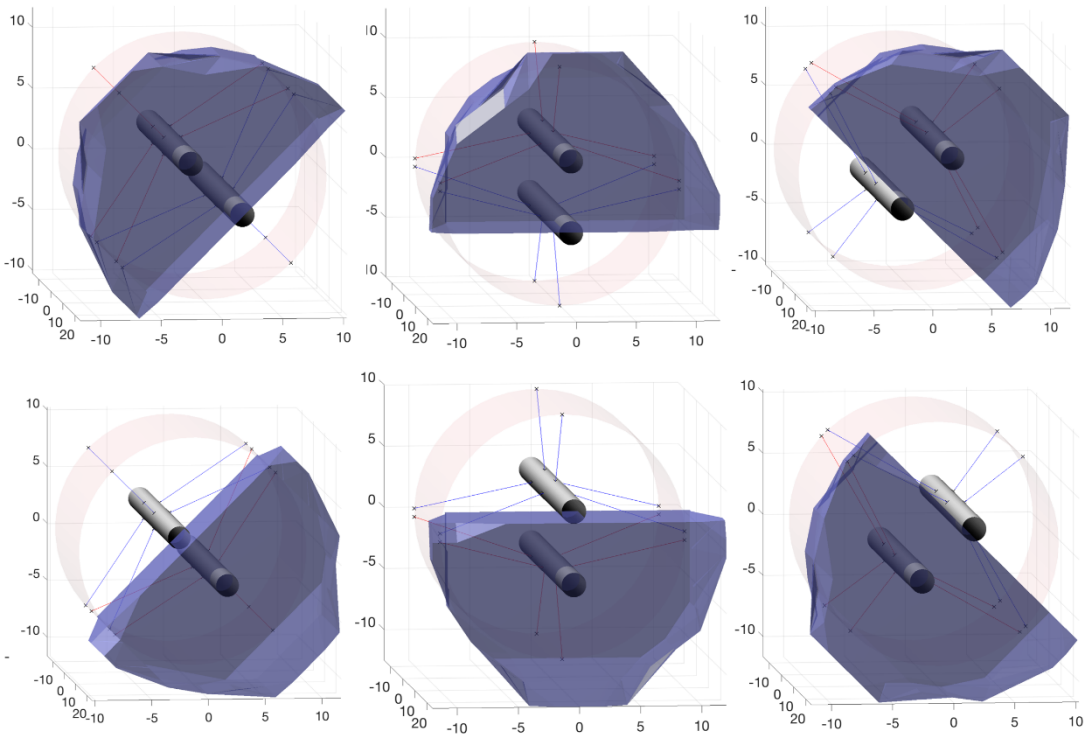


Figure 3.13: Corresponding workspace of the laser arm for the 6 configurations shown in figure 3.12.

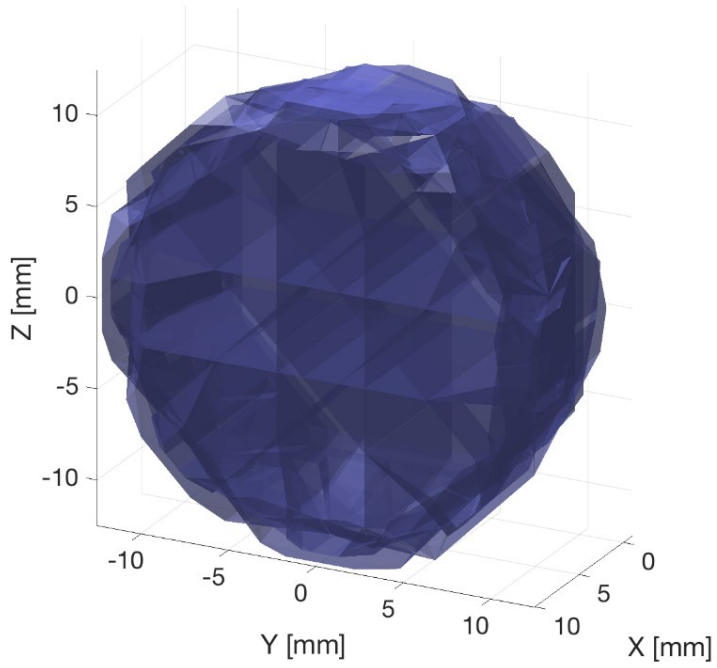


Figure 3.14: The total controllable workspace of the laser fibre arm for the 6 configurations in figure 3.12 (28 mm diameter cylinder with 11 mm depth).

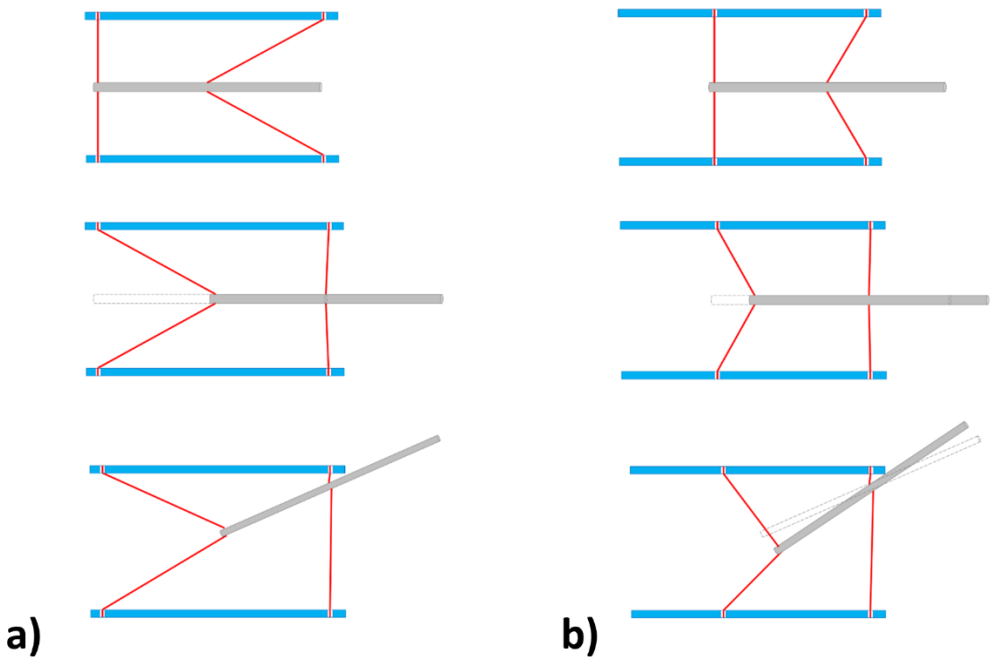


Figure 3.15: Relationship between a maximum range of translation and rotation and the distance between entry points in one plane. a) Longest distance between entry points: larger range of translation but smaller range of rotation. b) Short distance between entry points: smaller range of translation but larger range of rotation.

The cable locations can be adjusted based on patient-specific data and operational needs. Due to the intrinsic feature of CDPM, the maximum range of translation and rotation cannot simultaneously be achieved in one fixed configuration type. The maximum horizontal translation distance can be defined as the maximum horizontal moving distance of the over-tube. If the attachment points on the over-tube are fixed, the larger distance between entry points, the larger range of translation but the smaller the range of rotation (see figure 3.15).

The configuration TLP CDPMs will use twelve cables fashioned, as shown in Figure 3.10a) to fulfil the requirement of specification.

3.2.3 Collision-free operation simulation

For a bimanual CDPR, the tool-tool, tool-camera, tool-cable, cable-camera and the cable-cable collision will affect the performance. Points in the controllable workspace will be unreachable when collisions occur, therefore it is necessary to detect and avoid collisions.

Based on a particular operation, the trajectories in the controllable workspace for each arm can be generated followed by collision detection. Besides the collision detection between tendons, the collision detection problem can be solved by calculating the distance between line segments. If the distance is smaller than a threshold value, a collision occurred. A collision between two cables can be detected by calculating the distance of a point (one attachment point) to a plane (formed by another attachment point and two entry points). When the distance is less or equal to zero, a collision occurred.

Figure 3.16 shows the result of a simulated operation of laser scan a with collision detection. The left arm (connected by blue cables) is for the forceps to pull and hold the tissue at the centre of the field of view. The right arm (connected by red cables) is to scan the laser fibre pattern, such as a straight line or an arc line. The results show that the generated configuration of TLP CDPMs could perform the operation of laser pattern scanning without collision.

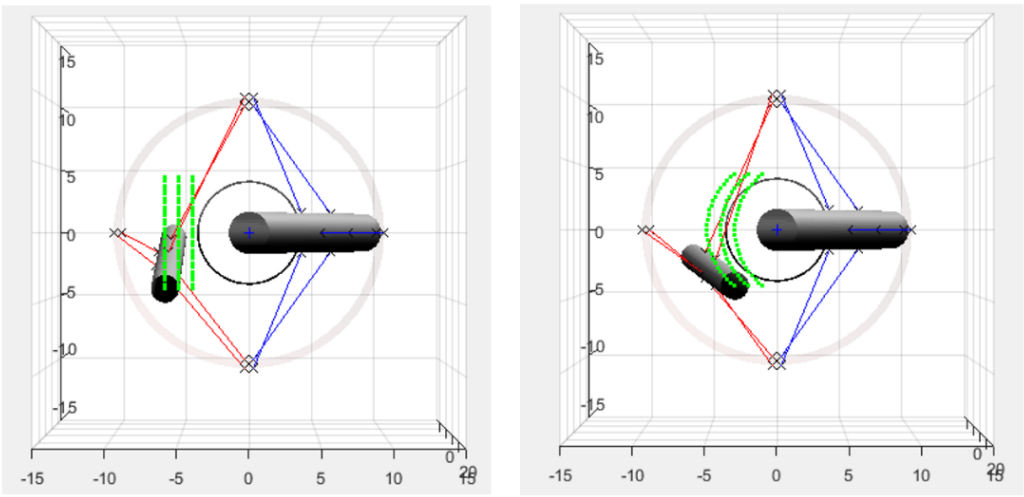


Figure 3.16: Result of the simulation operation of laser pattern scanning with collision detection.

In addition, collision detection can help to optimise the CDPMs configuration. For example, if the position of the end of camera far from the operation field, there is no collision between tool and camera and the over-tube is easy to manipulate. However, the field of view may be too large. If the position of the end of camera is close to the operative field, the view of the operative field is better. However, the over-tube may be difficult to manipulate to avoid the collision. The position of the proximal end of the endoscope could be determined based on simulation and collision detection.

3.3 Designs and prototypes of TLP CDPR

The sections above have demonstrated the potential of CDPM to generate precise laser scanning. To meet the requirements of TLP and avoid the need for a line-of-sight, the CDPM should be attached at the end of a flexible or curved instrument and inserted into the larynx through the curved airway. As discussed above, one feature of CDPR is their versatility and compatibility with a range of existing medical devices, such as semi-flexible/flexible endoscope or curved laryngeal blades. Also, they can be designed as a stand-alone TLP device, including manipulator, camera and light source, etc. In this section, two add-on designs: E*ndoTORS* and *LaryBladeTORS* robot and one stand-alone robotics: *LaryngoTORS* robot will be described and discussed. All designed TLP CDPR will use the resulting configuration simulated in section 3.2.2.

3.3.1 Design and prototype of *EndoTORS* robot

The conceptual design of the *EndoTORS* robot is shown in Figure 3.17, including a scaffold, two over-tubes, twelve cables and cable transmission tubes. The CDPMs are amounted at the end of an endoscope.

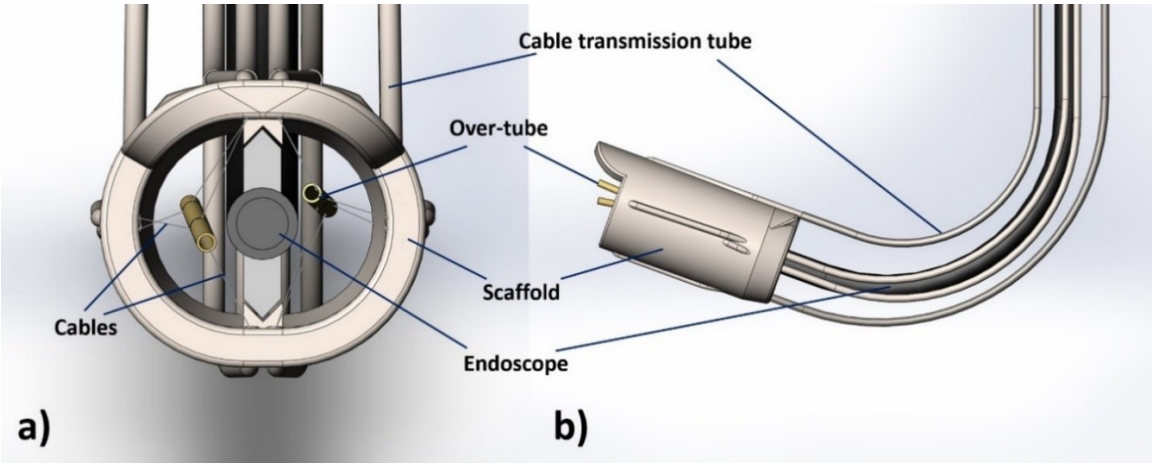


Figure 3.17: Render and core components of the EndoTORS robot, showing the CDPMs at the end of an endoscope.

A flexible laryngoscope or rhino-laryngoscope can be combined with the *EndoTORS* robot. The flexible endoscope may not generate enough force to lift the epiglottis to exposure the larynx. A mouth gag or a mouth retractor would need to be used to open the patient's mouth and lift the epiglottis. A semi-flexible endoscope also can be combined with the *EndoTORS* robot, such as the ENDOEYE FLEX 2D/3D (LTF S190-5-2D /LTF 190-10-3D, Olympus, Japan) which have been successfully used in the transoral endoscopic ultrasonic surgery (TOUSS) [169] (Fig 3.18).

Figure. 3.19 shows the prototype of the *EndoTORS* robot. The CDPMs is attached to the articulated tip of the ENDOEYE FLEX 3D endoscope [170]. The distal diameter of the endoscope is 10 mm and the angulation range is 100 degrees in four directions. The scaffold of the prototype *EndoTORS* robot was made by polylactide (PLA) 3D printing. A rigid and biocompatible material, such as the stainless steel can be used for further clinical research if required. The *EndoTORS* robot can connect with the motor units used in ESD CYCLOPS (Fig 1.10) via cable splitters (Fig 3.20a). The setup of the *EndoTORS* robot on a head and neck phantom is shown in Figure 3.21. A mouth gag is used to keep the mouth open (Fig 3.20b)

and the endoscopic view of the *EndoTORS* robot inside the test phantom is presented in Figure 3.21b.



Figure 3.18: Surgical instruments, ENDOEYE FLEX endoscope and the close view of the deflectable tip (left) and the setup of TOUSS (right). A support arm held an ENDOEYE FLEX 3D endoscope. The surgeon and assistant stuff wore 3D glasses to watch the 3D imaging offered by the 3D endoscope [169].

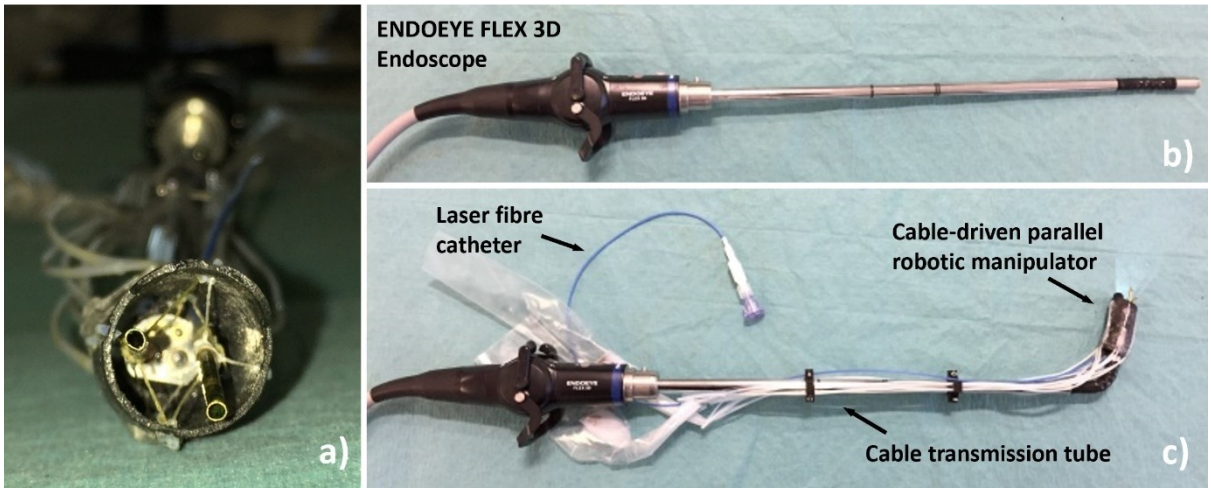


Figure 3.19: Early prototype of the EndoTORS robot. a) Front view of the robot showing the scaffold, cables and two over-tubes. b) and c) The robot mechanism assembled on a tip-articulating endoscope.

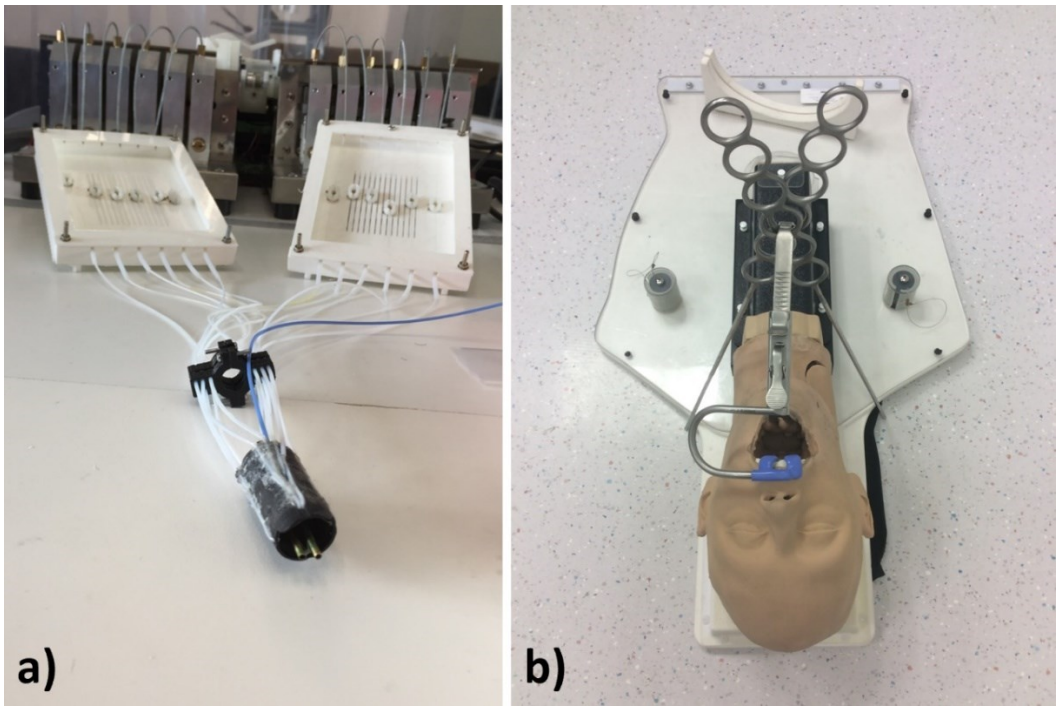


Figure 3.20: a) The EndoTORS robot connected with the motor units via cable splitters. b) The head and neck phantom with a mouth gag which is used to keep the mouth open.

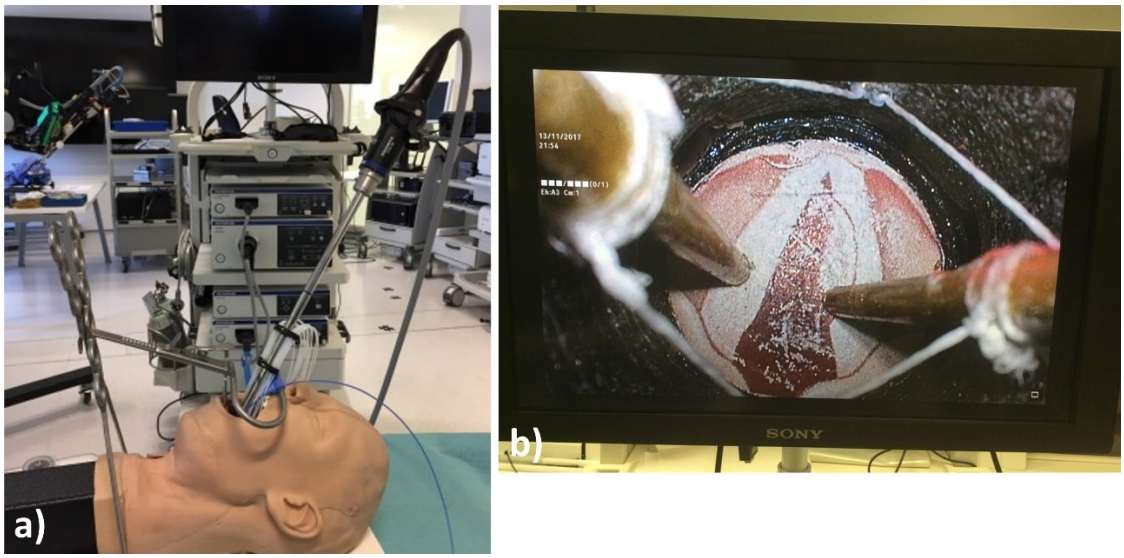


Figure 3.21: a) Setup of the EndoTORS robot on a head and neck phantom. b) Endoscopic view of the robot scaffold. A 20 mm diameter plastic cylinder with a 2D vocal cord lesion image was inserted in the phantom to simulate a target for laser incision.

3.3.2 Design and prototype of *LaryBladeTORS* robot

Recently, with the advanced semi-flexible/ flexible robotic systems used in TORS, such as da Vinci® SP (Intuitive Surgical Inc., USA) and Flex Robotic System (Medrobotics Inc., USA), mouth retractors or mouth gags with curved laryngeal blade have been developed for these

systems. For instance, the Satou's curved laryngopharyngoscope type S2 (Nagashima Medical Instruments, Tokyo, Japan) developed for Vinci® SP and the Flex Retractor for Flex Robotic System [103], [171], [172]. The curved laryngeal blade could offer better exposure of the larynx and accessibility of semi-flexible/ flexible robotic systems [171].

Figure 3.22 shows the Flex Retractor with serval curved blades and demonstrates the curved laryngeal blade with the Flex Robotic System [172]. A 2 DoF rotational control of the curved laryngeal blade can be generated by the Flex Retractor (Fig 3.23). The concept of *LaryBladeTORS* robot is to build the CDPM on the tip of a curved laryngeal blade. The design rendering and the prototyping of *LaryBladeTORS* robot are shown in Figure 3.24 and 3.25, respectively. The *LaryBladeTORS* robot can be mounted on a mouth retractor or a mouth gag, such as the Flex Retractor. The gear rack (Fig 3.24) can be utilised to adjust the insertion depth. The *LaryBladeTORS* robot body also can achieve 2 DoF rotational control steered by the mouth retractor like Flex Retractor shown in Figure 3.23.

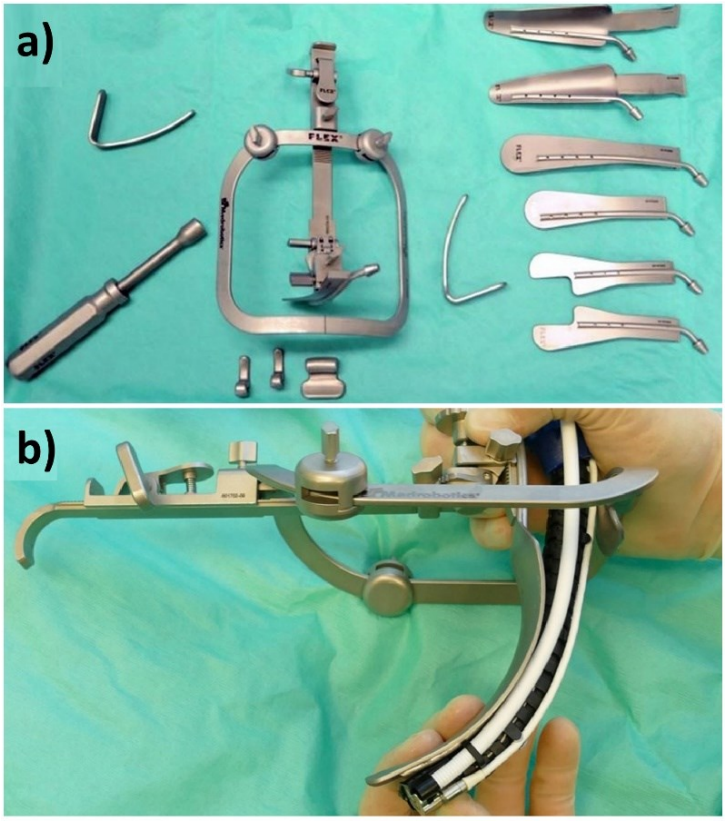


Figure3.22: a) Flex Retractor with curved laryngeal blades. b) The Curved laryngeal blade demonstrated with the Flex robotics system (Medrobotics Inc., USA) [172].

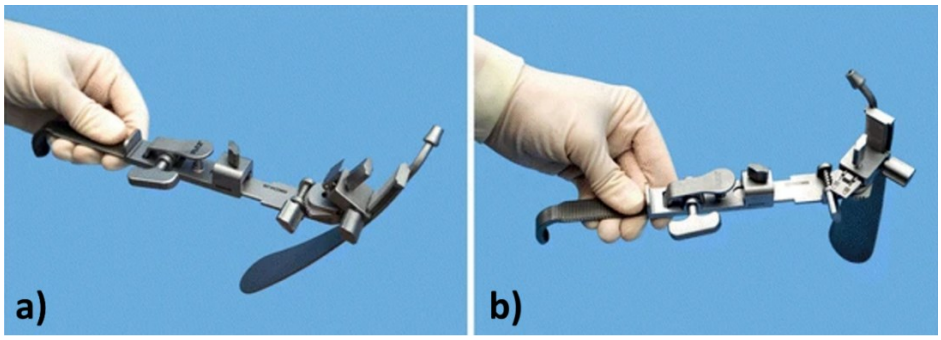


Figure 3.23: 2 DoF rotations of the curved laryngeal blade of the Flex Retractor [103].

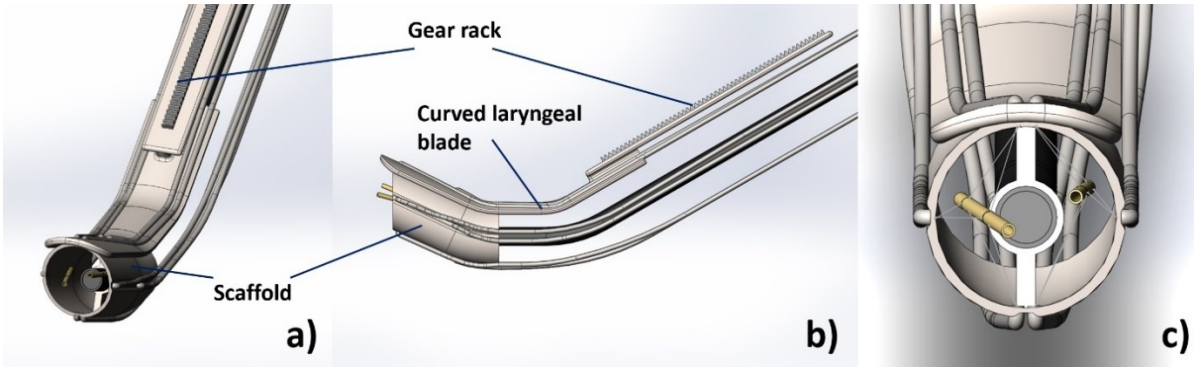


Figure 3.24: The render of LaryBladeTORS robot. a) overview, b) sideview and c) front view.

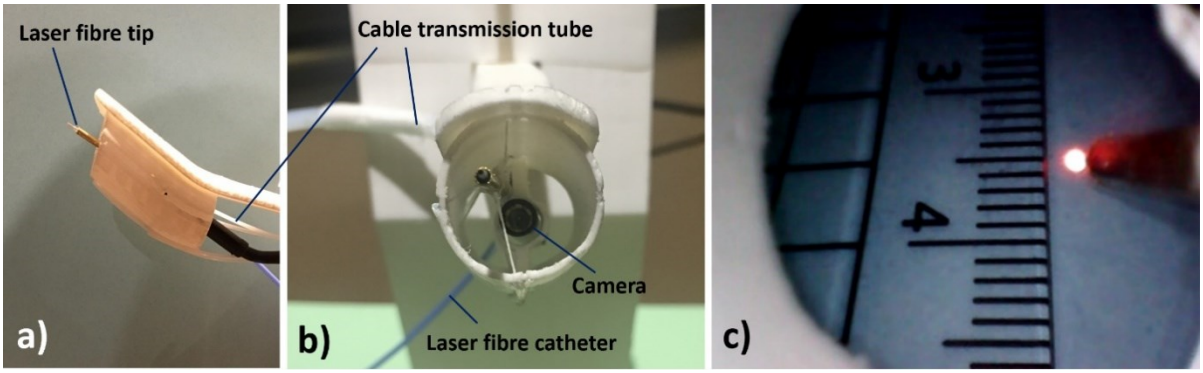


Figure 3.25: The prototype of LaryBladeTORS robot. a) side view, b) front view and c) view from camera, a red laser spot aiming beam projected on a paper screen placed at in front of the robot.

The robot body prototype was created by PLA via 3D printing. The final version of the robot body could be made from the same materials used in the Flex Retractor laryngeal blades. The curvature of the LaryBladeTORS robot body is highly patient specific. A USB camera (5.5 mm diameter, 640x480 pixels resolution) was used to offer visualisation of the operative field (Fig 3.25c). If the LaryBladeTORS robot body needed to be pulled out and re-inserted during the surgery, the CDPM could be designed to slide along the curved laryngeal blade via the built-in rail on the blade to avoid re-setup of the mouth retractor (Fig 3.26).

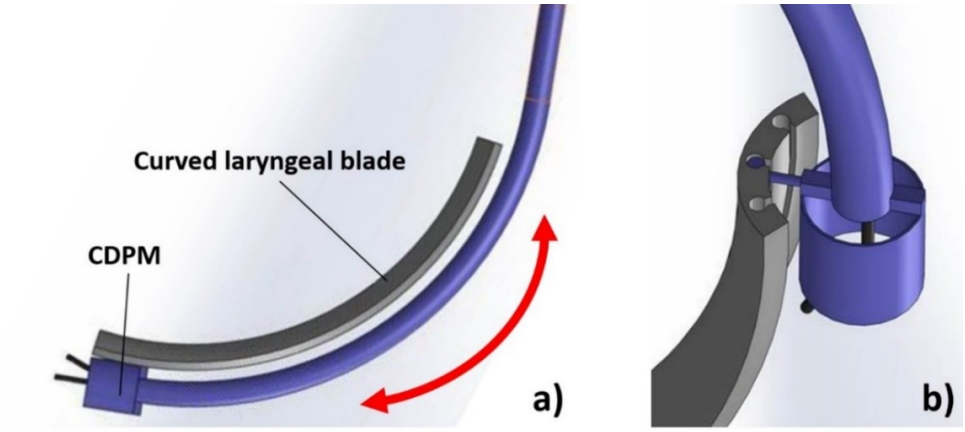


Figure 3.26: a) Side view of the curved laryngeal blade based CDPM. b) View of the inbuilt rail of the curved laryngeal blade.

3.3.3 Design and prototype of *LaryngoTORS* robot

The design of the *LaryngoTORS* robot is inspired by the indirect video laryngoscope. Figure 3.27 shows some examples of conventional laryngoscopes and video laryngoscopes. With the development of camera technology and the better understanding of airway configuration, indirect video laryngoscope can achieve a better outcome of larynx exposure and are more widely used in clinical practice [127], [173], [174]. The video laryngoscope, without the limitation of the direct line-of-sight, can utilise a laryngeal blade curvature matched to the airway (Fig 3.28) [173], [175]. The images can be displayed on a screen on the blade handle or an external screen for better visualisation during the inspection or intubation.

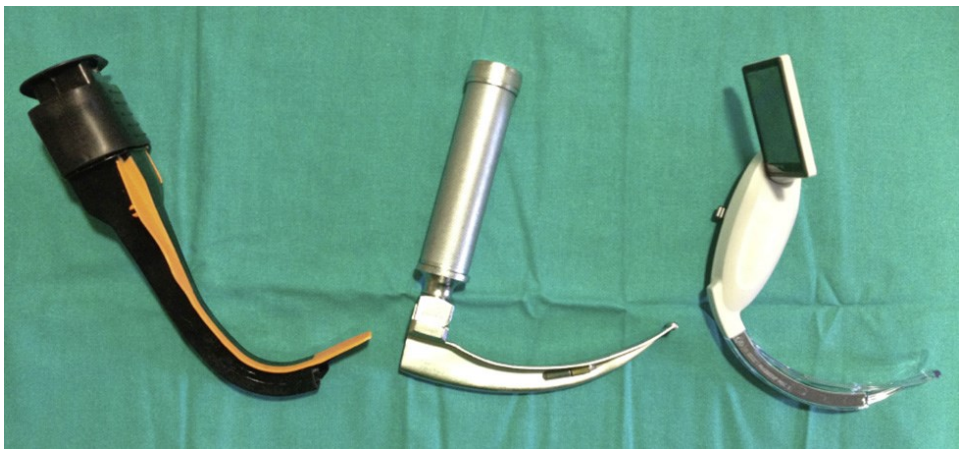


Figure 3.27: Conventional and video laryngoscope: Airtraq®NT video laryngoscopes (left), Macintosh laryngoscope (middle) and the new McGrath®MAC video laryngoscope (right) [175].

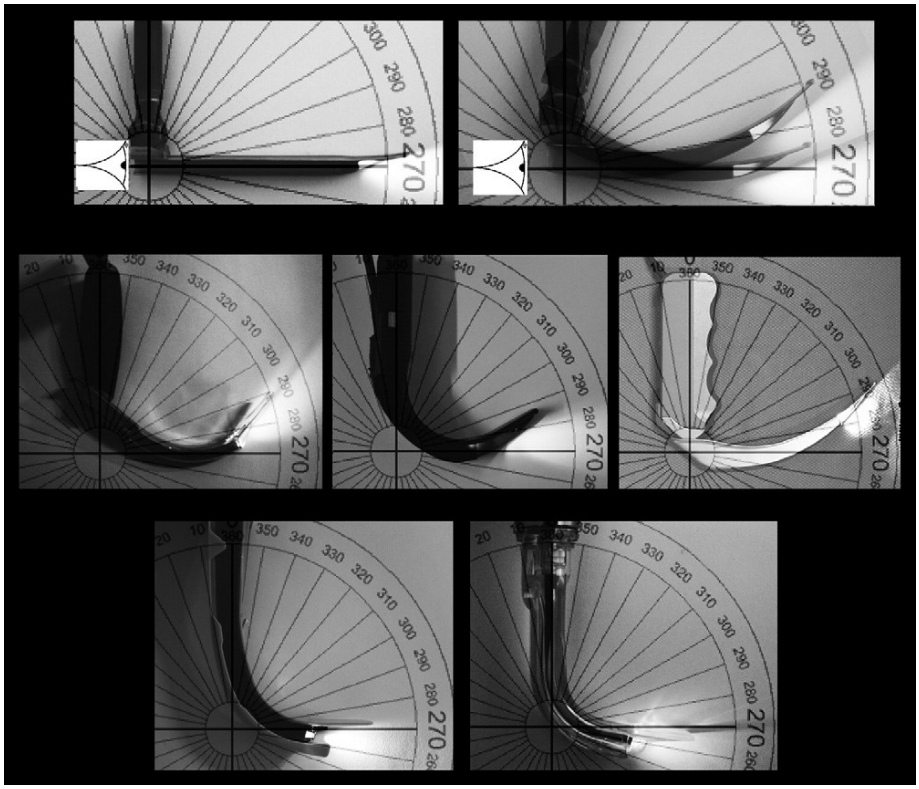


Figure 3.28: Demonstration of the curvature of the laryngeal blade and the view axis of different direct laryngoscopes (top row) and indirect video laryngoscopes (middle and bottom rows) [174].

The rendering of the *LaryngoTORS* robot is shown in Figure 3.29. The shape of the *LaryngoTORS* robot resembles an indirect video laryngoscope. For a bimanual robotic system, 12 motor units are required (Fig 3.29c). A scaffold housing a CDPM pair is attached at the end of a curved laryngeal blade. The angle θ is 20° (Fig. 3.29a), while it can be adjusted between 0°-70° according to patient requirements. Each cable is rolled on a spool which steered by a motor actuator and is transmitted through a pulley into a flexible transmission conduit (Fig 3.29b). Each pulley is connected to a force sensor to gain the tension data of each cable. The cables are connected via small openings positioned around the scaffold to two instrument-accommodating over-tubes housed within the scaffold. The Bowden cables are fixed to the scaffold. Six cables are connected per over-tube. The shape of the scaffold is based on the distal tip of conventional laryngoscopes, which is a hollow elliptical cylinder. The size of the scaffold, as mentioned in Table 3.2, is 22 x 20 mm (W x H). The shape and size of the scaffold also can be changed based on the specific request of the operative task and the patient's airway configuration.

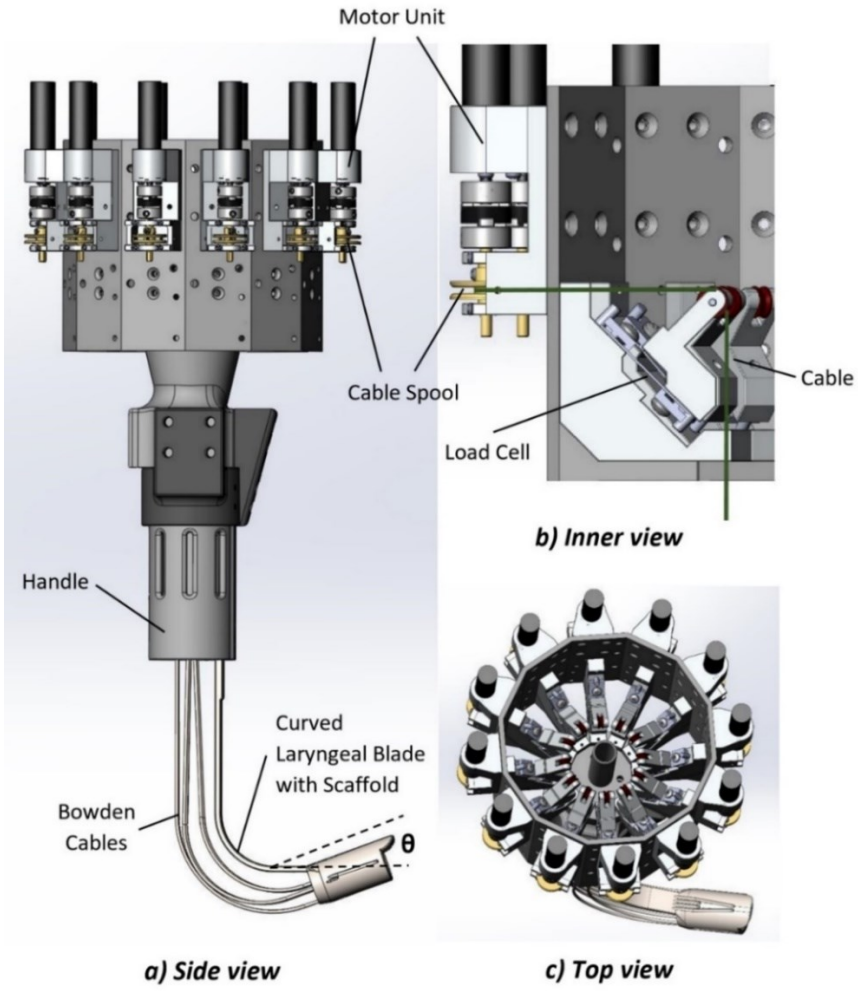


Figure 3.29: Design of the LaryngoTORS robotic system. a) Side view showing the main parts: motor unit, handle, Bowden cables for cable transmission and the curved laryngeal blade with the scaffold. b) Inner view showing the cable transmission. A force sensor is used to achieve tension control. c) Top view of the robot body [168] *©2020 IEEE.*

A prototype of the *LaryngoTORS* robot has been developed (Fig 3.30). The robot body is mounted on an adjustable surgical table support arm, which can be locked after the robot is placed into the desired position. A single end-effector was used in the first prototype, but as the two CDPMs are symmetrical the addition of the second over-tube does not affect the design. For cable actuation 6 brushless DC motors (1226S012B with a 64:1gear head, Faulhaber, Germany) and EtherCAT controllers (MC5004P, Faulhaber, Germany) are used. The tension on each cable is measured by a load cell (LCL-005, OMEGA Engineering, Inc., USA). A 6 mm pulley is built onto the loadcell. ADAQ interface (Instrument i100, GW Instruments, Inc., USA) is used to acquire the tensions from the loadcells. 6 mm cable spools are mounted on each motor. Motor control in teleoperation mode is achieved using a master

manipulator (Geomagic Touch, 3D Systems, USA), or programmatically from the computer. The laryngeal blade shown in Figure 3.32 includes a handle for the operator to place the robot, a curved laryngeal blade with the CDPM, Bowden cables (1.4 mm Round Wire Coil, Asahi Intec, Japan) with inner polytetrafluoroethylene (PTFE) tubing (Adtech Polymer Engineering Ltd., Germany), spectra cables (0.19 mm diameter, 13kgf, PowerPro, Shimano, Inc., Japan), a brass over-tube, a fibre sheath (Laser Fiber Sheath, Lumenis Ltd., Israel) and a 5 mm diameter USB camera (640x480 pixels resolution) with 6 LEDs.

The spectra cables are made of ultra-high-molecular-weight polyethylene (UHMW-PE). The UHMW-PE cables are extremely stiff for their cross-sectional area. These are not prone to fatigue and are rated for breaking at approximately 130 N (13 kgf). The cables from the motor unit are routed through the handle to the scaffold, via PTFE tubing within Bowden cables. The Bowden cables are fixed at the end of the handle onto the scaffold. PTFE is used to minimise friction between the cables and the Bowden transmission conduits. The cables are attached to the over-tube by creating a loop which is accurately adhered with glue.

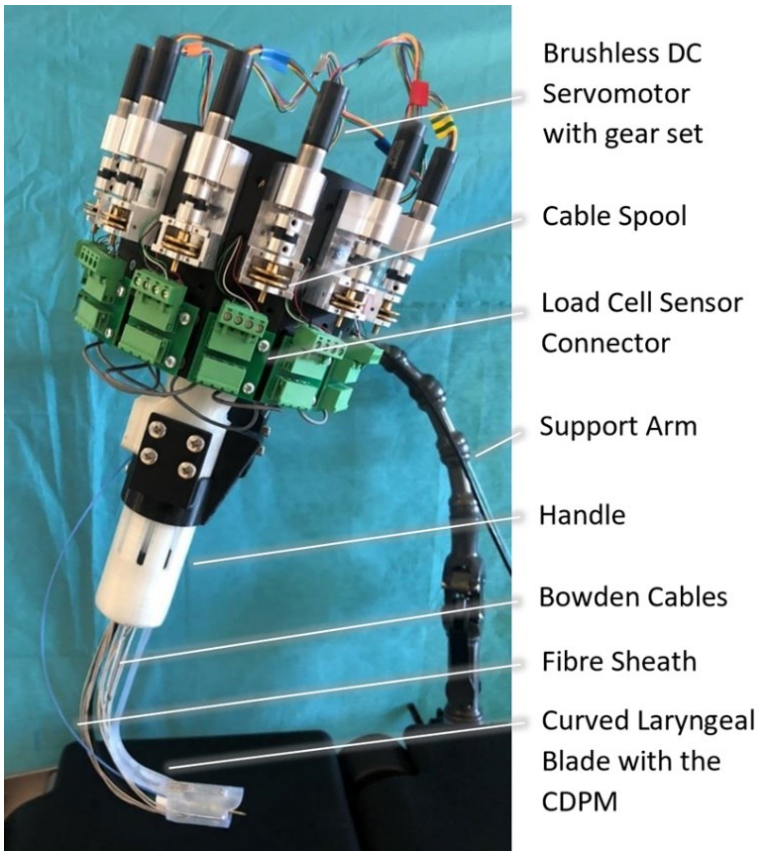


Figure 3.30: Early prototype of the LaryngoTORS robot.

Figures 3.31 and 3.32 show the details of main components and close-up view of an early prototype of the *LaryngoTORS* robot.

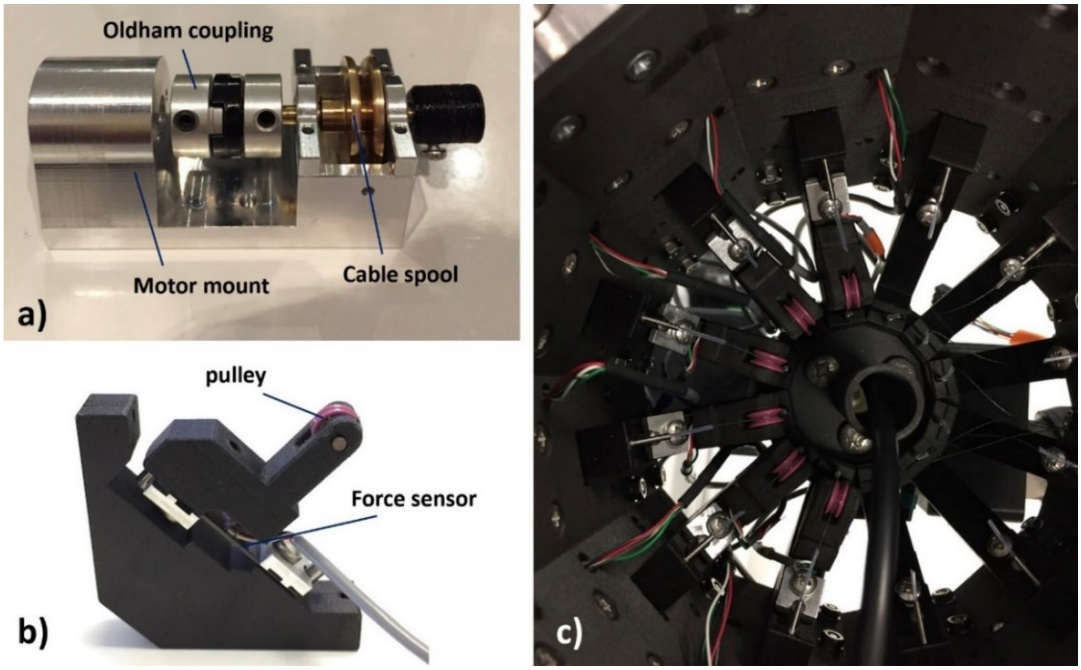


Figure 3.31: a) The motor mount unit, includes a base of the motor mount, an Oldham coupling and a cable spool. b) The force sensing unit, when the cable is transmitted through the pulley, the tension force can pass to the force sensor. c) Top view of the early prototype of the LaryngoTORS robot, six force sensing units are presented.

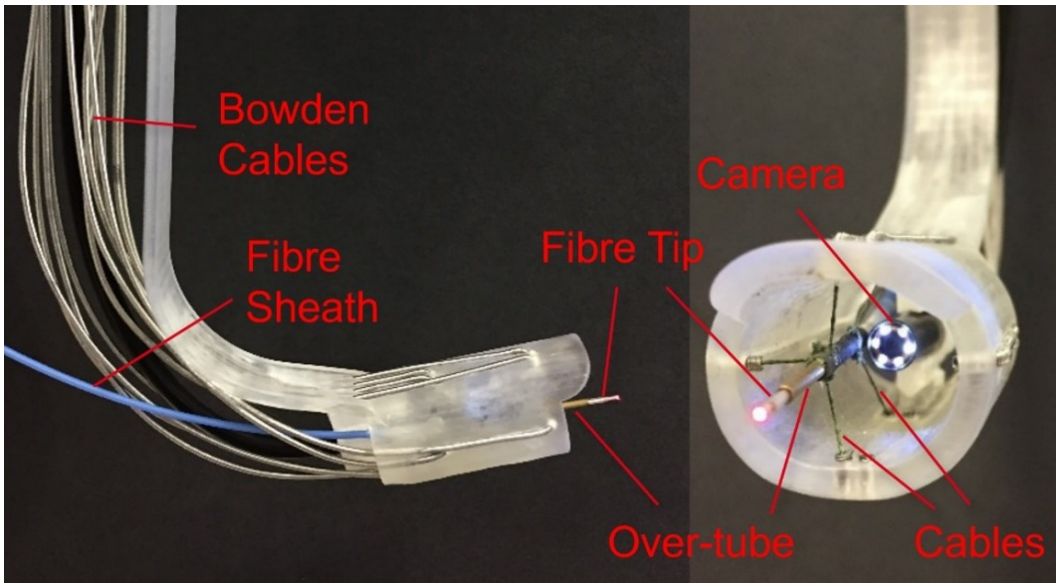


Figure 3.32: The side view and front view of the laryngeal blade of the early prototype LaryngoTORS robot [168] *©2020 IEEE.*

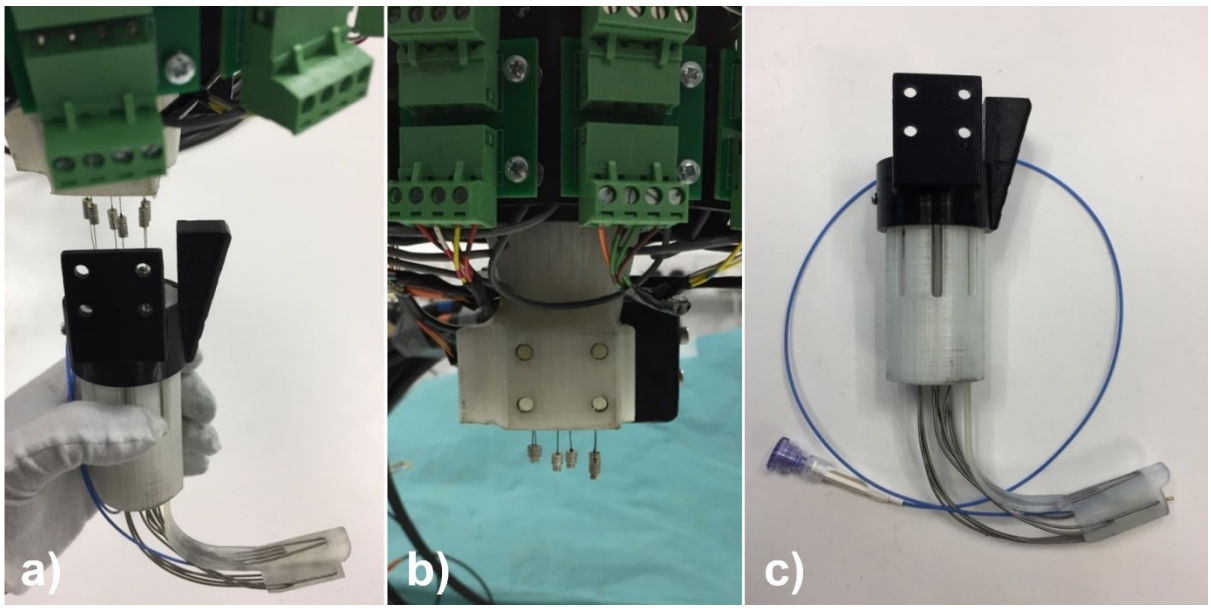


Figure 3.33: The detachable part (c) of the LaryngoTORS robot can be connected/disconnected from the robot (b) via cable connectors (a) [168] *©2020 IEEE.*

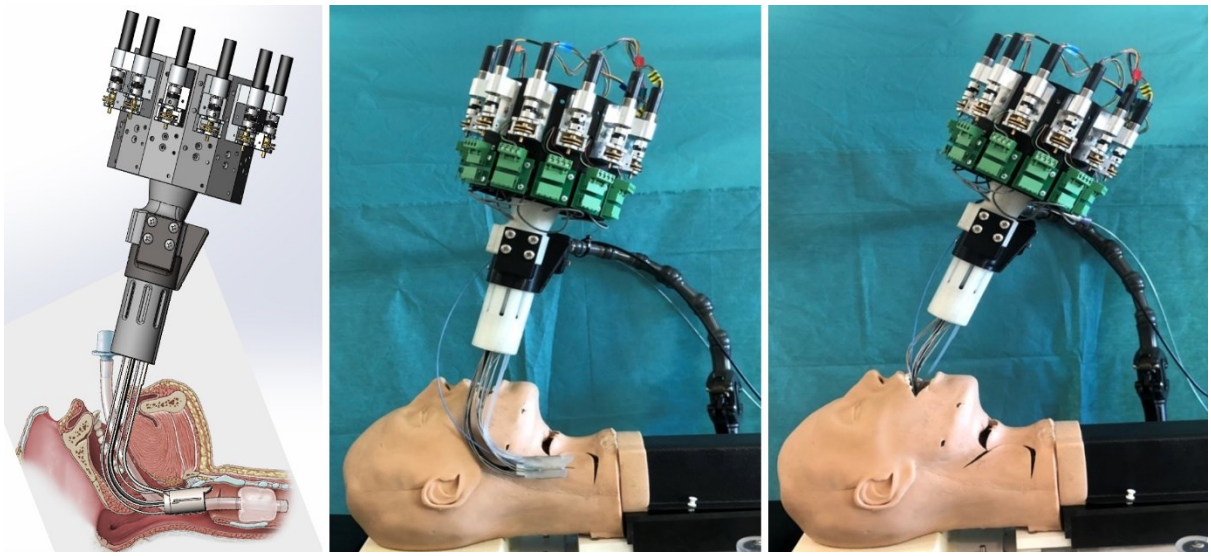


Figure 3.34: Schematic diagram of the positioning of LaryngoTORS robot in TLP (left) and demonstration of the operational position of the robot, based on a head and neck phantom (middle and right) [168] *©2020 IEEE.*

The *LaryngoTORS* robot is detachable. As shown in Figure 3.33, each cable is connected by a cable connector. The handle and the laryngeal blade (Fig 3.32) can be detached from the robotic body by disconnecting the cable connector. Figure 3.34 shows the positioning of the *LaryngoTORS* robot in TLP. The laryngeal blade of the *LaryngoTORS* robot can be inserted to exposure the larynx, and further validation will be discussed in the next chapter.

3.4 Conclusion

This chapter discussed the core principle and critical features of CDPM. A simulation workflow of TLP CDPM was introduced and the required specification was identified. A resulting simulation configuration was presented; each instrument has 5 DoF motion control. Although the narrow space of the larynx limited the workspace of CDPM, the resulting configuration could generate a sufficient controllable workspace. Extending the fibre tip from the over-tube will increase the controllable workspace significantly. The CDPM can be reconfigured to align the workspace with the operation field. Also, the CDPM configuration can be changed based on the patient specific data or according to the required task. Laser line and arc pattern scanning was simulated, and the resulting configuration could steer the fibre end tip in a collision-free workspace.

Three designs of CDPR for TLP are described: *EndoTORS, LaryBladeTORS* and *LaryngoTORS* robot. The *EndoTORS* robot combines the CDPM with a semi-flexible/flexible endoscope; the other two designs build the CDPM at the end of a curved laryngeal blade. All robots could overcome the limitations of the line-of-sight and demonstrate the potential to fulfil the requirements of TLP proposed in chapter 2. The *EndoTORS* and the *LaryBladeTORS* robot are versions that are an add-on to existing medical devices, a design decision that aimed to reduce the cost. The *EndoTORS* robot is currently based on the size specifications of the directional tip of the Olympus ENDOEYE endoscope, where bending point and tip length are fixed, which introduced restrictions of how the EndoTORS is coupled to it. A universal adapter for all common brand endoscopes or specific adapter for each brand will be required to firmly connect the robot with the endoscope. The *EndoTORS* robot will require extra setup time and training for users to assemble the robot with an endoscope. The *LaryBladeTORS* robot is designed for use with the mouth retractor for positioning in TLP. The *LaryBladeTORS* robot can be also used together with a mouth gag, but as a result, the 2 rotational DoF offered by the mouth retractor, such as Flex Retractor, will be lost. The *LaryBladeTORS* robot has to work with a mouth retractor or a mouth gag. It cannot work alone. Extra setup time and training for users to assemble the *LaryBladeTORS* robot with a mouth retractor or a mouth gag are required.

In contrast, the *LaryngoTORS* robot is a stand-alone type, without the above limitations and fully customisable. The *LaryngoTORS* robot can be moved with an adjustable support arm. The *LaryngoTORS* robot can be inserted into the larynx like the ordinary indirect video laryngoscope. It is convenient to operate and setup. This thesis focuses on the development and discussion of the *LaryngoTORS* robot. The early prototype was shown in this chapter, while validation tests and technical feasibility analysis will be described in the next chapter.

Chapter 4
Validations and Feasibility Considerations

This chapter focuses on the validation tests and feasibility analysis of the *LaryngoTORS* robot. The core technique of motion control of the robot is introduced first, and bench tests and *ex-vivo experiments* are described, and the experimental results are discussed. The design and prototype of a second version of *LaryngoTORS* robot for further preclinical study are presented. Finally, the feasibility considerations of the *LaryngoTORS* robot and the technical comparison between the state-of-the-art fibre-based laser scanning robotics systems are presented and discussed at the end of this chapter.

4.1 Motion Control

For the end-effector of *LaryngoTORS* robot, there are two types of motion control considered: 1) a master and slave type whereby a master manipulator (Geomagic Touch, 3D Systems, USA) is used to steer the end-effector; 2) an autonomous control type whereby the end-effector will follow the trajectory programmatically. While using the master controller, a PC with Linux operating system (Ubuntu 14.04 with real-time kernel patch 3.10.108) is used to

convert the motion commands from the task space of the controller to the joint space of the motors via inverse kinematics. The appropriate values are then sent to 6 daisy-chained motor controllers (MC 5004 P ET, Faulhaber GmbH & Co. KG, Germany). High-frequency EtherCAT communications (1 kHz) are utilised to transmit signals between the PC and motor controllers via ethernet cables. Each motor controller drives one brushless DC motor (1226S012B with a 64:1 gear head, Faulhaber, Germany) to rotate a 6 mm diameter spool to change the cable length to manipulate the over-tube to execute the desired motion in 5 DoF. Due to the high gear ratio and small spool size, the maximum speed is limited to 25 mm/s. Cable tensions are measured by load cells (LCL-005, Omega Engineering, USA) and read by a digitiser (Instrunet i100, GW Instruments, Inc., USA). The digitiser is connected to a Windows 10 single-board computer (LathePanda, Shanghai, China) to collect and send the tensions data to the master PC. The movement of the end-effector can be observed via a camera built in the laryngeal blade (Fig 4.2a).

An inverse proportional-derivative (PD) feedback control algorithm with tension optimisation is used to implement the motion control. The inverse PD control in the joint space can achieve high precision motion control and the intensive computation load of the forward kinematics to calculate the position of end-effector in the task space can be avoided [99], [160], [161], [176]. Similar to [160], the PD control law is defined as below:

$$\tau = K_P(q_d - q_m) + K_D(\dot{q}_d - \dot{q}_m) + K_t r t_d \tag{4-1}$$

where $\tau = [\tau_1, \tau_2, \dots, \tau_6]^T$ is the vector of motor torques, K_P and K_D are diagonal feedback matrices, q_d and $\dot{q}_d$ denote the vector of desired motor rotation position and velocity, and q_m, $\dot{q}_m$ are the measured motor position and velocity data, K_t denote the diagonal gain matrix, r is the radius of cable spool and t_d is the vector of desired cable tensions. Then, the execution motor rotation vector q_{exec} is calculated as equation 4-2:

$$q_{exec} = K_g\left(\frac{\tau}{r} - t_m\right) \tag{4-2}$$

The calculated motor torque τ is divided by the spool radius and compared with the measured cable tensions, t_m. A gain matrix K_g is multiplied with the error of cable tensions

between the calculated and measured tensions.

The desired cable tension distribution t_d needed to meet the conditions of static equilibrium is defined in section 3.1.6 and needs to be constrained within bounds, above a small positive tension ($t_{min} = 0.3N$) to prevent cable slackness and below a maximum force ($t_{max} = 30N$) to avoid cable break. In practice, as suggested in [177], the cable tension distribution can be described as an optimisation problem:

$$t_d = argmin(\|At - f\|_2)$$
$$s.t.:\ t_{min} \leq t_d \leq t_{min} + (t_{max} - t_{min})\alpha \tag{4-3}$$

In which A is the structure matrix and f is the external wrench vector (see section 3.1.5). Since the end tip of laser fibre is not in contact with tissue, the external wrench vector f is set as a zero vector. The scale factor $\alpha \in [0,1]$ is used to adjust the tension level. To minimise friction, the scale factor α is set as 0.1 to reduce the cable tensions. The solution is conducted by a bounded-variable least-squares method [178].

All gain factors of the diagonal matrix of K_P, K_D, K_t and K_g were determined heuristically and the gain factor values were set to 1800, 10000, 0.2 and 270, respectively. In the next section, a bench test was performed to evaluate the precision and repeatability of the generated scan paths. *Ex vivo* tests of path scanning on chicken tissue were also performed. The gain factor settings are the same throughout each of these tests.

4.2 Validations of *LaryngoTORS* Robot

The *LaryngoTORS* robot design and prototype were presented in chapter 3. By attaching the CDPM at the end of the curved laryngeal blade, the *LaryngoTORS* robot can avoid the requirement for the line-of-sight and obviate the drawbacks of using the straight suspension laryngoscope. In this section, several experiments of bench test and *ex-vivo* test are performed to verify if the *LaryngoTORS* robot could achieve precise and repeatable free path laser scanning to meet the requirements of the transoral laser phonosurgery (TLP) proposed in chapter 2.

4.2.1 Bench Test

4.2.1.1 Semi-autonomous path scan

As discussed in section 2.2, in the current TLM, the scan pattern is pre-programmed, such as the straight line, arc line and circle etc., and arbitrary free path scan is not allowed. For irregular pathological margins, using the pre-programmed pattern is inconvenient. It may be difficult to match irregular pathological margins perfectly while relying on pre-programmed paths. The operator would need to use many small-scale scan patterns to execute the laser cutting along the irregular margin, increasing the complexity of laser operation, and compromising accuracy. A free path scan can overcome this problem and improve the performance of laser scanning. In this section, a semi-autonomous free path scan technique is introduced, using control points to define and generate a free scan path that can be automatically executed by the *LaryngoTORS* robot. Figure 4.1 shows the workflow of the semi-autonomous free path scan.

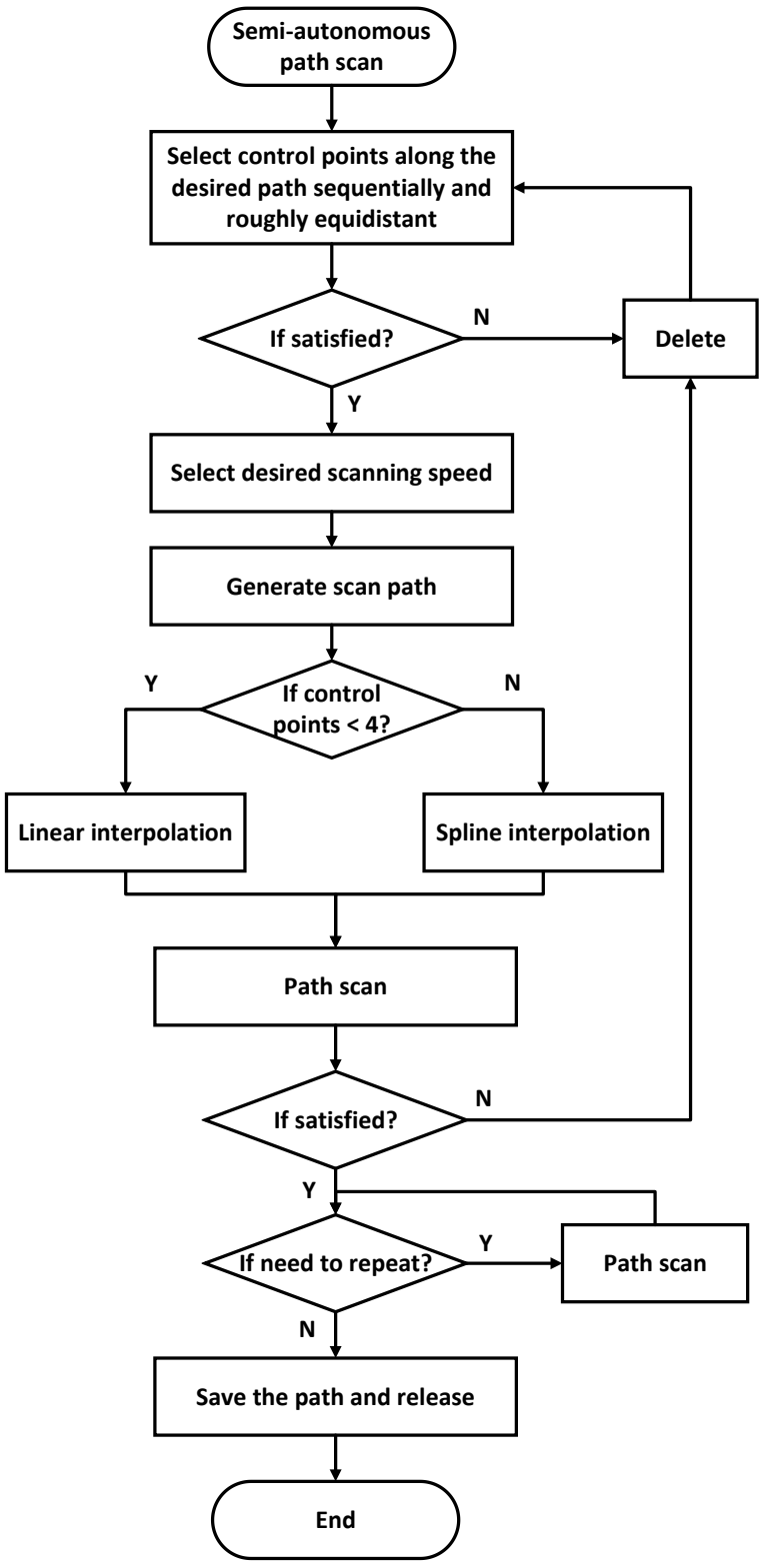


Figure 4.1: The workflow of the semi-autonomous free path scan.

Figure 4.2 and 4.3 show the setup of the experiment for the semi-autonomous free path scan. A laser fibre (FiberLase CO2 fiber, Lumenis Ltd., Israel) was inserted in the over-tube

through a fibre sheath (Laser Fiber Sheath, Lumenis Ltd., Israel) until the end tip was extended in front of the over-tube by 5 mm (Fig 4.2a). The distance between the end tip of the fibre and the front set of the cables is 20 mm, which is in accordance with the simulated configuration in section 3.2.2. A paper screen was attached at the front of the *LaryngoTORS* robot's scaffold (Fig 4.2b). A red aiming beam (635 nm, 1mW) was used during the experiment and the ideal pose of the fibre tip is normal to the target tissue, resulting in a red circular spot shape. The operator can adjust the pose based on the apparent spot shape of the aiming beam. Figure 4.3 shows the operation platform and the control panel interface of the semi-autonomous free path scan. The master manipulator is used to manipulate the end tip of fibre and determine desired control points in the workspace (Fig 4.3). The control points include a starting point, an endpoint, and roughly equidistant points to sparsely describe the desired trajectory. When the spot of the aiming beam is pointing to the desired position of the control point, activation of the button ① on the control panel records the pose (*x, y, z, yaw, pitch*) of the end-effector. All control points have been sequentially saved, the recorded pose data serves as the input data to generate the entire scan path via point interpolation. If the number of control points is equal or larger than 4, Catmull-Rom spline interpolation is used; otherwise, linear interpolation is used. The number of interpolation points is defined based on the selected scan speed. The scan speed can be changed by using the slider button ②. The command loop frequency is 1000 Hz. Therefore, moving 1,000 steps will take 1 second. Dividing the distance between control points by the selected speed yields the time interval between points in seconds. The time interval is then multiplied by 1000 and rounded to the nearest integer to obtain the number of interpolation points. Once the scan speed was defined, clicking the buttons ③ and ④ generates the scan path and execute the generated path scan respectively. If the scan speed needs to be changed, buttons ⑦ deletes the current path and reselects the speed to generate a new scan path with desired speed. Clicking button ④ can perform the path scan once and re-clicking it will repeat the same path scan. Pressing button ⑤ saves the generated path and button ⑥ deletes the recorded control points and the current scan path to restart. Button ⑧ is used to display the images from the USB camera (640x480 pixels resolution) (Fig 4.3).

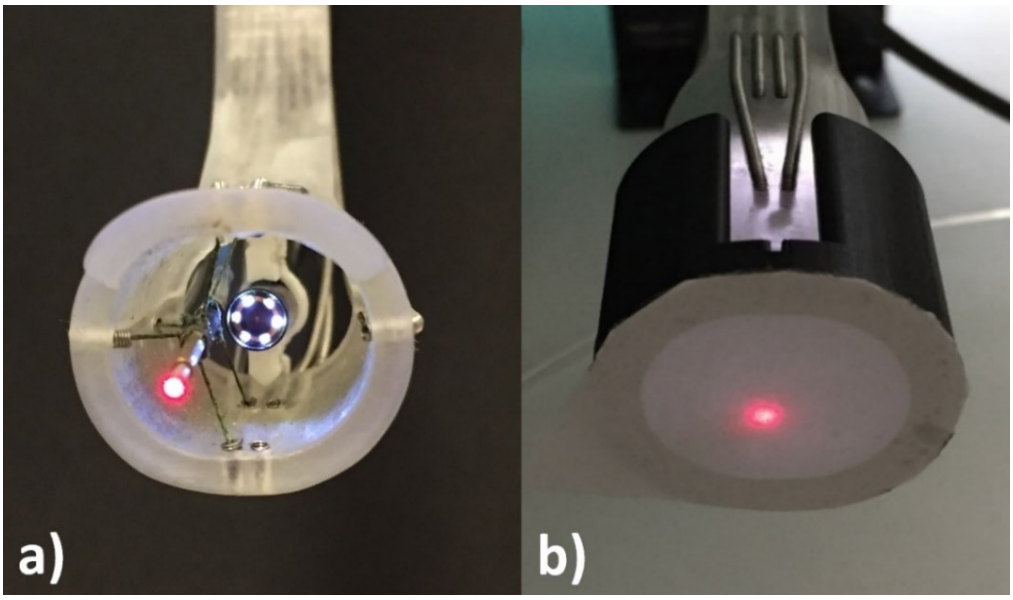


Figure 4.2: The test setup: a) A laser was inserted in the over-tube; a red aiming beam is transmitted through the fibre. A USB camera with 6 LEDs provides the visualisation of the operation field. b) A paper screen mounted in front of the scaffold [168] *©2020 IEEE.*

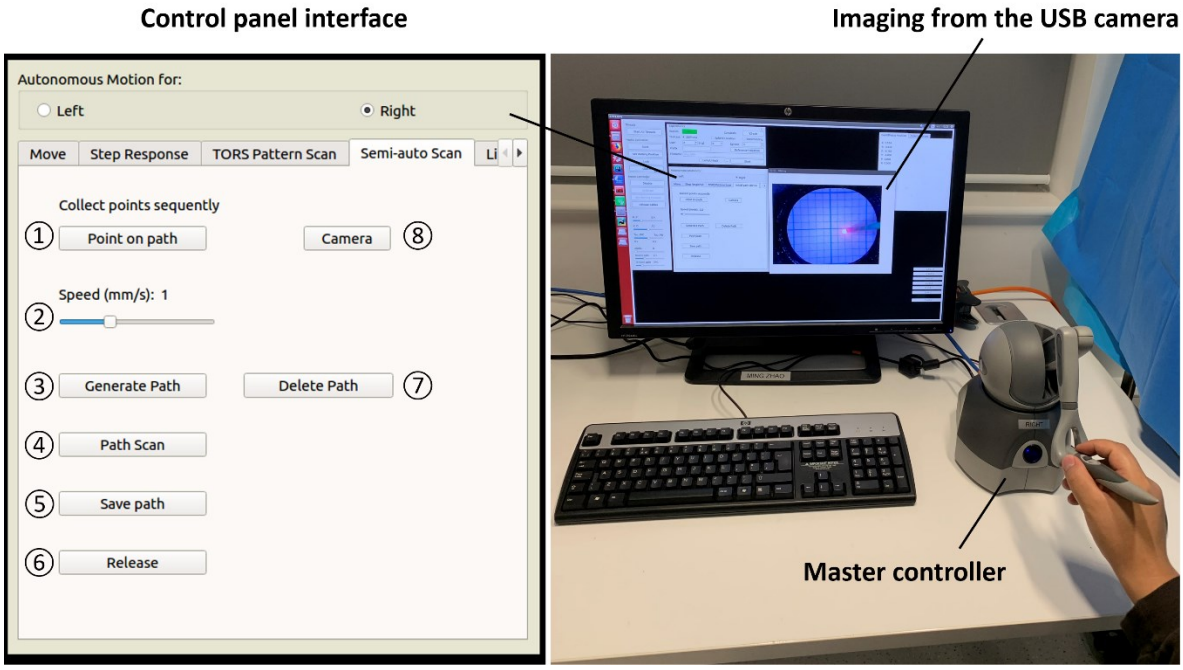


Figure 4.3: The control panel interface of the semi-autonomous free path scan (left) and the operation platform (right). The control panel interface includes 8 function buttons. ① push button: record the pose data of the control point; ② slider button: select the scan speed; ③ push button: generate the scan path; ④ push button: execute the path scan; ⑤ push button: save the current scan path; ⑥ push button: delete current control points and scan path; ⑦ push button: delete current generated path; ⑧ push button: display the imaging from the USB camera on the screen.

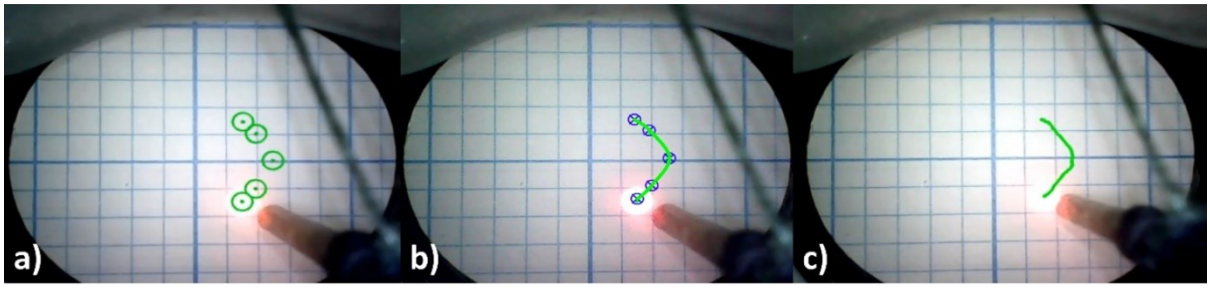


Figure 4.4: The bench test of a user-defined 6 × 2 mm arc line semi-autonomous scan on the paper screen. a) The camera view of 5 selected control points, b) control points (blue) and generated path (green), c) The actual executed scan path [168] *©2020 IEEE.*

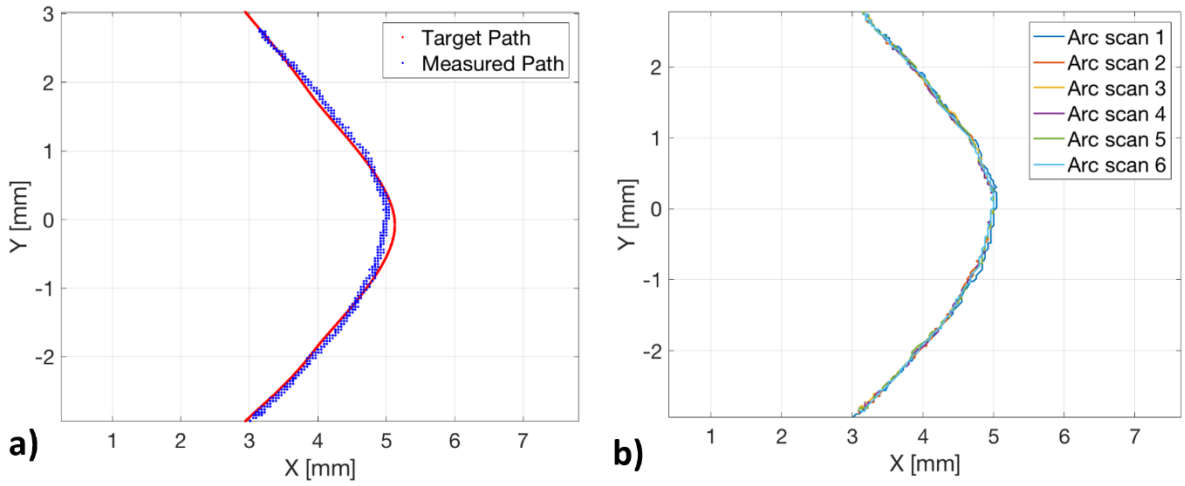


Figure 4.5: The experimental results of the arc line scan. a) Path scan precision and b) scanning repeatability over 6 scans [168] *©2020 IEEE.*

Figure 4.4 shows the bench test of a user-defined 6 × 2 mm arc line scan. Using MATLAB software, the path of the aiming spot centroid was visually tracked by the USB camera based on colour and shape features. The resolution of the USB Camera is 640x480. As shown in Figure 4.4, grid paper was used as the target screen. With the calibration and registration with the camera, 28 pixels correspond to 1 mm (therefore, 1 pixel ≈ 36 µm). A higher resolution camera can be used in future studies. The USB camera was used due to its low cost and convenience – a higher quality camera system would improve the resolution of the measurement. Figure 4.4a shows the 5 detected control points. Figure 4.4b demonstrates the arc line path generated by the 5 control points and Catmull-Rom spline interpolation [179]. The actual executed scan path was recorded (Fig 4.4c) and compared with the generated scan path (ground-truth). The experimental results are shown in Fig. 4.5 and the RMSE and maximum absolute error (MAE) are shown in Table 4.1. The RMSE between the tracked and

generated path was 0.054 ± 0.028 mm at a velocity of 0.5 mm/s. During 6 repetitions, the repeatability was 0.027±0.020 mm RMSE. The measured cable tension forces and motor positions for 3 arc line scans are shown in Figure 4.6. Furthermore, two straight line semi-autonomous scans in the horizontal and vertical directions were performed at a speed of 0.5 mm/s. The experimental results of the horizontal and vertical line scan are shown in Figure 4.7 and 4.8, respectively. The RMSE and MAE of the precision and repeatability of the two straight line scans are also presented in Table 4.1.

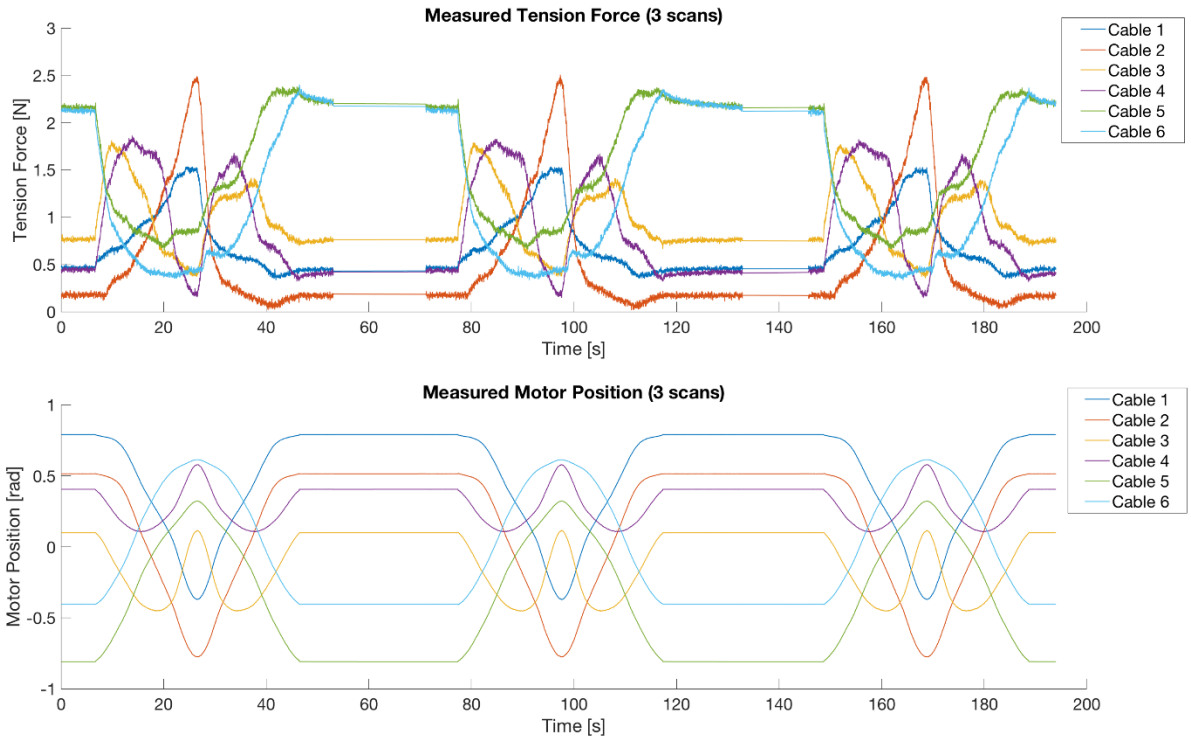


Figure 4.6: The measured tension forces (top) and respective measured motor positions (bottom) for three consecutive arc scans [168] *©2020 IEEE.*

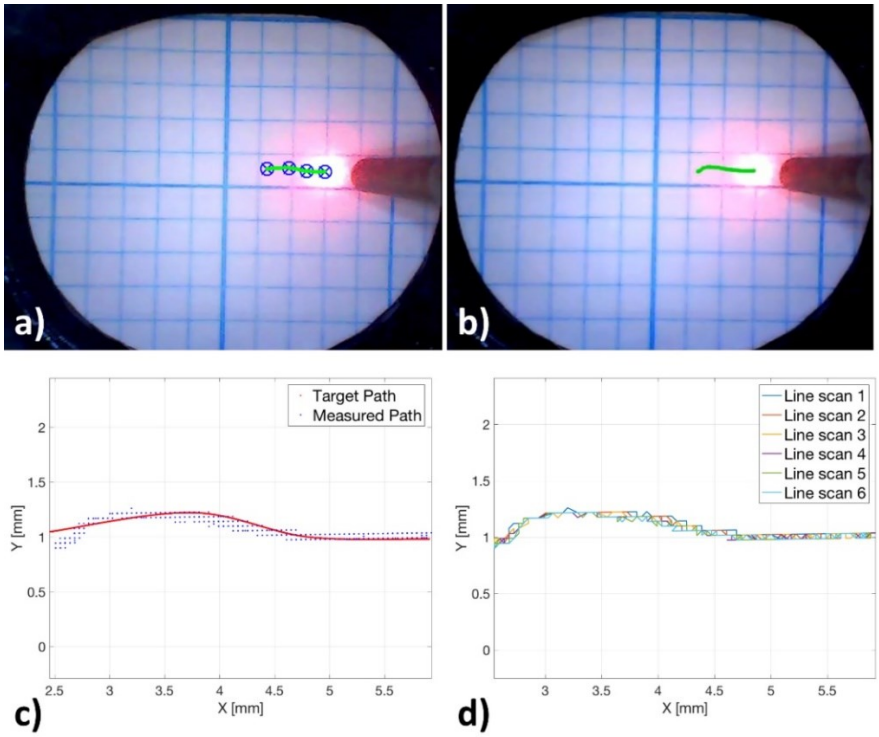


Figure 4.7: The experimental results of the horizontal line path scan. a) 4 control points (blue) described horizontal line path (green). b) The actual executed scan path detected by the camera. c-d) Precision and repeatability over 6 scans [168] *©2020 IEEE.*

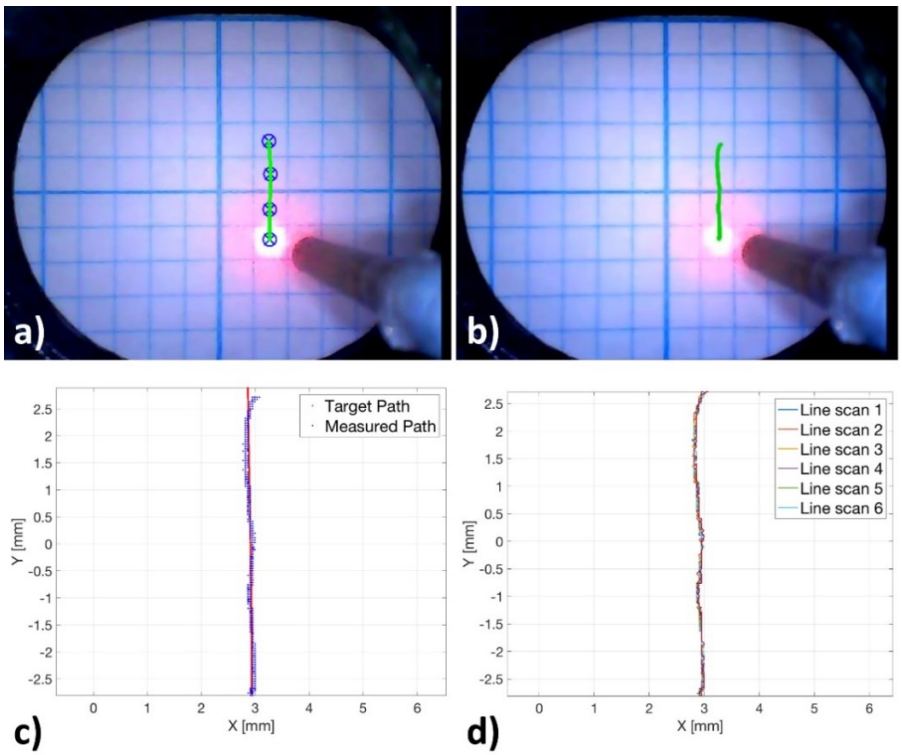


Figure 4.8: The experimental results of the vertical line path scan. a-b) The camera view of a 4 control points (blue) that described a vertical line path (green) (a) and the executed scan path (b). c-d) Scan precision and repeatability over 6 scans [168] *©2020 IEEE*.

Table 4.1:Experimental results of precision and repeatability with different scan paths at a speed of 0.5 mm/s

Experiments		*RMSE (mm)*	*MAE (mm)*
Arc line	Precision	0.054± 0.028	0.183
	Repeatability	0.027± 0.020	0.099
Horizontal line	Precision	0.050± 0.033	0.167
	Repeatability	0.037± 0.026	0.098
Vertical line	Precision	0.042± 0.024	0.213
	Repeatability	0.027± 0.022	0.157

As shown in Table 4.1, motion repeatability is high. The repeatability of cable tension forces and respective motor positions shown in Figure 4.6 is consistent with the performance of the path scanning repeatability. By enabling the user to set the control points manually, any effects of friction, backlash and hysteresis, cable winding, cable elongation and fibre stiffness are intrinsically taken into consideration. Subsequent repetition of the motion through the same points is executed with high precision.

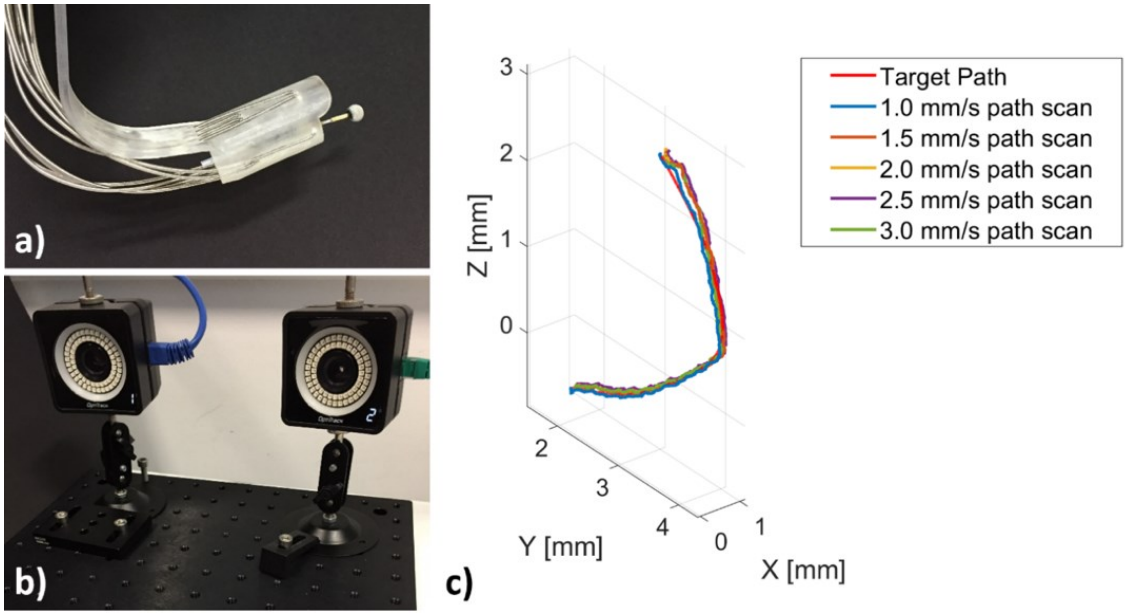


Figure 4.9: The bench test of semi-autonomous path scan at increasing velocities of 1.0, 1.5, 2.0, 2.5 and 3.0 mm/s. a) A positive optical tracking marker was attached at the end of over-tube. b) Two calibrated Optitrack Prime 13 cameras. c) The measured results of path scan with different speed via optical tracking [168] *©2020 IEEE.*

Table 4.2: Experimental results of precision with various speeds

Speeds	*RMSE (mm)*	*MAE (mm)*
1.0 mm/s	0.091± 0.031	0.183
1.5 mm/s	0.086± 0.053	0.260
2.0 mm/s	0.097± 0.051	0.255
2.5 mm/s	0.099± 0.056	0.289
3.0 mm/s	0.086± 0.045	0.252

The precision of path scanning over a range of end-effector velocities was assessed. Since the frame rate of the USB camera was only 30 frames per second (FPS), the image of the aiming spot becomes blurry for high motion speed. Therefore, I used a 120 FPS optical tracking device (Optitrack Prime 13 Camera, NaturalPoint, Inc., USA) to measure the same scan path executed at various speeds of 1.0, 1.5, 2.0, 2.5 and 3.0 mm/s. Figure 4.9 shows the setup of the experiment. A retroreflective ball marker for optical tracking was attached at the end of the over-tube (Fig 4.9a). Two calibrated Optitrack Prime 13 cameras were used to detect and record the motion of the ball marker (Fig 4.9b). The control points were manually defined using the procedures mentioned above. The executed scan path at different speeds were measured and compared with the ground-truth scan path (Fig 4.9c). The RMSE and MAE for each velocity respectively was calculated and are presented in Table 4.2. Scan path execution precision was not significantly affected by increasing velocities, with the RMSE remaining below 0.1mm. The RMSE is larger than the experimental results performed on the paper screen, which may be due to a calibration error introduced by the OptiTrack Prime 13 cameras (calibration residual mean error: 0.014 mm) and the fact that motions were tracked in 3D compared to 2D when measured on the paper target.

The high precision and repeatability of the semi-autonomous path scan performed by the *LaryngoTORS* robot aligns well with the requirements of laser operation in TLP. *Ex vivo* tests of the semi-autonomous path scan have been carried out on chicken tissue with a 2 μm medical laser for further validation (see section 4.2.2).

4.2.1.2 Force exertion of *LaryngoTORS* end-effector

The *LaryngoTORS* robot can be developed as a bimanual robot based on two CDPM end-effectors. As discussed in section 3.2, two over-tubes can be used to manipulate a laser fibre tip and an auxiliary surgical instrument such as a gripper or forceps. The end tip of the laser fibre does not make contact the tissue, but the gripper or forceps need to interact with the tissue for holding, stretching and retracing. These interactions will require a certain exertion force of the end-effector, which is evaluated in this section.

Figure 4.10 shows the experiment setup of the force exertion test. A new CDPM was made with parameters and specifications identical to previous one (shown in Fig 4.2a). Only the length of the over-tube is extended, which can be easily clamped and attached to a force sensor (Nano 17, ATI Automation, USA) (Fig 4.10c), and a 16-bit DAQ (NI USB-6259, National Instruments, USA) for acquiring the force data. The over-tube was placed at the homing position, the geometric centre of the workspace (Fig 4.10b). The centre of the force sensor was aligned with the over-tube (Fig 4.10c). Force tests along the X, Y and Z axes were executed individually as depicted in Figure 4.10b and 4.10c. During each test, the master controller was manipulated to move along the testing axes through the workspace in both directions. The maximum exerted forces measured in the 3 axes are presented in Table 4.1. Each cable tension during the force exertion test was measured by a full-bridge strain gauge sensor (LCL-005, Omega Engineering, USA) and read by a DAQ (Instrunet i100, GW Instruments, Inc., USA). The measured results of exerted forces and cable tensions are displayed in Figure 4.11.

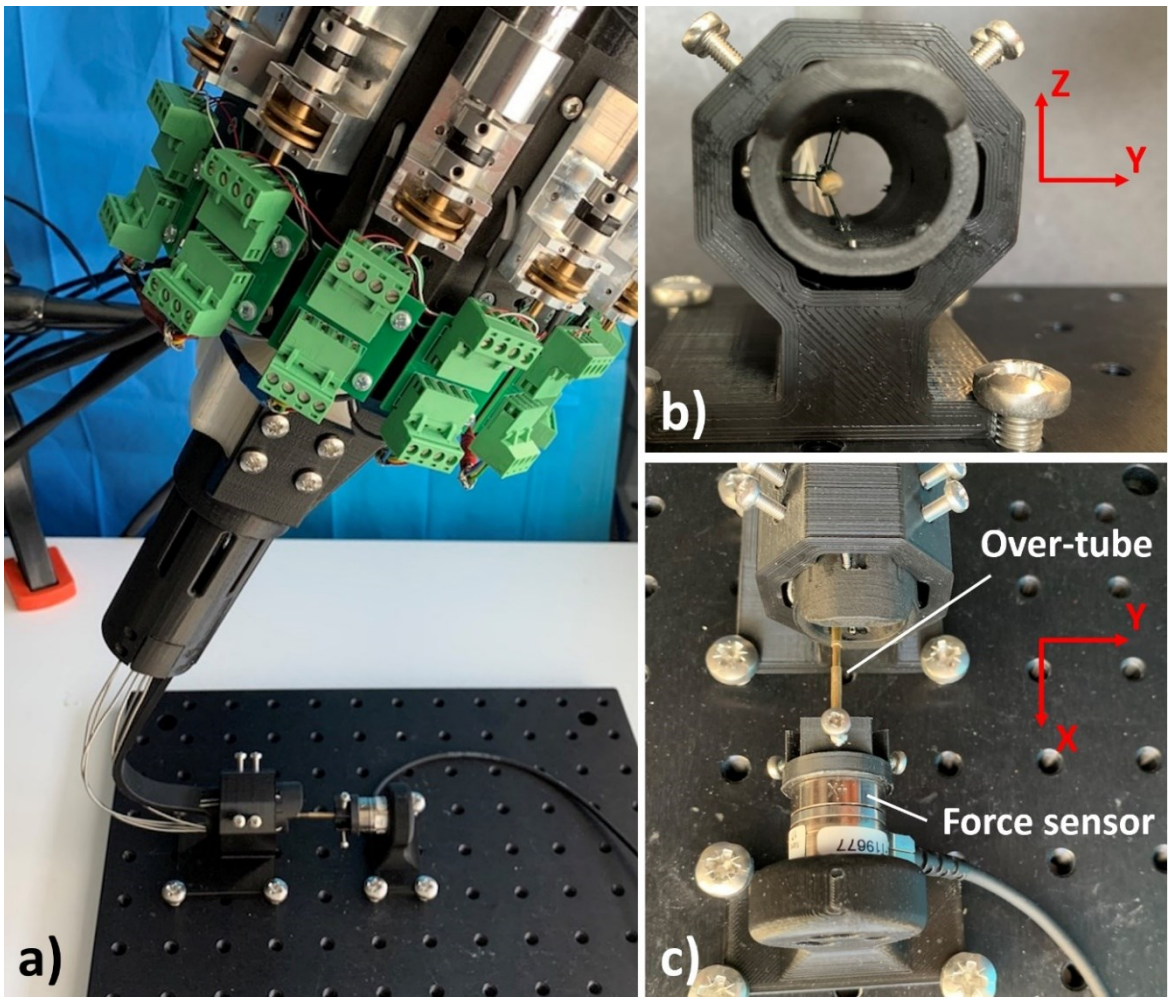
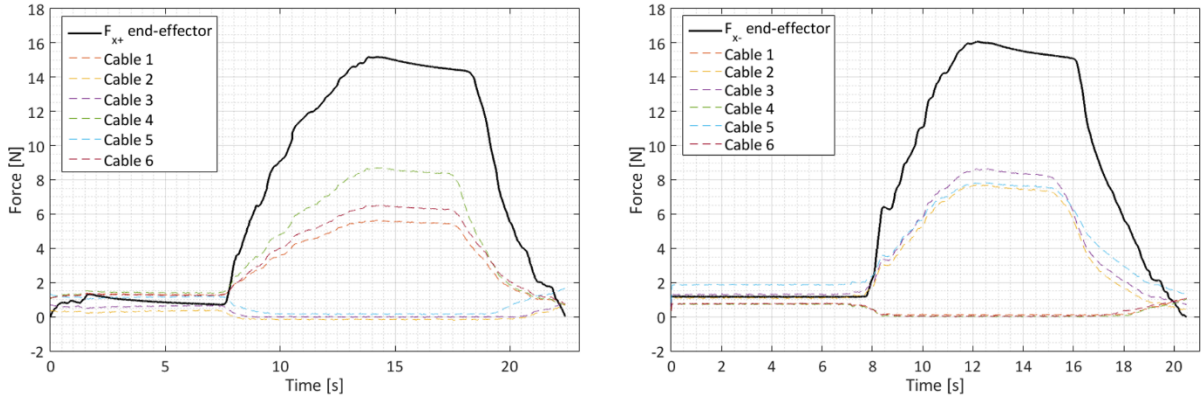


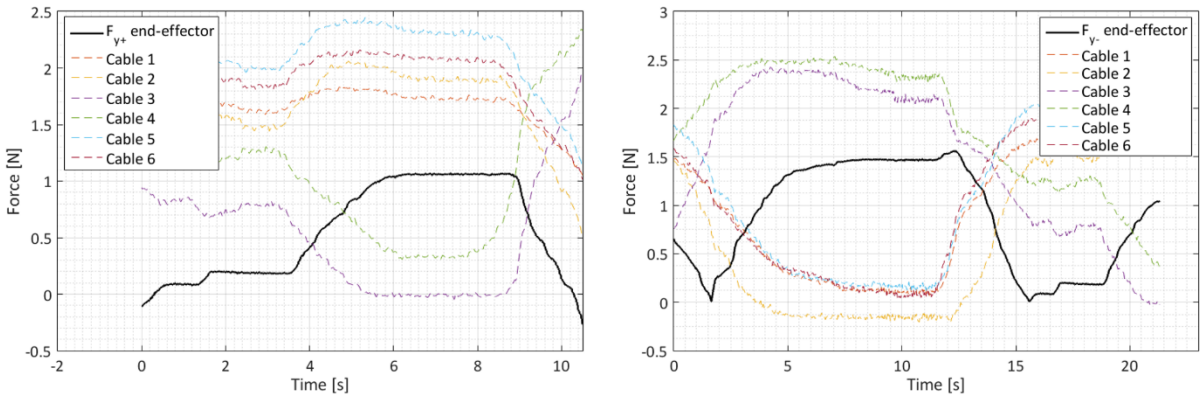
Figure 4.10: The setup of the force exertion test of the end-effector of LaryngoTORS robot. a) The overview of the experimental setup. b) The front view of the CDPM which the end-effector at the homing position. c) The top view of the experimental setup. The end-effector was aligned with the centre of the force sensor and was mounted on it. The axes directions of the force test are axes are shown in b) and c).

Table 4.3: Maximum forces measured in both directions along the three axes.

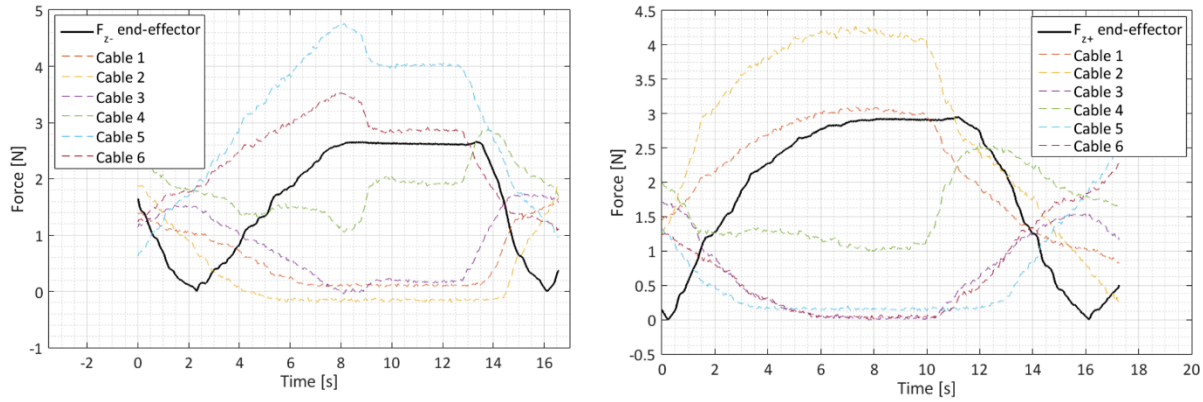
Direction	+X	-X	+Y	-Y	+Z	-Z
Maximum Force [N]	15.18	16.08	1.07	1.57	2.95	2.67



a) *Measured* results *of exerted forces and cable tensions along +X (left) and -X (right) axes.*



b) Measured results of exerted forces and cable tensions along +Y (left) and -Y (right) axes.



c) Measured results of exerted forces and cable tensions along +Z (left) and -Z (right) axes.

Figure 4.11: Measured results of exerted forces and cable tensions along +X, -X, +Y, -Y, +Z and -Z axes directions.

The maximum pulling force (-X direction) is 16.08 N which is similar to the maximum lifting force (16 N) that can be exerted by the robotic microsurgical forceps systems developed in [118] and [180]. The first prototype CYCLOPS robot (Fig 1.8) was able to exert 65 N force

[97]. The exerted force of the end-effector of *LaryngoTORS* robot is lower because, in comparison with the first prototype CYCLOPS robot, the sizes of the CDPM and workspace of *LaryngoTORS* robot are smaller. Due to the inverse dynamics control in the joint space, when the master controller was moved out of the boundary of the workspace, the motor will start to rotate in the reverse direction which will reduce the cable tension rapidly. As shown in Figure 4.11, the maximum cable tension force is lower than 10 N, which is below the upper limit of cable tension (30 N). The exerted forces can be enhanced by increasing cable tensions. However, as argued by Chauhan *et al.* [166], the soft laryngeal tissues are thin (around 3-5 mm) and delicate, need to be carefully handled to avoid lesion or rupture of the tissue, and the interaction force with tissue could be reduced and released as the laser cutting or ablation progresses. The current exerted force of the end-effector of *LaryngoTORS* robot should be sufficient for holding, stretching and retracting of the target tissue during the laser cutting or ablation.

4.2.2 *Ex vivo* Test

In this section, *ex vivo* tests were carried out for further assessment of the performance of the *LaryngoTORS* robot. *Ex vivo* tissue laser ablation was executed first and followed by the validation test of the semi-autonomous free path scan on chicken tissue. All the *ex vivo* tests were performed with a 2 μm wavelength thulium YAG medical laser (RevoLix jr, LISA Laser Products GmbH, Germany). The laser output mode was selected as continuous wave (CW) and the laser beam was delivered by a 272 μm laser fibre (FlexiFib-SU fiber, LISA Laser Products GmbH, Germany) (Fig 4.12).

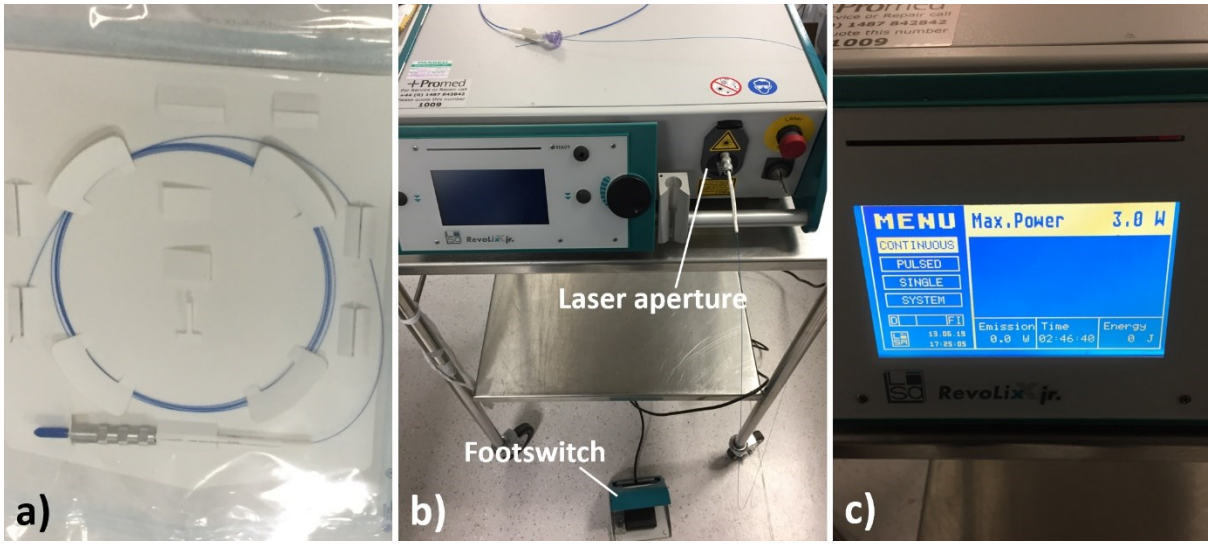


Figure 4.12: The medical laser equipment: a) 272 µm laser fibre (FlexiFib-SU fiber, LISA Laser Products GmbH, Germany). b) Setup of the thulium YAG laser device (RevoLix jr, LISA Laser Products GmbH, Germany). The laser fibre was connected to the laser aperture. A footswitch pedal was used to control the laser output. c) An example of laser setting screen. The laser output power was set to 3 W at CW mode.

4.2.2.1 *Ex vivo* tissue test of laser ablation

A piece of chicken leg tissue was cleaned with water and fixed on a tissue holder. As shown in Figure 4.13, the chicken tissue was used to simulate the right-side vocal cord. The tissue holder was mounted at the front of the *LaryngoTORS* robot. The laser fibre was inserted into the over-tube through the laser fibre sheath. The fibre tip needs to be extended outside of the over-tube and can be observed with the camera. The insert distance of the fibre tip was adjusted based on the size of the spot of the aiming beam. When the end tip of fibre was close to the tissue, the spot of the aiming beam became small and sharp, and the nut of the fibre sheath was locked to ensure the fibre tip moved with the over-tube. A pair of miniature grasping forceps (8593HM, KARL STORZ, GmbH., Germany) was used to stretch and hold the chicken tissue (Fig 4.14a). The laser power was set to 3 W using CW mode. Figure 4.14 shows the procedure of the laser ablation on the chicken tissue, which was performed by manipulating the master controller of the robot manually. As shown in Figure 4.15, an around 7×4 mm tissue was excised, and the incision path was approximately a 10 × 5 mm curved line. The excessive tissue coagulation and carbonisation in the vicinity of the ablation path is caused by using a 2 μm wavelength laser. Cutting performance can be improved by using a CO_2 laser, which can offer improved tissue cutting [145].

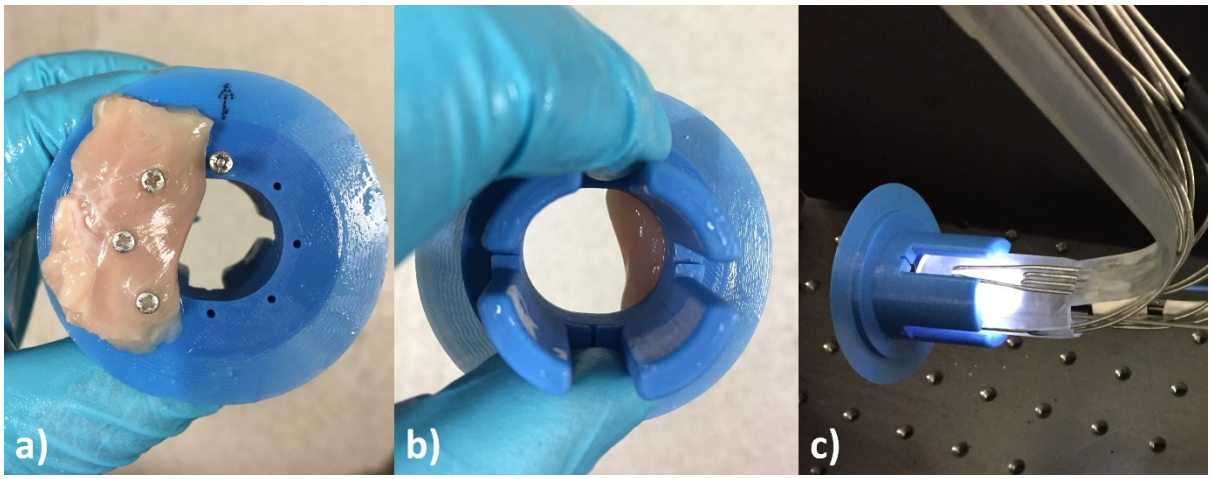


Figure 4.13: a) Rear view of the tissue holder, a piece of chicken tissue was screwed on the tissue holder. b) Front view of the tissue holder, the chicken tissue was used to simulate the right-side vocal cord. c) Attached the tissue holder at the front of the robot.

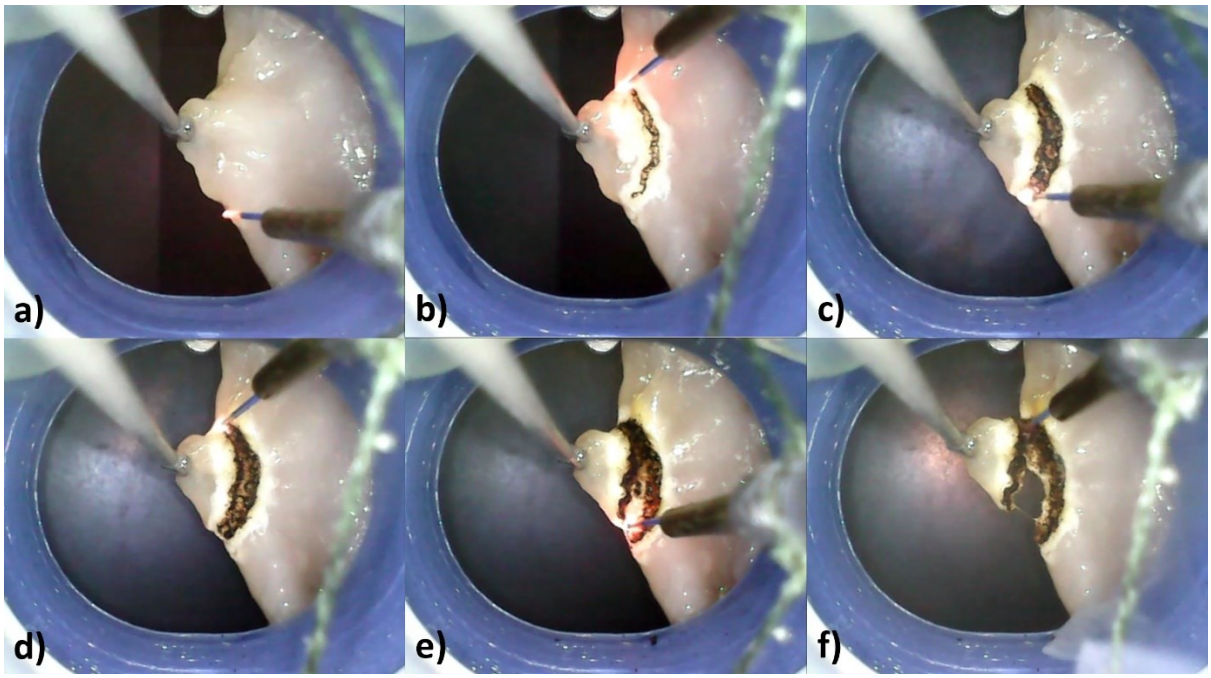


Figure 4.14: a-f) Time sequence of the procedure of the laser ablation on a piece of chicken tissue [168] *©2020 IEEE.*

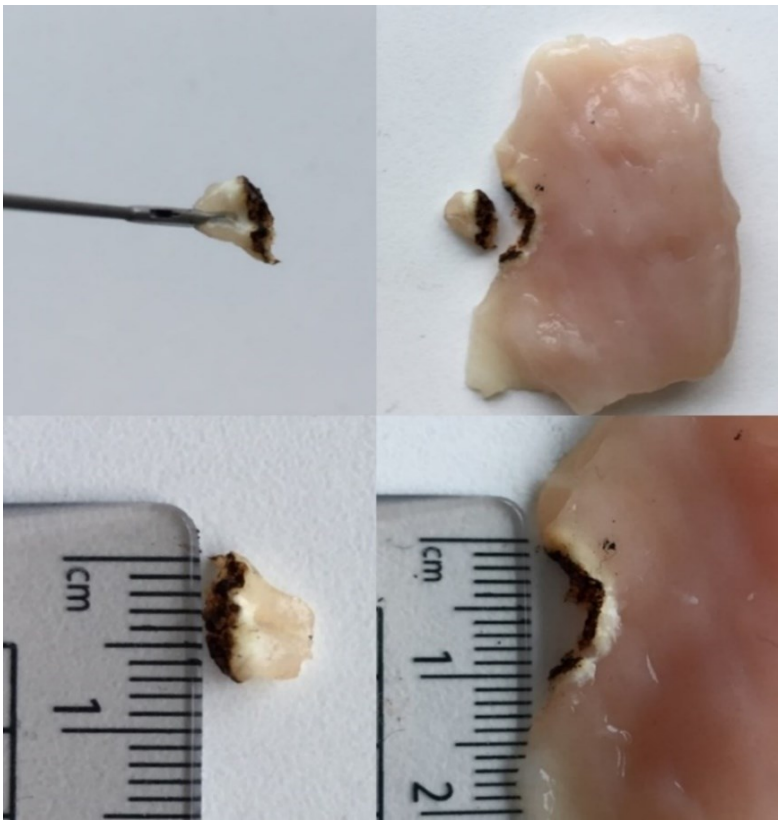


Figure 4.15: The result of the ex vivo tissue laser ablation. A 7×4 mm sized piece of chicken tissue was successfully removed. The incision path was an approximately 10 × 5 mm arc line[168] *©2020 IEEE.*

4.2.2.2 *Ex vivo* tissue test of the semi-autonomous free path scan

Ex vivo testing has also been carried out to evaluate the performance of the semi-autonomous free path scan, again using chicken tissue. As shown in Figure 4.16, a 6 mm diameter semi-circular target was placed on a piece of chicken tissue. Using the same method as the bench test presented in section 4.2.1.1, user-defined control points and were used to describe the scan path. In this case four control points defined the straight line and five control points defined the curved line scan paths generated along the straight and arc margins, respectively. The experimental results of performed path scans along the margins of the target are shown in Figure 4.16. In addition, two arbitrary path laser scans were performed without the semi-circular target. Figure 4.17 shows the results of two arbitrary scan paths, one shaped like a number “3” that was described by 8 control points and another one in a letter “D” shape, defined by 9 control points. All the scan paths were executed at a speed of 2.0 mm/s.

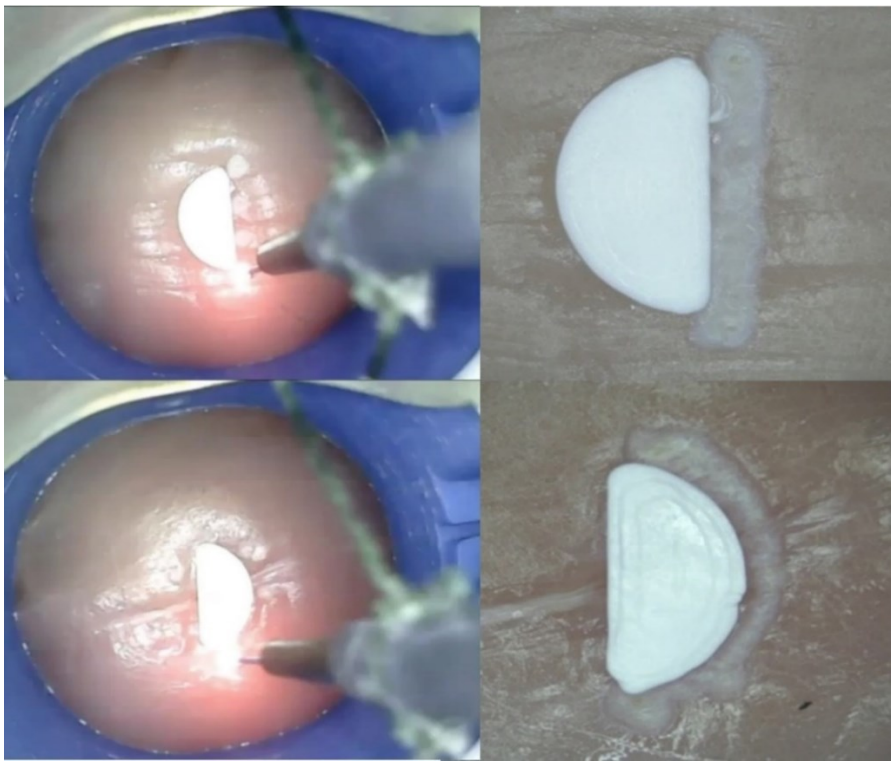


Figure 4.16: The ex vivo semi-autonomous laser path scan along with the straight (top row) and arc (bottom row) margins of the attached target [168] *©2020 IEEE.*

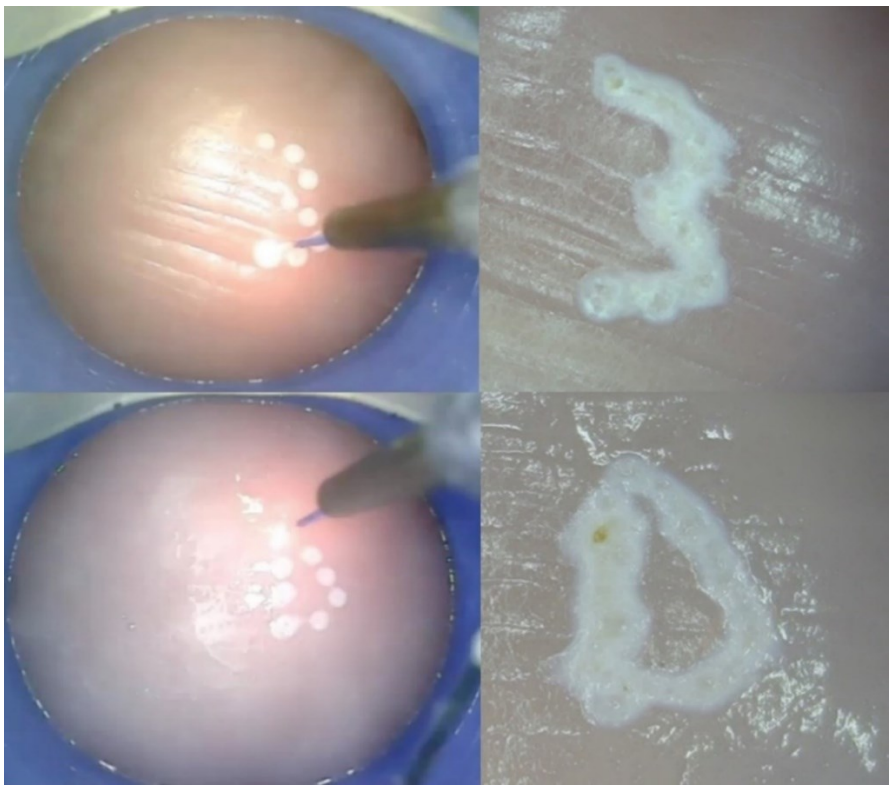


Figure 4.17: Ex vivo laser arbitrary path scans, The scan paths shaped as a number "3" (top row) and a letter "D" (bottom row) [168] *©2020 IEEE.*

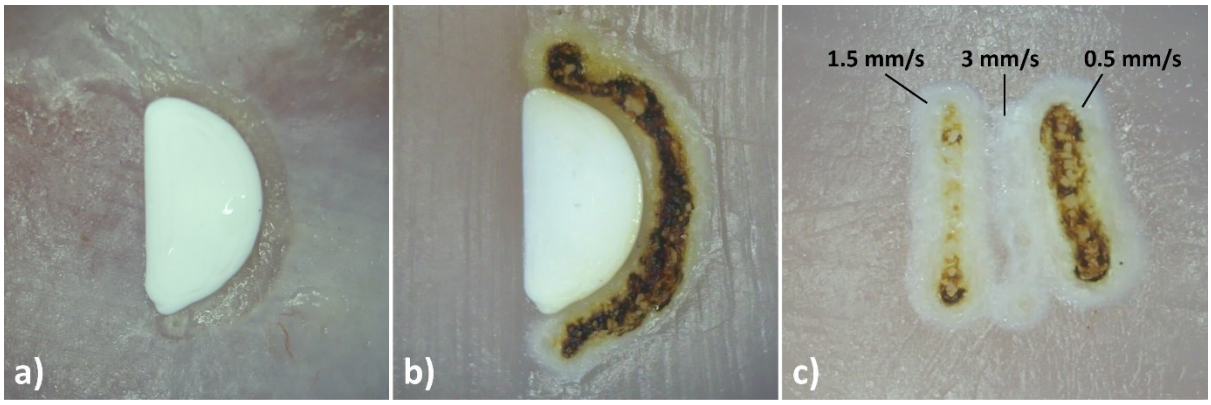


Figure 4.18: Results of laser cutting with different laser power and scanning speeds. a) 1 W, 2 mm/s. b) 5 W, 2 mm/s. c) 3 W at 0.5, 1.5 and 3 mm/s.

During the control point selection, when the aiming beam pointed to the desired position, the high power (3 W) laser beam was fired for a short time (around 1 second) to burn a spot on the tissue. The burned spots can be utilised to indicate the location of control points. The path was checked with aiming beam first and if the path scan was corrected, the path scan button on the control panel interface (Fig 4.3) and footswitch pedal could be pressed simultaneously to start the laser scan. The footswitch pedal was released when the scan finished. As demonstrated in Figure 4.16 and 4.17, all generated scan paths were executed successfully. The video can be found at https://ieeexplore.ieee.org/document/8968404/media#media.

A preliminary test of the laser path scan at different powers and speeds was performed. As expected, for a constant scan speed of 2 mm/s, low laser power (1 W) cannot generate sufficient tissue reaction and high power (5 W) excessively burned the tissue (Fig 4.18 a and b). For a constant power of 3 W at different speeds, the laser's effect was limited at high speed and excessively burned at low speed (Fig 4.18c). The laser power and scan speed settings need to be further studied on human tissue.

4.3 Second version of *LaryngoTORS* robot

The experimental results of bench tests and *ex vivo* tissue tests have demonstrated the *LaryngoTORS* robot has the potential to fulfil the requirements for TLP. The robot should be further evaluated by a preclinical study such as a cadaver trial. An updated version of the *LaryngoTORS* robot has been designed and manufactured for further preclinical study. The

second version of *LaryngoTORS* robot is introduce and discussed in this section.

In the initial version of *LaryngoTORS* robot, Bowden cables from the handle to the scaffold were suspended (Fig 3.30). A mouth gag was required to keep the mouth open and prevent the tooth or lip from squeezing Bowden cables and blocking the motion of laser fibre. Figure 4.19 shows the design and prototype of the second version of *LaryngoTORS* robot. Only the handle and laryngeal blade were redesigned, while other parts of the robot remained the same. The new handle and laryngeal blade were printed on a Form 2 3D printer (Formlabs Inc., USA) using 'tough' resin material. The new laryngeal blade is semi-closed with Bowden cables fixed directly to it (Fig 4.19b and Fig 4.21c) and is designed to keep the mouth open and leave the motion of the laser fibre undisturbed. The *LaryngoTORS* robot body weighs only 1.5 kg and can be held by a support arm. The robot can be held with a single hand by holding the handle of the robot. The placement of the robot can be done by a single operator. A hook on the handle can be utilised to attach to supports used for lifting the epiglottis. The hook can be replaced by a rod which can be connected to a suspension supporter (Fig 4.20c).

A pair of bent miniature grasping forceps (8593HM, KARL STORZ, GmbH., Germany) can be inserted through the side opening of the laryngeal blade and used to hold the target tissue for laser cutting, ablation or photocoagulation (Fig 4.21). The second version of the *LaryngoTORS* robot was assessed by Dr Guri Sandhu (Consultant ENT Surgeon) on a head and neck phantom (AirSim Advance X, TruCorp Ltd., Ireland). As shown in Figure 4.22, the vocal cords can be exposed clearly, and the miniature grasping forceps can be manipulated to grasp and hold a piece of the vocal cord.

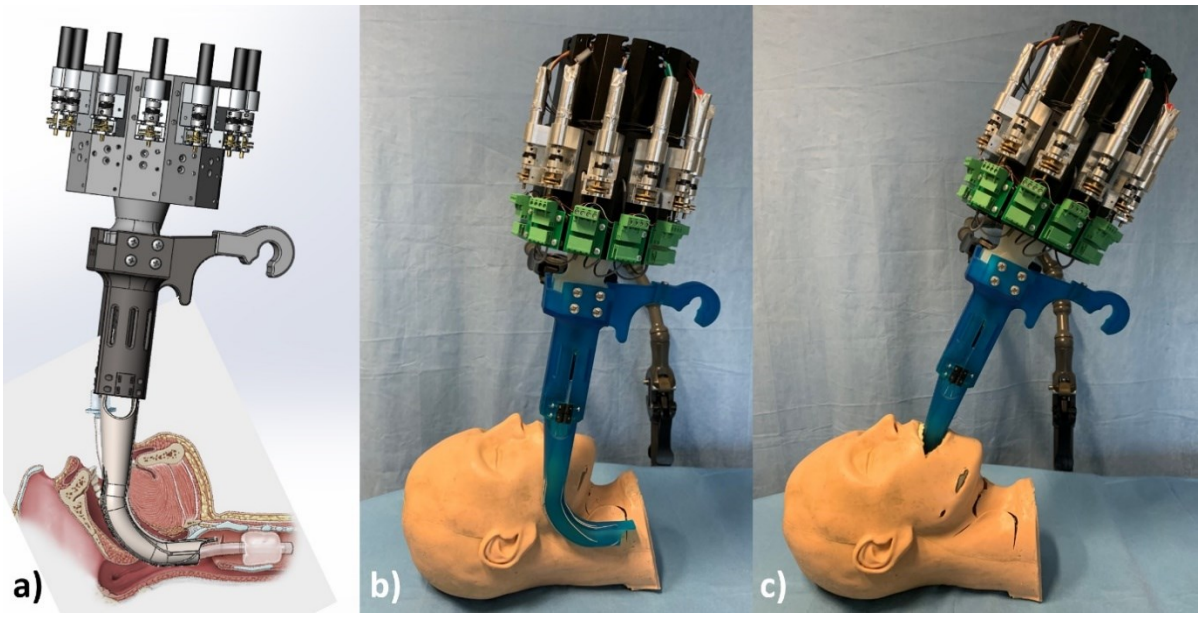


Figure 4.19: a) Conceptual schematic of the second version of LaryngoTORS robot. b) The manufactured LaryngoTORS robot based on the new design. c) The new laryngeal blade is semi-closed which can keep the mouth open and a mouth gag is not required.

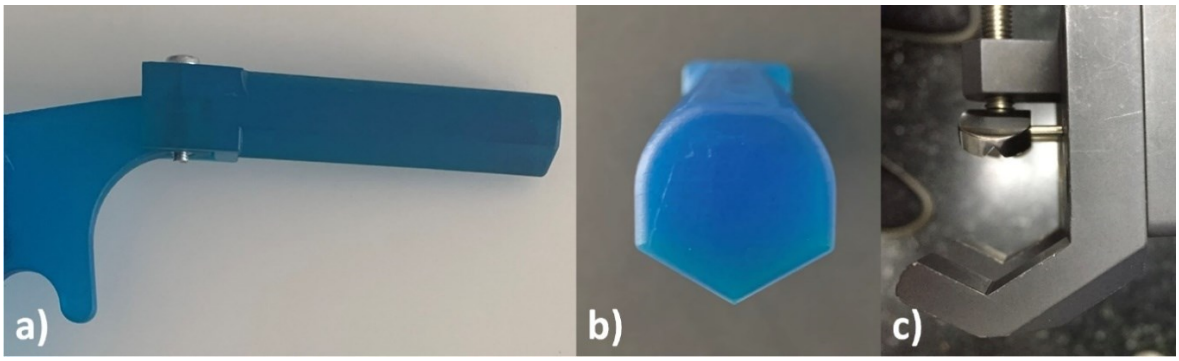


Figure 4.20: a-b) Side and front view of the rod on the handle. c) The rod can be fitted in a suspension supporter (image source: Charing Cross Hospital, London, UK).

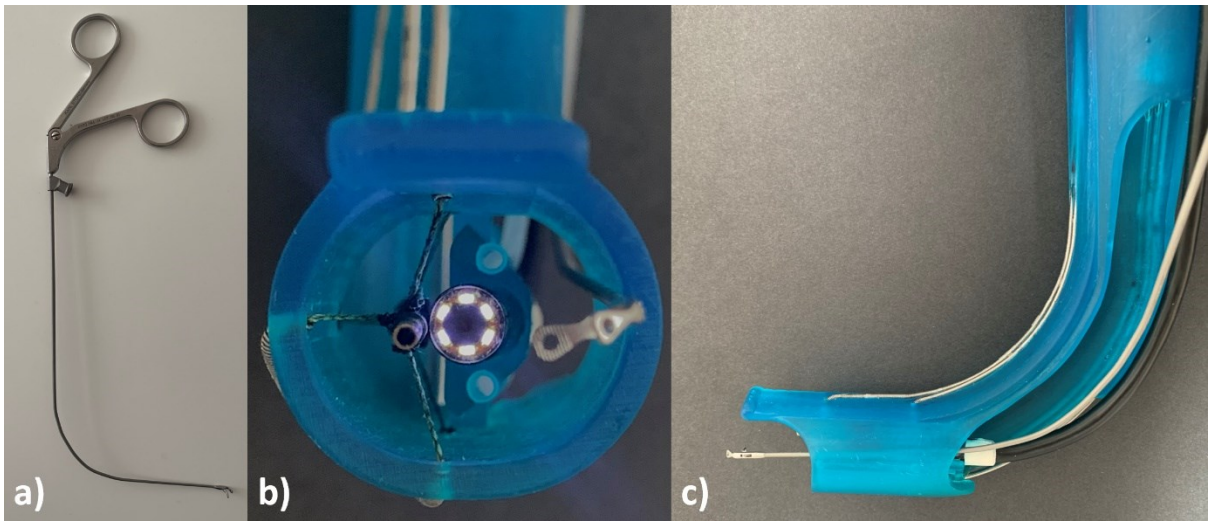


Figure 4.21: a) A pair of bent miniature grasping forceps (8593HM, KARL STORZ, GmbH., Germany). b-c) The front and side view of the LaryngTORS robot with the miniature grasping forceps.

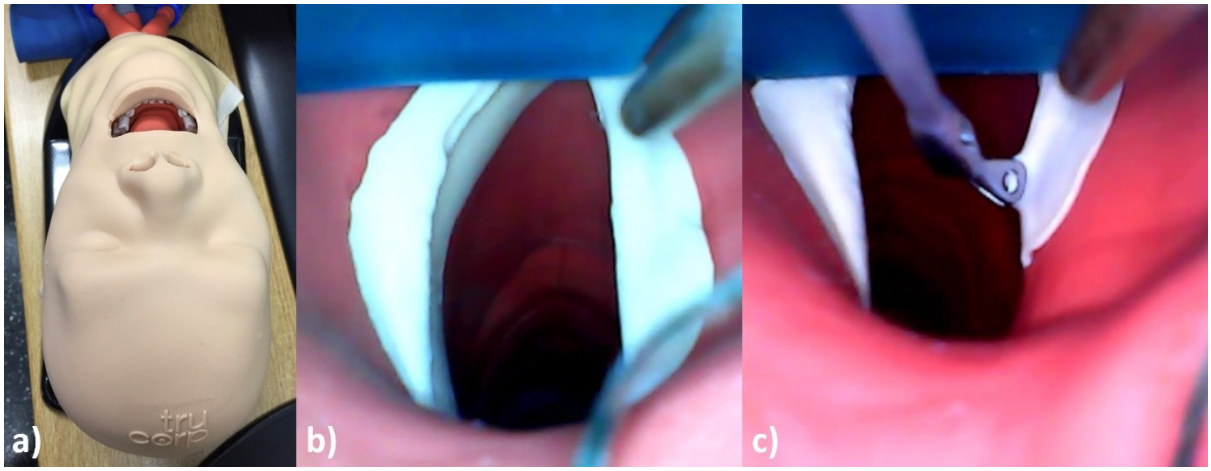


Figure 4.22: a) The AirSim Advance X head and neck phantom (TruCorp Ltd., Ireland). b) The exposure of the larynx of the phantom. c) A piece of the right-side vocal cord was grasped and held by the miniature grasping forceps. (image source: Charing Cross Hospital, London, UK).

As for the previous version (Fig 3.33), the laryngeal blade (with the CDPM) of the second version is also detachable. The laryngeal blade can be assembled to or detached from the robot by connecting or disconnecting the cable connecter (Fig 4.23a). The exact mechanism for cable connection will be investigated in future work. The cable distribution configuration can be allocated based on the position of the target tissue. Two symmetrical laryngeal blades were manufactured (Fig 4.23b and Fig 4.24). One laryngeal blade with a right-hand side CDPM and another one allocated the CDPM at the left-hand side. The right-hand side and left-hand side laryngeal blade are designed to align with the right and left vocal cord respectively and

perform the vocal cordectomy. Since other parts of the robot have not been changed, and the parameters and specifications of the CDPM are identical with the previous version, the performance of the second version should be same with the previous one. A check was performed (Fig 4.24 c and d), confirming the performance of the two laryngeal blades are consistent with the first version.

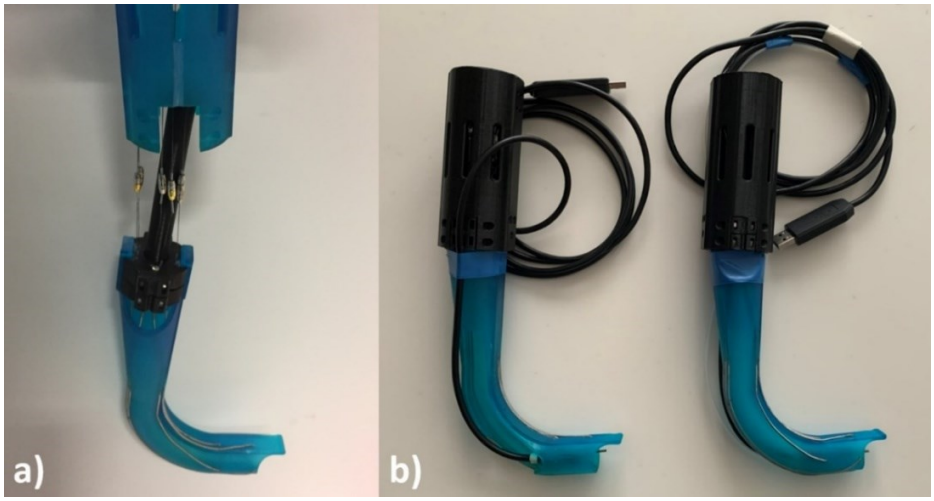


Figure 4.23: a) The laryngeal blade can be connected/disconnected via cable connectors. b) The detached right-hand side and left-hand side laryngeal blade.

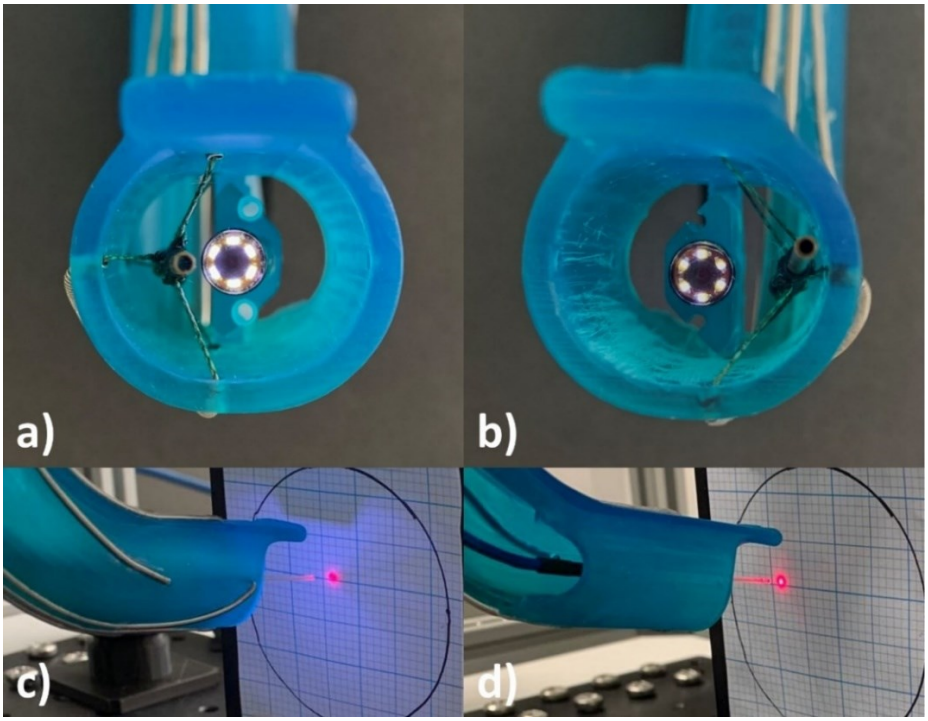


Figure 4.24: a-b) The front view of the right-hand side and left-hand side CDPM. c-d) The performance of two side CDPMs was checked with the laser fibre and aiming beam.

4.4 Discussion

As argued in [100], many emerging surgical robotic systems suffer from clinical applicability problems, such as the limitations of controllability, workspace or sterilisation. These problems slow down or even prevent new techniques and devices translating into the clinic. For further preclinical studies, the technical feasibility considerations of the *LaryngoTORS* robot for TLP are discussed in this section. The comparison between the state-of-the-art fibre-based laser scanning robotics systems is presented at the end of this section.

4.4.1 Technical feasibility analysis

4.4.1.1 Workspace and customised laryngeal blade

As discussed in section 3.2.2, the static workspace of one set of CDPM is approximately a 28 mm diameter half cylinder with 11 mm depth (Fig 3.10). For reaching deeper targets, the fibre tip can be extended more from the over-tube. It could be completed in the operation room by the clinicians. By loosening the end cap of the fibre sheath, the fibre is movable in the sheath. Inserting the fibre further and tightening the end cap to secure fibre, then the fibre is fixed in the sheath. Extending the fibre tip from the over-tube will increase the controllable workspace significantly. Further, as the specification of the laryngeal blade can be customised, the cable distribution configuration can be modified based on task-specific requirements. And the workspace of the CDPM can align with the location of the target tissue. Various laryngeal blades with different specifications and configurations can be chosen and switched for different clinical needs. Thus, the *LaryngoTORS* robot could serve enough controllable workspace to meet the requirements of various surgical tasks.

Although the shape and size of the laryngeal blade can be fully customisable based on patient specific anatomy, it still may not be suitable for a small number of patients with a difficult airway [181]. If the volumetric space of the larynx is too small to accommodate or even insert a proper laryngeal blade, the *LaryngoTORS* robot cannot work. This situation would also be the same for conventional TLM operations. The patient may require open surgery or other therapy.

4.4.1.2 Ventilation and smoke management

A conventional laser-resistant tracheal intubation tube can be used with the *LaryngoTORS* robot in TLP for ventilation. However, if working in a narrow space, the shape and size of the scaffold of the laryngeal blade may need to be modified to offer a space that can accommodate the intubation tube. The modification will compromise the performance of the *LaryngoTORS* robot. Here we recommend using tubeless field techniques for ventilation, such as using a medical air jet device, the ventilation can be achieved with the use of a slim tube or no tube at all [182].

A laser plume will be generated during the laser beam working on the soft tissue, such as laser incision, ablation or photocoagulation. The laser plume obscures the operative field and is noxious to those who come into contact with it [183]. Laser smoke may contain viable tissue particulates and should be effectively controlled. A commercial smoke evacuator designed for use with surgical lasers needs to be used. A vacuum tube can be allocated on the laryngeal blade of *LaryngoTORS* robot for laser smoke aspiration.

As shown in Figure 4.25, two tubes were mounted next to the camera. One tube can connect to a medical air jet machine for ventilation and another one can connect with a smoke evacuator. The tube for jet ventilation or smoking aspiration also can be mounted at other locations around the scaffold.

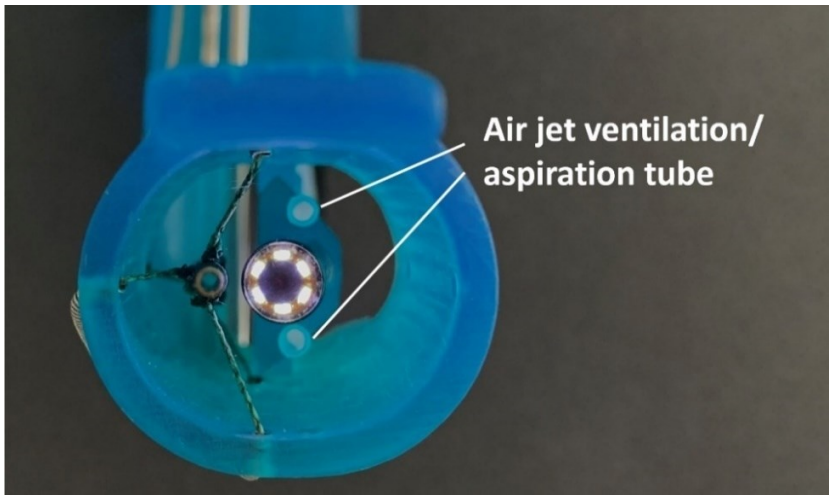


Figure 4.25: Two tubes are attached next to the camera—one for air jet ventilation and another one for smoke aspiration.

4.4.1.3 Biocompatibility and sterilisation

For further clinical trials, the laryngeal blade of *LaryngoTORS* robot will be made by a rigid and biocompatible material, such as the stainless steel or plastic which have been widely used in the suspension laryngoscope or indirect video laryngoscope. The material can also withstand high temperature and pressure and can be sterilised. Since the laryngeal blade is made from low-cost components, it could be offered as a single-use part. Valuable parts such as the motor units and the motor controller could be draped to prevent contamination, and do not require sterilisation. Thus, costs and management of sterilisation and the risks of patient cross-contamination can be avoided, while the performance degradation due to repeated sterilisation will be obviated.

4.4.1.4 Electrical safety

Since the end-effector of the *LaryngoTORS* robot is manipulated by cable actuation, the CDPM part is devoid electrical components. Due to this benefit, the risk of electrical safety is low. With a camera, the *LaryngoTORS* robot could be categorised as a BF type device according to the safety standard EN/IEC 60601-1. By using qualified medical level electrical components and power supply, the *LaryngoTORS* robot could meet the electrical safety requirements of EN/IEC 60601-1. Furthermore, with proper shielding of the motor units and controller, the *LaryngoTORS* robot could comply with the electromagnetic compatibility requirements of standard EN/IEC 60601-1-2. The robot system can effectively prevent electromagnetic interference and would not emit electromagnetic energy that might affect other medical devices; it can work with other qualified medical devices in the operative field safely.

4.4.1.5 Fibre compatibility

As mentioned in section 4.2, *LaryngoTORS* robot is compatible with commercial laser fibres. A CO_2 laser fibre (FiberLase CO_2 fiber, Lumenis Ltd., Israel) and a 272 μm laser fibre (FlexiFib-SU fiber, LISA Laser Products GmbH, Germany) for thulium YAG laser were directly used in bench and *ex vivo* test, respectively. Currently, with a fibre sheath (Laser Fiber

Sheath, Lumenis Ltd., Israel), any optical fibre up to a maximum outer diameter of 1.2 mm can be accommodated, and no modification of the fibre or the system is required. And the fibre is replaceable during the surgery. When the fibre tip needs to renew due to quality degradation, it can be pulled out and the new fibre re-accommodated through the fibre sheath.

4.4.1.6 Device ergonomics

The ergonomics of using the *LaryngoTORS* robot are different from TLM, as the surgeon can teleoperate the tip of fibre via the master controller and the control panel interface (Fig 4.3). The camera in the laryngeal blade offers visualisation of the operation field. The images acquired by the camera can be displayed on the screen. Thus, the control platform, including the screen, chair and master controller, can be adjusted based on the surgeon needs and preferences. The current *LaryngoTORS* robot only has one set of CDPM to steer the laser fibre tip. The miniature grasping forceps need to be manipulated manually, which could be controlled by the first surgical assistant. As discussed in section 3.2, a second CDPM can be manufactured to control the forceps, and then all the instruments can be teleoperated remotely. The *LaryngoTORS* robot has the potential to offer better ergonomics compared to the current TLM method. However, the ergonomics and usability of the robot should be further evaluated by surgeons in a clinical environment.

4.4.2 Technical comparison with other fibre-based laser scanning robotics systems

The performance and technical feasibility of the *LaryngoTORS* robot have been demonstrated and discussed above. As introduced in section 2.4, various fibre-based laser scanning robotic systems have been developed for TLP. Besides the CDPR, there are two types of fibre-based laser scanning robotic system, a MEMS controlled mirror steering and a magnetically controlled fibre steering laser scanning system, can achieve non-contact laser ablation with laser scanning. The MEMS controlled mirror steering laser scanning systems, include the μRALP robotic system developed by Mattos *et al.* [138], a compact laser-steering end-effector manufactured by Bothner *et al.* [136] and a microrobotic laser steering system developed by York *et al.* [137]. And a magnetically controlled laser scanner has been

developed by Acemoglu *et al.* [139]. Literature shows that all these systems could be expected to offer high precision laser scanning and have the potential to be used in TLP. Here, we make a technical comparison between these robotic systems.

Table 4.4: Technical comparison with other fibre-based laser scanning robotics system

	***LaryngoTORS* robot**	**µRALP robotic system** [138], [143]	**Magnetic laser scanner** [139], [141]	**Laser-steering end-effector** [136]	**Microrobotic laser steering system** [137]
Distal size	22 x 20 mm, ellipse	Ø18 mm	Ø13 mm	Ø15 mm	Ø6 mm
Workspace	28 mm diameter half cylinder with 11 mm depth	20 x 20 mm^2	4 x 4 mm^2	18 x 10 mm^2	18 x 18 mm^2
Maximum speed	25 mm/s	65 mm/s	94 mm/s	2000 mm/s	3900 mm/s
Working distance	1 mm	20 mm	30 mm	20 mm	25 mm
Controllable DoF	5 DoF	2 DoF			
Fibre compatibility	Directly compatible with the commercial fibres	Fibre needs to be pre-assembled in the robotic miniature laser scanner.			
Laser aperture quality control	The fibre end tip is the laser aperture. It may contact the tissue accidentally. But the fibre end tip can be renewed simply	The laser aperture is an optical element, such as a focusing lens and/or a deflection mirror. The laser aperture at the end of the robot, which will be inserted in the larynx, easily contaminated, challenging to maintain quality			

As shown in Table 4.4, the distal size of *LaryngoTORS* and µRALP robotic system are bigger than other systems. However, *LaryngoTORS* and µRALP are integrated surgery robotic systems, including both cameras and light sources. As shown in Figure 4.21b), the *LaryngoTORS* robot can offer a space for an auxiliary surgical instrument such as grippers or forceps. The other systems are designed as miniature laser scanners, which were conceived to be used with other devices, such as a flexible endoscope or the end-effector of a robotic arm. A relatively large workspace can be generated by the *LaryngoTORS* robot. However, as

mentioned above, other miniature laser scanners can be mounted or work with a driven mechanism such as a robotic arm. The entire workspace could be enlarged by the driven mechanism. Compared to other systems, the maximum scan speed of the current *LaryngoTORS* robot is quite slow, especially compared to the microrobotic laser steering system developed by York *et al.,* which can reach up to 3900 mm/s [137]. Due to the use of the high ratio gear set (64:1 gear head, Faulhaber, Germany) and small cable spool size (6 mm diameter), the maximum speed of the current *LaryngoTORS* robot is limited to 25 mm/s. The maximum of the *LaryngoTORS* robot can be increased by using a larger size cable spool and lower ratio gear head, such as 16:1 or 4:1[184]. As introduced in the chapter 3, high speed is one feature of CDPR. With proper motor set and controller, high speed motion can be achieved by a CDPR [148], [153], [159]. As argued by York *et al.* [137], the laser scan speed affects the duration of laser irradiation which is a critical factor that affects the outcomes of laser-tissue interaction. High laser scanning speed could improve laser cutting precision and reduce thermal damage. However, as discussed in chapter one, the laser-tissue interaction depends on the combination of laser parameters, such as wavelength, power density and irradiation duration. The scanning method can also affect the thermal damage of the surrounding tissue. Non-sequential laser scanning can minimise the accumulation of thermal damage [58]. As discussed in section 4.2.2.2, the proper laser parameter settings, such as the power and scan speed, need to be further evaluated on human tissue.

The main difference between *LaryngoTORS* robot and other systems is the working principle. The *LaryngoTORS* robot uses a CDPM to control the motion of a bare end fibre tip in 5 DoF. The spot size of laser beam depends on the spot size at the end of the fibre tip, divergence angle and the distance between the fibre tip and the target. The spot size at the end of a CO_2 fibre tip can reach to 320 μm [38]. The fibre size of solid lasers, as mentioned in chapter two, can be even slimmer. For instance, the Thulium YAG laser fibre (FlexiFib-SU fiber, LISA Laser Products GmbH, Germany) used in *ex vivo* tests is only 272 μm (Fig 4.12). Similar to the operation of the robotic laser instrument (Fig 1.6), the surgeon can adjust the pose and the distance of the fibre tip based on the shape and size of the aiming beam spot. For the CO_2 fibre (FiberLase CO2 fiber, Lumenis Ltd., Israel) used in the bench top test, the spot

size at 1 mm distance is around 400 μm. To achieve a precise incision, the fibre tip needs to be close to the target tissue to achieve a small spot size. In contrast, other systems combined a fibre tip with mirrors and/or optical lenses to steer the laser beam only in 2 DoF. Due to the 2 DoF beam control, an adjustable laser focusing unit is required to maintain the beam focusing on a target tissue for precision laser cutting. However, good laser focusing remains an issue to be addressed. All systems are required to carefully manage the laser beam quality.

Compared to other systems, the *LaryngoTORS* robot can provides advantages in fibre compatibility and laser aperture quality control. As discussed in the previous section, by using a fibre sheath (Laser Fiber Sheath, Lumenis Ltd., Israel), the *LaryngoTORS* robot is directly compatible with commercial laser fibres. Clinical staff can insert or remove the fibre from the robot during the surgery. In contrast, for other systems, the fibre tip needs to be pre-assembled in the robotic miniature laser scanner. Precise alignment, calibration and validation test are required, which could not be performed by clinical staff. And there does not seem to be a practical way of replacing the fibre during the surgery. Furthermore, since nearly all commercial laser fibres are single-use or reusable up to a limited number of times, the miniature laser scanner may need to be discarded after one or limited uses. The final laser aperture of the *LaryngoTORS* robot is the bare end of the fibre. When the fibre tip needs to be renewed due to quality degradation, it can be removed and renewed. The operation of fibre tip renewal is simple and can be performed by clinical staff during the surgery. However, the laser aperture of other systems is an optical element, such as a focusing lens and/or a deflection mirror. Since the laser aperture will be inserted into the larynx, it could be easily contaminated. If the laser beam is blocked and absorbed by pollutants, it will cause damage and eventually breakage of the laser aperture. It may be challenging to maintain quality during the surgery.

Currently, all systems are still at the preclinical stage and have to face critical challenges to become practical for clinical use. The performance in clinical applications needs to be further evaluated.

4.5 Conclusion

The *LaryngoTORS* robot is the first CDPM system that has been developed for TLP. The experimental results of bench and *ex vivo* tests have demonstrated that high precision and high repeatability of the semi-autonomous free path scan can be achieved. By using a curved laryngeal blade and a built-in camera, a straight suspension laryngoscope will not be required. It is less traumatic to the patient and the post-operative pains could be reduced. As the laser operation can be teleoperated, the direct line-of-sight through a surgical microscope is not required, which is also more ergonomic for the surgeon. When compared to other fibre-based laser scanning robotic systems for TLP, the *LaryngoTORS* robot provides advantages in large workspace, high controllability and technical feasibility, such as fibre compatibility and laser aperture quality control. Currently, the *LaryngoTORS* robot is ready for further preclinical trials, such as cadaver experiments. The robotic system has shown the technical feasibility and applicability for use in TLP; the requirements for TLP proposed in chapter 2 can be expected to be fulfilled. It is a promising direction to continue to develop in the future. This research showed that CDPM has sufficiently high precision and high repeatability to control a fibre for surgical tasks. The *LaryngoTORS* robot is not limited to applications in laser therapy but also can be used for fibre-based diagnosis or biopsy, such as endomicroscopy, hyperspectral imaging and intraoperative optical coherence tomography (OCT). A preliminary study of the applicability of *LaryngoTORS* robot for optical biopsy in the larynx will be discussed in the next chapter.

Chapter 5

Robotic-assisted Fibre-based Optical Biopsy of the Larynx

The potential of *LaryngoTORS* robot to execute path scans with high precision and repeatability along the target margin has been demonstrated in chapter 4. A striking advantage of *LaryngoTORS* robot is its ability to provide precise fibre distal tip control. This is particularly advantageous for integrating robotic scanning with miniaturised high-resolution optical biopsy techniques like probe-based confocal laser endomicroscopy (pCLE) for real-time tissue imaging. Such robot-assisted optical biopsy has the potential to allow examination of large anatomical areas like the entire surface of surgically excised specimens in a timely manner with microscopic resolution.

This chapter presents investigations on the integration of the *LaryngoTORS* robot with fibre/probe-based optical biopsy for rapid *ex vivo* imaging of the larynx. Feasibility studies and experiments are carried out using two optical biopsy systems: pCLE and hyperspectral fibre-optic sensing. The experimental results will be presented and discussed. The assessment of CDPR for optical biopsy of the larynx is summarised at the end of this chapter.

5.1 Fibre-based Optical Biopsy of the Larynx

Confocal laser endomicroscopy (CLE), hyperspectral imaging (HSI) and optical coherence tomography (OCT) are popular optical biopsy techniques and can be utilised to detect laryngeal diseases, such as the polyp, leukoplakia and laryngeal cancer etc. [105], [185]–[189]. Compare to the conventional excision biopsy, such optical biopsy techniques offer two main advantages. A key benefit is that the optical biopsy methods are non-invasive to the test tissue status. Especially for the patient with lesions on vocal cords, multiple biopsies are often required to be carried out. The patient's voice may be changed due to the scars generated by conventional biopsy. In contrast, optical biopsy techniques will not suffer this problem. Another advantage of the optical biopsy is that can be used intraoperatively. The surgeon can acquire real-time feedback, no need to wait for the result of the pathological examination.

CLE enables *in vivo* confocal imaging of biomedical tissue cellular structures. Recent research shows that CLE can be used to detect head and neck disorders successfully, especially in the detection of squamous cell carcinomas (SCC) which is the most common cancer in the vocal cords [105], [185], [186], [190]–[192]. The pCLE delivered the confocal imaging via flexible fibre bundles which can go through the curved airways. Figure 5.1 shows a typical confocal image of healthy mucosa and a typical example of SCC. As demonstrated in Figure 5.1, the healthy mucosa and SCC can be distinguished easily from the confocal laser imaging [185]. A rigid endoscope has been previously demonstrated to acquire CLE images of the larynx intraoperatively [190], [191], [193]. However, a straight suspension laryngoscope is needed to create a straight working channel for the rigid endoscope. The patient may have lesions and postoperative pains due to using the suspension laryngoscope. For *in vivo* imaging in routine clinical practice, it is desirable to use a flexible endoscopic device that can be integrated with flexible pCLE fibre bundle to reach at difficult places with causing minimum patient trauma.

One challenge of using pCLE for optical biopsy is its relatively small field of view (FOV) due to the miniaturised size of the fibre bundle used. The FOV can be expanded via mosaicking to create a large imaging area [194]–[197]. However, high quality and sufficient

overlap between consecutive confocal imaging are required for mosaic generation. Thus, optimum probe pose, and consistent tissue-contact are needed to be maintained, while performing pCLE scanning. Literature shows that recently a few robotic devices and tools have been utilised to assist in the execution of the consistent pCLE scanning [198]–[200]. However, to the author's knowledge, there is no robotic system can perform the pCLE scanning of the larynx. The da Vinci® surgical robotic system (Intuitive Surgical Inc., USA) can be used to perform the pCLE scanning. The probe of CLE can be held and precisely controlled by the robotic instrument of the da Vinci® robot [201], [202]. However, due to the strict requirements of mosaic generation, an extra contact force, depth or visual servoing control is needed to achieve qualified pCLE scanning [203]–[205]. Further, as discussed in Chapter 2, the dimensions of the robotic instrument of the da Vinci® robot is too big to perform the scan in the larynx.

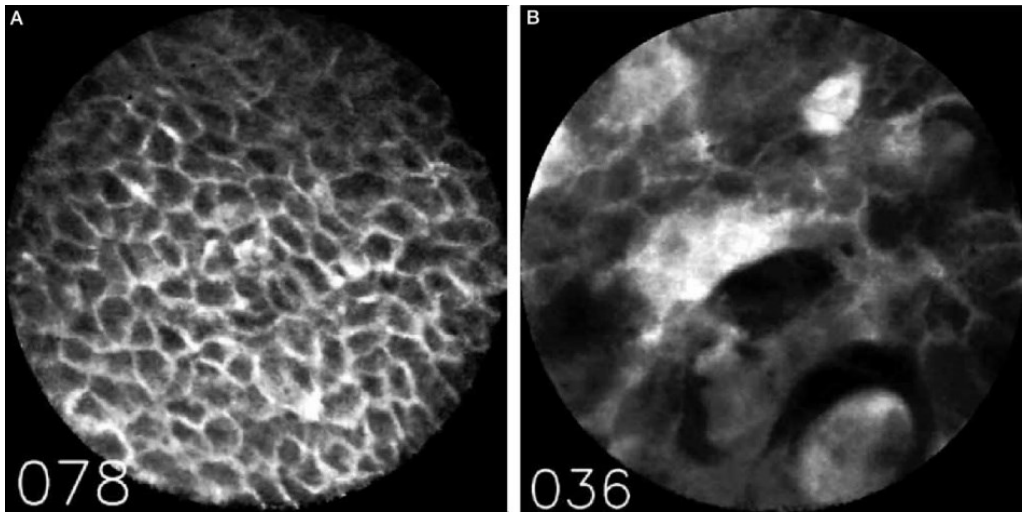


Figure 5.1: A typical confocal image of healthy mucosa (left) and a typical example of the confocal image of SCC (right) [185].

Another widely used method for intra-operative tissue imaging is HSI. For HSI, a set of monochromatic images of the same target area are captured over a range of wavelengths with a fixed interval, usually 10 nm. The unique characteristic absorption peaks of wavelengths can be used to describe and identify various tissue types. Thus, HSI can be used to detect laryngeal lesions and cancer [187], [188], [206]. The fibre-based hyperspectral sensing by using a fibre probe which is connected with a white light source and a spectrometer can achieve the reflectance spectra of the target tissue at the sample point which contacted with

the probe. The reflectance spectra acquired by the hyperspectral sensing probe is consistent with the spectra generated by HSI [207], [208]. The fibre-based hyperspectral sensing can generate real-time reflectance spectra of the test tissue rapidly. Compared to HSI, fibre-based hyperspectral sensing is a more practical technique to be used intraoperatively. However, similar to the pCLE, the precise control of the hyperspectral sensing probe remains a major challenge.

LaryngoTORS robot has demonstrated the excellent performance on motion control. The robot has the potential to be used in the fibre-based optical biopsy of the larynx. The details of the *LaryngoTORS* robot-assisted pCLE and hyperspectral fibre-optic sensing are presented in section 5.2 and 5.3, respectively. The fibre-based OCT of the larynx will not be discussed in this chapter. However, due to the similarity with other fibre-based optical biopsy techniques, the *LaryngoTORS* robot could also work with the fibre-based OCT. Related research will be performed in the future.

5.2 Robotics-assisted Probe-based Confocal Laser Imaging of the Larynx

In this section, experiments of pCLE with *LaryngoTORS* robot were carried out on lens paper and *ex vivo* porcine tissue. Initially, we performed the pCLE tests on the lens paper and porcine tissue dyed by 0.01% acriflavine solution to evaluate the ability of *LaryngoTORS* robot on the pCLE fibre bundle manipulation and confocal laser imaging acquisition. To demonstrate the possibility of use in humans, a second experiment was performed on porcine tissue stained by fluorescein solution which is one of the FDA approved dyes for human use. The semi-autonomous free path scan (see section 4.2) was executed, and the generated video mosaicking was assessed. The method and experimental results are presented in section 5.2.1 and 5.2.2, respectively.

5.2.1 Materials and Methods

A commercial pCLE system, Cellvizio system with a GastroFlex UHD probe (Mauna Kea Technologies, France), was used in all pCLE experiments (Fig 5.2). The GastroFlex UHD probe has 30,000 fibre bundle imaging elements and a micro-objective lens which can offer

approximately 1.2 μm resolution confocal laser imaging with 240 μm FOV at 55 to 65 μm confocal depth [209]. As mentioned in the previous section, the confocal depth is relatively superficial and the FOV is quite small. Thus, the GastroFlex UHD probe needs to be carefully controlled to contact with the target tissue at proper pose and position. Also, the video mosaicking is required to enlarge the imaging area to overcome the limitation of the small FOV of the GastroFlex UHD probe. Figure 5.3 shows the experiment setup. Since the inner diameter of the over-tube is only 1.2 mm but the outer diameter of the GastroFlex UHD probe is 2.6 mm, the probe could not be accommodated in the over-tube. A custom-designed and 3-D printed probe adapter was used to attach the probe at the end of the over-tube. Similar to the *ex vivo* tests performed in chapter 4, the test target was fixed on a target holder which can be mounted at the front of the scaffold of the *LaryngoTORS* robot. Before being mounted on the robot, the test targets were dyed. For the experiments, a lens paper and a piece of porcine tissue were stained with 0.02% acriflavine solution and another porcine tissue was dyed with 0.1% fluorescein solution. For the lens paper, the test was executed after dyed. For the two porcine tissue, both stained with their solution for 1 min and then washed with saline before the test (Fig 5.4). The captured confocal laser images were displayed on the monitor of the Cellvizio system. The probe and test target were visualised via the camera built-in the laryngeal blade (Fig 5.3 c and e).

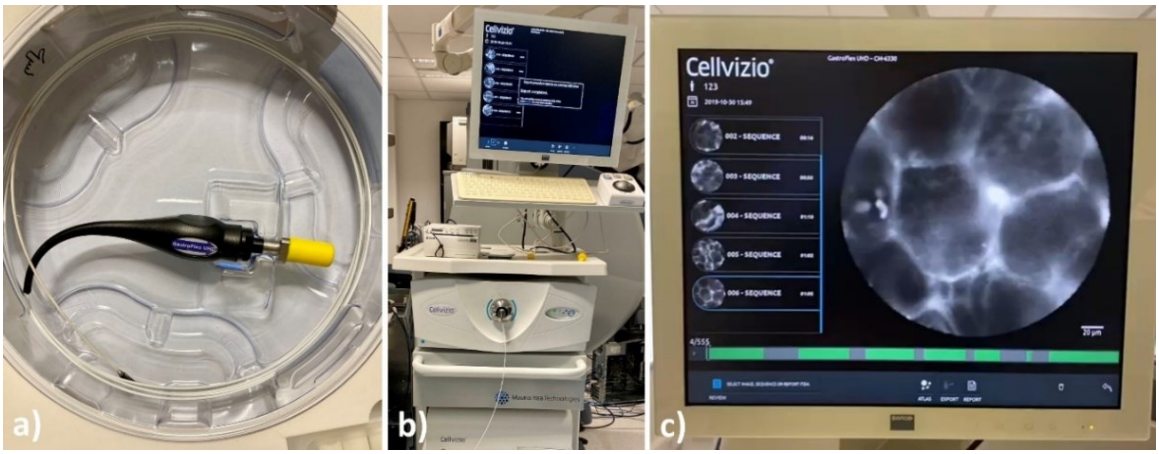


Figure 5.2: The Cellvizio confocal laser imaging system. a) The GastroFlex UHD probe. b) The Cellvizio system. c) The captured imaging displayed on the monitor.

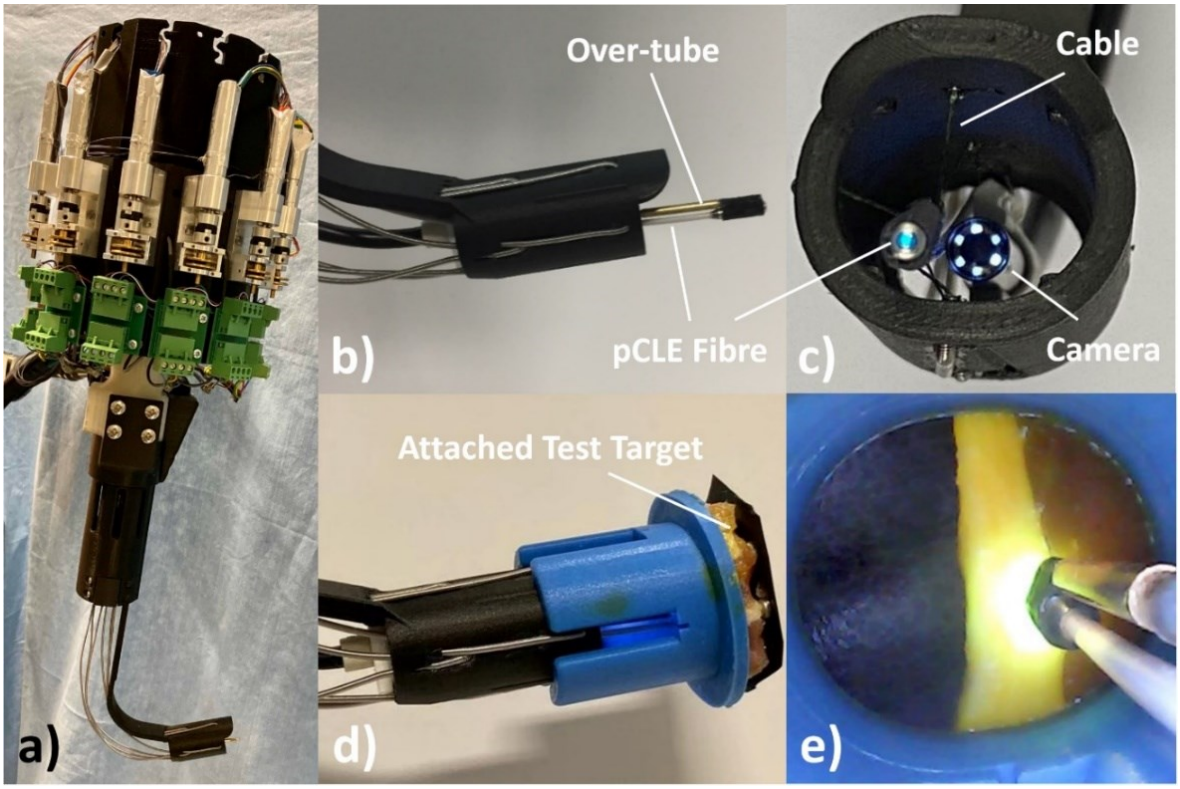


Figure 5.3: The experimental setup: a) Overview of the LaryngoTORS robot. b) Side view of the CDPM with a GastroFlex UHD probe. The probe is attached at the end of the over-tube. c) Front view of the robot with the probe. A USB camera was utilised to offer the vision of the operation field. d) A test target sample was attached to the front of the robot. e) The end view from the camera.

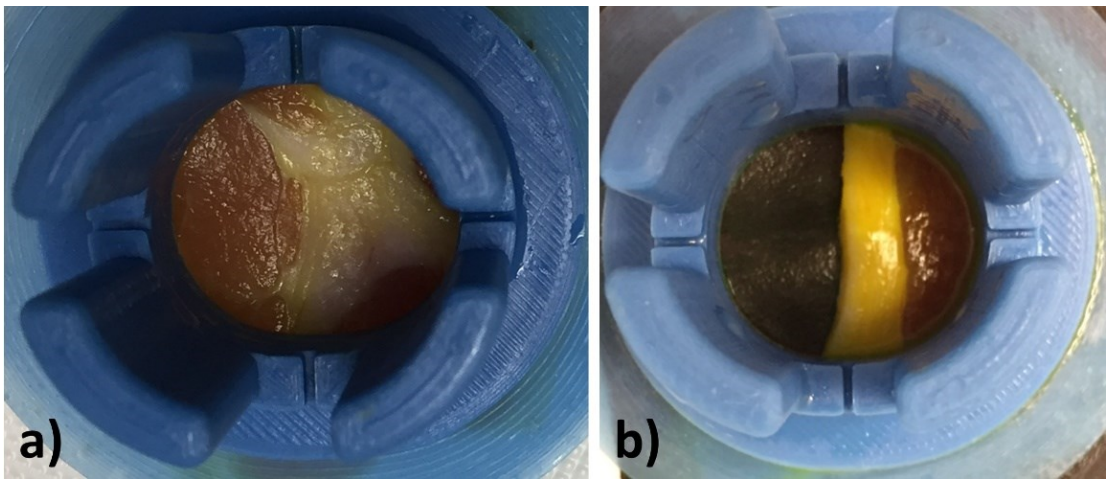


Figure 5.4: Two porcine tissue samples stained with 0.02% acriflavine solution (a) and with 0.1% fluorescein solution (b).

A master controller (Geomagic Touch, 3D Systems, USA) was used to manipulate the probe via steering the over-tube. The probe was gently moved to contact with the lens paper or porcine tissue to achieve a clear confocal laser imaging. As shown in Figure 5.4b), a piece of porcine fat tissue was placed at the right side of the holder and used to simulate the right-

side vocal cord. As the semi-autonomous free path scan, a user-defined pCLE scanning path was generated via control points and Catmull-Rom spline interpolation. The experimental results are demonstrated below.

5.2.2 Experimental Results

Figure 5.5 shows two representative imaging results detected on the lens paper and porcine fat tissue dyed with acriflavine solution. The highlighted paper fibre and cell nuclei are visible in the acquired images. A 4-control points defined pCLE scanning was performed on the porcine fat tissue which was stained by fluorescein solution. The control points were manually defined. The GastroFlex UHD probe was placed at the desired location of the control point. When a clear confocal laser image was displayed on the screen, the pose and position of the end-effector of *LaryngoTORS* robot was recorded. The endo view from the camera and confocal imaging of the 4 control points are demonstrated in Figure 5.6. Adipocytes of the fat tissue are clearly visible in captured confocal imaging of each control point. The pose and position of the end-effector at 4 control points were recorded sequentially. The scanning path was generated via spline interpolation and the scan velocity was set to 1 mm/s. The pCLE scanning along the defined path was executed by *LaryngoTORS* robot autonomously. The generated pCLE scanning path was shown in Figure 5.7 a) and b) in 3D and 2D, respectively. The result of the mosaic image formed from the video data of pCLE scanning is presented in Figure 5.7 c). The codes of image mosaicking are based on the original programming developed by Dr Michael Hughes [195] and Dr Haojie Zhang. The reconstructed mosaic image correlates well with the generated scanning path, as shown in Figure 5.7 b). Due to the high precision and repeatability of the path scan (see chapter 4, section 4.2), a proper tissue contact can be repeated precisely at each control point and maintained at each point in the path via the point interpolation. Thus, the mosaic image can be formed, which benefits from the excellent smooth motion control of *LaryngoTORS* robot.

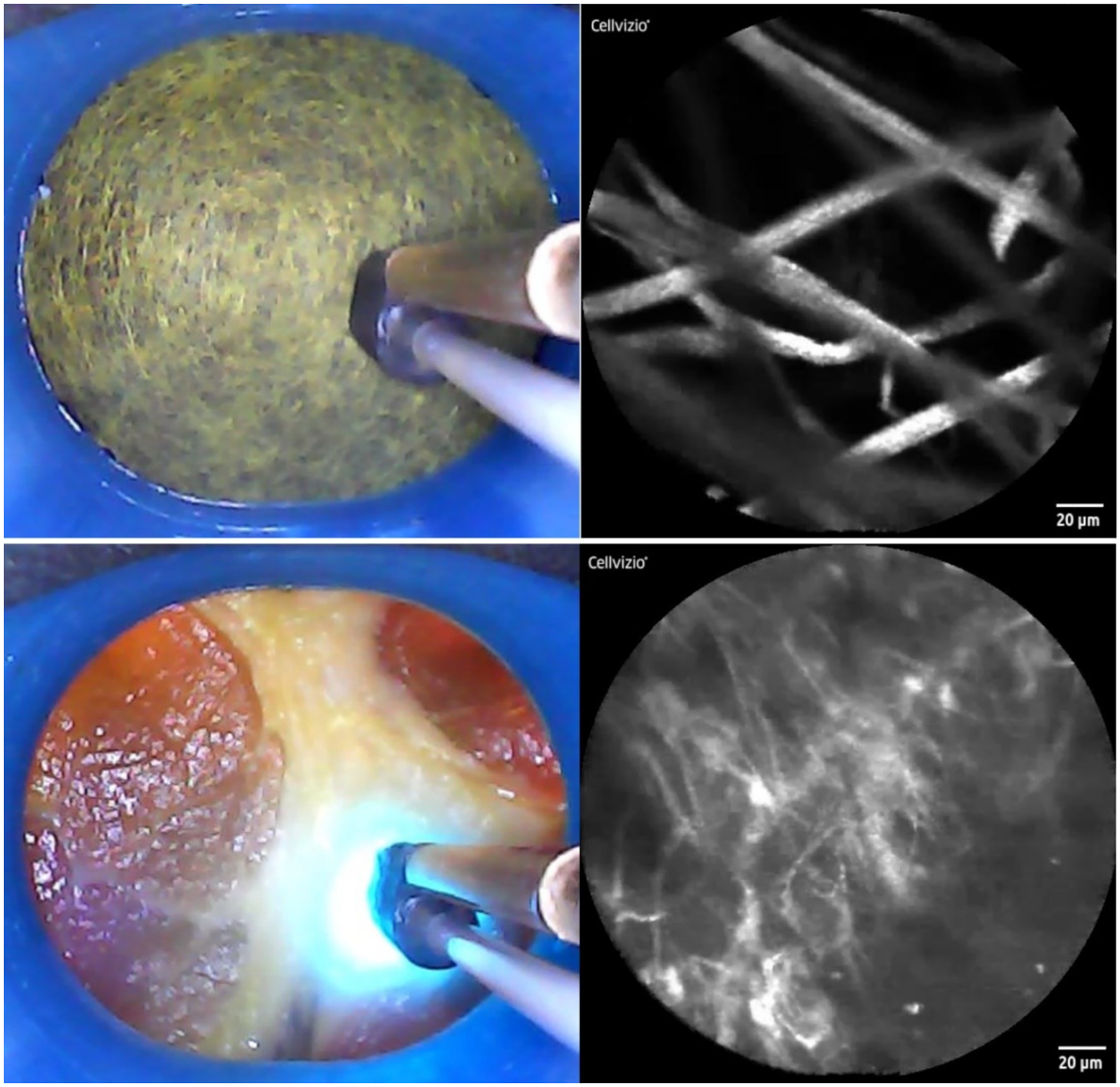


Figure 5.5: Two representative results of the pCLE test on lens paper (top row) and porcine tissue (bottom row). The endo view from the camera (left) and the acquired confocal imaging (right) are demonstrated.

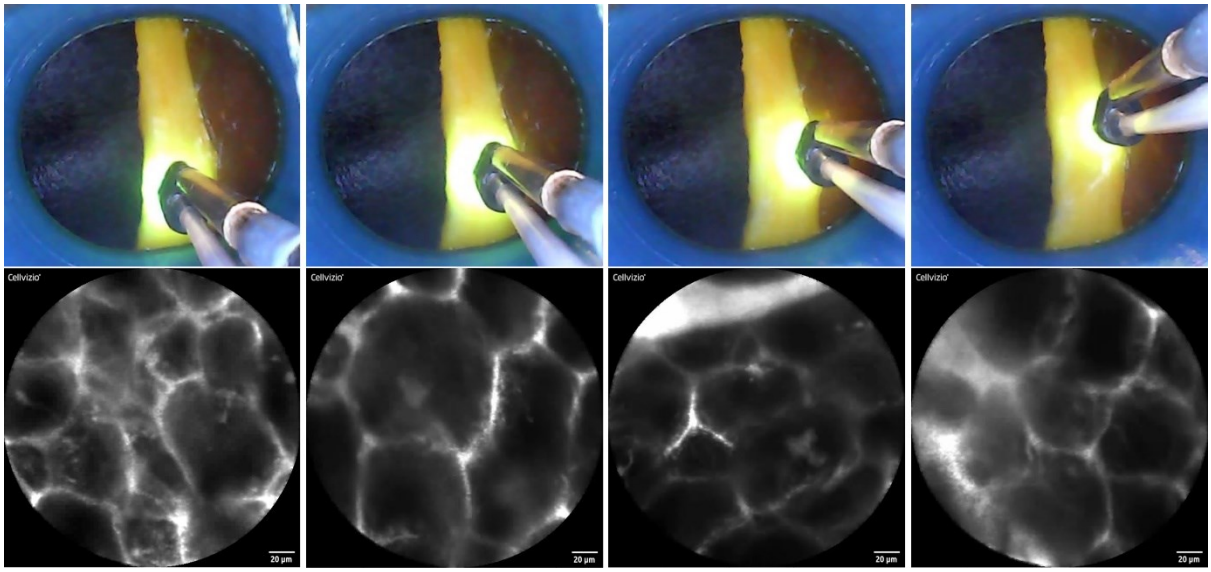


Figure 5.6: The camera view (top row) and confocal imaging (bottom row) captured at 4 control points.

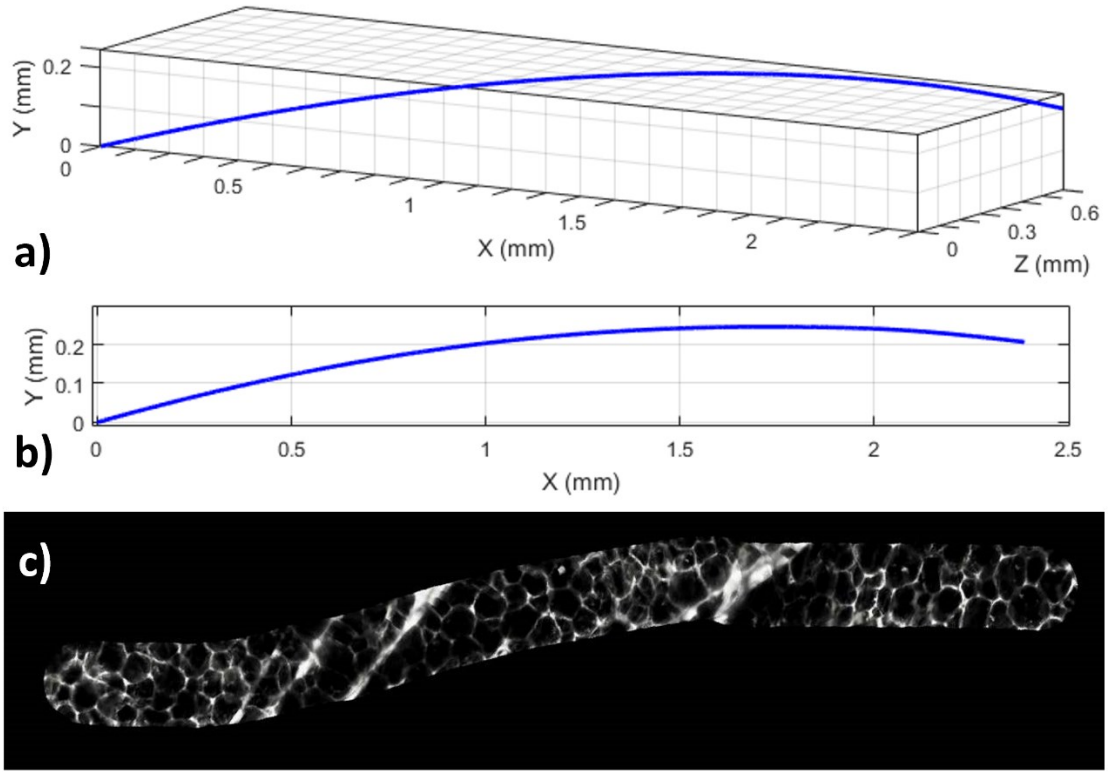


Figure 5.7: a-b) Demonstration of the generated scan path of confocal scanning in 3D and 2D respectively. c) The result of video mosaicking of the confocal laser scanning executed on the porcine fat tissue [210].

5.2.3 Discussion

This study explores the possibility of using *LaryngoTORS* robot to manipulate the probe of the fibre bundle to acquire high-quality confocal laser imaging of the larynx. The experimental results demonstrate that *LaryngoTORS* robot can perform precise pCLE scanning on a simulated vocal cord and mosaic images can be formed from scanning results. No force or depth sensor was used during these tests, demonstrating the potential to maintain tissue contact without additional sensors.

The scan speed depends on the frame rate and the FOV of the pCLE imaging system and the demands of the mosaic generation. The frame rate and FOV of the Cellvizio system are 12 fps and 240 μm. Therefore, without overlap, the maximum scan speed is 2.88 mm/s. However, since the sufficient overlap between consecutive confocal imaging is required for mosaic generation, thus the scan speed is settled at 1 mm/s. The scan speed could be increased by using an imaging system with a wider FOV and higher frame rate.

A common method used in clinical practice is to sample multiple smaller areas to perform the optical biopsy. A vision-based autonomous pCLE scan developed by Zhang *et al*. can generate an around 1 mm^2 area autonomous scan using a da Vinci® robot [203]. The *LaryngoTORS* system could be developed to scan multiple small areas and also an entire region of interest in the workspace. A proper area scanning function should be developed and evaluated in the future.

Currently, the diameter of GastroFlex UHD probe is larger than the inner diameter of the over-tube; it cannot be accommodated in the over-tube. A slimmer probe or a larger over-tube will be used for further tests. The CDPR, such as *LaryngoTORS*, has shown promising to be used in pCLE of the larynx.

5.3 Robotics-assisted Hyperspectral Fibre-optic Sensing of the Larynx

In this section, a slim probe with two fibre cores was manufactured as a hyperspectral optic-fibre sensor. A hyperspectral optical fibre sensing system was created. The manufactured hyperspectral optical-fibre sensing probe was combined with *LaryngoTORS* robot. A

preliminary test was carried out on porcine tissue. The method and experimental result are presented below.

5.3.1 Materials and Method

Figure 5.8 shows the schematic diagram of the hyperspectral optical-fibre sensing system setup. The proximal ends of two fibres were connected to a spectrometer and a white light source. The distal ends were accommodated in a probe. The probe can be held and manipulated by *LaryngoTORS* robot. A laptop is used to read and record the detected reflectance spectra.

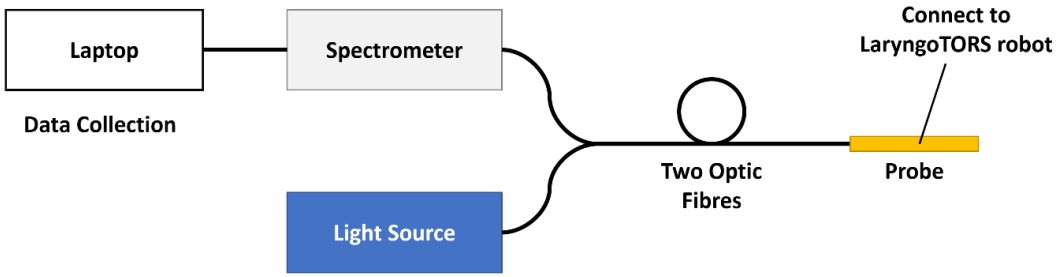


Figure 5.8: The schematic diagram of the setup of the hyperspectral optical-fibre sensing system. A two fibre cores probe is used to work with LaryngoTORS robot. One fibre is connected to a spectrometer and another fibre is connected to a white light source.

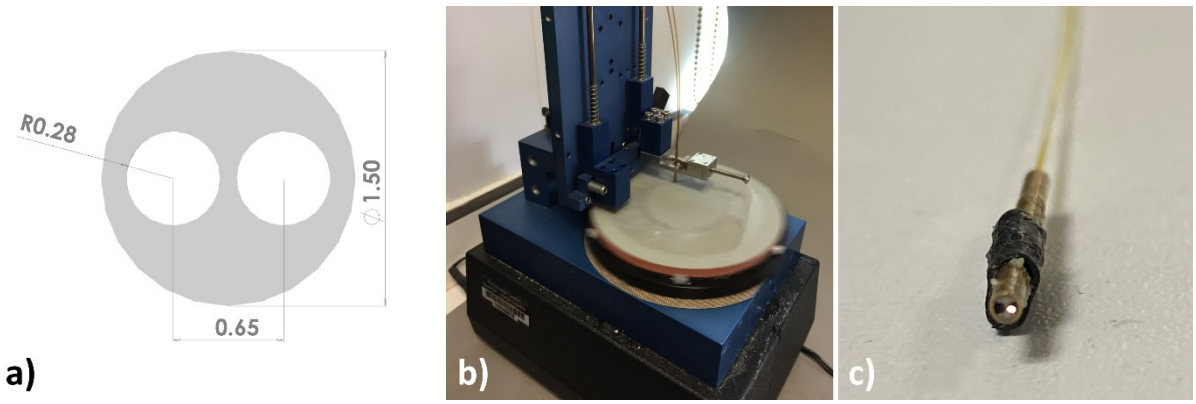


Figure 5.9: a) The dimensions of the cross-section of the probe, the unit of all parameters is in mm. b) The end face of the probe was polished by SpecPro Connector Polisher. c) The manufactured two cores fibre probe. The bright one was connected with the light source. The dark one was used to receive the reflection signals and transmitted to the spectrometer.

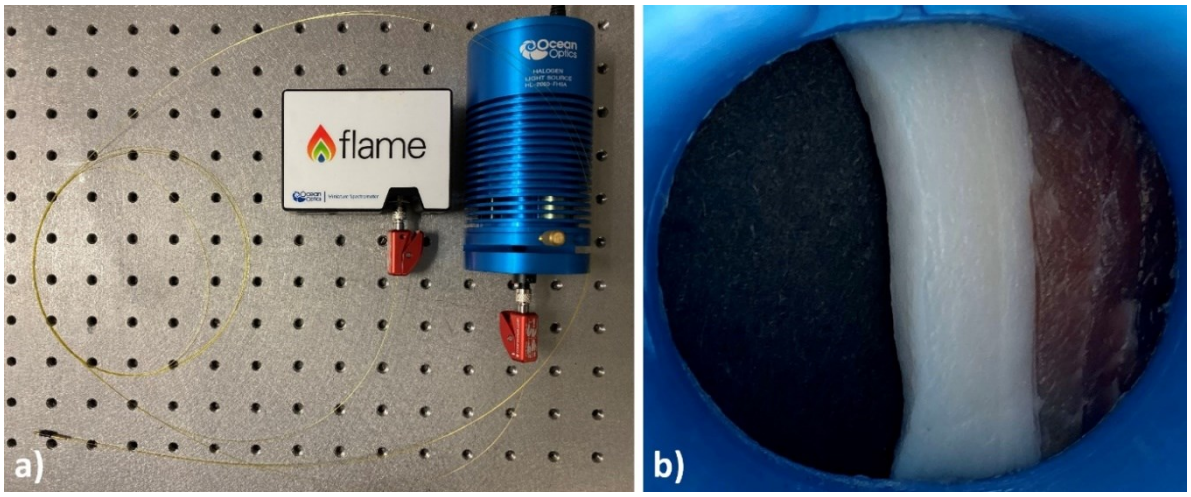


Figure 5.10: a) The experimental setup of the hyperspectral optical-fibre sensing system. Two fibre terminators with SMA 905 connectors were used to fix and connect two proximal ends to the spectrometer and the light source. b) A piece of clean porcine tissue, without any stained, was fixed on the target holder and mounted at the front of the robot.

The two cores fibre probe has 1.5 mm diameter with 25 mm length. Figure 5.9a shows the dimensions of the cross-section of the probe. For these experiments, two 2m length bare fibres (0.5 NA, wavelength range: 300-1200 nm, core diameter: 200 μm, outer diameter: 500 μm, FP200URT, Thorlabs Inc., USA) were used. One fibre was connected to a light source (HL-2000-FHSA, Ocean Optics, Inc., USA) and used to transmit the white light beam to the target tissue. Another fibre was used to receive the reflection from the tissue and delivered to the spectrometer (Flame UV-VIS Spectrometer, Ocean Optics, Inc., USA). The distal ends of two fibres were inserted and glued in the probe. The end face of the probe was polished by a fibre connector polisher with decreasing grit size from 30, 9, 3 to 0.3 μm (SpecPro Connector Polisher, Krell Technologies, Inc., USA) (Fig 5.9b and c). The proximal ends of two fibres were also polished and fixed in two fibre terminators with SMA 905 connectors (BFT1, Thorlabs Inc., USA) to connect to the spectrometer and the light source (Fig 5.10a).

Before the test, a calibration procedure was performed for noise offset and reflectance normalisation. The probe was faced to a 100% reflection mirror and a dark environment (the light source and all lights in the lab were turned off) individually. The captured results were counted as '100% reflection' and '0% reflection' respectively and inputted to the software (OceanView 1.6.7, Ocean Optics, Inc., USA). The test reflectance is calculated as below equation. The calculation will be performed by the software automatically.

$$\text{Test Reflectance} = \frac{\text{Test tissue reflection} - 0\% \text{ reflection}}{100\% \text{ reflection} - 0\% \text{ reflection}} \quad (5\text{-}1)$$

The experimental setup is the same as the setup of the pCLE experiment, as shown in Figure 5.3. The only difference is that the pCLE probe is now replaced by the manufactured hyperspectral sensing probe and a piece of unstained clean porcine tissue was used as the test target (Fig 5.10b). The porcine tissue was also placed at the right side of the holder to simulate the right-side vocal cord. The hyperspectral sensing probe was manipulated manually via the master controller. The probe was used to detect at 3 different sample points of the fat and muscle of the porcine tissue sample separately. The detected reflectance spectra results are shown in the next section.

5.3.2 Experimental Results

The hyperspectral sensing probe was steadily contacted with three distinct sample points of the fat and the muscle tissue individually. Due to the homogeneity of the fat and the muscle tissue of the small porcine tissue sample (Fig 5.10b), the results tested at three distinct sample points on the same tissue type were identical. Two representative reflectance spectra detected from the porcine fat and muscle tissue are presented in Figure 5.11 and 5.12, respectively. As demonstrated in the two results, the reflectance properties of the fat and muscle of the porcine tissue have significant differences. The reflectance spectra of the porcine fat tissue have a higher reflection in the 500 nm to 650 nm region, which is not present in the muscle tissue reflectance spectra. From the reflectance spectra results, the two tissue types, fat and muscle, can be distinguished easily.

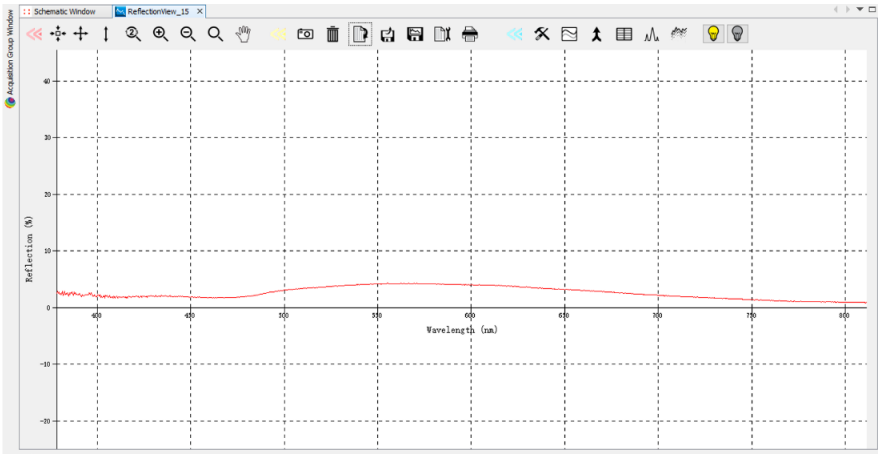


Figure 5.11: The acquired reflectance spectra of the porcine fat tissue. The reflectance is relatively high at the 500 nm to 650 nm region.

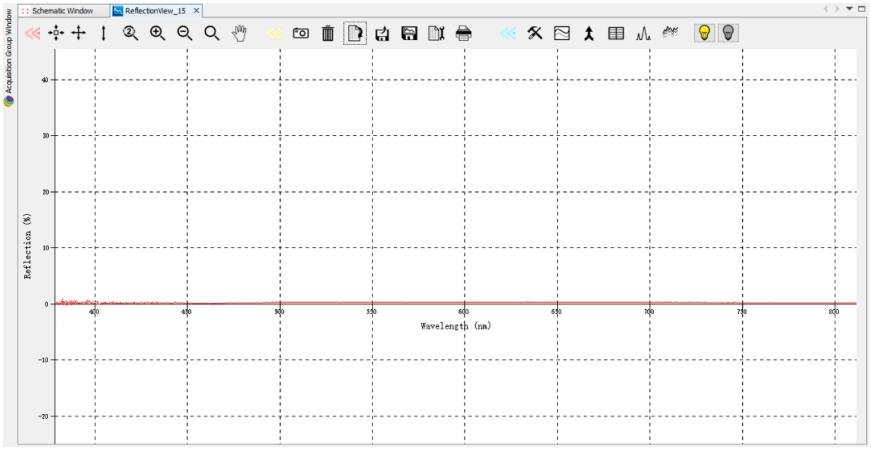


Figure 5.12: The captured reflectance spectra of the porcine muscle tissue. The reflectance curve is nearly flat, and reflectance is low in all range.

5.3.3 Discussion

The experimental results have demonstrated the detectability of the hyperspectral optic-fibre sensing probe via used *LaryngoTORS* robot. We observed that it is possible to control the probe effectively such that steady contact with the tissue is maintained. The reflectance spectra can be acquired from the test tissue directly. Unlike the pCLE, the contrast agent is not required. Thus, the adverse effects caused by the contrast agent can be avoided [185], [193], [209]. A 6-around-1 fibre bundle, using six fibres connecting to the light source and a single fibre connecting to the spectrometer [208], can be used to compare with the manufactured probe to further assess the detectability of the probe. With these preliminary results, *LaryngoTORS* assisted optical biopsy could be a valuable tool for examining the

tumour status of the larynx intraoperatively and in a timely manner. Whilst preliminary results are promising, the consistency of reflectance characteristics detected by the hyperspectral optic-fibre sensing probe and HSI samples need to be further evaluated for different tissue pathologies to evaluate the full potential of the proposed system.

5.4 Conclusion

Benefiting from the highly precise motion control, the *LaryngoTORS* robot has demonstrated the potential to be utilised to control the distal tip position of the pCLE or a hyperspectral sensing optic-fibre because the *LaryngoTORS* robot allows gentle and steady contact with the target tissue. Thus, high quality and informative confocal laser imaging or reflectance spectra could be captured. Furthermore, the *LaryngoTORS* robot can be expected to execute precise pCLE scanning and mosaic images can be reconstructed. A proper area scan function should be developed and evaluated in the future.

With a curved laryngeal blade and a built-in camera, the *LaryngoTORS* robot can image the larynx through a curved airway. The fibre-based optical biopsy methods use flexible fibre to acquire signals. The end tip of the fibre or probe can also reach the target tissue through the curved airway, which the straight suspension laryngoscope is not required. By avoiding the use of a straight suspension laryngoscope, it is less traumatic to the patient.

Therefore, *LaryngoTORS* robot demonstrates the potential to be an efficient robotic tool for the application of the fibre-based optical biopsy of the larynx. While the robot-assisted optical biopsy is demonstrated by integrating the *LaryngoTORS* robot, the results are not limited to just these two imaging systems. In future, it is possible to integrate other fibre-based methods such as diffuse or fluorescence spectroscopy and intraoperative OCT with *LaryngoTORS* robot. Due to the rapid real-time detection of fibre-based optical biopsy, the diagnosis can be executed during the TLP. A precision diagnosis could improve the accuracy of the targeting and save the non-target healthy tissue. The position of detected sample points or the generated pCLE scanning path could be used to define the control points and the scan path of the treatment laser. In addition, fibre-based optical biopsy is a non-invasive method. A significant benefit is that it will not generate any scar on the tested tissue, especially for the

vocal cord. The potential risk of voice change can be obviated, which is an essential requirement for a voice user such as a professional singer. The fibre-based optical biopsy of the larynx is a promising direction. A specific laryngeal blade of *LaryngoTORS* robot for the fibre-based optical biopsy of the larynx could be developed in the future.

Chapter 6

Conclusion and Future Work

6.1 Achievements of this Thesis

TLP is a common surgical application in otolaryngology, using a laser beam to perform vaporisation, incision, ablation, or photocoagulation on the soft tissues of the larynx. Research in transoral laser surgery in the larynx started at the early 1970s. Currently, medical lasers used in TLP are well developed. The outcomes of TLP increasingly depend on the laser delivery technique, and TLP has developed free beam and fibre delivery techniques. As presented in Chapter 2, both techniques have significant drawbacks: in the free beam delivery technique, due to the inherent limitation of the line-of-sight, the straight suspension laryngoscope can cause discomfort or damage, and the manipulability and ergonomics are poor. For fibre delivery, current robotic systems, both commercial and research-based, have not yet addressed a number of significant limitations related to laser scanning.

This study focused on the development of a novel CDPR for TLP to fulfil the fundamental requirements proposed in Chapter 2: (i) Avoid the use of a suspension laryngoscope by obviating the need for a line-of-sight. Provide a solution to access and exposure the larynx through a curved pathway. (ii) Provide precise, repeatable, healthy tissue sparing, user-driven

and semi-autonomous control of the laser. (iii) Provide a technically feasible and practicable solution.

Chapter 3 discussed the core principles and critical features of CDPMs. A framework of CDPM simulation for TLP was introduced. The required specification was identified, and a resulting simulation configuration was presented that could steer the fibre end tip in 5 DoF. Laser line and arc pattern scans were simulated, and the resulting configuration could generate a sufficient controllable workspace. The CDPM could be configured to align the workspace with the operative field. Also, the CDPM configuration could be decided and manufactured preoperatively based on patient-specific data and according to the required task.

Various designs and early prototypes of CDPMs for TLP were discussed in Chapter 3. The *LaryngoTORS* robot was inspired by the indirect video laryngoscope by attaching a CDPM to the end of a curved laryngeal blade. It could be inserted into the larynx like the ordinary indirect video laryngoscope. By using a curved laryngeal blade and a built-in camera, a straight suspension laryngoscope is not be required, there is less trauma to the patient, and the post-operative pain can be reduced.

This thesis focuses on the development and testing of the *LaryngoTORS* robot. Validation tests and feasibility analysis were presented in Chapter 4, and the core technique of motion control of the *LaryngoTORS* robot was introduced. An approach to semi-autonomous free path scanning was addressed and validated in bench and *ex vivo* tests, demonstrating high precision and repeatability of the semi-autonomous free path scan. When compared to other robotic systems for TLP, the *LaryngoTORS* robot provides advantages in the large workspace, high controllability, and technical feasibility, such as fibre compatibility and laser aperture quality control.

A second version of the *LaryngoTORS* robot was designed and developed considering feasibility factors, such as customisation, ventilation and smoke management, biocompatibility and sterilisation, electrical safety, fibre compatibility and device ergonomics. The robot system is ready for further preclinical trials, such as cadaver experiments. It is expected to fulfil the technical requirements for TLP.

Fibre-based optical biopsy techniques have proven their ability to detect disorders of the larynx. In Chapter 5, experiments using pCLE and hyperspectral fibre-optic sensing were performed by the *LaryngoTORS* robot. High quality and informative confocal laser imaging or reflectance spectra were captured. Furthermore, accurate pCLE scanning could be executed by the robot and mosaic images reconstructed. Due to the rapid real-time detection of fibre-based optical biopsy, the surgical margin could potentially be defined in TLP. The position of detected sample points or the generated pCLE scanning path could be used to determine the control points and the scan path of the treatment laser. A precision surgical margin can then save the non-target healthy tissue. The *LaryngoTORS* robot has demonstrated the potential to be an efficient robotic tool for the application of the fibre-based optical biopsy of the larynx.

6.2 Future Research Directions

Cadaver trial and usability study

A cadaver trial will be scheduled in the near future for further validation of the *LaryngoTORS* robot. As mentioned in Chapter 4, an updated version of *LaryngoTORS* robot has been manufactured. The technical feasibility of the robot, such as laser smoke management and fibre compatibility have been considered. As shown in Figures 4.23 and 4.24, two laryngeal blades, right-hand and left-hand side, were manufactured. The two laryngeal blades are each planned to be used for vocal cordectomy during the cadaver trial, on both sides of the vocal cords. The performance of the robot, such as the fibre tip manipulability and the semi-autonomous free path scan function will be evaluated. The optimal parameter settings for laser scanning, such as power density and speed, could also be studied. The current specifications, such as the shape and size of the robot, controllable workspace and the scan speed, can be examined. These specifications can be modified and adjusted based on the feedback of the cadaver trial.

The usability will be evaluated during the cadaver trial. Dedicated questionnaires and surveys can be utilised for qualitative analysis. The user experience of the robot, such as the path generation method and the ergonomics, can be assessed. These activities will aim to identify problems and the direction for further improving the robot for TLP.

Bimanual robotic system for TLP

The current *LaryngoTORS* robot only has one set of CDPM to steer the laser fibre tip, but it could be developed as a bimanual robotic system. An auxiliary surgical instrument such as grippers or forceps is needed to hold, stretch and retract the target tissue. If a second robotic arm was used to manipulate the auxiliary surgical instrument, then all the instruments could be teleoperated. As mentioned in chapter 3, a second CDPM could be built to control the auxiliary surgical instrument. As shown in Figure 6.1, a total of 12 motor units and cables can be assembled on the current L*aryngoTORS* robot. The second CDPM can be easily manufactured. However, the design of a miniature flexible/semi-flexible instrument, which will work with the second CDPM, still needs to be addressed. Another option is to use other mechanism types, such as articulating robotic microsurgical forceps [118], [166]. Comparison studies need to be performed for further assessment.

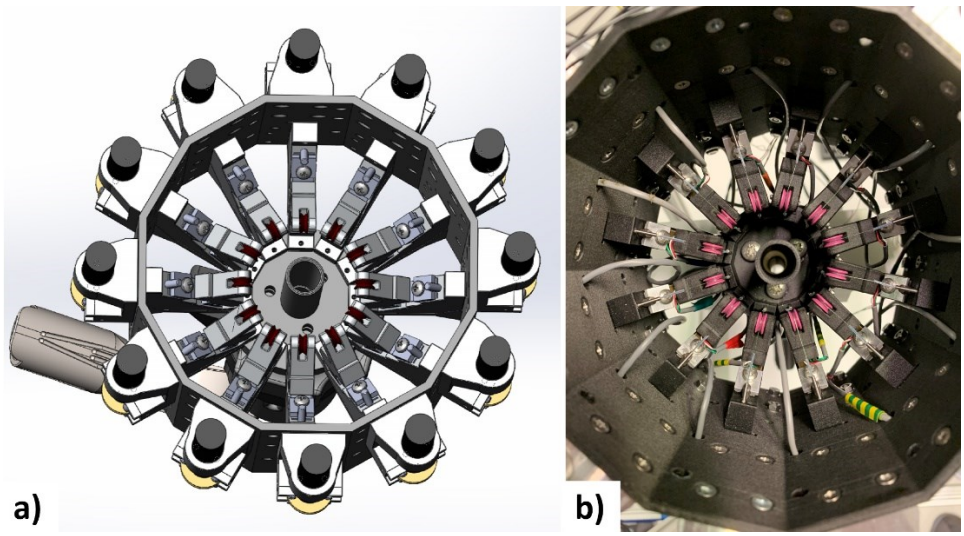


Figure 6.1: The top view of the design (a) and manufactured (b) LaryngoTORS robot.

Vision-based techniques for TLP

Contemporary computer vision techniques could be used for improving the performance of robotic-assisted TLP. One example is tissue surface reconstruction, which could be utilised for laser incision path planning [211]. Another example is vision-based motion tracking of the surgical instrument or the laser incision path, which is fundamental for visual servoing control [88], [204], [212]. Furthermore, vision-based tracking of soft tissue motion and the incision

path could reduce the effects of tissue motions or deformation when using the path scan function [213].

Tissue surface reconstruction can be achieved via a mono or stereo camera. In recent years, many learning-based algorithms have been able to extract shape or depth maps from a mono camera [214]–[216]. A preliminary study of learning-based photometric stereo via mono camera was performed to generate an estimated normal map to perceive the shape of a target surface. An illumination fibre was steered by the *LaryngoTORS* robot and multiple images of a test target under different light directions were captured by the camera of the *LaryngoTORS* robot. As shown in Figure 6.2, the captured images were utilised to generate the normal map via an uncalibrated photometric stereo fully convolutional network [217] (more details are presented in Appendix A).

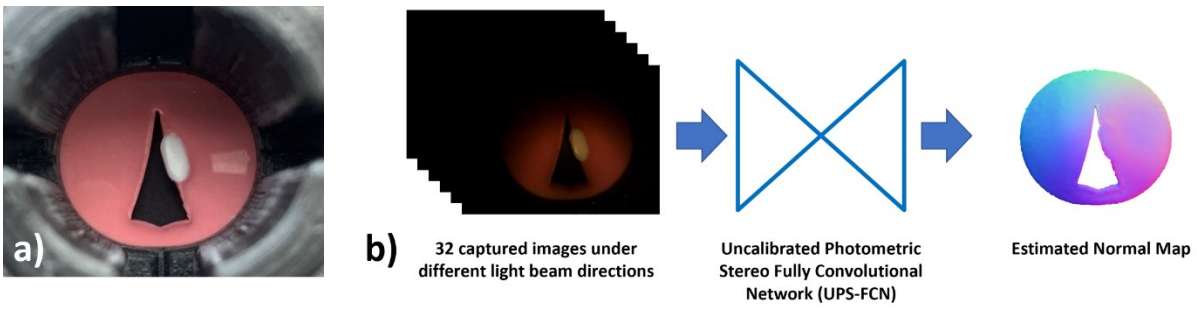


Figure 6.2: a) A test target made by silicone rubber was fixed on a target holder, which was attached to the front of the robot. b) The estimated normal map of the target surface via an uncalibrated photometric stereo fully convolutional network (UPS-FCN).

As shown in Figure 6.3, the camera of the *LaryngoTORS* robot can be replaced by a stereo camera. Stereo vision could be achieved by using two miniature cameras (2.5 mm diameter, 400x400 resolution, MD-V1001L-91, MISUMI ELECTRONICS CORP., Taiwan). Two commercial video rhino-laryngoscopes, such as the Olympus ENF-V3 or ENF-VH video rhino-laryngoscopes could be used for high quality stereo imaging. Stereo vision-based techniques for TLP can be combined with the *LaryngoTORS* robot and further evaluated in the future.

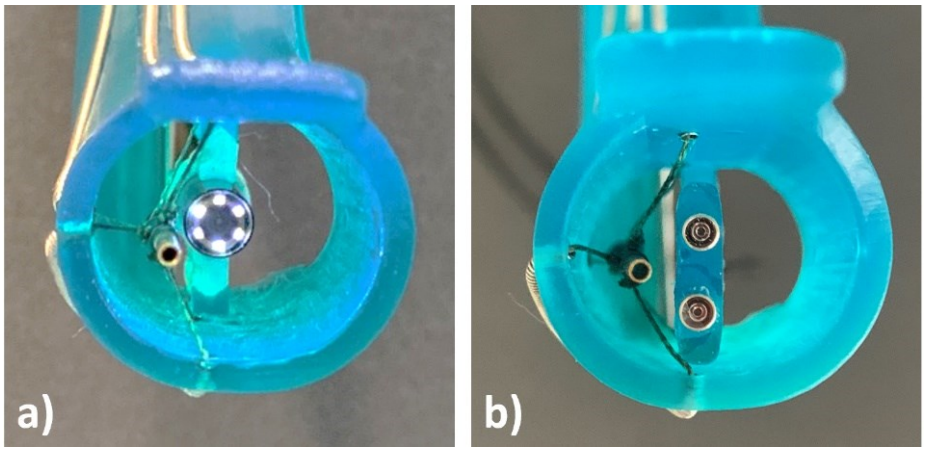


Figure 6.3: The laryngoTORS robot with a mono (a) and stereo (a) camera.

Fully autonomous laser task operation

Once the bimanual robotic system is built and the stereo vision is established, via advanced feature tracking techniques, the key features of the laser surgery tasks could be recorded, such as the motion of the end tip of the laser and the instrument, the pose and position of the forceps for grasping a target tissue, the deformation of the target tissue during laser ablation and the dynamic changes of the laser incision path during the surgery. Through collecting this data from well-trained practitioners and combining this with advanced learning-based techniques such as learning from demonstration [218], [219], the robot could learn to perform a laser task automatically on a target tissue pre-defined by a surgeon. This is the ultimate long-term goal of this study.

6.3 Conclusion

In this study, a novel CDPR for TLP, the *LaryngoTORS* robot, has been developed. High precision and high repeatability of the semi-autonomous free path scan can be achieved by the developed robotic system. The performance has been shown for various bench and *ex vivo* tests. The technical feasibility of the robot for TLP was also considered and evaluated. The *LaryngoTORS* robot has demonstrated promise for use in TLP. Patients, surgeons, and hospitals could benefit from this advanced TLP robotic system. The final goal of the robotic-assisted TLP is achieving full robotic autonomy in TLP. Then the surgical precision, efficiency and execution of the TLP could be further improved and enhanced. However, in medicine, the

ultimate goal is to prevent, eliminate or screen for disease at an earlier stage and to address the problem via pharmaceutical or advanced biotechniques such as cell and gene therapy. This will save the patients from suffering the pains of TLP. However, based on current medical developments surgery robotics will retain a major role in TLP for some time to come.

References

[1] N. Stewart, A. C. Lim, P. M. Lowe, and G. Goodman, “Lasers and laser-like devices: Part one,” *Australas. J. Dermatol.*, vol. 54, no. 3, pp. 173–183, 2013, doi: https://doi.org/10.1111/ajd.12034.

[2] D. V Palanker, M. S. Blumenkranz, and M. F. Marmor, “Fifty Years of Ophthalmic Laser Therapy,” *Arch. Ophthalmol.*, vol. 129, no. 12, pp. 1613–1619, 2011, doi: 10.1001/archophthalmol.2011.293.

[3] M. R. Adelman, L. J. Tsai, E. P. Tangchitnob, and B. S. Kahn, “Laser technology and applications in gynaecology,” *J. Obstet. Gynaecol. (Lahore).*, vol. 33, no. 3, pp. 225–231, 2013, doi: 10.3109/01443615.2012.747495.

[4] C. M. Chiesa-Estomba, J. A. González-García, E. Larruscain, C. Calvo-Henríquez, M. Mayo-Yáñez, and J. A. Sistiaga-Suarez, “CO2 Transoral Laser Microsurgery in Benign, Premalignant and Malignant (Tis, T1, T2) Lesion of the Glottis. A Literature Review,” *Medicines*, vol. 6, no. 3, 2019, doi: 10.3390/medicines6030077.

[5] A. S. Neubauer and M. W. Ulbig, “Laser Treatment in Diabetic Retinopathy,” *Ophthalmologica*, vol. 221, no. 2, pp. 95–102, 2007, doi: 10.1159/000098254.

[6] A. Nonaka *et al.*, “Cataract Surgery for Residual Angle Closure after Peripheral Laser Iridotomy,” *Ophthalmology*, vol. 112, no. 6, pp. 974–979, 2005, doi: https://doi.org/10.1016/j.ophtha.2004.12.042.

[7] At. Jain *et al.*, “Effect of Pulse Duration on Size and Character of the Lesion in Retinal Photocoagulation,” *Arch. Ophthalmol.*, vol. 126, no. 1, pp. 78–85, 2008, doi: 10.1001/archophthalmol.2007.29.

[8] H. K. Soong and J. B. Malta, “Femtosecond Lasers in Ophthalmology,” *Am. J. Ophthalmol.*, vol. 147, no. 2, pp. 189-197.e2, 2009, doi: https://doi.org/10.1016/j.ajo.2008.08.026.

[9] J. R. Samples *et al.*, “Laser Trabeculoplasty for Open-Angle Glaucoma: A Report by the American Academy of Ophthalmology,” *Ophthalmology*, vol. 118, no. 11, pp. 2296–2302, 2011, doi: https://doi.org/10.1016/j.ophtha.2011.04.037.

[10] J. M. Krauss and C. A. Puliafito, “Lasers in ophthalmology,” *Lasers Surg. Med.*, vol. 17, no. 2, pp. 102–159, 1995, doi: https://doi.org/10.1002/lsm.1900170203.

[11] S. Watanabe, “Basics of laser application to dermatology,” *Arch. Dermatol. Res.*, vol. 300, no. 1, pp. 21–30, 2008, doi: 10.1007/s00403-007-0801-6.

[12] T. Y. Loh, C. H. Cotton, J. B. Vasic, and G. N. Goldberg, “Current Practices in Pediatric Dermatology Laser Therapy: An International Survey,” *Lasers Surg. Med.*, vol. n/a, no. n/a, doi: https://doi.org/10.1002/lsm.23327.

[13] S. Mehraban and A. Feily, “308nm excimer laser in dermatology,” *J. lasers Med. Sci.*, vol. 5, no. 1, pp. 8–12, 2014.

[14] M. Boord, “Laser in Dermatology,” *Clin. Tech. Small Anim. Pract.*, vol. 21, no. 3, pp. 145–149, 2006, doi:

https://doi.org/10.1053/j.ctsap.2006.05.007.

[15] D. C. Wu, M. P. Goldman, H. Wat, and H. H. L. Chan, “A Systematic Review of Picosecond Laser in Dermatology: Evidence and Recommendations,” *Lasers Surg. Med.*, vol. 53, no. 1, pp. 9–49, 2021, doi: https://doi.org/10.1002/lsm.23244.

[16] N. M. Fried, “Thulium fiber laser lithotripsy: An in vitro analysis of stone fragmentation using a modulated 110-watt Thulium fiber laser at 1.94 μm,” *Lasers Surg. Med.*, vol. 37, no. 1, pp. 53–58, 2005, doi: https://doi.org/10.1002/lsm.20196.

[17] S. Pierre and G. M. Preminger, “Holmium laser for stone management,” *World J. Urol.*, vol. 25, no. 3, pp. 235–239, 2007, doi: 10.1007/s00345-007-0162-y.

[18] S. L. Hecht and J. S. Wolf, “Techniques for Holmium Laser Lithotripsy of Intrarenal Calculi,” *Urology*, vol. 81, no. 2, pp. 442–445, 2013, doi: https://doi.org/10.1016/j.urology.2012.11.021.

[19] N. M. Fried, “Therapeutic applications of lasers in urology: an update,” *Expert Rev. Med. Devices*, vol. 3, no. 1, pp. 81–94, 2006, doi: 10.1586/17434440.3.1.81.

[20] A. Zarrabi and A. J. Gross, “The evolution of lasers in urology,” *Ther. Adv. Urol.*, vol. 3, no. 2, pp. 81–89, 2011, doi: 10.1177/1756287211400494.

[21] A. J. Marks and J. M. H. Teichman, “Lasers in clinical urology: state of the art and new horizons,” *World J. Urol.*, vol. 25, no. 3, pp. 227–233, 2007, doi: 10.1007/s00345-007-0163-x.

[22] P. Kronenberg and O. Traxer, “Update on lasers in urology 2014: current assessment on holmium:yttrium–aluminum–garnet (Ho:YAG) laser lithotripter settings and laser fibers,” *World J. Urol.*, vol. 33, no. 4, pp. 463–469, 2015, doi: 10.1007/s00345-014-1395-1.

[23] H. Sago, K. Ishii, R. Sugibayashi, K. Ozawa, M. Sumie, and S. Wada, “Fetoscopic laser photocoagulation for twin–twin transfusion syndrome,” *J. Obstet. Gynaecol. Res.*, vol. 44, no. 5, pp. 831–839, 2018, doi: https://doi.org/10.1111/jog.13600.

[24] M. Nakata, M. Sumie, S. Murata, I. Miwa, M. Matsubara, and N. Sugino, “Fetoscopic laser photocoagulation of placental communicating vessels for twin-reversed arterial perfusion sequence,” *J. Obstet. Gynaecol. Res.*, vol. 34, no. 4pt2, pp. 649–652, 2008, doi: https://doi.org/10.1111/j.1447-0756.2008.00901.x.

[25] C. Phillips, T. Hillard, S. Salvatore, P. Toozs-Hobson, and L. Cardozo, “Lasers in gynaecology,” *Eur. J. Obstet. Gynecol. Reprod. Biol.*, vol. 251, pp. 146–155, 2020, doi: https://doi.org/10.1016/j.ejogrb.2020.03.034.

[26] T.-H. Kim, H.-J. Oh, C.-S. Choi, D.-H. Yeom, and S.-C. Choi, “Clinical usefulness of transpapillary removal of common bile duct stones by frequency doubled double pulse Nd:YAG laser,” *World J. Gastroenterol.*, vol. 14, no. 18, pp. 2863–2866, May 2008, doi: 10.3748/wjg.14.2863.

[27] T. Ogura and K. Higuchi, “A review of treatment options for bile duct stones,” *Expert Rev. Gastroenterol. & Hepatol.*, vol. 10, no. 11, pp. 1271–1278, 2016, doi: 10.1080/17474124.2016.1212658.

[28] N. S. Nishioka, “Applications of lasers in gastroenterology,” *Lasers Surg. Med.*, vol. 16, no. 3, pp. 205–214, 1995, doi: https://doi.org/10.1002/lsm.1900160302.

[29] A. Maydeo, B. E. A. Kwek, S. Bhandari, M. Bapat, and V. Dhir, “Single-operator cholangioscopy-guided laser lithotripsy in patients with difficult biliary and pancreatic ductal stones (with videos),” *Gastrointest. Endosc.*, vol. 74, no. 6, pp. 1308–1314, 2011, doi: https://doi.org/10.1016/j.gie.2011.08.047.

[30] M. F. Karasu *et al.*, “Comparison of Effects on Voice of Diode Laser and Cold Knife Microlaryngology Techniques for Vocal Fold Polyps,” *J. Voice*, vol. 28, no. 3, pp. 387–392, 2014, doi: https://doi.org/10.1016/j.jvoice.2013.10.017.

[31] M. L. Hinni *et al.*, “Transoral Laser Microsurgery for Advanced Laryngeal Cancer,” *Arch. Otolaryngol. Neck Surg.*, vol. 133, no. 12, pp. 1198–1204, 2007, doi: 10.1001/archotol.133.12.1198.

[32] K. M. Van Abel *et al.*, “Transoral Robotic Surgery Using the Thulium:YAG Laser: A Prospective Study,” *Arch. Otolaryngol. Neck Surg.*, vol. 138, no. 2, pp. 158–166, Feb. 2012, doi: 10.1001/archoto.2011.1199.

[33] N. N. Mohamed, S. S. Sorour, M. W. El-Anwar, A. S. Quriba, and M. A. Mahdy, “Comparison Between Laser- and Diathermy-Assisted Posterior Cordotomy for Bilateral Vocal Cord Abductor Paralysis,” *JAMA Otolaryngol. Neck Surg.*, vol. 139, no. 9, pp. 923–930, Sep. 2013, doi: 10.1001/jamaoto.2013.3554.

[34] A. Tahir, “The Evolution of Laser in Laryngology,” *Int. J. Otolaryngol. Head Neck Surg.*, vol. 04, no. 02, pp. 137–140, Feb. 2015, doi: 10.4236/ijohns.2015.42024.

[35] K. Durmus, C. Kucur, I. O. Uysal, P. T. Dziegielewski, and E. Ozer, “Feasibility and Clinical Outcomes of Transoral Robotic Surgery and Transoral Robot-Assisted Carbon Dioxide Laser for Hypopharyngeal Carcinoma,” *J. Craniofac. Surg.*, vol. 26, no. 1, 2015.

[36] C. Samara, C. B. Rohde, C. L. Gilleland, S. Norton, S. J. Haggarty, and M. F. Yanik, “Large-scale in vivo femtosecond laser neurosurgery screen reveals small-molecule enhancer of regeneration,” *Proc. Natl. Acad. Sci.*, vol. 107, no. 43, pp. 18342 LP – 18347, Oct. 2010, doi: 10.1073/pnas.1005372107.

[37] C. Lagman *et al.*, “Laser neurosurgery: A systematic analysis of magnetic resonance-guided laser interstitial thermal therapies,” *J. Clin. Neurosci.*, vol. 36, pp. 20–26, 2017, doi: https://doi.org/10.1016/j.jocn.2016.10.019.

[38] R. W. Ryan, T. Wolf, R. F. Spetzler, S. W. Coons, Y. Fink, and M. C. Preul, “Application of a flexible CO2 laser fiber for neurosurgery: laser-tissue interactions,” *J. Neurosurg. JNS*, vol. 112, no. 2, pp. 434–443, doi: 10.3171/2009.7.JNS09356.

[39] E. Khalkhal, M. Rezaei-Tavirani, M. R. Zali, and Z. Akbari, “The Evaluation of Laser Application in Surgery: A Review Article,” *J. lasers Med. Sci.*, vol. 10, no. Suppl 1, pp. S104–S111, 2019, doi: 10.15171/jlms.2019.S18.

[40] B. Azadgoli and R. Y. Baker, “Laser applications in surgery,” *Ann. Transl. Med.*, vol. 4, no. 23, p. 452, Dec. 2016, doi: 10.21037/atm.2016.11.51.

[41] E. F. Bernstein, K. T. Schomacker, L. D. Basilavecchio, J. M. Plugis, and J. D. Bhawalkar, “A novel dual-wavelength, Nd:YAG, picosecond-domain laser safely and effectively removes multicolor tattoos,” *Lasers Surg. Med.*, vol. 47, no. 7, pp. 542–548, 2015, doi: https://doi.org/10.1002/lsm.22391.

[42] L. A. Cowan, K. T. Khine, V. Chopra, D. T. Fazio, and B. A. Francis, “Refractory Open-Angle Glaucoma After Neodymium–Yttrium-Aluminum-Garnet Laser Lysis of Vitreous Floaters,” *Am. J. Ophthalmol.*, vol. 159, no. 1, pp. 138–143, 2015, doi: https://doi.org/10.1016/j.ajo.2014.10.006.

[43] K. Ozyurt, E. Colgecen, H. Baykan, P. Ozturk, and M. Ozkose, “Treatment of Superficial Cutaneous Vascular Lesions: Experience with the Long-Pulsed 1064 nm Nd:YAG Laser,” *Sci. World J.*, vol. 2012, p. 197139, 2012, doi: 10.1100/2012/197139.

[44] J. A. Parrish, R. R. Anderson, T. Harrist, B. Paul, and G. F. Murphy, “Selective thermal effects with pulsed irradiation from lasers: From organ to organelle,” *J. Invest. Dermatol.*, vol. 80, no. Suppl., pp. 75–80, 1983, doi: 10.1111/1523-1747.ep12537266.

[45] L. Carroll and T. R. Humphreys, “LASER-tissue interactions,” *Clin. Dermatol.*, vol. 24, no. 1, pp. 2–7, 2006, doi: https://doi.org/10.1016/j.clindermatol.2005.10.019.

[46] S. Marcos, S. Barbero, L. Llorente, and J. Merayo-Lloves, “Optical Response to LASIK Surgery for Myopia from Total and Corneal Aberration Measurements,” *Invest. Ophthalmol. Vis. Sci.*, vol. 42, no. 13, pp. 3349–3356, 2001.

[47] K. D. Solomon *et al.*, “LASIK World Literature Review: Quality of Life and Patient Satisfaction,” *Ophthalmology*, vol. 116, no. 4, pp. 691–701, 2009, doi: https://doi.org/10.1016/j.ophtha.2008.12.037.

[48] R. Weijer *et al.*, “Low-power photodynamic therapy induces survival signaling in perihilar cholangiocarcinoma cells,” *BMC Cancer*, vol. 15, no. 1, p. 1014, 2015, doi: 10.1186/s12885-015-1994-2.

[49] T. Kobayashi, N. Seki, Y. H. Song, and T. Dejima, “GreenLight HPS laser 120 W vs diode laser 300 W vaporization of the prostate for the treatment of benign prostatic hyperplasia in Japanese patients: A prospective, single-center, randomized clinical trial,” *LUTS Low. Urin. Tract Symptoms*, vol. 13, no. 1, pp. 31–37, 2021, doi: https://doi.org/10.1111/luts.12324.

[50] R. M. Verdaasdonk and C. F. P. van Swol, “Laser light delivery systems for medical applications,” *Phys. Med. Biol.*, vol. 42, no. 5, pp. 869–894, May 1997, doi: 10.1088/0031-9155/42/5/010.

[51] V. Cennamo *et al.*, “Cholangioscopy using a new type of cholangioscope for the diagnosis of biliary tract disease: A case series,” *Endoscopy*, vol. 44, no. 9, pp. 878–881, Sep. 2012, doi: 10.1055/s-0032-1310016.

[52] H. Neuhaus *et al.*, “Randomized study of intracorporeal laser lithotripsy versus extracorporeal shock-wave lithotripsy for difficult bile duct stones,” *Gastrointest. Endosc.*, vol. 47, no. 5, pp. 327–334, 1998, doi: https://doi.org/10.1016/S0016-5107(98)70214-7.

[53] J. I. Martínez-Salamanca, C. Martínez Ballesteros, A. Tewari, and J. A. Carballido, “Robotic surgery and laser technology: An opportunity for discovery,” *Arch. Españoles Urol.*, vol. 61, no. 9, pp. 1157–1162, 2008.

[54] M. Remacle, F. Hassan, D. Cohen, G. Lawson, and M. Delos, “New computer-guided scanner for improving CO2 laser-assisted microincision,” *Eur. Arch. Oto-Rhino-Laryngology Head Neck*, vol. 262, no. 2, pp. 113–119, 2005, doi: 10.1007/s00405-004-0746-8.

[55] D. Cohen, G. Siegel, J. Krespi, Y. Schechter, and M. Slatkine, “Middle Ear Laser Office Ventilation (LOV) with a CO2 Laser Flashscanner,” *J. Clin. Laser Med. Surg.*, vol. 16, no. 2, pp. 107–109, 1998, doi: 10.1089/clm.1998.16.107.

[56] M. Lapidoth, M. E. Yagima Odo, and L. M. Odo, “Novel Use of Erbium:YAG (2,940-nm) Laser for Fractional Ablative Photothermolysis in the Treatment of Photodamaged Facial Skin: A Pilot Study,” *Dermatologic Surg.*, vol. 34, no. 8, pp. 1048–1053, 2008, doi: https://doi.org/10.1111/j.1524-

4725.2008.34204.x.

[57] W.-R. Lee, S.-C. Shen, M.-H. Pai, H.-H. Yang, C.-Y. Yuan, and J.-Y. Fang, “Fractional laser as a tool to enhance the skin permeation of 5-aminolevulinic acid with minimal skin disruption: A comparison with conventional erbium:YAG laser,” *J. Control. Release*, vol. 145, no. 2, pp. 124–133, 2010, doi: https://doi.org/10.1016/j.jconrel.2010.03.017.

[58] M. T. Clementoni, P. Gilardino, G. F. Muti, D. Beretta, and R. Schianchi, “Non-sequential fractional ultrapulsed CO2 resurfacing of photoaged facial skin: Preliminary clinical report,” *J. Cosmet. Laser Ther.*, vol. 9, no. 4, pp. 218–225, 2007, doi: 10.1080/14764170701632901.

[59] J. H.-J. Lock and K. C. S. Fong, “An update on retinal laser therapy,” *Clin. Exp. Optom.*, vol. 94, no. 1, pp. 43–51, 2011, doi: https://doi.org/10.1111/j.1444-0938.2010.00529.x.

[60] K. Y. Lin and S. Y. Lu, “Panretinal navigated laser photocoagulation for PDR,” *Retin. Today*, vol. JAN/FEB, pp. 65–70, 2014.

[61] L. He, K. Sheehy, and W. Culbertson, “Femtosecond laser-assisted cataract surgery,” *Curr. Opin. Ophthalmol.*, vol. 22, no. 1, 2011.

[62] S. G. Farah, D. T. Azar, C. Gurdal, and J. Wong, “Laser in situ keratomileusis: Literature review of a developing technique,” *J. Cataract Refract. Surg.*, vol. 24, no. 7, pp. 989–1006, 1998, doi: https://doi.org/10.1016/S0886-3350(98)80056-4.

[63] P. Padmanabhan, M. Mrochen, S. Basuthkar, D. Viswanathan, and R. Joseph, “Wavefront-guided versus wavefront-optimized laser in situ keratomileusis: Contralateral comparative study,” *J. Cataract Refract. Surg.*, vol. 34, no. 3, pp. 389–397, 2008, doi: https://doi.org/10.1016/j.jcrs.2007.10.028.

[64] M. Moshirfar, T. J. Shah, D. F. Skanchy, S. H. Linn, P. Kang, and D. S. Durrie, “Comparison and analysis of FDA reported visual outcomes of the three latest platforms for LASIK: wavefront guided Visx iDesign, topography guided WaveLight Allegro Contoura, and topography guided Nidek EC-5000 CATz,” *Clin. Ophthalmol.*, vol. 11, pp. 135–147, Jan. 2017, doi: 10.2147/OPTH.S115270.

[65] D. Z. Reinstein, T. J. Archer, and M. Gobbe, “Small incision lenticule extraction (SMILE) history, fundamentals of a new refractive surgery technique and clinical outcomes,” *Eye Vis.*, vol. 1, no. 1, p. 3, 2014, doi: 10.1186/s40662-014-0003-1.

[66] D. V Palanker *et al.*, “Femtosecond Laser–Assisted Cataract Surgery with Integrated Optical Coherence Tomography,” *Sci. Transl. Med.*, vol. 2, no. 58, pp. 58ra85 LP-58ra85, Nov. 2010, doi: 10.1126/scitranslmed.3001305.

[67] T. V Roberts *et al.*, “Femtosecond laser cataract surgery: technology and clinical practice,” *Clin. Experiment. Ophthalmol.*, vol. 41, no. 2, pp. 180–186, Mar. 2013, doi: https://doi.org/10.1111/j.1442-9071.2012.02851.x.

[68] S. Y. P. Ewe *et al.*, “A Comparative Cohort Study of Visual Outcomes in Femtosecond Laser-Assisted versus Phacoemulsification Cataract Surgery,” *Ophthalmology*, vol. 123, no. 1, pp. 178–182, 2016, doi: https://doi.org/10.1016/j.ophtha.2015.09.026.

[69] S. J. Bali, C. Hodge, M. Lawless, T. V Roberts, and G. Sutton, “Early Experience with the Femtosecond Laser for Cataract Surgery,” *Ophthalmology*, vol. 119, no. 5, pp. 891–899, 2012, doi:

https://doi.org/10.1016/j.ophtha.2011.12.025.

[70] A. S. Neubauer *et al.*, “Navigated macular laser decreases retreatment rate for diabetic macular edema: a comparison with conventional macular laser,” *Clin. Ophthalmol.*, vol. 7, pp. 121–128, 2013, doi: 10.2147/OPTH.S38559.

[71] T. Somoskeoy and P. Shah, “Safety and efficacy of the use of navigated retinal laser as a method of laser retinopexy in the treatment of symptomatic retinal tears,” *Eye*, vol. 35, no. 4, pp. 1256–1260, 2021, doi: 10.1038/s41433-020-1050-6.

[72] D. S. Finley *et al.*, “Effect of Holmium:YAG Laser Pulse Width on Lithotripsy Retropulsion in Vitro,” *J. Endourol.*, vol. 19, no. 8, pp. 1041–1044, Oct. 2005, doi: 10.1089/end.2005.19.1041.

[73] Y.-S. Kwon, K. Tae, and B.-J. Yi, “Suspension laryngoscopy using a curved-frame trans-oral robotic system,” *Int. J. Comput. Assist. Radiol. Surg.*, vol. 9, no. 4, pp. 535–540, 2014, doi: 10.1007/s11548-013-0944-1.

[74] P. P. Rao, “Robotic surgery: new robots and finally some real competition!,” *World J. Urol.*, vol. 36, no. 4, pp. 537–541, 2018, doi: 10.1007/s00345-018-2213-y.

[75] A. Hussain, A. Malik, M. U. Halim, and A. M. Ali, “The use of robotics in surgery: a review,” *Int. J. Clin. Pract.*, vol. 68, no. 11, pp. 1376–1382, 2014, doi: https://doi.org/10.1111/ijcp.12492.

[76] M. Diana and J. Marescaux, “Robotic surgery,” *Br. J. Surg.*, vol. 102, no. 2, pp. e15–e28, 2015, doi: 10.1002/bjs.9711.

[77] “Q2 2020 Intuitive Investor Presentation,” *Intuitive Surgical Inc.*, [Online]. Available: http://isrg.gcs-web.com/static-files/7b0470fb-cfd2-456a-b6eb-24af76d68f6d. [Accessed: 31-Mar-2020].

[78] J. L. Lee, H. A. Alsaleem, and J. C. Kim, “Robotic surgery for colorectal disease: review of current port placement and future perspectives,” *Ann. Surg. Treat. Res.*, vol. 98, no. 1, pp. 31–43, Jan. 2020, doi: 10.4174/astr.2020.98.1.31.

[79] R. K. Orosco, A. Arora, J. P. Jeannon, and F. C. Holsinger, “Next-Generation Robotic Head and Neck Surgery,” *ORL*, vol. 80, no. 3–4, pp. 213–219, 2018, doi: 10.1159/000490599.

[80] W. Kneist, H. Stein, and M. Rheinwald, “Da Vinci Single-Port robot-assisted transanal mesorectal excision: a promising preclinical experience,” *Surg. Endosc.*, vol. 34, no. 7, pp. 3232–3235, Jul. 2020, doi: 10.1007/s00464-020-07444-4.

[81] K. M. Van Abel, L. X. Yin, D. L. Price, J. R. Janus, J. L. Kasperbauer, and E. J. Moore, “One-year outcomes for da Vinci single port robot for transoral robotic surgery,” *Head Neck*, vol. 42, no. 8, pp. 2077–2087, 2020, doi: https://doi.org/10.1002/hed.26143.

[82] M. M. Chen, R. K. Orosco, G. C. Lim, and F. C. Holsinger, “Improved transoral dissection of the tongue base with a next-generation robotic surgical system,” *Laryngoscope*, vol. 128, no. 1, pp. 78–83, 2018, doi: https://doi.org/10.1002/lary.26649.

[83] S. E. Barton and A. R. Gargiulo, “Robot-assisted laparoscopic myomectomy and adenomyomectomy with a flexible CO2 laser device,” *J. Robot. Surg.*, vol. 7, no. 2, pp. 157–162, 2013, doi: 10.1007/s11701-012-0360-5.

[84] M. Remacle, N. Matar, G. Lawson, V. Bachy, M. Delos, and M.-C. Nollevaux, “Combining a new CO2 laser wave guide with transoral robotic surgery: a feasibility study on four patients with malignant tumors,” *Eur. Arch. Oto-Rhino-Laryngology*, vol. 269, no. 7, pp. 1833–1837, 2012, doi: 10.1007/s00405-011-1838-x.

[85] S. C. Desai, C.-K. Sung, D. W. Jang, and E. M. Genden, “Transoral Robotic Surgery Using a Carbon Dioxide Flexible Laser for Tumors of the Upper Aerodigestive Tract,” *Laryngoscope*, vol. 118, no. 12, pp. 2187–2189, 2008, doi: https://doi.org/10.1097/MLG.0b013e31818379e4.

[86] R. V Smith, “Transoral Robotic Surgery for Larynx Cancer,” *Otolaryngol. Clin. North Am.*, vol. 47, no. 3, pp. 379–395, 2014, doi: https://doi.org/10.1016/j.otc.2014.03.003.

[87] R. J. Hendrick, C. R. Mitchell, S. D. Herrell, and I. I. I. Robert J. Webster, “Hand-held transendoscopic robotic manipulators: A transurethral laser prostate surgery case study,” *Int. J. Rob. Res.*, vol. 34, no. 13, pp. 1559–1572, 2015, doi: 10.1177/0278364915585397.

[88] S. Yang, R. A. MacLachlan, and C. N. Riviere, “Toward automated intraocular laser surgery using a handheld micromanipulator,” in *2014 IEEE/RSJ International Conference on Intelligent Robots and Systems*, 2014, pp. 1302–1307, doi: 10.1109/IROS.2014.6942725.

[89] M. Yip and N. Das, “Robot autonomy for surgery,” in *The Encyclopedia of Medical Robotics*, pp. 281–313.

[90] A. Brodie and N. Vasdev, “The future of robotic surgery,” *Ann. R. Coll. Surg. Engl.*, vol. 100, no. Supplement 7, pp. 4–13, 2018, doi: 10.1308/rcsann.supp2.4.

[91] H. Ashrafian, O. Clancy, V. Grover, and A. Darzi, “The evolution of robotic surgery: surgical and anaesthetic aspects,” *BJA Br. J. Anaesth.*, vol. 119, no. suppl_1, pp. i72–i84, 2017, doi: 10.1093/bja/aex383.

[92] T. Haidegger, “Autonomy for Surgical Robots: Concepts and Paradigms,” *IEEE Trans. Med. Robot. Bionics*, vol. 1, no. 2, pp. 65–76, May 2019, doi: 10.1109/TMRB.2019.2913282.

[93] S. Panesar, Y. Cagle, D. Chander, J. Morey, J. Fernandez-Miranda, and M. Kliot, “Artificial Intelligence and the Future of Surgical Robotics,” *Ann. Surg.*, vol. 270, no. 2, 2019.

[94] H. D. Taghirad, *Parallel Robots: Mechanics and Control*. CRC Press, 2013.

[95] T. J. C. O. Vrielink, M. Zhao, A. Darzi, and G. P. Mylonas, “ESD CYCLOPS: A New Robotic Surgical System for GI Surgery,” in *2018 IEEE International Conference on Robotics and Automation (ICRA)*, May 2018, pp. 150–157, doi: 10.1109/ICRA.2018.8462698.

[96] M. Runciman, J. Avery, M. Zhao, A. Darzi, and G. P. Mylonas, “Deployable, Variable Stiffness, Cable Driven Robot for Minimally Invasive Surgery,” *Front. Robot. AI*, vol. 6, p. 141, 2020, doi: 10.3389/frobt.2019.00141.

[97] G. P. Mylonas, V. Vitiello, T. P. Cundy, A. Darzi, and G. Yang, “CYCLOPS: A versatile robotic tool for bimanual single-access and natural-orifice endoscopic surgery,” in *2014 IEEE International Conference on Robotics and Automation (ICRA)*, May 2014, pp. 2436–2442, doi: 10.1109/ICRA.2014.6907198.

[98] K. Miyashita, T. Oude Vrielink, and G. Mylonas, “A cable-driven parallel manipulator with force sensing

capabilities for high-accuracy tissue endomicroscopy," *Int. J. Comput. Assist. Radiol. Surg.*, vol. 13, no. 5, pp. 659–669, 2018, doi: 10.1007/s11548-018-1717-7.

[99] T. J. C. O. Vrielink, "Cable-driven parallel mechanisms for minimally invasive robotic surgery," Imperial College London, 2019.

[100] V. Vitiello, S. Lee, T. P. Cundy, and G. Yang, "Emerging Robotic Platforms for Minimally Invasive Surgery," *IEEE Rev. Biomed. Eng.*, vol. 6, pp. 111–126, 2013, doi: 10.1109/RBME.2012.2236311.

[101] M. Mandapathil, B. Greene, and T. Wilhelm, "Transoral surgery using a novel single-port flexible endoscope system," *Eur. Arch. Oto-Rhino-Laryngology*, vol. 272, no. 9, pp. 2451–2456, 2015, doi: 10.1007/s00405-014-3177-1.

[102] A. H. Mendelsohn, M. Remacle, S. Van Der Vorst, V. Bachy, and G. Lawson, "Outcomes following transoral robotic surgery: Supraglottic laryngectomy," *Laryngoscope*, vol. 123, no. 1, pp. 208–214, 2013, doi: https://doi.org/10.1002/lary.23621.

[103] P. Hasskamp, S. Lang, L. Holtmann, B. A. Stuck, and S. Mattheis, "First use of a new retractor in transoral robotic surgery (TORS)," *Eur. Arch. Oto-Rhino-Laryngology*, vol. 273, no. 7, pp. 1913–1917, 2016, doi: 10.1007/s00405-015-3719-1.

[104] N. Sethi *et al.*, "Transoral robotic surgery using the Medrobotic Flex® system: the Adelaide experience," *J. Robot. Surg.*, vol. 14, no. 1, pp. 109–113, 2020, doi: 10.1007/s11701-019-00941-2.

[105] C.-A. O. Nathan *et al.*, "Confocal Laser Endomicroscopy in the Detection of Head and Neck Precancerous Lesions," *Otolaryngol. Neck Surg.*, vol. 151, no. 1, pp. 73–80, 2014, doi: 10.1177/0194599814528660.

[106] M. S. Strong and G. J. Jako, "Laser Surgery in the Larynx Early Clinical Experience with Continuous CO2 Laser," *Ann. Otol. Rhinol. Laryngol.*, vol. 81, no. 6, pp. 791–798, Dec. 1972, doi: 10.1177/000348947208100606.

[107] M. L. Schrijvers *et al.*, "Higher laryngeal preservation rate after CO2 laser surgery compared with radiotherapy in T1a glottic laryngeal carcinoma," *Head Neck*, vol. 31, no. 6, pp. 759–764, 2009, doi: https://doi.org/10.1002/hed.21027.

[108] T. Ross, N. S. Tolley, and Z. Awad, "Novel Energy Devices in Head and Neck Robotic Surgery - A Narrative Review," *Robot. Surg.*, vol. 7, pp. 25–39, Apr. 2020, doi: 10.2147/RSRR.S247455.

[109] H. H. Arroyo, L. Neri, C. Y. Fussuma, and R. Imamura, "Diode Laser for Laryngeal Surgery: a Systematic Review," *Int. Arch. Otorhinolaryngol.*, vol. 20, pp. 172–179, 2016.

[110] M. C. Pierce, S. D. Jackson, M. R. Dickinson, and T. A. King, "Laser–tissue interaction with a high-power 2-μm fiber laser: Preliminary studies with soft tissue," *Lasers Surg. Med.*, vol. 25, no. 5, pp. 407–413, Jan. 1999, doi: https://doi.org/10.1002/(SICI)1096-9101(1999)25:5<407::AID-LSM7>3.0.CO;2-9.

[111] B. Temelkuran, S. D. Hart, G. Benoit, J. D. Joannopoulos, and Y. Fink, "Wavelength-scalable hollow optical fibres with large photonic bandgaps for CO2 laser transmission," *Nature*, vol. 420, no. 6916, pp. 650–653, 2002, doi: 10.1038/nature01275.

[112] L. Fichera, "Bringing the light inside the body to perform better surgery," *Sci. Robot.*, vol. 6, no. 50, p. eabf1523, Jan. 2021, doi: 10.1126/scirobotics.abf1523.

[113] "AcuPulse DUO CO2 laser," *Lumenis Ltd.* [Online]. Available: https://lumenis.co.uk/medical/co2-products/acupulse-duo/. [Accessed: 31-Mar-2020].

[114] "BEACON Advanced Energy Laser System," *OmniGuide Inc.* [Online]. Available: https://www.omni-guide.com/technology/co2/laser/. [Accessed: 31-Mar-2020].

[115] M. Rubinstein and W. B. Armstrong, "Transoral laser microsurgery for laryngeal cancer: A primer and review of laser dosimetry," *Lasers Med. Sci.*, vol. 26, no. 1, pp. 113–124, 2011, doi: 10.1007/s10103-010-0834-5.

[116] L. S. Mattos, N. Deshpande, G. Barresi, L. Guastini, and G. Peretti, "A novel computerized surgeon–machine interface for robot-assisted laser phonomicrosurgery," *Laryngoscope*, vol. 124, no. 8, pp. 1887–1894, 2014, doi: https://doi.org/10.1002/lary.24566.

[117] A. Fiorelli, S. Mazzone, A. Mazzone, and M. Santini, "The digital AcuBlade laser system to remove huge vocal fold granulations following subglottic airway stent," *Interact. Cardiovasc. Thorac. Surg.*, vol. 17, no. 3, pp. 591–593, 2013, doi: 10.1093/icvts/ivt226.

[118] M. Chauhan, N. Deshpande, D. G. Caldwell, and L. S. Mattos, "Design and Modeling of a Three-Degree-of-Freedom Articulating Robotic Microsurgical Forceps for Trans-Oral Laser Microsurgery," *J. Med. Device.*, vol. 13, no. 2, 2019, doi: 10.1115/1.4043017.

[119] G. Dagnino, L. S. Mattos, G. Becattini, M. Dellepiane, and D. G. Caldwell, "Comparative evaluation of user interfaces for robot-assisted laser phonomicrosurgery," in *2011 Annual International Conference of the IEEE Engineering in Medicine and Biology Society*, Aug. 2011, pp. 7376–7379, doi: 10.1109/IEMBS.2011.6091718.

[120] G. Dagnino, L. S. Mattos, and D. G. Caldwell, "A vision-based system for fast and accurate laser scanning in robot-assisted phonomicrosurgery," *Int. J. Comput. Assist. Radiol. Surg.*, vol. 10, no. 2, pp. 217–229, 2015, doi: 10.1007/s11548-014-1078-9.

[121] "Direct laryngoscopy," *Katholieke Universiteit Leuven*. [Online]. Available: https://www.kuleuven.be/cltr/en/larynx/dir_laryn.htm. [Accessed: 31-Mar-2020].

[122] L. M. Akst, K. C. Olds, M. Balicki, P. Chalasani, and R. H. Taylor, "Robotic microlaryngeal phonosurgery: Testing of a 'steady-hand' microsurgery platform," *Laryngoscope*, vol. 128, no. 1, pp. 126–132, 2018, doi: https://doi.org/10.1002/lary.26621.

[123] G. S. Weinstein and B. W. O'Malley, *Transoral Robotic Surgery (TORS)*. Plural Publishing, Incorporated, 2011.

[124] Y. M. Park *et al.*, "Transoral Robotic Surgery (TORS) in Laryngeal and Hypopharyngeal Cancer," *J. Laparoendosc. Adv. Surg. Tech.*, vol. 19, no. 3, pp. 361–368, 2009, doi: 10.1089/lap.2008.0320.

[125] F. T. Kayhan, K. H. Kaya, A. Altintas, and I. Sayin, "Transoral Robotic Supraglottic Partial Laryngectomy," *J. Craniofac. Surg.*, vol. 25, no. 4, 2014.

[126] Y. M. Park *et al.*, "The First Human Trial of Transoral Robotic Surgery Using a Single-Port Robotic System in the Treatment of Laryngo-Pharyngeal Cancer," *Ann. Surg. Oncol.*, vol. 26, no. 13, pp. 4472–4480, 2019, doi: 10.1245/s10434-019-07802-0.

[127] K. B. Greenland, M. J. Edwards, N. J. Hutton, V. J. Challis, M. G. Irwin, and J. W. Sleigh, "Changes in airway configuration with different head and neck positions using magnetic resonance imaging of normal airways: a new concept with possible clinical applications," *BJA Br. J. Anaesth.*, vol. 105, no. 5, pp. 683–690, Nov. 2010, doi: 10.1093/bja/aeq239.

[128] D. T. Friedrich *et al.*, "Potential Advantages of a Single-Port, Operator-Controlled Flexible Endoscope System for Transoral Surgery of the Larynx," *Ann. Otol. Rhinol. Laryngol.*, vol. 124, no. 8, pp. 655–662, Mar. 2015, doi: 10.1177/0003489415575548.

[129] M. Remacle, V. M. N. Prasad, G. Lawson, L. Plisson, V. Bachy, and S. Van der Vorst, "Transoral robotic surgery (TORS) with the Medrobotics Flex™ System: first surgical application on humans," *Eur. Arch. Oto-Rhino-Laryngology*, vol. 272, no. 6, pp. 1451–1455, 2015, doi: 10.1007/s00405-015-3532-x.

[130] E. Funk, D. Goldenberg, and N. Goyal, "Demonstration of transoral robotic supraglottic laryngectomy and total laryngectomy in cadaveric specimens using the Medrobotics Flex System," *Head Neck*, vol. 39, no. 6, pp. 1218–1225, 2017, doi: https://doi.org/10.1002/hed.24746.

[131] S. Lang *et al.*, "A european multicenter study evaluating the flex robotic system in transoral robotic surgery," *Laryngoscope*, vol. 127, no. 2, pp. 391–395, Feb. 2017, doi: https://doi.org/10.1002/lary.26358.

[132] S. Lescano, D. Zlatanov, M. Rakotondrabe, and N. Andreff, "Kinematic Analysis of a Meso-Scale Parallel Robot for Laser Phonomicrosurgery," in *Interdisciplinary Applications of Kinematics*, 2015, pp. 127–135.

[133] S. Lescano, M. Rakotondrabe, and N. Andreff, "Precision prediction using interval exponential mapping of a parallel kinematic smart composite microstructure," in *2015 IEEE/RSJ International Conference on Intelligent Robots and Systems (IROS)*, 2015, pp. 1994–1999, doi: 10.1109/IROS.2015.7353640.

[134] K. Rabenorosoa, B. Tasca, A. Zerbib, P. Rougeot, N. Andreff, and T. E. Pengwang, "Squipabot: A Mesoscale Parallel Robot for a Laser Phonosurgery," *Int. J. Optomechatronics*, vol. 9, no. 4, pp. 310–324, 2015, doi: 10.1080/15599612.2015.1059534.

[135] S. Patel, M. Rajadhyaksha, S. Kirov, Y. Li, and R. Toledo-Crow, "Endoscopic laser scalpel for head and neck cancer surgery," in *Photonic Therapeutics and Diagnostics VIII*, 2012, vol. 8207, pp. 341–351, doi: 10.1117/12.909172.

[136] S. A. Bothner, P. A. York, P. C. Song, and R. J. Wood, "A Compact Laser-Steering End-Effector for Transoral Robotic Surgery," in *2019 IEEE/RSJ International Conference on Intelligent Robots and Systems (IROS)*, Nov. 2019, pp. 7091–7096, doi: 10.1109/IROS40897.2019.8968255.

[137] P. A. York, R. Peña, D. Kent, and R. J. Wood, "Microrobotic laser steering for minimally invasive surgery," *Sci. Robot.*, vol. 6, no. 50, p. eabd5476, Jan. 2021, doi: 10.1126/scirobotics.abd5476.

[138] L. S. Mattos and N. Andreff, "The µRALP Project : New Technologies and Systems for Robot-Assisted Laser Phonomicrosurgery," in *3rd Joint Workshop on New Technologies for Computer/Robot Assisted Surgery*, 2013.

[139] A. Acemoglu and L. S. Mattos, "Magnetic laser scanner for endoscopic microsurgery," in *2017 IEEE International Conference on Robotics and Automation (ICRA)*, 2017, pp. 4215–4220, doi: 10.1109/ICRA.2017.7989485.

[140] A. Acemoglu, N. Deshpande, and L. S. Mattos, "Towards a Magnetically-Actuated Laser Scanner for

Endoscopic Microsurgeries," *J. Med. Robot. Res.*, vol. 03, no. 02, p. 1840004, 2018, doi: 10.1142/S2424905X18400044.

[141] A. Acemoglu, D. Pucci, and L. S. Mattos, "Design and Control of a Magnetic Laser Scanner for Endoscopic Microsurgeries," *IEEE/ASME Trans. Mechatronics*, vol. 24, no. 2, pp. 527–537, 2019, doi: 10.1109/TMECH.2019.2896248.

[142] A. Acemoglu, *A Magnetic Laser Scanner for Endoscopic Microsurgery*, 1st ed. Springer, Cham, 2020.

[143] R. Renevier, B. Tamadazte, K. Rabenorosoa, L. Tavernier, and N. Andreff, "Endoscopic Laser Surgery: Design, Modeling, and Control," *IEEE/ASME Trans. Mechatronics*, vol. 22, no. 1, pp. 99–106, 2017, doi: 10.1109/TMECH.2016.2595625.

[144] D. Kundrat *et al.*, "Toward Assistive Technologies for Focus Adjustment in Teleoperated Robotic Non-Contact Laser Surgery," *IEEE Trans. Med. Robot. Bionics*, vol. 1, no. 3, pp. 145–157, Aug. 2019, doi: 10.1109/TMRB.2019.2931438.

[145] A. Acemoglu and S. Leonardo Mattos, "Non-Contact Tissue Ablations with High-Speed Laser Scanning in Endoscopic Laser Microsurgery," in *2018 40th Annual International Conference of the IEEE Engineering in Medicine and Biology Society (EMBC)*, Jul. 2018, pp. 3660–3663, doi: 10.1109/EMBC.2018.8513055.

[146] S. Abdelaziz, L. Esteveny, L. Barbé, P. Renaud, B. Bayle, and M. de Mathelin, "Development of a MR-compatible cable-driven manipulator: Design and technological issues," in *2012 IEEE International Conference on Robotics and Automation*, May 2012, pp. 1488–1494, doi: 10.1109/ICRA.2012.6225302.

[147] E. Christoforou, E. Akbudak, A. Ozcan, M. Karanikolas, and N. V Tsekos, "Performance of interventions with manipulator-driven real-time MR guidance: implementation and initial in vitro tests," *Magn. Reson. Imaging*, vol. 25, no. 1, pp. 69–77, 2007, doi: https://doi.org/10.1016/j.mri.2006.08.016.

[148] S. Qian, B. Zi, W.-W. Shang, and Q.-S. Xu, "A Review on Cable-driven Parallel Robots," *Chinese J. Mech. Eng.*, vol. 31, no. 1, p. 66, 2018, doi: 10.1186/s10033-018-0267-9.

[149] C. Gosselin, "Cable-driven parallel mechanisms: state of the art and perspectives," *Mech. Eng. Rev.*, vol. 1, no. 1, pp. DSM0004–DSM0004, 2014, doi: 10.1299/mer.2014dsm0004.

[150] S. Abdolshah, "Trajectory planning and control of cable-driven parallel robots," University of Padova, 2016.

[151] V. L. Schmidt, *Modeling Techniques and Reliable Real-Time Implementation of Kinematics for Cable-Driven Parallel Robots Using Polymer Fiber Cables*. Fraunhofer Verlag, 2017.

[152] C. Alias, I. Nikolaev, E. G. Correa Magallanes, and B. Noche, "An Overview of Warehousing Applications based on Cable Robot Technology in Logistics," in *2018 IEEE International Conference on Service Operations and Logistics, and Informatics (SOLI)*, Jul. 2018, pp. 232–239, doi: 10.1109/SOLI.2018.8476760.

[153] X. Tang, "An Overview of the Development for Cable-Driven Parallel Manipulator," *Adv. Mech. Eng.*, vol. 6, p. 823028, 2014, doi: 10.1155/2014/823028.

[154] W. Kraus, *Force control of cable-driven parallel robots*. Fraunhofer Verlag, 2016.

[155] R. Verhoeven, “Analysis of the Workspace of Tendon-based Stewart Platforms,” 2004.

[156] M. Gouttefarde, D. Daney, and J. Merlet, “Interval-Analysis-Based Determination of the Wrench-Feasible Workspace of Parallel Cable-Driven Robots,” *IEEE Trans. Robot.*, vol. 27, no. 1, pp. 1–13, Feb. 2011, doi: 10.1109/TRO.2010.2090064.

[157] M. Hiller, S. Fang, S. Mielczarek, R. Verhoeven, and D. Franitza, “Design, analysis and realization of tendon-based parallel manipulators,” *Mech. Mach. Theory*, vol. 40, no. 4, pp. 429–445, 2005, doi: https://doi.org/10.1016/j.mechmachtheory.2004.08.002.

[158] Y. Shen, H. Osumi, and T. Arai, “Manipulability measures for multi-wire driven parallel mechanisms,” in *Proceedings of 1994 IEEE International Conference on Industrial Technology - ICIT ’94*, Dec. 1994, pp. 550–554, doi: 10.1109/ICIT.1994.467141.

[159] S. Kawamura, H. Kino, and C. Won, “High-speed manipulation by using parallel wire-driven robots,” *Robotica*, vol. 18, no. 1, pp. 13–21, 2000, doi: DOI: 10.1017/S0263574799002477.

[160] Shiqing Fang, D. Franitza, M. Torlo, F. Bekes, and M. Hiller, “Motion control of a tendon-based parallel manipulator using optimal tension distribution,” *IEEE/ASME Trans. Mechatronics*, vol. 9, no. 3, pp. 561–568, 2004, doi: 10.1109/TMECH.2004.835336.

[161] J. Huang, M. Hiller, and S. Fang, “Simulation Modeling of the Motion Control of a Two Degree of Freedom, Tendon Based, Parallel Manipulator in Operational Space Using MATLAB,” *J. China Univ. Min. Technol.*, vol. 17, no. 2, pp. 179–183, 2007, doi: https://doi.org/10.1016/S1006-1266(07)60067-4.

[162] W. Kraus, V. Schmidt, P. Rajendra, and A. Pott, “Load identification and compensation for a Cable-Driven parallel robot,” in *2013 IEEE International Conference on Robotics and Automation*, 2013, pp. 2485–2490, doi: 10.1109/ICRA.2013.6630915.

[163] Y. Suilu, W. Zhao, L. Qi, and C. Yixin, “Stiffness analysis of a wire-driven parallel manipulator,” in *2012 IEEE International Conference on Computer Science and Automation Engineering (CSAE)*, 2012, vol. 3, pp. 31–34, doi: 10.1109/CSAE.2012.6272901.

[164] A. Moradi, “Stiffness Analysis of Cable-Driven Parallel Robots,” 2013.

[165] L. S. Mattos, D. G. Caldwell, M. Dellepiane, and E. Grant, “Design and control of a robotic system for assistive laser phonomicrosurgery,” in *2010 Annual International Conference of the IEEE Engineering in Medicine and Biology*, Aug. 2010, pp. 5411–5415, doi: 10.1109/IEMBS.2010.5626496.

[166] M. Chauhan *et al.*, “A robotic microsurgical forceps for transoral laser microsurgery,” *Int. J. Comput. Assist. Radiol. Surg.*, vol. 14, no. 2, pp. 321–333, 2019, doi: 10.1007/s11548-018-1887-3.

[167] “Endoscopes and Instruments for ENT – Esophagoscopy – Bronchoscopy,” *STORZ SE & Co. KG.KARL*. [Online]. Available: https://www.karlstorz.com/cps/rde/xbcr/karlstorz_assets/ASSETS/3331528.pdf. [Accessed: 06-Dec-2019].

[168] M. Zhao, T. J. C. O. Vrielink, A. A. Kogkas, M. S. Runciman, D. S. Elson, and G. P. Mylonas, “LaryngoTORS: A Novel Cable-Driven Parallel Robotic System for Transoral Laser Phonosurgery,” *IEEE Robot. Autom. Lett.*, vol. 5, no. 2, pp. 1516–1523, Apr. 2020, doi: 10.1109/LRA.2020.2969186.

[169] M. M. Fernández-Fernández, L. Montes-Jovellar, P. L. Parente Arias, and P. Ortega del Alamo, “TransOral

endoscopic UltraSonic Surgery (TOUSS): a preliminary report of a novel robotless alternative to TORS," *Eur. Arch. Oto-Rhino-Laryngology*, vol. 272, no. 12, pp. 3785–3791, 2015, doi: 10.1007/s00405-014-3423-6.

[170] M. Zhao, T. J. C. O. Vrielink, A. A. Kogas, D. Elson, and G. Mylonas, "Prototype Designs of a Cable-driven Parallel Robot for Transoral Laser Surgery," in *Conference Proceedings Hamlyn Symposium on Medical Robotics*, 2019.

[171] K. Eguchi, J. Y. K. Chan, I. Tateya, A. Shimizu, F. C. Holsinger, and T. Sugimoto, "Curved Laryngopharyngoscope With Flexible Next-Generation Robotic Surgical System for Transoral Hypopharyngeal Surgery: A Preclinical Evaluation," *Ann. Otol. Rhinol. & Laryngol.*, vol. 128, no. 11, pp. 1023–1029, 2019, doi: 10.1177/0003489419856391.

[172] S. Mattheis, T. Hussain, B. Höing, P. Haßkamp, L. Holtmann, and S. Lang, "Robotics in laryngeal surgery," *Oper. Tech. Otolaryngol. Neck Surg.*, vol. 30, no. 4, pp. 284–288, 2019, doi: https://doi.org/10.1016/j.otot.2019.09.012.

[173] E. Cavus and V. Dörges, "The development of direct laryngoscopy," *Trends Anaesth. Crit. Care*, vol. 4, no. 1, pp. 3–9, 2014, doi: https://doi.org/10.1016/j.tacc.2013.08.001.

[174] R. M. Levitan, J. W. Heitz, M. Sweeney, and R. M. Cooper, "The Complexities of Tracheal Intubation With Direct Laryngoscopy and Alternative Intubation Devices," *Ann. Emerg. Med.*, vol. 57, no. 3, pp. 240–247, 2011, doi: https://doi.org/10.1016/j.annemergmed.2010.05.035.

[175] M. Á. Gómez-Ríos *et al.*, "A randomised crossover trial comparing the Airtraq® NT, McGrath® MAC and Macintosh laryngoscopes for nasotracheal intubation of simulated easy and difficult airways in a manikin," *Brazilian J. Anesthesiol. English Ed.*, vol. 66, no. 3, pp. 289–297, 2016, doi: https://doi.org/10.1016/j.bjane.2014.10.009.

[176] P. Gholami, M. M. Aref, and H. D. Taghirad, "On the control of the KNTU CDRPM: A cable driven redundant parallel manipulator," in *2008 IEEE/RSJ International Conference on Intelligent Robots and Systems*, 2008, pp. 2404–2409, doi: 10.1109/IROS.2008.4650740.

[177] A. Saracino, T. J. C. Oude-Vrielink, A. Menciassi, E. Sinibaldi, and G. P. Mylonas, "Haptic Intracorporeal Palpation Using a Cable-Driven Parallel Robot: A User Study," *IEEE Trans. Biomed. Eng.*, vol. 67, no. 12, pp. 3452–3463, Dec. 2020, doi: 10.1109/TBME.2020.2987646.

[178] P. Stark and R. Parker, "Bounded-variable least-squares: an algorithm and applications," 1995.

[179] E. Catmull and R. Rom, "A class of local interpolating splines," R. E. BARNHILL and R. F. B. T.-C. A. G. D. RIESENFELD, Eds. Academic Press, 1974, pp. 317–326.

[180] N. Deshpande, M. Chauhan, C. Pacchierotti, D. Prattichizzo, D. G. Caldwell, and L. S. Mattos, "Robot-assisted microsurgical forceps with haptic feedback for transoral laser microsurgery," in *2016 38th Annual International Conference of the IEEE Engineering in Medicine and Biology Society (EMBC)*, Aug. 2016, pp. 5156–5159, doi: 10.1109/EMBC.2016.7591888.

[181] J. J. Henderson, M. T. Popat, I. P. Latto, and A. C. Pearce, "Difficult Airway Society guidelines for management of the unanticipated difficult intubation," *Anaesthesia*, vol. 59, no. 7, pp. 675–694, Jul. 2004, doi: https://doi.org/10.1111/j.1365-2044.2004.03831.x.

[182] K. L. Pearson and B. E. McGuire, “Anaesthesia for laryngo-tracheal surgery, including tubeless field techniques,” *BJA Educ.*, vol. 17, no. 7, pp. 242–248, Jul. 2017, doi: 10.1093/bjaed/mkx004.

[183] J. M. Garden, M. K. O’Banion, A. D. Bakus, and C. Olson, “Viral Disease Transmitted by Laser-Generated Plume (Aerosol),” *Arch. Dermatol.*, vol. 138, no. 10, pp. 1303–1307, Oct. 2002, doi: 10.1001/archderm.138.10.1303.

[184] “Planetary Gearheads Series 12/4,” *FAULHABER GMBH & CO. KG*. [Online]. Available: https://www.faulhaber.com/en/products/series/124/. [Accessed: 28-Jan-2021].

[185] M. Goncalves *et al.*, “Probe-based confocal laser endomicroscopy in detecting malignant lesions of vocal folds,” *Acta Otorhinolaryngol. Ital.*, vol. 39, no. 6, pp. 389–395, Dec. 2019, doi: 10.14639/0392-100X-2121.

[186] V. Volgger, S. Girschick, S. Ihrler, A. S. Englhard, H. Stepp, and C. S. Betz, “Evaluation of confocal laser endomicroscopy as an aid to differentiate primary flat lesions of the larynx: A prospective clinical study,” *Head Neck*, vol. 38, no. S1, pp. E1695–E1704, Apr. 2016, doi: https://doi.org/10.1002/hed.24303.

[187] B. Regeling *et al.*, “Hyperspectral Imaging Using Flexible Endoscopy for Laryngeal Cancer Detection,” *Sensors*, vol. 16, no. 8. 2016, doi: 10.3390/s16081288.

[188] R. Martin, B. Thies, and A. O. H. Gerstner, “Hyperspectral hybrid method classification for detecting altered mucosa of the human larynx,” *Int. J. Health Geogr.*, vol. 11, no. 1, p. 21, 2012, doi: 10.1186/1476-072X-11-21.

[189] L. Wittig, C. Betz, and D. Eggert, “Optical coherence tomography for tissue classification of the larynx in an outpatient setting-a translational challenge on the verge of a resolution?,” *Transl. Biophotonics*, vol. 3, no. 1, p. e202000013, 2021, doi: https://doi.org/10.1002/tbio.202000013.

[190] T. Just and H. W. Pau, “Intra-operative application of confocal endomicroscopy using a rigid endoscope,” *J. Laryngol. Otol.*, vol. 127, no. 6, pp. 599–604, 2013, doi: DOI: 10.1017/S0022215113000765.

[191] T. Just *et al.*, “Confocal endomicroscopy of the larynx,” in *Photonic Therapeutics and Diagnostics VIII*, 2012, vol. 8207, pp. 426–432, doi: 10.1117/12.921265.

[192] M. Goncalves, H. Iro, A. Dittberner, A. Agaimy, and C. Bohr, “Value of confocal laser endomicroscopy in the diagnosis of vocal cord lesions,” *Eur. Rev. Med. Pharmacol. Sci.*, vol. 21, no. 18, pp. 3990–3997, 2017.

[193] B. Pogorzelski, U. Hanenkamp, M. Goetz, R. Kiesslich, and J. Gosepath, “Systematic Intraoperative Application of Confocal Endomicroscopy for Early Detection and Resection of Squamous Cell Carcinoma of the Head and Neck: A Preliminary Report,” *Arch. Otolaryngol. Neck Surg.*, vol. 138, no. 4, pp. 404–411, Apr. 2012, doi: 10.1001/archoto.2012.213.

[194] M. Hughes and G.-Z. Yang, “Line-scanning fiber bundle endomicroscopy with a virtual detector slit,” *Biomed. Opt. Express*, vol. 7, no. 6, pp. 2257–2268, 2016, doi: 10.1364/BOE.7.002257.

[195] M. Hughes and G.-Z. Yang, “High speed, line-scanning, fiber bundle fluorescence confocal endomicroscopy for improved mosaicking,” *Biomed. Opt. Express*, vol. 6, no. 4, pp. 1241–1252, 2015, doi: 10.1364/BOE.6.001241.

[196] H. Zhang, K. Vyas, and G.-Z. Yang, “Line scanning, fiber bundle fluorescence HiLo endomicroscopy with confocal slit detection,” *J. Biomed. Opt.*, vol. 24, no. 11, pp. 1–7, Nov. 2019, doi: 10.1117/1.JBO.24.11.116501.

[197] K. Vyas, M. Hughes, B. G. Rosa, and G.-Z. Yang, “Fiber bundle shifting endomicroscopy for high-resolution imaging,” *Biomed. Opt. Express*, vol. 9, no. 10, pp. 4649–4664, 2018, doi: 10.1364/BOE.9.004649.

[198] M. J. Marques *et al.*, “En-face optical coherence tomography fluorescence endomicroscopy for minimally invasive imaging using a robotic scanner,” *J. Biomed. Opt.*, vol. 24, no. 6, pp. 1–15, Jun. 2019, doi: 10.1117/1.JBO.24.6.066006.

[199] S. Zuo, M. Hughes, and G.-Z. Yang, “Novel Balloon Surface Scanning Device for Intraoperative Breast Endomicroscopy,” *Ann. Biomed. Eng.*, vol. 44, no. 7, pp. 2313–2326, 2016, doi: 10.1007/s10439-015-1493-2.

[200] S. Zuo, M. Hughes, and G. Yang, “Flexible Robotic Scanning Device for Intraoperative Endomicroscopy in MIS,” *IEEE/ASME Trans. Mechatronics*, vol. 22, no. 4, pp. 1728–1735, Aug. 2017, doi: 10.1109/TMECH.2017.2700008.

[201] A. Gudeloglu, J. V Brahmbhatt, and S. J. Parekattil, “Robotic-assisted microsurgery for an elective microsurgical practice,” *Semin. Plast. Surg.*, vol. 28, no. 1, pp. 11–19, Feb. 2014, doi: 10.1055/s-0034-1368162.

[202] A. Lopez *et al.*, “Intraoperative Optical Biopsy during Robotic Assisted Radical Prostatectomy Using Confocal Endomicroscopy,” *J. Urol.*, vol. 195, no. 4, Part 1, pp. 1110–1117, 2016, doi: https://doi.org/10.1016/j.juro.2015.10.182.

[203] L. Zhang, M. Ye, P. Giataganas, M. Hughes, and G. Yang, “Autonomous scanning for endomicroscopic mosaicing and 3D fusion,” in *2017 IEEE International Conference on Robotics and Automation (ICRA)*, May 2017, pp. 3587–3593, doi: 10.1109/ICRA.2017.7989412.

[204] L. Zhang *et al.*, “From Macro to Micro: Autonomous Multiscale Image Fusion for Robotic Surgery,” *IEEE Robot. Autom. Mag.*, vol. 24, no. 2, pp. 63–72, 2017, doi: 10.1109/MRA.2017.2680543.

[205] P. Giataganas, M. Hughes, and G.-Z. Yang, “Force adaptive robotically assisted endomicroscopy for intraoperative tumour identification,” *Int. J. Comput. Assist. Radiol. Surg.*, vol. 10, no. 6, pp. 825–832, 2015, doi: 10.1007/s11548-015-1179-0.

[206] B. Regeling *et al.*, “Development of an image pre-processor for operational hyperspectral laryngeal cancer detection,” *J. Biophotonics*, vol. 9, no. 3, pp. 235–245, Mar. 2016, doi: https://doi.org/10.1002/jbio.201500151.

[207] C. D. Nawn, B. Souhan, R. C. III, C. Kneapler, N. Fell, and J. Y. Ye, “Distinguishing tracheal and esophageal tissues with hyperspectral imaging and fiber-optic sensing,” *J. Biomed. Opt.*, vol. 21, no. 11, pp. 1–10, Nov. 2016, doi: 10.1117/1.JBO.21.11.117004.

[208] C. D. Nawn, B. E. Souhan, R. C. III, C. Kneapler, N. Fell, and J. Y. Ye, “Spectral characterization of tracheal and esophageal tissues using a hyperspectral camera and fiber optic sensors,” in *Proc.SPIE*, Mar. 2016, vol. 9702, doi: 10.1117/12.2211406.

[209] S. S. Chauhan *et al.*, “Confocal laser endomicroscopy,” *Gastrointest. Endosc.*, vol. 80, no. 6, pp. 928–938, 2014, doi: https://doi.org/10.1016/j.gie.2014.06.021.

[210] M. Zhao, H. Zhang, G. P. Mylonas, and D. S. Elson, “Cable-Driven Parallel Robot Assisted Confocal Imaging of the Larynx,” in *Biophotonics Congress: Biomedical Optics 2020 (Translational, Microscopy, OCT, OTS, BRAIN)*, 2020, p. TTu4B.4, doi: 10.1364/TRANSLATIONAL.2020.TTu4B.4.

[211] Q. Huang, B. Wu, J. Lan, and X. Li, “Fully Automatic Three-Dimensional Ultrasound Imaging Based on Conventional B-Scan,” *IEEE Trans. Biomed. Circuits Syst.*, vol. 12, no. 2, pp. 426–436, 2018, doi: 10.1109/TBCAS.2017.2782815.

[212] J. Zhan, J. Cartucho, and S. Giannarou, “Autonomous Tissue Scanning under Free-Form Motion for Intraoperative Tissue Characterisation,” in *2020 IEEE International Conference on Robotics and Automation (ICRA)*, 2020, pp. 11147–11154, doi: 10.1109/ICRA40945.2020.9197294.

[213] A. Schoob, D. Kundrat, L. A. Kahrs, and T. Ortmaier, “Stereo vision-based tracking of soft tissue motion with application to online ablation control in laser microsurgery,” *Med. Image Anal.*, vol. 40, pp. 80–95, 2017, doi: https://doi.org/10.1016/j.media.2017.06.004.

[214] C. Godard, O. Mac Aodha, M. Firman, and G. Brostow, “Digging Into Self-Supervised Monocular Depth Estimation,” in *2019 IEEE/CVF International Conference on Computer Vision (ICCV)*, 2019, pp. 3827–3837, doi: 10.1109/ICCV.2019.00393.

[215] F. Tosi, F. Aleotti, M. Poggi, and S. Mattoccia, “Learning Monocular Depth Estimation Infusing Traditional Stereo Knowledge,” in *2019 IEEE/CVF Conference on Computer Vision and Pattern Recognition (CVPR)*, 2019, pp. 9791–9801, doi: 10.1109/CVPR.2019.01003.

[216] M. Goldman, T. Hassner, and S. Avidan, “Learn Stereo, Infer Mono: Siamese Networks for Self-Supervised, Monocular, Depth Estimation,” in *2019 IEEE/CVF Conference on Computer Vision and Pattern Recognition Workshops (CVPRW)*, 2019, pp. 2886–2895, doi: 10.1109/CVPRW.2019.00348.

[217] G. Chen, M. Waechter, B. Shi, K.-Y. K. Wong, and Y. Matsushita, “What Is Learned in Deep Uncalibrated Photometric Stereo?,” in *Computer Vision -- ECCV 2020*, 2020, pp. 745–762.

[218] S. Jin, Z. Wang, Y. Ou, and Y. Zhou, “Improved Learning Accuracy for Learning Stable Control from Human Demonstrations*,” in *2019 IEEE/RSJ International Conference on Intelligent Robots and Systems (IROS)*, 2019, pp. 2679–2685, doi: 10.1109/IROS40897.2019.8968274.

[219] S. Ambhore, “A Comprehensive Study on Robot Learning from Demonstration,” in *2020 2nd International Conference on Innovative Mechanisms for Industry Applications (ICIMIA)*, 2020, pp. 291–299, doi: 10.1109/ICIMIA48430.2020.9074946.

[220] R. J. Woodham, “Photometric Method For Determining Surface Orientation From Multiple Images,” *Opt. Eng.*, vol. 19, no. 1, pp. 139–144, 1980, doi: 10.1117/12.7972479.

[221] M. Holroyd, J. Lawrence, G. Humphreys, and T. Zickler, “A Photometric Approach for Estimating Normals and Tangents,” *ACM Trans. Graph.*, vol. 27, no. 5, Dec. 2008, doi: 10.1145/1409060.1409086.

[222] Y. Le Cun *et al.*, “Handwritten zip code recognition with multilayer networks,” in *[1990] Proceedings. 10th International Conference on Pattern Recognition*, Jun. 1990, vol. ii, pp. 35–40 vol.2, doi: 10.1109/ICPR.1990.119325.

[223] A. Krizhevsky, I. Sutskever, and G. E. Hinton, “ImageNet Classification with Deep Convolutional Neural Networks,” *Commun. ACM*, vol. 60, no. 6, pp. 84–90, May 2017, doi: 10.1145/3065386.

[224] E. Shelhamer, J. Long, and T. Darrell, “Fully Convolutional Networks for Semantic Segmentation,” *IEEE Trans. Pattern Anal. Mach. Intell.*, vol. 39, no. 4, pp. 640–651, Apr. 2017, doi: 10.1109/TPAMI.2016.2572683.

[225] X. Zhang, J. Zou, K. He, and J. Sun, “Accelerating Very Deep Convolutional Networks for Classification and Detection,” *IEEE Trans. Pattern Anal. Mach. Intell.*, vol. 38, no. 10, pp. 1943–1955, Oct. 2016, doi: 10.1109/TPAMI.2015.2502579.

[226] H. Santo, M. Samejima, Y. Sugano, B. Shi, and Y. Matsushita, “Deep Photometric Stereo Network,” in *2017 IEEE International Conference on Computer Vision Workshops (ICCVW)*, Oct. 2017, pp. 501–509, doi: 10.1109/ICCVW.2017.66.

[227] G. Chen, K. Han, and K.-Y. K. Wong, “PS-FCN: A Flexible Learning Framework for Photometric Stereo,” in *Computer Vision -- ECCV 2018*, 2018, pp. 3–19.

[228] G. Chen, K. Han, B. Shi, Y. Matsushita, and K. K. K. Wong, “Self-Calibrating Deep Photometric Stereo Networks,” in *2019 IEEE/CVF Conference on Computer Vision and Pattern Recognition (CVPR)*, Jun. 2019, pp. 8731–8739, doi: 10.1109/CVPR.2019.00894.

[229] K. Enomoto, M. Waechter, K. N. Kutulakos, and Y. Matsushita, “Photometric Stereo via Discrete Hypothesis-and-Test Search,” in *2020 IEEE/CVF Conference on Computer Vision and Pattern Recognition (CVPR)*, Jun. 2020, pp. 2308–2316, doi: 10.1109/CVPR42600.2020.00238.

[230] T. Collins and A. Bartoli, “3D Reconstruction in Laparoscopy with Close-Range Photometric Stereo,” in *Medical Image Computing and Computer-Assisted Intervention -- MICCAI 2012*, 2012, pp. 634–642.

[231] K.-H. Tan, J. Kobler, P. Dietz, R. Raskar, and R. S. Feris, “Shape-Enhanced Surgical Visualizations and Medical Illustrations with Multi-flash Imaging,” in *Medical Image Computing and Computer-Assisted Intervention -- MICCAI 2004*, 2004, pp. 438–445.

Appendix A: A Qualitative Study of Photometric Stereo in Robotics Surgery via Fibre-delivered Illumination

The shape of the tissue surface is vital information for laser incision path planning and the optimisation of the pose and position of the fibre tip. For the surgeon, it is effortless to perceive the shape of the surface of the target tissue. However, in robotics, it remains a challenge. The photometric stereo technique can offer a normal map of the object surface via a single camera [220]. The generated normal map can be used to describe the shape of the object surface. In this section, a preliminary qualitative study of photometric stereo was performed by *LaryngoTORS* robot. The experimental results are presented and discussed.

A.1 Learning-Based Photometric Stereo

In the photometric stereo technique, multiple images of a static object captured under different lighting directions are used to estimate the normal map of the object surface. During image capture, the location and position of the camera and the object need to be fixed [220], [221]. Photometric stereo has a long history in computer vision and fruitful approaches have been developed. However, in the early approaches, two main limitations affect the applicability of the photometric stereo technique in practice. One limitation is the Lambertian reflectance model assumption. Since most of the objects are non-Lambertian, it is difficult to apply on real-world objects. Another one is the light directions need to be precisely calibrated. It cannot work on the cases which the light directions are unknown or uncalibrated.

With the development of deep learning techniques [222]–[225], learning-based

photometric stereo algorithms have been developed in recent years [217], [226]–[229]. And with the continuing efforts of computer vision engineers and researchers in the past few years, the limitations of traditional methods of photometric stereo have been tackled. PS-FCN is a learning-based photometric stereo network for non-Lambertian surface [227] and SDPS-Net can work on the non-Lambertian surface with uncalibrated light directions [228].

Currently, the learning-based photometric stereo techniques have not been widely used in surgical applications. The conditions of photometric stereo techniques may not be easily fulfilled in surgery. First, the target region may have moving tissues and its movement cannot be prevented. Second, in surgical applications, the light source is usually built into the camera. The light's direction can only be changed by moving the camera. To capture multiple images under different light directions by a fixed camera, a modified photometric stereo endoscope [230] or an extra light source device [231], where the light direction can be steered, is required. However, in TLP, the conditions of photometric stereo can be fulfilled by *LaryngoTORS* robot effortlessly. The target tissue can be held by an auxiliary instrument, such as a vocal cord holder. A static region nearby the instrument could be achieved. Fibre-based illumination can be utilised, and different lighting directions can be generated via steering the end tip of the illumination fibre manipulated by the *LaryngoTORS* robot.

In this section, an experiment of photometric stereo via fibre-based illumination was carried out on a simulated target. The method and experimental results are presented in section A.2 and A.3, respectively.

A.2 Materials and Method

A non-Lambertian test target made from silicone rubber (Ecoflex 00-35, Smooth-on, Inc., USA) was used to simulate vocal folds, and a small piece of white protrusion was used to simulate a lesion on the vocal cord (Fig A.1a). The experiment setup is shown in Figure A.1. Similar to the pCLE tests performed in chapter 5, the simulated target was fixed on a target holder (Fig A.1b) and the holder was mounted in front of the scaffold of *LaryngoTORS* robot (Fig A.1d). A 1.5 m length bare fibre (0.22 NA, core diameter: 400 μm, outer diameter: 480 μm, FG400LEP, Thorlabs Inc., USA) was used. The proximal end of the fibre was connected

to a light source (HL-2000-FHSA, Ocean Optics, Inc., USA) via a fibre terminator with SMA 905 connectors (BFT1, Thorlabs Inc., USA) (Fig A.1e). The distal end of the fibre was positioned in the over-tube of *LaryngoTORS* robot (Fig A.1c). The light source direction can be steered by manipulating the pose of the over-tube.

The experiment was performed three times under different light intensity levels: high, medium and low, which corresponding the shutter opening in approximately 80%, 50% and 20% respectively. The pose of the fibre end tip was manipulated randomly in the workspace of the robot. Each time, 32 images under different light beam directions were captured. During the image capture, the light source of the camera was turned off. A well-trained UPS-FCN model [217] was utilised to estimate the normal of the test target surface. The dimensions of each captured image are $640 \times 480 \times 3$. The captured 32 images were converted into a 640×480×96 matrix and input to the UPS-FCN model. The experimental results are presented in the next section.

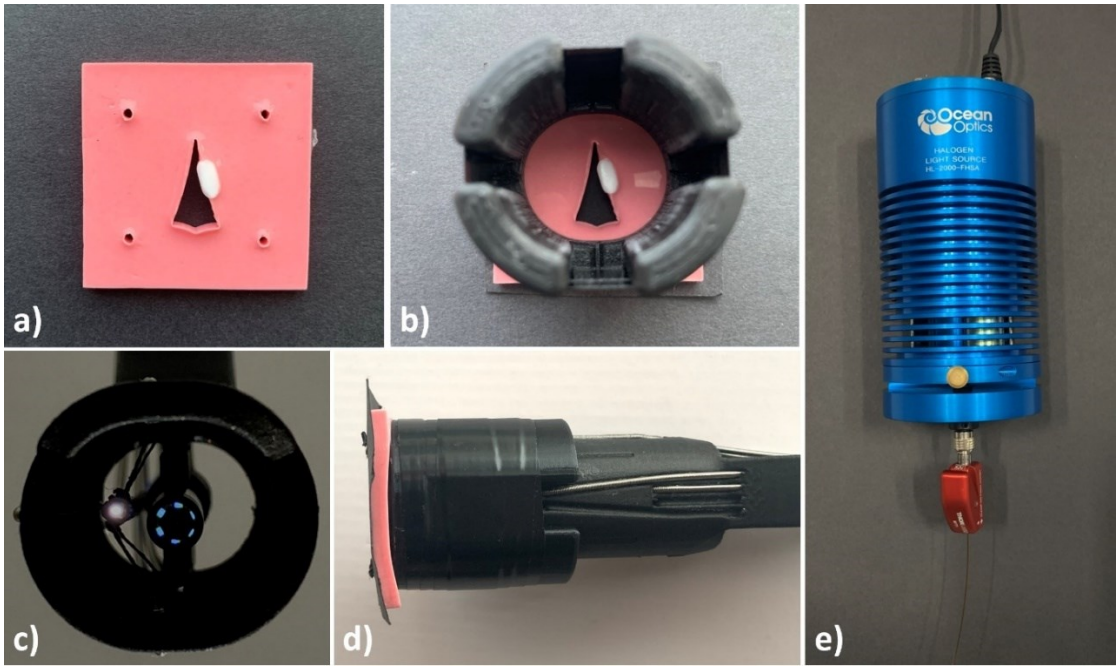


Figure A.1: The experimental setup: a) A test target made by silicone rubber. b) The test target was fixed on a target holder c) Front view of the robot with the fibre. A white light beam was delivered by the fibre. A USB camera was utilised to offer the vision of the target field. d) The test target was attached to the front of the robot. e) A fibre terminator with SMA 905 connectors was used to fix and connect the proximal end of the fibre to the light source.

A.3 Experimental Results

Figure A.2-A.4 shows 8 representative images of each 32 captured images under different light beam directions with high, medium and low light intensity level respectively. The estimated normal maps of the target surface under each light intensity level are shown in Figure A.5.

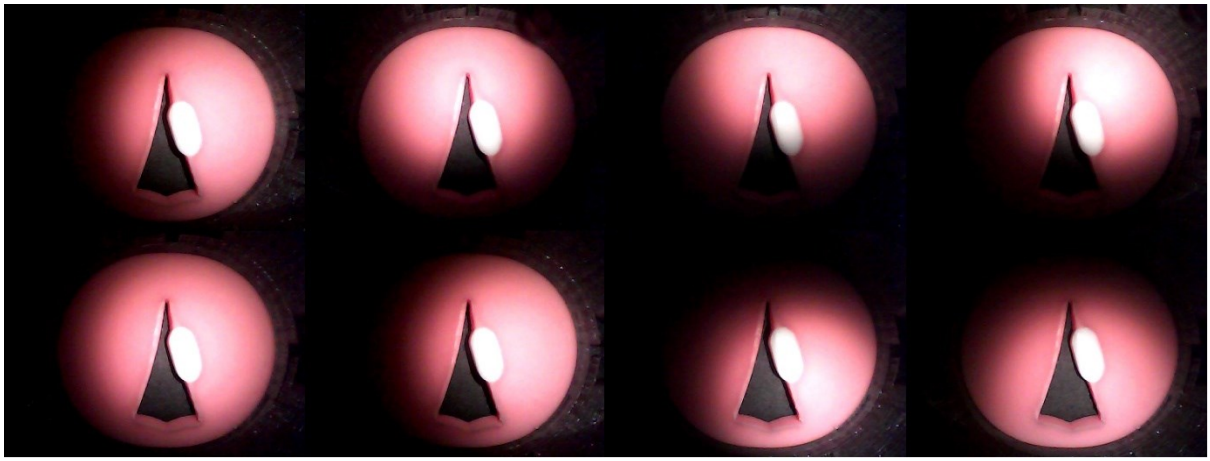


Figure A..2: Sample images captured under different light beam directions with high light intensity.

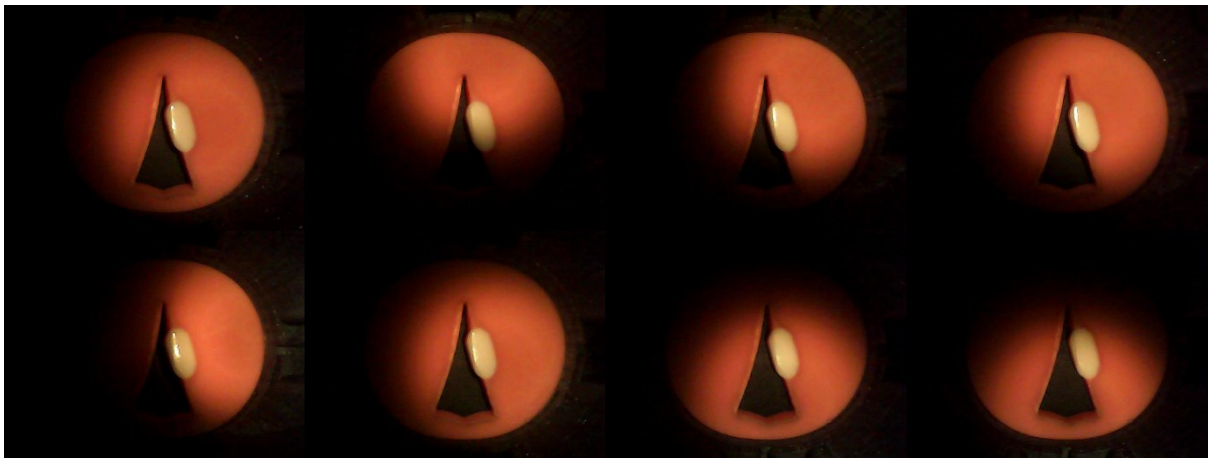


Figure A.3: Sample images captured under different light beam directions with medium light intensity.



Figure A.4: Sample images captured under different light beam directions with low light intensity.

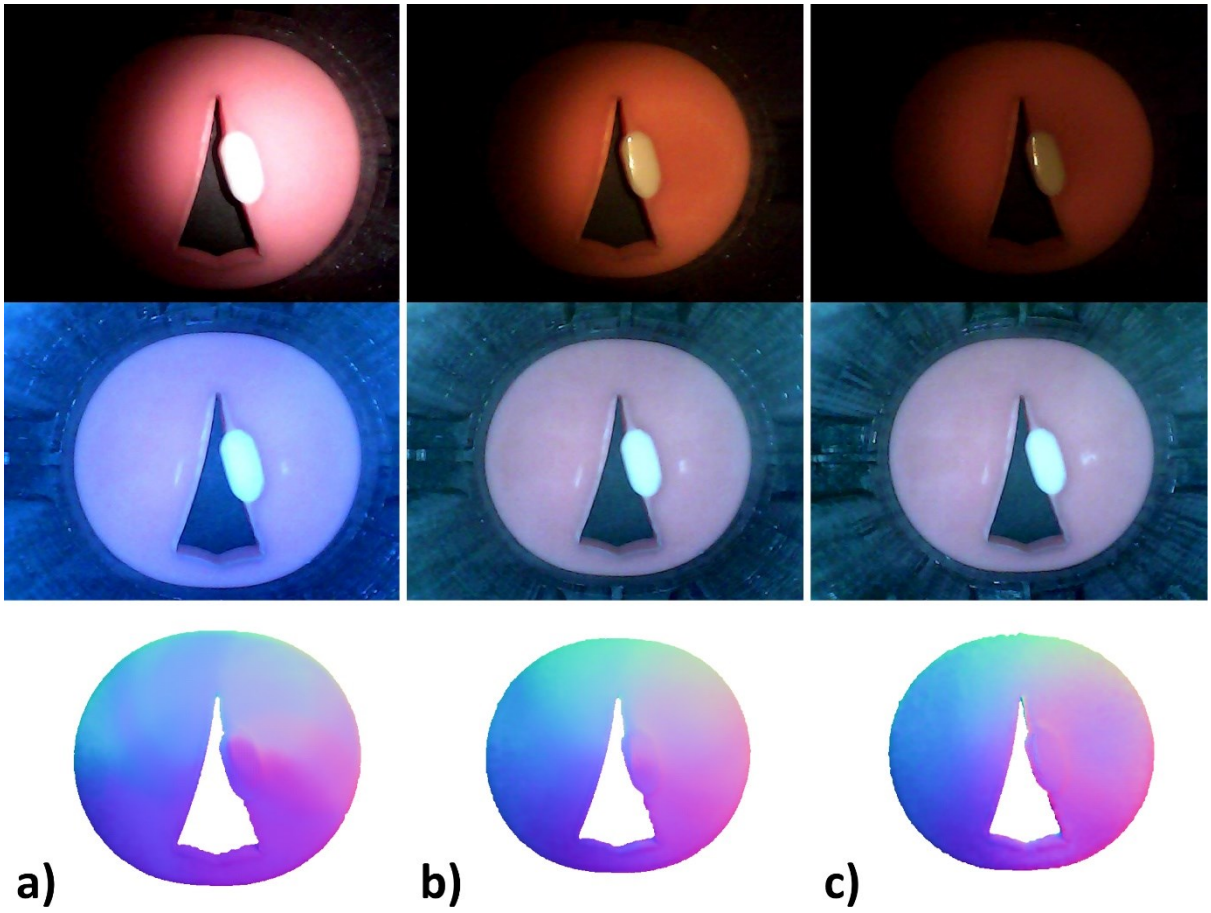


Figure A.5: The generated normal map of the target surface under high, medium and low light intensity level are demonstrated at the bottom row in column a), b) and c) respectively. The images at the top row are used to indicate the light intensity level. The images shown in the middle row are captured only under the light source of the camera.

Compared to the images captured under the light source of the camera (middle row in Figure A.5), the generated normal maps under different light intensities can reflect the shape of the test target's surface. Such as the shape of the simulated lesion has been correctly

represented in the generated normal maps. In the three normal maps, the normal surface generated from the images under low light intensity contains more fine details of the target surface than the one generated under high light intensity, such as on the edge of simulated vocal folds. Some detailed features may be covered by the high-intensity light beam. As argued by Chan et al. [217], the captured specular highlights are vital clues for the normal surface estimation. The specular highlights in the captured images can be extracted and fused in the global features fusion layer in the UPS-FCN model. As shown at the top row in Figure A.5, the specular highlights in the images captured under medium and low light intensities have not been presented in the image capture under high light intensity.

A.4 Discussion

This study has demonstrated the possibility of applying photometric stereo techniques in robotic surgery via fibre-based illumination, in which the light beam direction can be steered using robotics. Since the ground truth of the target surface is unknown, the preliminary results were evaluated qualitatively. Quantitative studies on the data acquired in surgical applications need to be performed for further assessments. The normal map can be utilised to describe the shape of the target tissue. Furthermore, the surface 3D reconstruction could be achieved based on the surface normal. These are fundamentals for autonomous robotic surgery. It is a promising direction to be further developed in the future.

Appendix B: Copyright Permissions for usage of Figures

Figure	Source of work	Permission Note
1.1	N. Stewart, A. C. Lim, P. M. Lowe, and G. Goodman, "Lasers and laser-like devices: Part one," Australas. J. Dermatol., vol. 54, no. 3, pp. 173–183, 2013, doi: https://doi.org/10.1111/ajd.12034.	RightsLink® Licence Number 4956110270500
1.2a	D. V Palanker, M. S. Blumenkranz, and M. F. Marmor, "Fifty Years of Ophthalmic Laser Therapy," Arch. Ophthalmol., vol. 129, no. 12, pp. 1613–1619, 2011, doi: 10.1001/archophthalmol.2011.293.	RightsLink® Licence Number 4956121166545
1.2b 1.2c	J. I. Martínez-Salamanca, C. Martínez Ballesteros, A. Tewari, and J. A. Carballido, "Robotic surgery and laser technology: An opportunity for discovery," Arch. Españoles Urol., vol. 61, no. 9, pp. 1157–1162, 2008	Licensed under the Creative Commons Attribution-NonCommercial 3.0 Unported (CC BY-NC 3.0)
1.3 (left)	M. Lapidoth, M. E. Yagima Odo, and L. M. Odo, "Novel Use of Erbium:YAG (2,940-nm) Laser for Fractional Ablative Photothermolysis in the Treatment of Photodamaged Facial Skin: A Pilot Study," Dermatologic Surg., vol. 34, no. 8, pp. 1048–1053, 2008, doi: https://doi.org/10.1111/j.1524-146 4725.2008.34204.x.	RightsLink® Licence Number 5039050052648
1.3 (right)	K. Y. Lin and S. Y. Lu, "Panretinal navigated laser photocoagulation for PDR," Retin. Today, vol. JAN/FEB, pp. 65–70, 2014.	Permission is granted. (see letter below)
1.4a	D. V Palanker et al., "Femtosecond Laser–Assisted Cataract Surgery with Integrated Optical Coherence Tomography," Sci. Transl. Med., vol. 2, no. 58, pp. 58ra85 LP-58ra85, Nov. 2010, doi: 10.1126/scitranslmed.3001305.	RightsLink® Licence Number 4956171407564
1.4b	T. V Roberts et al., "Femtosecond laser cataract surgery: technology and clinical practice," Clin. Experiment. Ophthalmol., vol. 41, no. 2, pp. 180–186, Mar. 2013, doi: https://doi.org/10.1111/j.1442- 9071.2012.02851.x.	RightsLink® Licence Number 4956180194316
1.5	L. He, K. Sheehy, and W. Culbertson, "Femtosecond laser-assisted cataract surgery," Curr. Opin. Ophthalmol., vol. 22, no.	RightsLink® Licence Number

	1, 2011.	4956180703333
1.6a	S. C. Desai, C.-K. Sung, D. W. Jang, and E. M. Genden, “Transoral Robotic Surgery Using a Carbon Dioxide Flexible Laser for Tumors of the Upper Aerodigestive Tract,” Laryngoscope, vol. 118, no. 12, pp. 2187–2189, 2008, doi: https://doi.org/10.1097/MLG.0b013e31818379e4.	RightsLink® Licence Number 4956181275982
1.6b	R. V Smith, “Transoral Robotic Surgery for Larynx Cancer,” Otolaryngol. Clin. North Am., vol. 47, no. 3, pp. 379–395, 2014, doi: https://doi.org/10.1016/j.otc.2014.03.003.	RightsLink® Licence Number 4956191092588
1.6c	M. Remacle, N. Matar, G. Lawson, V. Bachy, M. Delos, and M.-C. Nollevaux, “Combining a new CO2 laser wave guide with transoral robotic surgery: a feasibility study on four patients with malignant tumors,” Eur. Arch. Oto-Rhino-Laryngology, vol. 269, no. 7, pp. 1833–1837, 2012, doi: 10.1007/s00405-011-1838- x.	RightsLink® Licence Number 4956200232891
1.7a	R. J. Hendrick, C. R. Mitchell, S. D. Herrell, and I. I. I. Robert J. Webster, “Hand-held transendoscopic robotic manipulators: A transurethral laser prostate surgery case study,” Int. J. Rob. Res., vol. 34, no. 13, pp. 1559–1572, 2015, doi: 10.1177/0278364915585397.	Permission is granted at no cost for use of content in a Master's Thesis and/or Doctoral Dissertation, subject to the following limitations. (see letter below)
1.7b	S. Yang, R. A. MacLachlan, and C. N. Riviere, “Toward automated intraocular laser surgery using a handheld micromanipulator,” in 2014 IEEE/RSJ International Conference on Intelligent Robots and Systems, 2014, pp. 1302–1307, doi: 10.1109/IROS.2014.6942725.	IEEE default permission for usage in thesis/dissertation
1.8	G. P. Mylonas, V. Vitiello, T. P. Cundy, A. Darzi, and G. Yang, “CYCLOPS: A versatile robotic tool for bimanual single-access and natural-orifice endoscopic surgery,” in 2014 IEEE International Conference on Robotics and Automation (ICRA), May 2014, pp. 2436–2442, doi: 10.1109/ICRA.2014.6907198.	IEEE default permission for usage in thesis/dissertation
1.9a	K. Miyashita, T. Oude Vrielink, and G. Mylonas, “A cable-driven parallel manipulator with force sensing 149 capabilities for high-accuracy tissue endomicroscopy,” Int. J. Comput. Assist. Radiol. Surg., vol. 13, no. 5, pp. 659–669, 2018, doi: 10.1007/s11548-018-1717-7.	This article is distributed under the terms of the Creative Commons Attribution 4.0 International License (http://creativecommons.org/licenses/by/4.0/)
1.9b	O. Vrielink and T. J. Corman, “Cable-driven parallel mechanisms for minimally invasive robotic surgery,” Imperial College London, 2019.	Permission is granted. (see letter below)

1.10-1.12	T. J. C. O. Vrielink, M. Zhao, A. Darzi, and G. P. Mylonas, “ESD CYCLOPS: A New Robotic Surgical System for GI Surgery,” in 2018 IEEE International Conference on Robotics and Automation (ICRA), May 2018, pp. 150–157, doi: 10.1109/ICRA.2018.8462698.	IEEE default permission for usage in thesis/dissertation
1.13-1.15	T. J. C. O. Vrielink, “Cable-driven parallel mechanisms for minimally invasive robotic surgery,” Imperial College London, 2019	Permission is granted. (Same as Figure. 1.9b, see letter below)
2.1	L. S. Mattos, N. Deshpande, G. Barresi, L. Guastini, and G. Peretti, “A novel computerized surgeon– machine interface for robot-assisted laser phonomicrosurgery,” Laryngoscope, vol. 124, no. 8, pp. 1887– 1894, 2014, doi: https://doi.org/10.1002/lary.24566.	RightsLink® Licence Number 4956211283567
2.2-2.4	M. Rubinstein and W. B. Armstrong, “Transoral laser microsurgery for laryngeal cancer: A primer and review of laser dosimetry,” Lasers Med. Sci., vol. 26, no. 1, pp. 113–124, 2011, doi: 10.1007/s10103-010- 0834-5.	This is an open access article distributed under the terms of the Creative Commons Attribution Noncommercial License (https://creativecommons.org/licenses/by-nc/2.0), which permits any noncommercial use, distribution, and reproduction in any medium, provided the original author(s) and source are credited.
2.5	A. Fiorelli, S. Mazzone, A. Mazzone, and M. Santini, “The digital AcuBlade laser system to remove huge vocal fold granulations following subglottic airway stent,” Interact. Cardiovasc. Thorac. Surg., vol. 17, no. 3, pp. 591–593, 2013, doi: 10.1093/icvts/ivt226.	RightsLink® Licence Number 4956220567081
2.6	https://www.kuleuven.be/cltr/en/larynx/dir_laryn.htm	Permission is granted. (see letter below)
2.7	G. Dagnino, L. S. Mattos, and D. G. Caldwell, “A vision-based system for fast and accurate laser scanning in robot-assisted phonomicrosurgery,” Int. J. Comput. Assist. Radiol. Surg., vol. 10, no. 2, pp. 217–229, 2015, doi: 10.1007/s11548-014-1078-9.	RightsLink® Licence Number 4956410098265
2.8	L. M. Akst, K. C. Olds, M. Balicki, P. Chalasani, and R. H. Taylor, “Robotic microlaryngeal phonosurgery: Testing of a ‘steady-hand’microsurgery platform,” Laryngoscope, vol. 128, no. 1, pp. 126–132, 2018, doi: https://doi.org/10.1002/lary.26621.	RightsLink® Licence Number 4956411098238

2.9a	Y. M. Park et al., “Transoral Robotic Surgery (TORS) in Laryngeal and Hypopharyngeal Cancer,” J. Laparoendosc. & Adv. Surg. Tech., vol. 19, no. 3, pp. 361–368, 2009, doi: 10.1089/lap.2008.0320.	Permission is granted. (see letter below)
2.9b	M. M. Chen, R. K. Orosco, G. C. Lim, and F. C. Holsinger, “Improved transoral dissection of the tongue base with a next-generation robotic surgical system,” Laryngoscope, vol. 128, no. 1, pp. 78–83, 2018, doi: https://doi.org/10.1002/lary.26649.	RightsLink® Licence Number 4956431020636
2.10	Y. M. Park et al., “The First Human Trial of Transoral Robotic Surgery Using a Single-Port Robotic System in the Treatment of Laryngo-Pharyngeal Cancer,” Ann. Surg. Oncol., vol. 26, no. 13, pp. 4472– 4480, 2019, doi: 10.1245/s10434-019-07802-0.	RightsLink® Licence Number 4956460863602
2.11a	M. Remacle, V. M. N. Prasad, G. Lawson, L. Plisson, V. Bachy, and S. Van der Vorst, “Transoral robotic surgery (TORS) with the Medrobotics FlexTM System: first surgical application on humans,” Eur. Arch. Oto-Rhino-Laryngology, vol. 272, no. 6, pp. 1451–1455, 2015, doi: 10.1007/s00405-015-3532-x.	RightsLink® Licence Number 4956510425692
2.11b	N. Sethi et al., “Transoral robotic surgery using the Medrobotic Flex® system: the Adelaide experience,” J. Robot. Surg., vol. 14, no. 1, pp. 109–113, 2020, doi: 10.1007/s11701-019-00941-2.	RightsLink® Licence Number 4956510653068
2.12a	M. Mandapathil, B. Greene, and T. Wilhelm, “Transoral surgery using a novel single-port flexible endoscope system,” Eur. Arch. Oto-Rhino-Laryngology, vol. 272, no. 9, pp. 2451–2456, 2015, doi: 10.1007/s00405-014-3177-1.	RightsLink® Licence Number 4956510839168
2.12b	E. Funk, D. Goldenberg, and N. Goyal, “Demonstration of transoral robotic supraglottic laryngectomy and total laryngectomy in cadaveric specimens using the Medrobotics Flex System,” Head Neck, vol. 39, no. 6, pp. 1218–1225, 2017, doi: https://doi.org/10.1002/hed.24746.	RightsLink® Licence Number 5035680229571
2.13	D. T. Friedrich et al., “Potential Advantages of a Single-Port, Operator-Controlled Flexible Endoscope System for Transoral Surgery of the Larynx,” Ann. Otol. Rhinol. Laryngol., vol. 124, no. 8, pp. 655–662, Mar. 2015, doi: 10.1177/0003489415575548.	Permission is granted at no cost for use of content in a Master's Thesis and/or Doctoral Dissertation, subject to the following limitations. You may use a single excerpt or up to 3.
2.14	S. Lang et al., “A european multicenter study evaluating the flex robotic system in transoral robotic surgery,” Laryngoscope, vol. 127, no. 2, pp. 391–395, Feb. 2017, doi: https://doi.org/10.1002/lary.26358.	RightsLink® Licence Number 4956641495407
2.15-2.16	R. K. Orosco, A. Arora, J. P. Jeannon, and F. C. Holsinger, “Next-	Permission is granted.

	Generation Robotic Head and Neck Surgery," ORL, vol. 80, no. 3–4, pp. 213–219, 2018, doi: 10.1159/000490599.	(see letter below)
2.17	Y. M. Park et al., "The First Human Trial of Transoral Robotic Surgery Using a Single-Port Robotic System in the Treatment of Laryngo-Pharyngeal Cancer," Ann. Surg. Oncol., vol. 26, no. 13, pp. 4472– 4480, 2019, doi: 10.1245/s10434-019-07802-0.	RightsLink® Licence Number 4956460863602 Same as Figure 2.10
2.18-2.22	R. Renevier, B. Tamadazte, K. Rabenorosoa, L. Tavernier, and N. Andreff, "Endoscopic Laser Surgery: Design, Modeling, and Control," IEEE/ASME Trans. Mechatronics, vol. 22, no. 1, pp. 99–106, 2017, doi: 10.1109/TMECH.2016.2595625.	IEEE default permission for usage in thesis/dissertation
2.23a	A. Acemoglu, N. Deshpande, and L. S. Mattos, "Towards a Magnetically-Actuated Laser Scanner for 152 Endoscopic Microsurgeries," J. Med. Robot. Res., vol. 03, no. 02, p. 1840004, 2018, doi: 10.1142/S2424905X18400044.	Permission is granted. (see letter below)
2.23b	A. Acemoglu and L. S. Mattos, "Magnetic laser scanner for endoscopic microsurgery," in 2017 IEEE International Conference on Robotics and Automation (ICRA), 2017, pp. 4215–4220, doi: 10.1109/ICRA.2017.7989485.	IEEE default permission for usage in thesis/dissertation
2.24	A. Acemoglu, N. Deshpande, and L. S. Mattos, "Towards a Magnetically-Actuated Laser Scanner for 152 Endoscopic Microsurgeries," J. Med. Robot. Res., vol. 03, no. 02, p. 1840004, 2018, doi: 10.1142/S2424905X18400044.	Permission is granted. (see letter below) Same as Figure 2.23a
2.25	A. Acemoglu, D. Pucci, and L. S. Mattos, "Design and Control of a Magnetic Laser Scanner for Endoscopic Microsurgeries," IEEE/ASME Trans. Mechatronics, vol. 24, no. 2, pp. 527–537, 2019, doi: 10.1109/TMECH.2019.2896248.	IEEE default permission for usage in thesis/dissertation
2.26a	A. Acemoglu and L. S. Mattos, "Magnetic laser scanner for endoscopic microsurgery," in 2017 IEEE International Conference on Robotics and Automation (ICRA), 2017, pp. 4215–4220, doi: 10.1109/ICRA.2017.7989485.	IEEE default permission for usage in thesis/dissertation
2.26b	A. Acemoglu, N. Deshpande, and L. S. Mattos, "Towards a Magnetically-Actuated Laser Scanner for 152 Endoscopic Microsurgeries," J. Med. Robot. Res., vol. 03, no. 02, p. 1840004, 2018, doi: 10.1142/S2424905X18400044.	Permission is granted. (see letter below) Same as Figure 2.23a
2.27	D. Kundrat et al., "Toward Assistive Technologies for Focus Adjustment in Teleoperated Robotic NonContact Laser Surgery," IEEE Trans. Med. Robot. Bionics, vol. 1, no. 3, pp. 145–157, Aug. 2019, doi: 10.1109/TMRB.2019.2931438.	IEEE default permission for usage in thesis/dissertation

3.1	V. L. Schmidt, Modeling Techniques and Reliable Real-Time Implementation of Kinematics for CableDriven Parallel Robots Using Polymer Fiber Cables. Fraunhofer Verlag, 2017.	Permission is granted. (see letter below)
3.2a	S. Qian, B. Zi, W.-W. Shang, and Q.-S. Xu, "A Review on Cable-driven Parallel Robots," Chinese J. Mech. Eng., vol. 31, no. 1, p. 66, 2018, doi: 10.1186/s10033-018-0267-9.	This article is distributed under the terms of the Creative Commons Attribution 4.0 International License (http://creativecommons.org/licenses/by/4.0/), which permits unrestricted use, distribution, and reproduction in any medium, provided you give appropriate credit to the original author(s) and the source, provide a link to the Creative Commons license, and indicate if changes were made.
3.2b	C. Gosselin, "Cable-driven parallel mechanisms: state of the art and perspectives," Mech. Eng. Rev., vol. 1, no. 1, pp. DSM0004–DSM0004, 2014, doi: 10.1299/mer.2014dsm0004.	Permission is granted. (see letter below)
3.3	C. Alias, I. Nikolaev, E. G. Correa Magallanes, and B. Noche, "An Overview of Warehousing Applications based on Cable Robot Technology in Logistics," in 2018 IEEE International Conference on Service Operations and Logistics, and Informatics (SOLI), Jul. 2018, pp. 232–239, doi: 10.1109/SOLI.2018.8476760.	IEEE default permission for usage in thesis/dissertation
3.4	R. Verhoeven, "Analysis of the Workspace of Tendon-based Stewart Platforms," 2004.	Permission is granted. (see letter below)
3.5	V. L. Schmidt, Modeling Techniques and Reliable Real-Time Implementation of Kinematics for CableDriven Parallel Robots Using Polymer Fiber Cables. Fraunhofer Verlag, 2017.	Permission is granted. (see letter below) Same as Figure 3.1
3.10	M. Zhao, T. J. C. O. Vrielink, A. A. Kogkas, M. S. Runciman, D. S. Elson, and G. P. Mylonas, "LaryngoTORS: A Novel Cable-Driven Parallel Robotic System for Transoral Laser Phonosurgery," IEEE Robot. Autom. Lett., vol. 5, no. 2, pp. 1516–1523, Apr. 2020, doi: 10.1109/LRA.2020.2969186.	IEEE default permission for usage in thesis/dissertation
3.11	A. H. Mendelsohn, M. Remacle, S. Van Der Vorst, V. Bachy, and G. Lawson, "Outcomes following transoral robotic surgery: Supraglottic laryngectomy," Laryngoscope, vol. 123, no. 1, pp. 208–214, 2013, doi: https://doi.org/10.1002/lary.23621.	RightsLink® Licence Number 4957301212631
3.18	M. M. Fernández-Fernández, L. Montes-Jovellar, P. L. Parente Arias, and P. Ortega del Alamo, "TransOral 154 endoscopic	This is an open access article distributed under the terms of the

	UltraSonic Surgery (TOUSS): a preliminary report of a novel robotless alternative to TORS," Eur. Arch. Oto-Rhino-Laryngology, vol. 272, no. 12, pp. 3785–3791, 2015, doi: 10.1007/s00405-014- 3423-6.	Creative Commons CC BY license, which permits unrestricted use, distribution, and reproduction in any medium, provided the original work is properly cited.
3.22	S. Mattheis, T. Hussain, B. Höing, P. Haßkamp, L. Holtmann, and S. Lang, "Robotics in laryngeal surgery," Oper. Tech. Otolaryngol. Neck Surg., vol. 30, no. 4, pp. 284–288, 2019, doi: https://doi.org/10.1016/j.otot.2019.09.012.	RightsLink® Licence Number 5052720764433
3.23	P. Hasskamp, S. Lang, L. Holtmann, B. A. Stuck, and S. Mattheis, "First use of a new retractor in transoral robotic surgery (TORS)," Eur. Arch. Oto-Rhino-Laryngology, vol. 273, no. 7, pp. 1913–1917, 2016, doi: 10.1007/s00405-015-3719-1.	RightsLink® Licence Number 5052731488673
3.27	M. Á. Gómez-Ríos et al., "A randomised crossover trial comparing the Airtraq® NT, McGrath® MAC and Macintosh laryngoscopes for nasotracheal intubation of simulated easy and difficult airways in a manikin," Brazilian J. Anesthesiol. (English Ed., vol. 66, no. 3, pp. 289–297, 2016, doi: https://doi.org/10.1016/j.bjane.2014.10.009.	This article is distributed under the terms of the Creative Commons Attribution 4.0 International License (CC BY-NC-ND 4.0)
3.28	R. M. Levitan, J. W. Heitz, M. Sweeney, and R. M. Cooper, "The Complexities of Tracheal Intubation With Direct Laryngoscopy and Alternative Intubation Devices," Ann. Emerg. Med., vol. 57, no. 3, pp. 240–247, 2011, doi: https://doi.org/10.1016/j.annemergmed.2010.05.035.	RightsLink® Licence Number 4957340114713
3.29 3.32-3.34 4.2 4.4-4.9 4.14-4.17	M. Zhao, T. J. C. O. Vrielink, A. A. Kogkas, M. S. Runciman, D. S. Elson, and G. P. Mylonas, "LaryngoTORS: A Novel Cable-Driven Parallel Robotic System for Transoral Laser Phonosurgery," IEEE Robot. Autom. Lett., vol. 5, no. 2, pp. 1516–1523, Apr. 2020, doi: 10.1109/LRA.2020.2969186.	IEEE default permission for usage in thesis/dissertation
5.1	M. Goncalves et al., "Probe-based confocal laser endomicroscopy in detecting malignant lesions of vocal folds," Acta Otorhinolaryngol. Ital., vol. 39, no. 6, pp. 389–395, Dec. 2019, doi: 10.14639/0392-100X-2121.	Permission is granted. (see letter below)
5.7	M. Zhao, H. Zhang, G. P. Mylonas, and D. S. Elson, "Cable-Driven Parallel Robot Assisted Confocal Imaging of the Larynx," in Biophotonics Congress: Biomedical Optics 2020 (Translational, Microscopy, OCT, OTS, BRAIN), 2020, p. TTu4B.4, doi: 10.1364/TRANSLATIONAL.2020.TTu4B.4.	Permission is granted. (see letter below)

Permission letter Figure 1.3 (left)

26 Nov 2020

Dear Sir or Madam,

I am completing my PhD thesis at Imperial College London entitled 'Cable-Driven Parallel Robot for Transoral Laser Phonosurgery'.

I seek your permission to reprint, in my thesis, an image extract from:

> K. Y. Lin and S. Y. Lu, "Panretinal navigated laser photocoagulation for PDR," *Retin. Today*, vol. JAN, no. FEB/-, pp. 65–70, 2014.

The extract to be reproduced is

> Figure 2, page 67, January/February 2014 retina today

I would like to include the extract in my thesis which will be added to Spiral, Imperial's institutional repository http://spiral.imperial.ac.uk/ and made available to the public under a Creative Commons Attribution Non-Commercial 4.0 International Licence (CC BY-NC).

If you are happy to grant me all the permissions requested, please return a signed copy of this letter. If you wish to grant only some of the permissions requested, please list these and then sign.

Yours sincerely,

Ming Zhao

Permission granted for the use requested above:

I confirm that I am the copyright holder of the extract above and hereby give permission to include it in your thesis which will be made available, via the internet, for non-commercial purposes under the terms of the user licence.

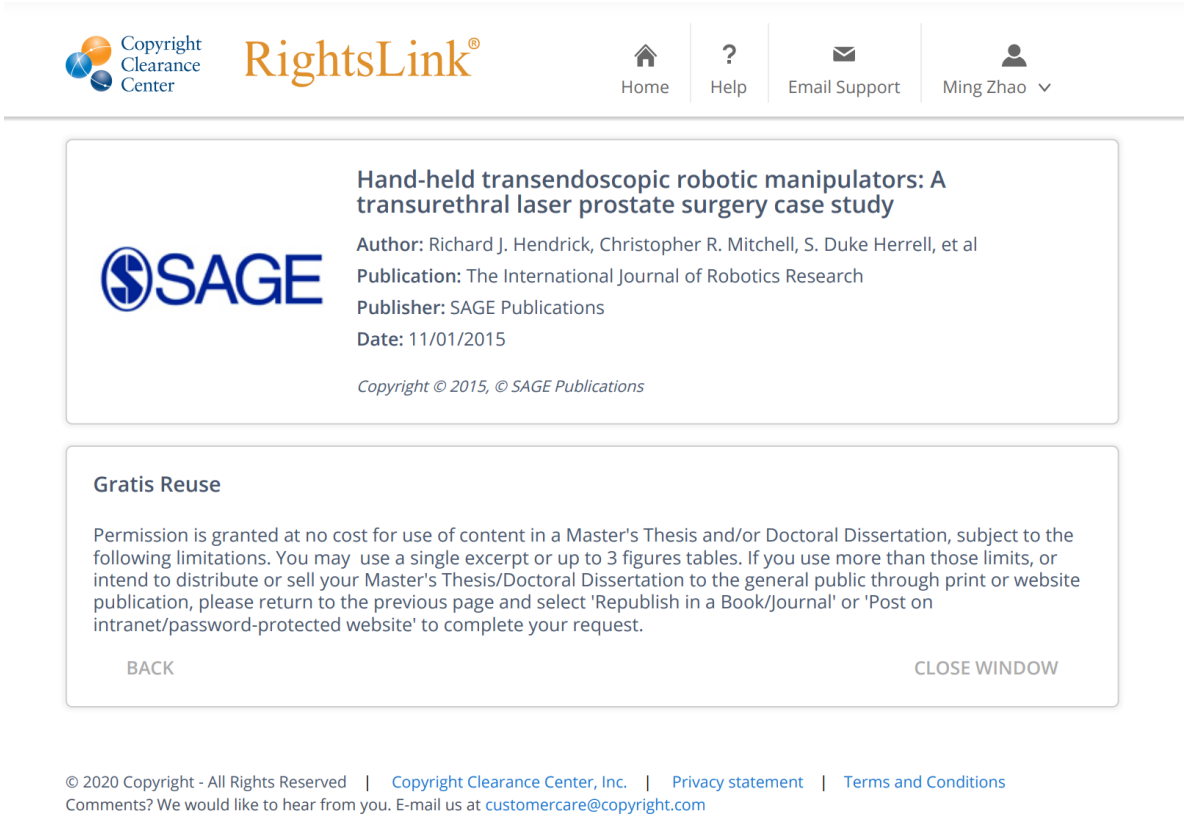
Signed: 

Name: Stephanie Lu, MD.

Organisation: University of California, Irvine.

Job title: Associate Professor of Clinical Health Science

Permission letter Figure 1.7a



Copyright Clearance Center RightsLink®

Home | Help | Email Support | Ming Zhao

SAGE

Hand-held transendoscopic robotic manipulators: A transurethral laser prostate surgery case study

Author: Richard J. Hendrick, Christopher R. Mitchell, S. Duke Herrell, et al

Publication: The International Journal of Robotics Research

Publisher: SAGE Publications

Date: 11/01/2015

Copyright © 2015, © SAGE Publications

Gratis Reuse

Permission is granted at no cost for use of content in a Master's Thesis and/or Doctoral Dissertation, subject to the following limitations. You may use a single excerpt or up to 3 figures tables. If you use more than those limits, or intend to distribute or sell your Master's Thesis/Doctoral Dissertation to the general public through print or website publication, please return to the previous page and select 'Republish in a Book/Journal' or 'Post on intranet/password-protected website' to complete your request.

BACK CLOSE WINDOW

© 2020 Copyright - All Rights Reserved | Copyright Clearance Center, Inc. | Privacy statement | Terms and Conditions
Comments? We would like to hear from you. E-mail us at customercare@copyright.com

Permission letter Figure 1.9b, 1.13, 1.14 and 1.15

16 April 2021

Dear Dr Oude Vrielink,

I am completing my PhD thesis at Imperial College London entitled 'Cable-Driven Parallel Robot for Transoral Laser Phonosurgery'.

I seek your permission to reprint, in my thesis, an image extract from your thesis:

> *T. J. C. Oude Vrielink, "Cable-driven parallel mechanisms for minimally invasive robotic surgery," Imperial College London, 2019.*

The extract to be reproduced is

> *Page 105, Figure 4.17.*
>
> *Page 150, Figure 6.9, 6.10.*
>
> *Page 191, Figure 8.1.*

I would like to include the extract in my thesis which will be added to Spiral, Imperial's institutional repository http://spiral.imperial.ac.uk/ and made available to the public under a Creative Commons Attribution-NonCommercial 4.0 International Licence (CC BY-NC).

If you are happy to grant me all the permissions requested, please return a signed copy of this letter. If you wish to grant only some of the permissions requested, please list these and then sign.

Yours sincerely,

Ming Zhao

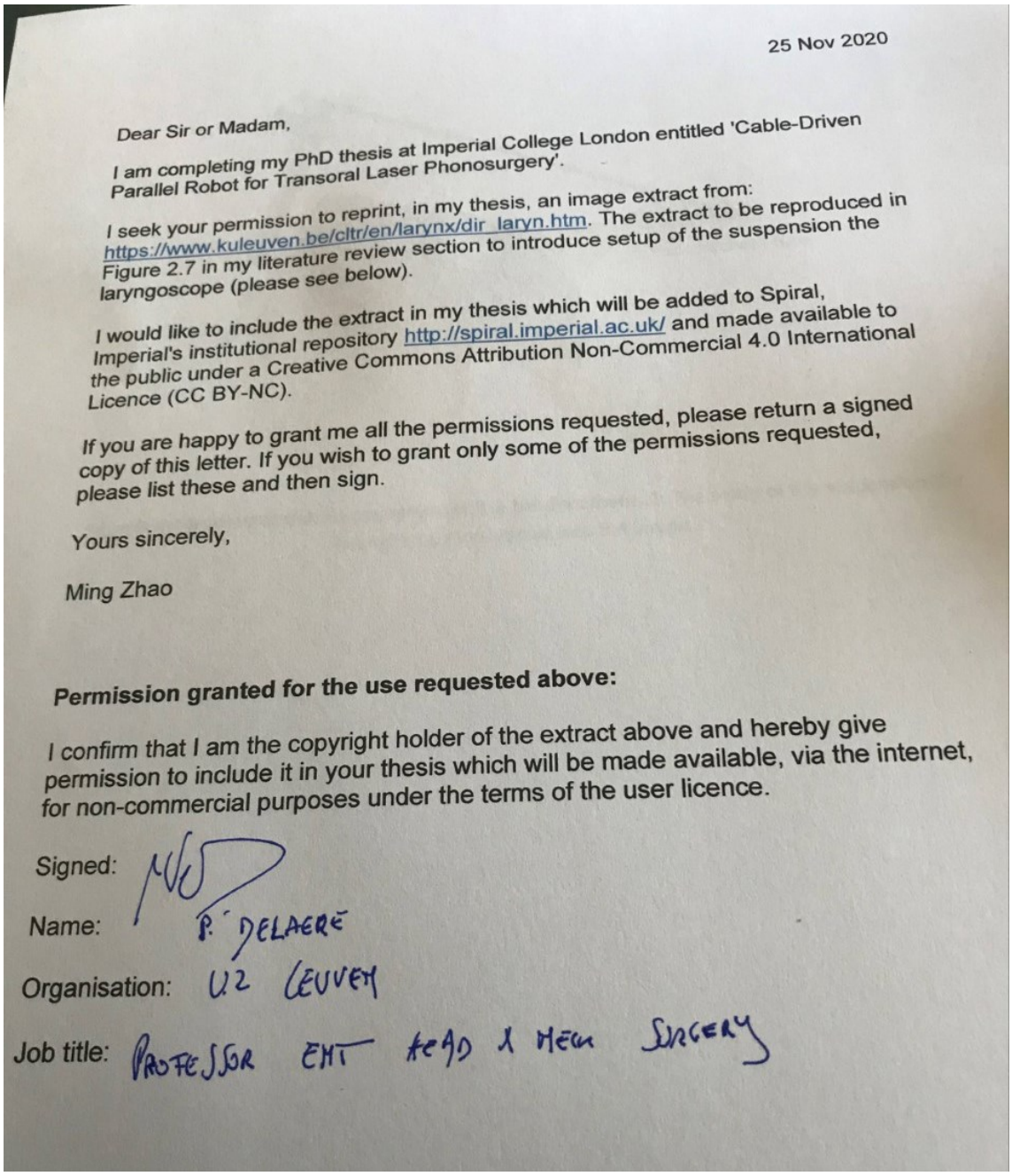
Permission granted for the use requested above:

I confirm that I am the copyright holder of the extract above and hereby give permission to include it in your thesis which will be made available, via the internet, for non-commercial purposes under the terms of the user licence.

Signed: 

Name: Timo J.C. Oude Vrielink

Permission letter Figure 2.6



25 Nov 2020

Dear Sir or Madam,

I am completing my PhD thesis at Imperial College London entitled 'Cable-Driven Parallel Robot for Transoral Laser Phonosurgery'.

I seek your permission to reprint, in my thesis, an image extract from: https://www.kuleuven.be/cltr/en/larynx/dir_laryn.htm. The extract to be reproduced in Figure 2.7 in my literature review section to introduce setup of the suspension the laryngoscope (please see below).

I would like to include the extract in my thesis which will be added to Spiral, Imperial's institutional repository http://spiral.imperial.ac.uk/ and made available to the public under a Creative Commons Attribution Non-Commercial 4.0 International Licence (CC BY-NC).

If you are happy to grant me all the permissions requested, please return a signed copy of this letter. If you wish to grant only some of the permissions requested, please list these and then sign.

Yours sincerely,

Ming Zhao

Permission granted for the use requested above:

I confirm that I am the copyright holder of the extract above and hereby give permission to include it in your thesis which will be made available, via the internet, for non-commercial purposes under the terms of the user licence.

Signed:

Name: P. DELAERE

Organisation: U2 LEUVEN

Job title: PROFESSOR ENT HEAD & NECK SURGERY

Permission letter Figure 2.9a

26 Nov 2020

Dear Sir or Madam,

I am completing my PhD thesis at Imperial College London entitled 'Cable-Driven Parallel Robot for Transoral Laser Phonosurgery'.

I seek your permission to reprint, in my thesis, an image extract from:

> Y. M. Park *et al.*, "Transoral robotic surgery (TORS) in laryngeal and hypopharyngeal cancer," *J. Laparoendosc. Adv. Surg. Tech.*, vol. 19, no. 3, pp. 361–368, 2009, doi: 10.1089/lap.2008.0320.

The extract to be reproduced is

> Figure 1, page 362
>
> Jun 1, 2009, Journal of Laparoendoscopic & Advanced Surgical Techniques

I would like to include the extract in my thesis which will be added to Spiral, Imperial's institutional repository http://spiral.imperial.ac.uk/ and made available to the public under a Creative Commons Attribution-NonCommercial 4.0 International Licence (CC BY-NC).

If you are happy to grant me all the permissions requested, please return a signed copy of this letter. If you wish to grant only some of the permissions requested, please list these and then sign.

Yours sincerely,

Ming Zhao

Permission granted for the use requested above:

I confirm that I am the copyright holder of the extract above and hereby give permission to include it in your thesis which will be made available, via the internet, for non-commercial purposes under the terms of the user licence.

Signed: 

Name: Karen Ballen

Organisation: Mary Ann Liebert, Inc., publishers

Job title: Open Access Manager

Permission letter Figure 2.15 and 2.16

AW: Requested Karger Material

Rights and Permissions <permission@karger.com>

Fri 27/11/2020 14:16

To: Zhao, Ming <m.zhao15@imperial.ac.uk>

This email from permission@karger.com originates from outside Imperial. Do not click on links and attachments unless you recognise the sender. If you trust the sender, add them to your safe senders list to disable email stamping for this address.

Dear Ming Zhao,

Thank you for your email. As to your request, I am pleased to inform you that permission is granted hereby to reprint your article

Orosco R, K, Arora A, Jeannon J, P, Holsinger F, C: Next-Generation Robotic Head and Neck Surgery. ORL 2018;80:213-219. doi: 10.1159/000490599

as a chapter in the printed and electronic version of your **thesis/doctoral dissertation**, provided that proper credit will be given to the original source and that S. Karger AG, Basel will be mentioned.

Please note that this is a non-exclusive permission, hence any further use, edition, translation or distribution, either in print or electronically, requires written permission again as this permission is valid for the above mentioned purpose only.

This permission applies only to copyrighted content that S. Karger AG owns, and not to copyrighted content from other sources. If any material in our work appears with credit to another source, you must also obtain permission from the original source cited in our work. All content reproduced from copyrighted material owned by S. Karger AG remains the sole and exclusive property of S. Karger AG. The right to grant permission to a third party is reserved solely by S. Karger AG.

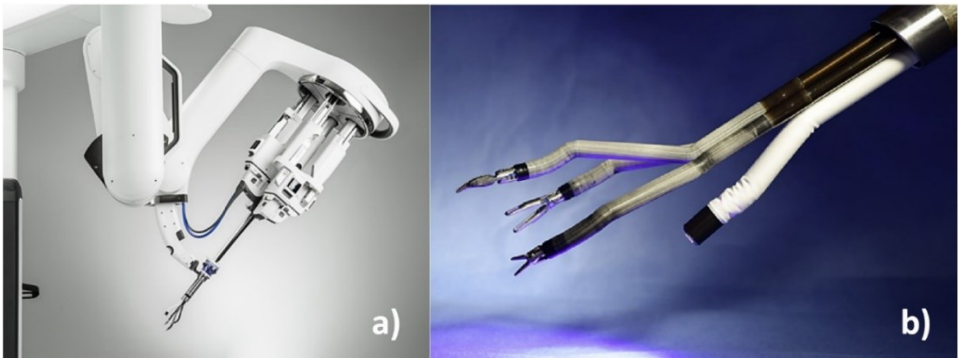
Thank you for your understanding and cooperation.

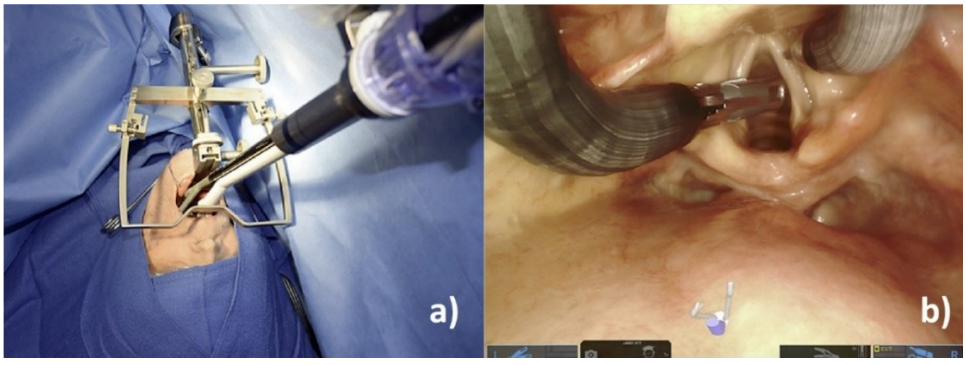
Hopefully, I have been of assistance to you with the above.

Kind regards

Samuel Lei

Rights & Permission Manager
ePartner Manager
s.lei@karger.com





Permission letter Figure 2.23a, 2.24 and 2.26b

26 Nov 2020

Dear Sir or Madam,

I am completing my PhD thesis at Imperial College London entitled 'Cable-Driven Parallel Robot for Transoral Laser Phonosurgery'.
I seek your permission to reprint, in my thesis, an image extract from:

> A. Acemoglu, N. Deshpande, and L. S. Mattos, "Towards a Magnetically-Actuated Laser Scanner for Endoscopic Microsurgeries," *J. Med. Robot. Res.*, vol. 03, no. 02, p. 1840004, 2018, doi: 10.1142/s2424905x18400044.

The extract to be reproduced is

> Figure 2, 3 and 11 (please see below).

I would like to include the extract in my thesis which will be added to Spiral, Imperial's institutional repository http://spiral.imperial.ac.uk/ and made available to the public under a Creative Commons Attribution-NonCommercial 4.0 International Licence (CC BY-NC).

If you are happy to grant me all the permissions requested, please return a signed copy of this letter. If you wish to grant only some of the permissions requested, please list these and then sign.

Yours sincerely,

Ming Zhao

Permission granted for the use requested above:

I confirm that I hereby give permission to include it in your thesis which will be made available, via the internet, for non-commercial purposes under the terms of the user licence.

Signed: 

Name: Alperen Acemoglu

Organisation: Istituto Italiano di Tecnologia, Genoa, Italy

Job title: Postdoctoral researcher

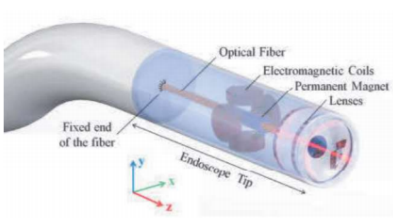


Figure 2

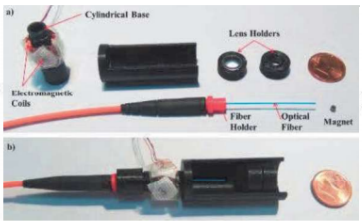


Figure 3

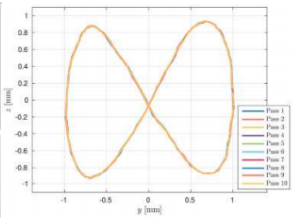


Figure 11

Permission letter Figure 3.1 and 3.5

27 Nov 2020

Dear Sir or Madam,

I am completing my PhD thesis at Imperial College London entitled 'Cable-Driven Parallel Robot for Transoral Laser Phonosurgery'.

I seek your permission to reprint, in my thesis, an image extract from:

> V. L. Schmidt, *Modeling Techniques and Reliable Real-Time Implementation of Kinematics for Cable-Driven Parallel Robots using Polymer Fiber Cables*. 2017.

The extract to be reproduced is

> Figure 1.1 and 2.1 (please see below).

I would like to include the extract in my thesis which will be added to Spiral, Imperial's institutional repository http://spiral.imperial.ac.uk/ and made available to the public under a Creative Commons Attribution-NonCommercial 4.0 International Licence (CC BY-NC).

If you are happy to grant me all the permissions requested, please return a signed copy of this letter. If you wish to grant only some of the permissions requested, please list these and then sign.

Yours sincerely,

Ming Zhao

Permission granted for the use requested above:

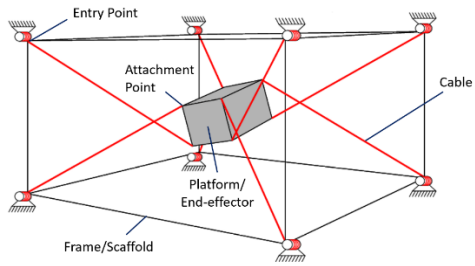
I confirm that I am the copyright holder of the extract above and hereby give permission to include it in your thesis which will be made available, via the internet, for non-commercial purposes under the terms of the user licence.

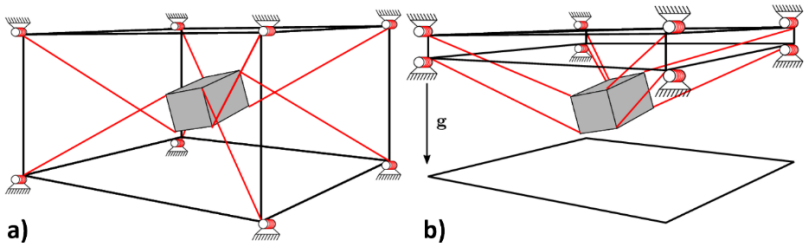
Signed: V. Schmidt

Name: Valentin Schmidt

Organisation: Fraunhofer IPA (ex.)

Job title: Research Engineer





Permission letter Figure 3.2b

27 Nov 2020

Dear Sir or Madam,

I am completing my PhD thesis at Imperial College London entitled 'Cable-Driven Parallel Robot for Transoral Laser Phonosurgery'.

I seek your permission to reprint, in my thesis, an image extract from:

> C. GOSSELIN, "Cable-driven parallel mechanisms: state of the art and perspectives," *Mech. Eng. Rev.*, vol. 1, no. 1, pp. DSM0004–DSM0004, 2014, doi: 10.1299/mer.2014dsm0004.

The extract to be reproduced is

> Figure 7 (please see below).

I would like to include the extract in my thesis which will be added to Spiral, Imperial's institutional repository http://spiral.imperial.ac.uk/ and made available to the public under a Creative Commons Attribution-NonCommercial 4.0 International Licence (CC BY-NC).

If you are happy to grant me all the permissions requested, please return a signed copy of this letter. If you wish to grant only some of the permissions requested, please list these and then sign.

Yours sincerely,

Ming Zhao

Permission granted for the use requested above:

I confirm that I am the copyright holder of the extract above and hereby give permission to include it in your thesis which will be made available, via the internet, for non-commercial purposes under the terms of the user licence.

Signed: Osamu Inoue

Name: Osamu Inoue

Organisation: The Japan Society of Mechanical Engineers

Job title: Publishing Department Manager

Date: 1st December 2020



Permission letter Figure 3.4

30 Nov 2020

Dear Sir or Madam,

I am completing my PhD thesis at Imperial College London entitled 'Cable-Driven Parallel Robot for Transoral Laser Phonosurgery'.

I seek your permission to reprint, in my thesis, an image extract from:

> R. Verhoeven, "Analysis of the workspace of tendon-based Stewart platforms," Universität Duisburg-Essen, Fakultät für Ingenieurwissenschaften~…, 2004.

The extract to be reproduced is

> Figure 2.8 (please see below).

I would like to include the extract in my thesis which will be added to Spiral, Imperial's institutional repository http://spiral.imperial.ac.uk/ and made available to the public under a Creative Commons Attribution-NonCommercial 4.0 International Licence (CC BY-NC).

If you are happy to grant me all the permissions requested, please return a signed copy of this letter. If you wish to grant only some of the permissions requested, please list these and then sign.

Yours sincerely,

Ming Zhao

Permission granted for the use requested above:

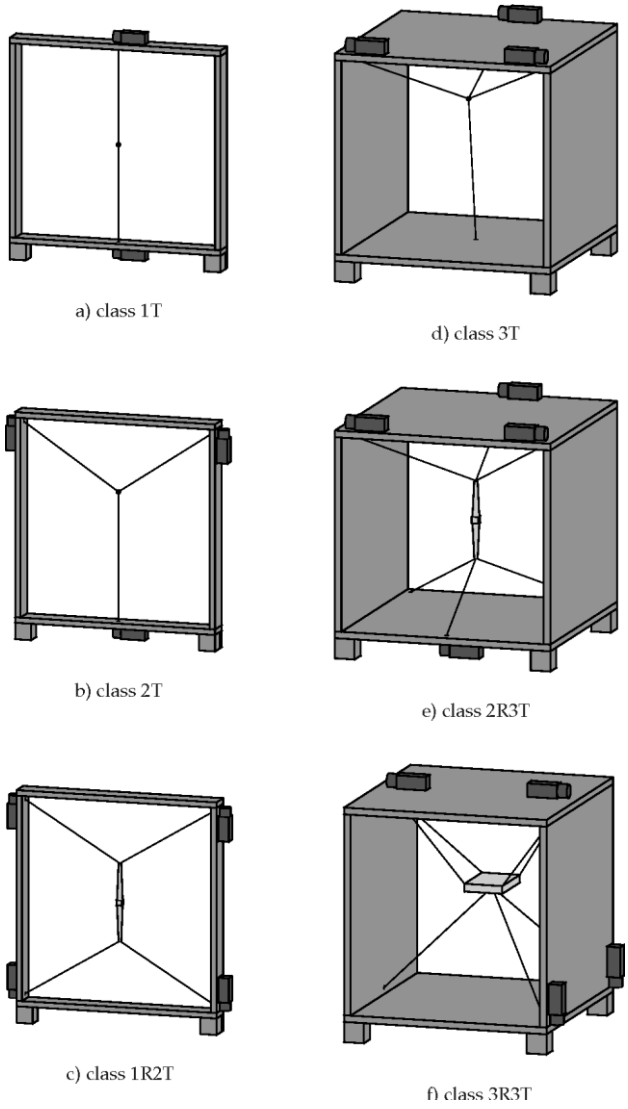
I confirm that I am the copyright holder of the extract above and hereby give permission to include it in your thesis which will be made available, via the internet, for non-commercial purposes under the terms of the user licence.

Signed:

Name: Richard Verhoeven

Organisation: Universität Duisburg-Essen

Job title: Former PhD student



Permission letter Figure 5.1

Re: Copyright permission usage in PhD dissertation_Ming Zhao

SusannaCampigli <scampigli@pacinieditore.it>
Tue 01/12/2020 18:12
To: Zhao, Ming <m.zhao15@imperial.ac.uk>

1 attachments (12 KB)
PastedGraphic-4.tiff;

This email from scampigli@pacinieditore.it originates from outside Imperial. Do not click on links and attachments unless you recognise the sender. If you trust the sender, add them to your safe senders list to disable email stamping for this address.

Dear Sir,
We confirm that we grant the permission to reproduce the figure from Acta Otorhynolaringologica Italica in your Phd thesis. At terms and condition you explain in your request (presence on Spiral, Imperial's institutional repository http://spiral.imperial.ac.uk/ and made available to the public under a Creative Commons Attribution Non-Commercial 4.0 International Licence (CC BY-NC).
No fee is requested. You only have to respect general rules to correctly cite the figure and the source.
Best regards
Susanna Campigli

Il giorno 01 dic 2020, alle ore 08:02, Lisa Andreazzi <landreazzi@pacinieditore.it> ha scritto:

Permission letter Figure 5.7

RE: Copyright permission usage in PhD dissertation_Ming Zhao

pubscopyright <copyright@osa.org>
Mon 07/12/2020 14:16
To: Zhao, Ming <m.zhao15@imperial.ac.uk>; pubscopyright <copyright@osa.org>

This email from copyright@osa.org originates from outside Imperial. Do not click on links and attachments unless you recognise the sender. If you trust the sender, add them to your safe senders list to disable email stamping for this address.

Dear Dr. Zhao,

Thank you for contacting The Optical Society.

For the use of material from M. Zhao, H. Zhang, G. P. Mylonas, and D. S. Elson, "Cable-Driven Parallel Robot Assisted Confocal Imaging of the Larynx," in Biophotonics Congress: Biomedical Optics 2020 (Translational, Microscopy, OCT, OTS, BRAIN), OSA Technical Digest (Optical Society of America, 2020), paper TTu4B.4:

> OSA only has copyright for the compilation of the conference proceedings, not the individual papers themselves. As the authors retain copyright to the individual paper, an OSA credit statement is not needed, although we do request a complete citation be included in any publication or adjacent to any posting.

Please let me know if you have any questions.

Kind Regards,
Hannah Greenwood

Hannah Greenwood
December 7, 2020
Authorized Agent, The Optical Society

The Optical Society (OSA)
2010 Massachusetts Ave., NW
Washington, DC 20036 USA
www.osa.org
Season's Greetings from OSA!
Please note that the OSA office will be closed for the holidays from Friday, 25 December 2020 reopening Monday, 4 January 2021.

Reflecting a Century of Innovation